EPFL

Thèse n° 10 482

Adaptive Finite Elements With Large Aspect Ratio. Application to Aluminium Electrolysis.

Présentée le 23 février 2024

Faculté des sciences de base
Groupe Picasso
Programme doctoral en mathématiques

pour l'obtention du grade de Docteur ès Sciences

par

Paride PASSELLI

Acceptée sur proposition du jury

Prof. F. Nobile, président du jury
Prof. M. Picasso, directeur de thèse
Prof. A. Lozinski, rapporteur
Dr N. Chailly, rapporteuse
Prof. S. Deparis, rapporteur

École polytechnique fédérale de Lausanne

2024

Alla mia amata famiglia:
Katiuska, Maruska e Roberto.

Acknowledgements

This thesis was a wonderful, challenging and tough journey. It wouldn't have been feasible without the help of many people. I owe my total gratitude to all of them. The following words are an attempt to express my gratitude to all of you.

First of all I want to thank my supervisor Prof. Marco Picasso, who allowed me to work on such an interesting topic. I am grateful for his constant support, his teachings, his advice and for his continuous trust in me. Collaborating with you was enriching and what I have learnt is priceless.

Next, I would like to thank the jury of my thesis. Prof. Fabio Nobile who accepted the role of president. Dr. Nadia Chailly, Prof. Simone Deparis and Prof. Alexei Lozinski for the interesting comments, advice and the formative discussion on my research.

A big thanks to Ycoor System for helping me with the Alucell software. Thank you Alexandre Masserey and Julien Hess for your help. I appreciate your patience and your constant motivation.

This thesis was funded by Rio Tinto Aluminium Pechiney. I would like to thank them for their trust in my work, their suggestions and the fruitful collaboration. Thanks to Prof. Jacques Rappaz for his, always appreciated, opinion and incredible knowledge.

Thanks to Dr. François Genoud. Collaborating with you in the teaching of "analyse avancée I" was a great work experience. I learnt a lot from you.

Thanks to the whole Picasso group. Having a nice work environment is a necessary condition to succeed. Thanks to Arwa Mrad, Dimitrios Gourzoulidis, Michele Barucca, Théophile Boinnard, Anna Peruso, Markus Renoldner, Ferhat Sindy, Ariane Cordonier, Alexandre Caboussat and all the others.

I want to express my sincere gratitude to all the friends I made during these years. Thanks to Emile Soutter for the industrial collaboration and for all the funny nights spent playing board games at his place. Thank you Jean Fornerod for all the nice moments (e.g. the "cave ouverte"). Thank you Léo Diserens for being such a positive person, for the amazing time spent together (even though sometimes a translator was necessary). You have been fundamental for my Ph.D. and I am happy to have made this experience with you. A special thanks to Samuel Dubuis, a big brother always there to support me. I appreciate your passion in mathematics, in particular in the wonderful world of anisotropic finite elements. A lot is due to you. Thanks to the best office mate possible Maude Girardin. Being in the office was like being at home. Thanks for all the moments spent together at SAT, in the mountains, travelling or doing research together. I owe

you a lot. Thanks to David Strütt, who passed from being "the nice assistant of Analysis III and IV" to a great friend. Thanks to Diane Guignard for the nice moments spent together. Big thanks to David Persson, always there for me when I needed. I loved every single moment spent together. Thank you Axel Séguin for the beers and the days in Ticino. Thanks to Boris Bonev and Clara Ramis, swimming together or eating together at Manira, are only part of the wonderful time we had. Thanks to Guillaume Buro for the nice concerts. Thanks again to each of you. You made this journey unforgettable.

A lot is due also to friends made before EPFL. Thanks to Nicola Stoira, the best friend I could ask for. Always there since day one and always ready to call and meet whenever I was facing a good or bad day. Thank you for being who you are and for being a certainty in my life. Thanks to the Mergoscia's Team: Sara Capella, a friend since we were two years old (even though you were unable to accept the established roles in games). Thanks Filippo Franscella, Laura Heggemann (adopted by Mergoscia) and Sofia Guntri, the "Tea" team. All the evenings spent together drinking tea, playing cards, watching movies or just talking were such a pleasure for me. Thanks to all the friends Omar Guerra, Marc Müller, Elia Bähler, Gioele Genazzi, Aura Martinelli (thanks for all the funny moments at Rolex!). Thanks to the "ticinesi" at EPFL, Lia Gander, Luca Pedrelli and Francesco Calignano. You helped me going through the tough journey of bachelor and master. Thanks to everyone.

Finally I want to thank my family. First, thanks to Tim Beltraminelli. Your support and help in these years was precious.

This part is dedicated to Katiuska, my sister. The person that was there to support me during all the journey. I always appreciate everything you did and you do for me, your constant support during these years was fundamental. You are the reason why I started EPFL and one of the only reasons why I was able to succeed. I can never express enough gratitude to you. Stopping living together will probably be one of the hardest part of my life. I love you.

L'ultima parte la dedico a voi, Mamma e Papi. Vi devo tutto e siete ciò che mi ha permesso di arrivare qui. Vi ringrazio, per esserci sempre stati e perché ci sarete sempre. Il vostro perenne aiuto e la vostra presenza sono la cosa più preziosa che ho. Vi voglio bene.

Lausanne, February 5, 2024 Paride Passelli

Abstract

The goal of this work is to use anisotropic adaptive finite elements for the numerical simulation of aluminium electrolysis. The anisotropic adaptive criteria are based on a posteriori error estimates derived for simplified problems. First, we consider the elliptic problem $-\nabla \cdot (\mu \cdot \nabla u) = f$ with $\mu > 0$ smooth, but strongly varying. We then study the steady Stokes equation $-\mu \Delta u + \nabla p = f$ with $\mu > 0$ constant and finally the nonlinear p-Laplace problem $-\nabla((\mu + |\nabla u|^{p-2})\nabla u) = f$ with $\mu \geq 0$ constant and $p \geq 2$. In particular, we focus on continuous piecewise linear finite elements with possibly large aspect ratio. Whenever possible, error estimates are proven to be equivalent to the numerical error with constants independent from the mesh aspect ratio. Numerical experiments confirming these predictions are presented.

Adaptive strategies based on the derived error estimates are proposed. Numerical experiments show sharpness of the estimates on adapted meshes. For a given accuracy the computational time is reduced.

Finally, numerical simulations of the aluminium electrolysis process, using adaptive meshes, are considered. The fluid-flow problem without and with gas is studied. Numerical results confirming a reduction of the computational time are presented.

Key words: A posteriori error estimates, Adaptive algorithms, Anisotropic finite elements, Elliptic problem, Nonlinear equation, p-Laplacian problem, Stokes equation, Aluminium electrolysis.

Résumé

Le but de ce travail est d'utiliser des éléments finis anisotropes adaptatifs pour la simulation numérique de l'électrolyse d'aluminium. Les critères d'adaptation anisotropes sont basés sur des estimateurs d'erreur a posteriori, dérivés pour des problèmes simplifiés. Dans un premier temps, nous considérons le problème elliptique $-\nabla \cdot (\mu \cdot \nabla u) = f$, où la fonction $\mu > 0$ est régulière, mais peut avoir de fort gradients. Nous étudions ensuite l'équation de Stokes stationnaire $-\mu\Delta u + \nabla p = f$, avec $\mu > 0$ constant. Finalement, nous nous intéressons au problème p-Laplacien nonlinéaire $-\nabla((\mu + |\nabla u|^{p-2})\nabla u) = f$, avec $\mu \geq 0$ constant et $p \geq 2$. Nous nous concentrons en particulier sur des éléments finis continus, linéaires par morceaux, pouvant avoir un grand rapport d'aspect. Lorsque cela est possible, l'équivalence des estimateurs d'erreur et de l'erreur numérique est démontrée, avec des constantes indépendantes du rapport d'aspect du maillage. Des résultats numériques confirmant ces prédictions sont présentés.

Des stratégies d'adaptation basées sur les estimateurs d'erreur dérivés sont proposées. Les expériences numériques démontrent la précision des estimateurs sur des maillages adaptés. En particulier, pour une précision donnée, le temps de calcul est réduit.

Finalement, des simulations numériques du processus d'électrolyse d'aluminium réalisées avec des maillages adaptatifs sont présentées. Le problème d'écoulement des fluides, avec et sans gaz, est présenté. Des résultats numériques confirmant une réduction du temps de calcul sont discutés.

Mots clefs : Estimateurs d'erreur a posteriori, Algorithmes adaptatifs, Elements finis anisotropes, Problèmes elliptiques, Problème nonlinéaire, P-Laplacian, Equation de Stokes, Electrolysis d'aluminium.

Table des matières

Notations

We introduce some notations used along this work.

Let $\Omega \subset \mathbb{R}^d$, $d = 2, 3$ a Lipschitz domain with boundary $\partial\Omega$. For $1 \leq p < +\infty$ we define

- $L^p(\Omega) = \{v : \Omega \to \mathbb{R} : v \text{ measurable and such that } \int_\Omega |u|^p < +\infty\}$
- $L^2_0(\Omega) = \{v \in L^2(\Omega) : \int_\Omega v = 0\}$
- $L^\infty(\Omega) = \{v : \Omega \to \mathbb{R} : v \text{ measurable and } \exists C > 0 \text{ such that } |v| \leq C \text{ a.e.}\}$

Let $n \in \mathbb{N}_+$, $\alpha = (\alpha_1, \ldots, \alpha_n) \in \mathbb{N}^n$ be a multi-index and $|\alpha| = \sum_{i=1}^n \alpha_i$, we define

- $D^\alpha v = \frac{\partial^{|\alpha|} v}{\partial_{x_1}^{\alpha_1} \cdots \partial_{x_n}^{\alpha_n}}$

Let $m \in \mathbb{N}_+$ and $1 \leq p \leq \infty$, the following Sobolev spaces are defined

- $W^{m,p}(\Omega) = \{v : \Omega \to \mathbb{R} : D^\alpha v \in L^p(\Omega) \ \forall \ |\alpha| \leq m\}$
- $W_0^{m,p}(\Omega) = \{v \in W^{m,p}(\Omega) : v_{|\partial\Omega} = 0\}$, where $v_{|\partial\Omega} = 0$ has to be understood in terms of traces.
- $H^m(\Omega) = W^{m,2}(\Omega)$
- $H_0^m(\Omega) = W_0^{m,2}(\Omega)$

Let $\mathbf{x} = (x_1, \ldots, x_d) \in \mathbb{R}^d$, $1 \leq p < \infty$ and $A \in \mathbb{R}^{d \times d}$, the following discrete norms notations are used

- p-norm : $|| \cdot ||_p = \left(\sum_{i=1}^d |x_i|^p\right)^{1/p}$
- infinity norm : $||\mathbf{x}||_\infty = \max_{1 \leq i \leq d} |x_i|$
- $||A||_p = \sup_{||\mathbf{x}||_p \neq 0} \frac{||A\mathbf{x}||_p}{||\mathbf{x}||_p}$

When no confusion is possible, we refer to the p-norm as $|\cdot|$. Let $1 \leq p < \infty$, the following continuous norms notations are used

- for $v \in L^p(\Omega)$, $||v||_{L^p(\Omega)} = \left(\int_\Omega ||v||_p^p\right)^{1/p}$

- for $v \in W^{m,p}(\Omega)$, $||v||_{W^{m,p}(\Omega)} = \left(\sum_{|\alpha| \leq m} ||D^\alpha v||^p_{L^p(\Omega)} \right)^{1/p}$
- for $v \in W^{m,p}(\Omega)$, $|v|_{W^{m,p}(\Omega)} = \left(\sum_{|\alpha| = m} ||D^\alpha v||^p_{L^p(\Omega)} \right)^{1/p}$
- for $v \in L^\infty(\Omega)$, $||v||_{L^\infty(\Omega)} = \inf\{C \geq 0 : |v| \leq C \text{ a.e.}\}$

Additionally we introduce the following frequent notations.

- For $h > 0$, $\mathcal{T}_h$ is a mesh of $\overline{\Omega}$ in element K_j of diameter $h_{K_j} \leq h$. We have $\overline{\Omega} = \cup_{K_j \in \mathcal{T}_h} K_j$ with $K_i \cap K_j = \emptyset$ if $i \neq j$.
- When $d = 2$, we consider triangular meshes.
- When $d = 3$, we consider tetrahedral meshes.
- We define ∂K_i a boundary element of K for $i = 1, \ldots, d+1$ (an edge of triangle K when $d = 2$ and a face of thetrahedron K when $d = 3$).
- We set $h = \max_{K \in \mathcal{T}_h} h_K$ as the mesh size.
- ρ_K is the diameter of the largest inscribed ball in K.
- $\gamma_K = \frac{h_K}{\rho_K}$ is the aspect ratio of K.
- We note ΔK the patch of element K, i.e. the set of elements sharing a vertex with K.
- $\hat{K}$ is a reference element and $T_K : \hat{K} \to K$ is an affine transformation.
- We refer to $\mathbf{r}_{i,K}$ as the i^{th} unit vector corresponding to the i^{th} stretching direction of K and $\lambda_{i,K}$ as the corresponding value of stretching. Both with respect to the affine map T_K.
- $\hat{C}$ denotes a positive constant depending only on $\hat{K}$, which may vary from line to line.
- u usually denotes the exact solution of a PDE.
- V_h is the usual finite elements space of continuous, piecewise linear, function, on element K with zero value of $\partial\Omega$.
- u_h denotes the piecewise continuous finite elements solution of a PDE.
- For any $v \in W^{m,p}(K)$ we denote $\hat{v} \in W^{m,p}(\hat{K})$ the corresponding function defined on the reference element $\hat{K}$ through changes of variable T_K.

Introduction

This work is financially supported by Rio Tinto Aluminium and motivated by the numerical simulation of aluminium electrolysis.

Aluminium is a widely used element in industrial productions, but can not be found in its pure form in nature. It is thus necessary to produce aluminium from other existing minerals. Hall-Héroult process produces pure aluminium (Al) from alumina (Al_2O_3). It is a complex method with an important carbon footprint. According to [24], it is responsible for 1.7% of the worldwide carbon footprint and for 3% of the worldwide electric current consumption. Optimizing such a process is thus essential. Measures and practical experiments are often expensive, complicate or even not possible. The development of mathematical models to describe such a phenomena is therefore fundamental.

Aluminium electrolysis can be modelled using partial differential equations (PDEs), whose exact solution is in most case out of reach. Numerical methods to build, efficiently and, with some guarantees, an approximated solution therefore need to be addressed. Since the geometry of the computational domain is complex, we will use the finite element method.

Let $\Omega \subset \mathbb{R}^d$, $d = 2, 3$, be the computational domain of a stationary partial differential equation $F(u) = 0$ with F a differential operator and u the solution. When using finite elements, a so-called mesh, of Ω is needed. Given $h > 0$, let $\mathcal{T}_h$ be a partition of Ω in non-overlapping polyhedrons K with diameter h_K less or equal than h. We denote u_h the approximate solution computed using the mesh $\mathcal{T}_h$. Assessing the precision of the finite element method is fundamental. If $||u - u_h||$ is a measure of the committed error, typical questions are : does $||u - u_h||$ go to 0 when h does ? How fast ? This kind of questions are addressed by a priori error analysis, which provides bounds of the form

$$||u - u_h|| \leq Ch^\alpha ||D^\beta u|| \tag{1}$$

with $\alpha > 0$ and D^β the derivative of order $\beta > 0$. The right hand side of the a priori error estimates involves the unknown exact solution. Having a computable right hand side could be very useful. This is the goal of a posteriori error analysis, which aim to derive error estimates of the form

$$||u - u_h|| \leq C\eta(u_h), \tag{2}$$

where C should be independent of u and h and $\eta(u_h)$ is computable once u_h is known.

Several classes of meshes can be considered and their characteristics may influence the error $||u - u_h||$. We focus in particular on

- shape regular meshes : meshes having aspect ratio of each element uniformly bounded by a constant independent of h ;
- anisotropic meshes : meshes with possible large aspect ratio.

A posteriori error estimates were first derived for shape regular meshes [8, 72, 58, 27, 71, 7, 1, 73, 12], the constant C in (2) depending on the aspect ratio. However having meshes with large aspect ratio can be considerably useful, typically when dealing with boundary layers or regions where the solution u has strong variations. In order to cope with this kind of meshes, a new framework has been introduced [33, 34, 43, 6]. New anisotropic a posteriori error estimates have been developed [43, 55, 74, 51, 23, 33, 34, 32, 62, 60, 52, 16, 14].

One of the first goal of this work is to derive a posteriori error estimates able to deal with anisotropic meshes and to prove and check numerically an equivalence with the numerical error, that is to say

$$C_1\eta(u_h) \leq ||u - u_h|| \leq C_2\eta(u_h).$$

Moreover we aim to prove the following characteristics of the error estimator $C\eta(u_h)$

- Independence of $\frac{\eta(u_h)}{||u-u_h||}$ from the solution u,
- Independence of $\frac{\eta(u_h)}{||u-u_h||}$ from the aspect ratio,
- Independence of $\frac{\eta(u_h)}{||u-u_h||}$ from the parameters of the PDE.

A second subject of interest is to implement adaptive finite elements. For a given accuracy, adaptive finite elements demonstrated their efficiency to solve PDEs at a reduced computational cost. The adaptive criteria is often based on an a posteriori error estimator. In the isotropic framework many works have been presented [10, 72, 58, 27, 71, 7, 1, 55, 75]. With the development of the new anisotropic framework, adaptive finite elements with large aspect ratio have been also studied [3, 15, 38, 65, 62, 5, 4, 32, 58]. In this work we present algorithms based on adaptive finite elements with possible large aspect ratio. The main goal of these algorithms is to build sequences of meshes, having possible large aspect ratio, for a prescribed accuracy. Roughly speaking, for a given accuracy TOL, we aim to construct meshes such that

$$||u - u_h|| \simeq \eta(u_h) \simeq TOL.$$

Consequently, the computational time to obtain an approximated solution for a given accuracy is reduced. This approach could be very useful, when simulating aluminium electrolysis, which requires huge computations.

To summarize, our main goals are :

- to derive a posteriori error estimates useful also when large aspect ratio meshes are considered ;
- to use adaptive finite elements based on the estimates to reduce the computational time needed to reach a given level of accuracy.
- to apply these algorithms to the numerical simulation of aluminium electrolysis.

The present work is divided in two parts : the first part (Chapter 1 to Chapter 4) deals with theoretical foundations and numerical experiments on academic problems. The second part (Chapter 5) is dedicated to the industrial application to aluminium electrolysis.

In **Chapter 1** the anisotropic finite elements setting [33, 34], used in the whole thesis is presented. Useful anisotropic interpolation error estimates in the L^p norm are proved.

In **Chapter 2**, the elliptic problem

$$\begin{aligned} -\nabla \cdot (\mu \nabla u) &= f && \text{in } \Omega, \\ u &= 0 && \text{on } \partial\Omega, \end{aligned}$$

where $\mu > 0$ is smooth but strongly varying, is studied. In Section 2.2, an anisotropic a posteriori error estimator is presented. Upper and a new lower bound for the numerical error $||\mu^{1/2}\nabla(u - u_h)||_{L^2(\Omega)}$ are proved. The equivalence between the error estimator and the numerical error, up to higher order terms, is demonstrated (Theorem 2.1). In Section 2.3, numerical experiments confirming theoretical predictions on non-adapted meshes are discussed. Adaptive algorithms, based on a posteriori error estimates, are introduced in section 2.4. Finally, numerical experiments with adapted-meshes, proving theoretical predictions and efficiency of the algorithms are discussed. This chapter is based on [29].

In **Chapter 3** the steady Stokes problem

$$\begin{aligned} -\operatorname{div}(\mu \nabla \mathbf{u}) + \nabla p &= \mathbf{f} && \text{in } \Omega, \\ \operatorname{div}(\mathbf{u}) &= 0 && \text{in } \Omega, \\ \mathbf{u} &= 0 && \text{on } \partial\Omega, \end{aligned}$$

where $\mu > 0$ is a constant, is presented. In Section 3.2 an upper bound of the numerical error is demonstrated (Theorem 3.1) and an error indicator for the semi-norm $\mu||\nabla(u - u_h)||_{L^2(\Omega)}$ is introduced. In Section 3.3 numerical experiments with non-adapted meshes showing sharpness of the error indicator are presented. We then present numerical results of adaptive algorithms based on the error indicator (Section 3.4).

Chapter 4 is based on [56]. The nonlinear p-Laplacian problem

$$\begin{aligned} -\nabla \cdot ((\mu + |\nabla u|^{p-2})\nabla u) &= f && \text{in } \Omega, \\ u &= 0 && \text{on } \partial\Omega \end{aligned}$$

where $\mu \geq 0$ is a constant, is considered. In section 4.2 anisotropic a posteriori error estimates for the $W_0^{1,p}$ norms and a quasi-norm are presented. A lower bound, for the quasi-norm only, is demonstrated and equivalence, up to higher order terms, of quasi-norm numerical error and error estimator is shown (Theorem 4.3). Numerical experiment with non-adapted meshes are discussed in Section 4.3. Applications of adaptive algorithms with the new error estimators are reported in Section 4.4.

In **Chapter 5** an application to aluminium electrolysis is presented. Sections 5.2 and 5.3 are dedicated to the study of adaptive meshes for the fluid-flow problem. An error indicator to construct adapted meshes for the fluid-domain is presented. Two different adaptation strategies are discussed and numerical experiments showing the benefits of adaptive meshes, when solving the fluid-flow problem are presented. In Section 5.4 we test our adaptive approach, when solving the fluid-flow problem taking into account a mixture model for diluted gas in the liquid flow. Numerical results are presented. In section 5.5 a different fluid domain is considered and numerical experiments with adaptive meshes are shown. A new adaptive strategy with an interest for industrial computation is discussed.

1 Mathematical setting

The goal of this chapter is to present the anisotropic setting which will be useful in the whole thesis. The framework of [33, 34] is used. Let $\Omega \subset \mathbb{R}^d$ be a polygon for $d = 2$ and a polyhedron for $d = 3$. For any $h > 0$, let $\mathcal{T}_h$ be any conformal mesh of Ω into elements K (triangles for $d = 2$, tetrahedra for $d = 3$) of diameter $h_K \leq h$. Let V_h be the usual finite elements space of continuous, piecewise linear, functions, on elements K of $\mathcal{T}_h$, with zero value on $\partial\Omega$. For any $K \in \mathcal{T}_h$ we denote by $T_K : \hat{K} \to K$ one of the affine transformation mapping the reference element $\hat{K}$ into K defined by

$$\mathbf{x} = T_K(\hat{\mathbf{x}}) = M_K \hat{\mathbf{x}} + \mathbf{t}_K, \tag{1.1}$$

where $M_K \in \mathbb{R}^{d\times d}$ and $\mathbf{t}_K \in \mathbb{R}^d$. Since M_K is invertible, it admits a singular value decomposition $M_K = R_K^T \Lambda_K P_K$, where R_K and P_K are orthogonal matrices and

$$\Lambda_K = \begin{pmatrix} \lambda_{1,K} & & \\ & \ddots & \\ & & \lambda_{d,K} \end{pmatrix}, \quad \lambda_{1,K} \geq \cdots \geq \lambda_{d,K} > 0, \qquad R_K = \begin{pmatrix} \mathbf{r}_{1,K}^T \\ \vdots \\ \mathbf{r}_{d,K}^T \end{pmatrix}.$$

In the above notations, $\mathbf{r}_{1,K}, \ldots, \mathbf{r}_{d,K}$ are the unit vectors corresponding to the directions of stretching of K and $\lambda_{1,K} \geq \cdots \geq \lambda_{d,K} > 0$ to the corresponding amplitude. A geometrical interpretation is shown in Figure 1.1 for $d = 2$. Note that, since T_K is not uniquely defined, then neither $\lambda_{i,K}, \mathbf{r}_{i,K}$, $i = 1, \ldots, d$ are.

In the standard isotropic finite elements theory, interpolation estimates involve constants that may depend on the aspect ratio, and thus yield a posteriori error estimates that are not optimal when using anisotropic finite elements. In next proposition we present interpolation estimates, independent of the mesh aspect ratio.

Let $R_h : W^{1,p}(\Omega) \to V_h$ be Clément's interpolant with $p \geq 2$ [22]. When using anisotropic meshes, some additional geometrical assumptions must be made in order to ensure that the constants involved in the interpolation estimates will not depend on the mesh aspect ratio. From now, it is assumed that

1. For each K, the cardinality of ΔK, that is the union of elements sharing a vertex with K, is uniformly bounded from above, independently of the mesh geometry.

2. For each K, the diameter of $\Delta\hat{K} = T_K^{-1}(\Delta K)$ is uniformly bounded from above, independently of the mesh geometry.

In particular, the second assumption excludes too distorted meshes, see for instance Figure 1.2 for an example of acceptable and unacceptable patch.

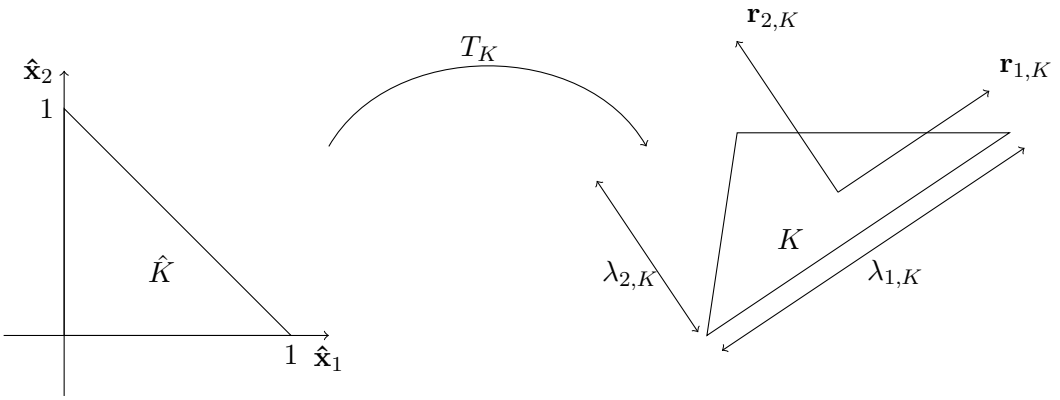

FIGURE 1.1 : Transformation T_K mapping the usual reference element $\hat{K}$ into a triangle K. The reference triangle is stretched in the direction $\mathbf{r}_{1,K}$ (resp. $\mathbf{r}_{2,K}$), with amplitude $\lambda_{1,K}$ (resp. $\lambda_{2,K}$).

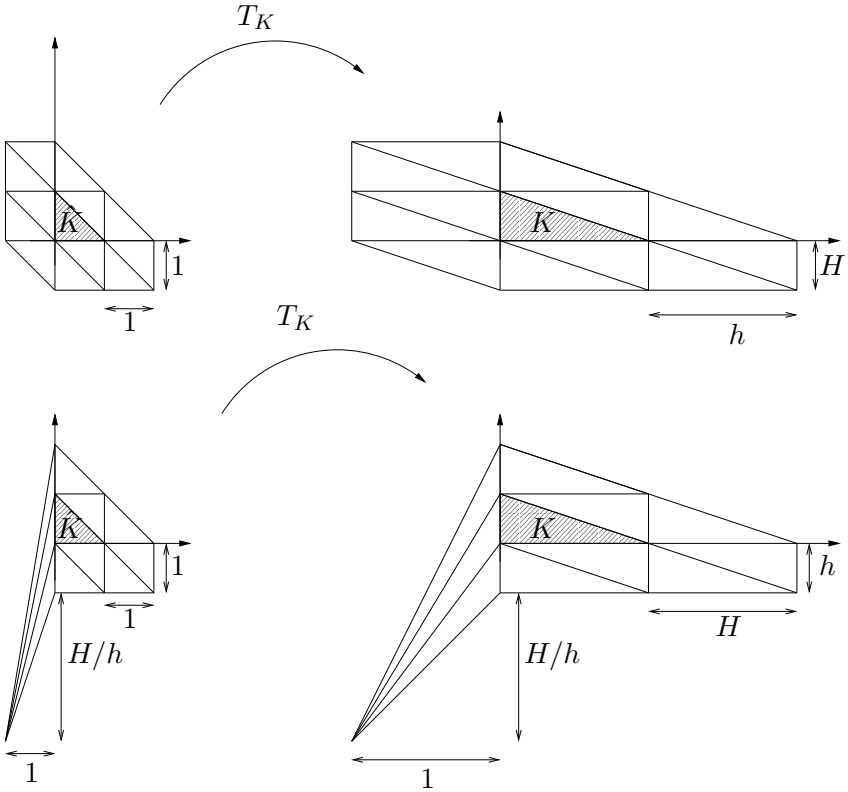

FIGURE 1.2 : Top : example of acceptable patch : the size of $\Delta_{\hat{K}}$ is independent of the aspect ratio H/h. Bottom : example of non-acceptable patch where the size of $\Delta_{\hat{K}}$ depends of the aspect ratio H/h.

It guarantees that all the quantities vary smoothly in the neighborhood of every element K. In practice, these assumptions seem to be fulfilled when using available anisotropic mesh generators [46, 39]. Proceeding as in [33, 34] for the case $p = 2$ and $d = 2$, we obtain the following.

Proposition 1.1 (Anisotropic Clément interpolation error estimate in the L^p norm)**.** *Let $p \geq 2$, there exists a constant $\hat{C} > 0$ depending only on the reference element $\hat{K}$ such that for all $v \in W^{1,p}(\Omega)$, for all $K \in \mathcal{T}_h$ and its elements boundaries ∂K_i for $i = 1, \ldots, d+1$ we have*

$$\left(\frac{\prod_{j=1}^{d} \lambda_{j,K}}{|\partial K_i|} \right)^{1/p} ||v - R_h(v)||_{L^p(\partial K_i)} + ||v - R_h(v)||_{L^p(K)} \leq \hat{C} \omega_{p,K}(v), \tag{1.2}$$

where

$$(\omega_{p,K}(v))^p = \sum_{i=1}^{d} \lambda_{i,K}^p ||\nabla v \cdot \mathbf{r}_{i,K}||^p_{L^p(\Delta K)}. \tag{1.3}$$

Before proving the proposition, we introduce the following Lemma, which is a generalization of what presented in Lemma 2.2 and 2.1 in [33].

Lemma 1.1. *Let $v \in W^{1,p}(K)$ and $\hat{v} \in W^{1,p}(\hat{K})$ the corresponding function defined on the reference element $\hat{K}$. Then there exist a constant $\hat{C} > 0$ such that*

$$||\hat{\nabla} \hat{v}||^p_{L^p(\hat{K})} \leq \hat{C} \sum_{i=1}^{d} \left(\frac{\lambda_{i,K}^p}{\prod_{j=1}^{d} \lambda_{j,K}} \right) ||\nabla v \cdot \mathbf{r}_{i,K}||^p_{L^p(K)}. \tag{1.4}$$

Similarly there exists a constant $\hat{C} > 0$ such that

$$||\nabla v||^p_{L^p(K)} \leq \hat{C} \sum_{i=1}^{d} \left(\frac{\prod_{j=1}^{d} \lambda_{j,K}}{\lambda_{i,K}^p} \right) ||\hat{\nabla} \hat{v} \cdot \mathbf{p}_{i,K}||^p_{L^p(\hat{K})}, \tag{1.5}$$

where $\mathbf{p}_{i,K}$ are the ith vectors of matrix P_K introduced after (1.1)*. Suppose now that $v \in W^{2,p}(K)$ and $\hat{v} \in W^{2,p}(\hat{K})$. Then there exists a constant $\hat{C} > 0$ such that*

$$||\hat{H}(\hat{v})||^p_{L^p(\hat{K})} \leq \hat{C} \sum_{i,j=1}^{d} \frac{(\lambda_{i,K} \lambda_{j,K})^p}{\prod_{l=1}^{d} \lambda_{l,K}} \int_K \left(\mathbf{r}_{i,K}^T H(v) \mathbf{r}_{j,K} \right)^p. \tag{1.6}$$

Here we define the Hessian matrix $H(v) \in \mathbb{R}^{d\times d}$

$$(H(v))_{i,j} = \frac{\partial^2 v}{\partial x_i \partial x_j}, \quad i,j = 1,\dots,d$$

and $||H(v)||^p_{L^p(K)} = \int_K ||H(v)||^p_p$, *where for* $\mathbf{x} \in \mathbb{R}^d$

$$||H(v)||_p = \sup_{||\mathbf{x}||_p \neq 0} \frac{||H(v)\mathbf{x}||_p}{||\mathbf{x}||_p}$$

represents the matrix p-norm for $d \times d$ *matrices.*

Remark 1.1. *Notice that when* $p = 2$, *then* (1.4), (1.5) *and* (1.6) *are equalities and are available for* $d = 2$ *in [33, 34].*

Proof. Using the affine map (1.1) previously defined we have

$$||\hat{\nabla}\hat{v}||^p_{L^p(\hat{K})} = ||M_K^T \nabla v||^p_{L^p(\hat{K})} = \int_{\hat{K}} ||P_K^T \Lambda_K R_K \nabla v||^p_p.$$

On finite spaces the following relations between vectorial norms can be proved : let $\mathbf{x} \in \mathbb{R}^d$, then we have

$$\begin{aligned} ||\mathbf{x}||_p &\leq ||\mathbf{x}||_2, \\ ||\mathbf{x}||_2 &\leq d^{1/2-1/p}||\mathbf{x}||_p, \end{aligned}$$

where $||\cdot||_p$ and $||\cdot||_2$ represent the p-norm and 2-norm respectively. Using these relations, the orthogonality properties of P_K and defining $\mathbf{\Phi} = \Lambda_K R_K \nabla v$ we have

$$\begin{aligned} ||\hat{\nabla}\hat{v}||^p_{L^p(\hat{K})} &\leq \int_{\hat{K}} ||P_K^T \Lambda_K R_K \nabla v||^p_2 = \int_{\hat{K}} < P_K^T \mathbf{\Phi}, P_K^T \mathbf{\Phi} >^{p/2} \\ &= \int_{\hat{K}} < P_K^T P_K \mathbf{\Phi}, \mathbf{\Phi} >^{p/2} = \int_{\hat{K}} ||\mathbf{\Phi}||^p_2 \leq d^{1/2-1/p} \int_{\hat{K}} ||\mathbf{\Phi}||^p_p, \end{aligned}$$

where $< \cdot, \cdot >$ represents the scalar product associated with the 2-norm in $\mathbb{R}^d$. We thus have

$$||\hat{\nabla}\hat{v}||^p_{L^p(\hat{K})} \leq d^{1/2-1/p} \int_{\hat{K}} \sum_{i=1}^d \lambda^p_{i,K} |\nabla v \cdot \mathbf{r}_{i,K}|^p = d^{1/2-1/p} \frac{1}{\prod_{i=1}^d \lambda_{i,K}} \int_K \sum_{i=1}^d \lambda^p_{i,K} |\nabla v \cdot \mathbf{r}_{i,K}|^p$$

$$= \hat{C} \sum_{i=1}^d \left(\frac{\lambda^p_{i,K}}{\prod_{j=1}^d \lambda_{j,K}} \right) ||\nabla v \cdot \mathbf{r}_{i,K}||^p_{L^p(K)}.$$

Which conclude the proof of (1.4). Inequality (1.5) is proven in a similar way. To prove

(1.6), we use the fact that for any symmetric matrix $A \in \mathbb{R}^{d\times d}$ and for any $\mathbf{x} \in \mathbb{R}^d$ we have

$$||A||_p := \sup_{||\mathbf{x}||_p\neq 0} \frac{||A\mathbf{x}||_p}{||\mathbf{x}||_p} \leq d^{1/2-1/p} \sup_{||\mathbf{x}||_2\neq 0} \frac{||A\mathbf{x}||_2}{||\mathbf{x}||_2} \leq d^{1/2-1/p}||A||_F,$$

where $||\cdot||_F$ is the Frobenius norm. Thus, we obtain

$$||\hat{H}(\hat{v})||^p_{L^p(\hat{K})} \leq \hat{C} \int_{\hat{K}} \left(||P_K^T \Lambda R_K H(v) R_K^T \Lambda P_K||_F^2\right)^{p/2}.$$

Using again orthogonality properties of P_K and defining $Q = \Lambda_K R_K$, we have

$$\begin{aligned}
||\hat{H}(\hat{v})||^p_{L^p(\hat{K})} &\leq \hat{C} \int_{\hat{K}} \left(||QH(v)Q^T||_F^2\right)^{p/2} \leq \hat{C} \int_{\hat{K}} \left(\sum_{i,j=1}^{d} \left(\lambda_{i,K}\lambda_{j,K}\mathbf{r}_{i,K}^T H(v)\mathbf{r}_{j,K}\right)^2\right)^{p/2} \\
&\leq \hat{C} \sum_{i,j=1}^{d} \int_{\hat{K}} (\lambda_{i,K}\lambda_{j,K})^p \left(\mathbf{r}_{i,K}^T H(v)\mathbf{r}_{j,K}\right)^p \\
&\leq \hat{C} \sum_{i,j=1}^{d} \frac{(\lambda_{i,K}\lambda_{j,K})^p}{\prod_{l=1}^{d} \lambda_{l,K}} \int_K \left(\mathbf{r}_{i,K}^T H(v)\mathbf{r}_{j,K}\right)^p,
\end{aligned}$$

which concludes the proof. □

We are now able to prove Proposition 1.1.

Proof. (Proposition 1.1) We have, using properties presented in [22]

$$\begin{aligned}
||v - R_h(v)||^p_{L^p(K)} &= \left(\prod_{j=1}^{d} \lambda_{j,K}\right) ||\hat{v} - \hat{R}_h(\hat{v})||^p_{L^p(\hat{K})} \leq \hat{C} h_{\hat{K}}^p \left(\prod_{j=1}^{d} \lambda_{j,K}\right) ||\hat{\nabla}\hat{v}||^p_{L^p(\Delta\hat{K})} \\
&= \hat{C} \left(\prod_{j=1}^{d} \lambda_{j,K}\right) \sum_{T\in\Delta\hat{K}} ||\hat{\nabla}\hat{v}||^p_{L^p(T)}.
\end{aligned}$$

Using (1.4) we obtain

$$||v - R_h(v)||^p_{L^p(K)} \leq \hat{C}(\omega_{p,K}(v))^p.$$

Proceeding in a similar way, we have for $i = 1, \ldots, d+1$

$$||v - R_h(v)||^p_{L^p(\partial K_i)} \leq \hat{C}|\partial K_i| ||\hat{v} - \hat{R}_h(\hat{v})||^p_{L^p(\partial\hat{K}_i)} \leq \hat{C}|\partial K_i| \sum_{T\in\Delta\hat{K}} ||\hat{\nabla}\hat{v}||^p_{L^p(T)}.$$

Using again (1.4), we conclude the proof. □

Remark 1.2. *When $p = 2$ we have as in [33, 34]*

$$(\omega_{2,K}(v))^2 = \sum_{i=1}^{d} \lambda_{i,K}^2 (\mathbf{r}_{i,K}^T G_K(v)\mathbf{r}_{i,K})),$$

with

$$(G_K(v))_{i,j} = \int_{\Delta K} \frac{\partial v}{\partial x_i} \frac{\partial v}{\partial x_j}, \quad i,j = 1,\dots,d.$$

When $p > d$, since $v \in W^{1,p}(\Omega)$, then $v \in \mathcal{C}^0(\bar{\Omega})$ thus the Lagrangian interpolant could be used. However this will not always be the case in this work, thus only Clément's interpolant is considered in this work. Anisotropic Lagrange interpolation error estimates can be found, for instance, in [28].

Remark 1.3. *Proposition 1.1 can be extended to cases of vector valued functions. Let $\mathbf{v} : \Omega \to \mathbb{R}^s$ be a vector valued function with $s = 2, 3$, then we adopt the following definition*

$$(\omega_{p,K}(\mathbf{v}))^p = \sum_{i=1}^{s} (\omega_{p,K}(v_i))^p,$$

where v_i are the components of $\mathbf{v}$ for $i = 1,\dots,s$.

2 Anisotropic adaptive finite elements for an elliptic problem with strongly varying diffusion coefficient

The goal of this section is to develop an error estimator for the elliptic problem $-\mathrm{div}(\mu\nabla u) = f$, where $\mu > 0$ is smooth but varying strongly. We will prove, theoretically and numerically, an equivalence between the error estimator and the numerical error $u - u_h$ up to higher order terms. Additionally adaptive algorithms, which will be reused along the whole thesis, are presented.

2.1 Problem statement and numerical method

Given $f : \Omega \to \mathbb{R}$ and $\mu : \Omega \to \mathbb{R}$, we search for $u : \Omega \to \mathbb{R}$ that is the solution of the elliptic equation

$$\begin{cases} -\mathrm{div}(\mu\nabla u) = f & \text{in } \Omega, \\ \\ u = 0 & \text{on } \partial\Omega. \end{cases} \tag{2.1}$$

We suppose $f \in L^2(\Omega)$ and $\mu \in L^\infty(\Omega)$ such that there exist $\mu_{\min}, \mu_{\max}$ such that

$$0 < \mu_{\min} \leq \mu(\mathbf{x}) \leq \mu_{\max}, \quad \text{a.e. } \mathbf{x} \in \Omega.$$

Problem (2.1) can be written in weak form as : find $u \in H_0^1(\Omega)$ such that

$$\int_\Omega \mu\nabla u \cdot \nabla v = \int_\Omega fv, \quad \forall\, v \in H_0^1(\Omega). \tag{2.2}$$

Under the above assumptions it can be shown, by an application of Lax-Milgram's lemma, that problem (2.2) is well-posed [37]. To approximate the solution of (2.2), we are looking

for $u_h \in V_h \subset H_0^1(\Omega)$ such that

$$\int_\Omega \mu \nabla u_h \cdot \nabla v_h = \int_\Omega f v_h \qquad \forall v_h \in V_h. \tag{2.3}$$

As before by an application of Lax-Milgram's lemma, we can prove well-posedness of (2.3). A priori error estimates of this numerical method in the anisotropic settings can be found in [28].

2.2 Anisotropic error estimator

We will introduce an error estimator $\sum_{K\in\mathcal{T}_h} \eta_K^2$. Under some additional conditions we will prove that the derived error estimator is equivalent to the numerical error $u - u_h$ in a H^1 semi-norm, that is to say there exists two constants $\hat{C}_1, \hat{C}_2 > 0$ that are independent of the data Ω, μ, f, the mesh size and aspect ratio such that

$$\hat{C}_1 \sum_{K\in\mathcal{T}_h} \eta_K^2 \leq \int_\Omega \mu |\nabla(u - u_h)|^2 \leq \hat{C}_2 \sum_{K\in\mathcal{T}_h} \eta_K^2 \tag{2.4}$$

up to higher order terms.

For all $K \in \mathcal{T}_h$, we define the L^2 projection of f onto the set of piecewise constant functions by

$$\Pi_K f = \frac{1}{|K|} \int_K f. \tag{2.5}$$

For a vector valued function $\mathbf{f} = (f_1, f_2)$, we denote $\Pi_K \mathbf{f} =: (\Pi_K f_1, \Pi_K f_2)$, and for any boundary element ∂K_i of K with $i = 1, \ldots, d+1$, we define

$$\Pi_{\partial K_i} f = \frac{1}{|\partial K_i|} \int_{\partial K_i} f.$$

We then define the local error estimator η_K^2 by

$$\begin{aligned} \eta_K^2 = \Bigg(& \| \Pi_K \left(f + \nabla \cdot (\mu \nabla u_h) \right) \|_{L^2(K)} \\ & + \frac{1}{2} \sum_{i=1}^{d+1} \left(\frac{|\partial K_i|}{\prod_{j=1}^{d} \lambda_{j,K}} \right)^{1/2} \| [\Pi_{\partial K_i} \mu \nabla u_h \cdot \mathbf{n}] \|_{L^2(\partial K_i)} \Bigg) \omega_{2,K}(u - u_h). \end{aligned} \tag{2.6}$$

Here $\mathbf{n}$ stands for the unit outer normal to K and $\omega_{2,K}(\cdot)$ is given by (1.3). For any boundary element ∂K_i of K with $i = 1, \ldots, d+1$, we denote $[\cdot]$ the jump across ∂K_i ($[\cdot] = 0$ if $\partial K_i \subset \partial\Omega$).

Remark 2.1. *Observe that error estimator* (2.6) *is not standard since it involves the exact solution in the term* $\omega_{2,K}(u-u_h)$*, and thus is not fully computable. However, in practice post-processing techniques can be applied in order to approximate the quantity* $G_K(u-u_h)$*, contained in* $\omega_{2,K}(u-u_h)$*, for instance Zienkiewicz–Zhu (ZZ) post-processing [2, 75, 76]. More precisely, we will replace*

$$\frac{\partial(u-u_h)}{\partial x_i} \text{ by } \Pi_h^{ZZ}\frac{\partial u_h}{\partial x_i} - \frac{\partial u_h}{\partial x_i}, \qquad i=1,\dots,d,$$

where, for any $v_h \in V_h$*, for any vertex* P *of the mesh*

$$\Pi_h^{ZZ}\frac{\partial v_h}{\partial x_i}(P) = \frac{\displaystyle\sum_{\substack{K\in\mathcal{T}_h\\ P\in K}} |K|\,\frac{\partial v_{h|K}}{\partial x_i}}{\displaystyle\sum_{\substack{K\in\mathcal{T}_h\\ P\in K}} |K|}$$

is an approximate $L^2(\Omega)$ *projection of* $\partial v_h/\partial x_i$ *onto* V_h*. It is well known [19, 76] that for elliptic equations and structured meshes superconvergence of the ZZ recovery occurs, implying that the post-processing is asymptotically exact, that is to say*

$$\lim_{h\to 0}\frac{\|\Pi_h^{ZZ}\nabla u_h - \nabla u_h\|_{L^2(\Omega)}}{\|\nabla u - \nabla u_h\|_{L^2(\Omega)}} = 1.$$

On general meshes, it was first proven that $\|\Pi_h^{ZZ}\nabla u_h - \nabla u_h\|_{L^2(\Omega)}$ *and the true error* $\|\nabla u - \nabla u_h\|_{L^2(\Omega)}$ *are equivalent, see for instance [44]. Finally, the superconvergence of the ZZ gradient recovery was finally shown for unstructured anisotropic meshes [18]. In practice the efficiency of the ZZ post-processing was demonstrated for instance in [60, 59, 62, 52, 63, 16, 53].*

2.2.1 Equivalence between the numerical error and the error estimator

We state now the main result of the section.

Theorem 2.1. *Assume that* $f \in L^2(\Omega)$ *and* $\mu \in W^{1,\infty}(\Omega)$*. Let* $u \in H_0^1(\Omega)$ *be the weak solution of* (2.1) *and* $u_h \in V_h$ *be the solution of* (2.3)*. Moreover, assume that there exists* $\hat{C} > 0$ *depending only on the reference element* $\hat{K}$ *such that, for all* $K \in \mathcal{T}_h$ *for* $j = 1,\dots,d-1$

$$\lambda_{j,K}^2(\mathbf{r}_{j,K}^T G_K(u-u_h)\mathbf{r}_{j,K}) \le \hat{C}\lambda_{d,K}^2(\mathbf{r}_{d,K}^T G_K(u-u_h)\mathbf{r}_{d,K}) \tag{2.7}$$

and assume $\lambda_{i,K}$ *vary smoothly around* K *for* $i = 1,\dots,d$*. Then there exists a constant* $\hat{C}_1 > 0$ *depending only on the reference element* $\hat{K}$ *such that*

$$\int_\Omega \mu|\nabla(u-u_h)|^2 \le \hat{C}_1 \sum_{K\in\mathcal{T}_h}(\eta_K^2 + \frac{\varepsilon_K^2}{\mu_{\min}}),$$

where

$$\varepsilon_K^2 = \lambda_{d,K}^2 \Big(||f - \Pi_K f||_{L^2(K)}^2 + ||(\nabla\mu - \Pi_K \nabla\mu)\cdot\nabla u_h||_{L^2(K)}^2 + \frac{1}{\lambda_{d,K}} \sum_{i=1}^{d+1} |||[(\mu - \Pi_{\partial K_i}\mu)\nabla u_h \cdot \mathbf{n}]|||_{L^2(\partial K_i)}^2 \Big). \tag{2.8}$$

Moreover, there exists a constant $\hat{C}_2 > 0$ depending only on the reference element $\hat{K}$ such that

$$\sum_{K\in\mathcal{T}_h} \eta_K^2 \leq \hat{C}_2 \sum_{K\in\mathcal{T}_h} \left(\left(1 + \frac{||\mu - \Pi_K\mu||_{L^\infty(\mathcal{P}_K)}}{\mu_{\min}} \right) \int_{\mathcal{P}_K} \mu |\nabla(u - u_u)|^2 + \frac{\varepsilon_K^2}{\mu_{\min}} \right),$$

where we denoted $\mathcal{P}_K = \Delta K \cup (\bigcup_{i=1}^{d+1} \Delta K^i)$ with K^i the ith element sharing a facet ∂K_i with K (see Figure 2.1).

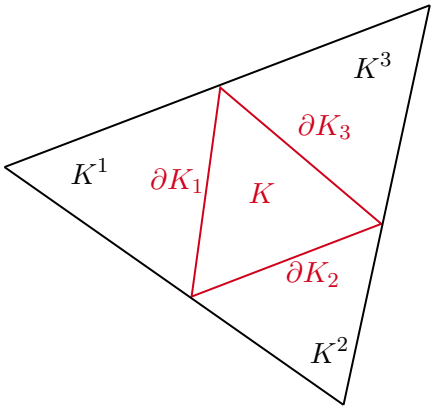

FIGURE 2.1 : Triangle K and corresponding triangles K^i sharing the edges ∂K_i with K.

Remark 2.2. *Assumption* (2.7)*, which is equivalent to the matching assumption discussed in [43] and was already used in [62], is satisfied whenever the errors in the directions $\mathbf{r}_{i,K}$ are equidistributed, which is precisely the goal of the adaptive algorithms discussed in section 2.4.*

Proof. (Theorem 1 : upper bound) Let $e = u - u_h$, using (2.1) and (2.3) we have, for any $v_h \in V_h$

$$\int_\Omega \mu |\nabla e|^2 = \int_\Omega f(e - v_h) - \int_\Omega \mu \nabla u_h \cdot \nabla(e - v_h).$$

By integration by parts over the elements K, we obtain

$$\begin{aligned}\int_\Omega \mu|\nabla e|^2 &= \sum_{K\in\mathcal{T}_h}\int_K (f+\operatorname{div}(\mu\nabla u_h))\,(e-v_h) + \frac{1}{2}\int_{\partial K}[\mu\nabla u_h\cdot\mathbf{n}](e-v_h)\\ &= \sum_{K\in\mathcal{T}_h}\int_K (\Pi_K f+\Pi_K\nabla\mu\cdot\nabla u_h)\,(e-v_h) + \frac{1}{2}\sum_{i=1}^{d+1}\int_{\partial K_i}[\Pi_{\partial K_i}\mu\nabla u_h\cdot\mathbf{n}](e-v_h)\\ &+ \sum_{K\in\mathcal{T}_h}\int_K (f-\Pi_K f)(e-v_h) + \sum_{K\in\mathcal{T}_h}\int_K(\nabla\mu-\Pi_K\nabla\mu)\cdot\nabla u_h(e-v_h)\\ &+ \frac{1}{2}\sum_{K\in\mathcal{T}_h}\sum_{i=1}^{d+1}\int_{\partial K_i}[(\mu-\Pi_{\partial K_i}\mu)\nabla u_h\cdot\mathbf{n}](e-v_h).\end{aligned}$$

Using Cauchy-Schwarz inequality, choosing $v_h = R_h e$ and by using interpolation error estimates (1.2) we obtain

$$\begin{aligned}\int_\Omega \mu|\nabla e|^2 \le \hat{C}\Big(&\sum_{K\in\mathcal{T}_h}\eta_K^2 + \sum_{K\in\mathcal{T}_h}\Big(||f-\Pi_K f||_{L^2(K)} + ||(\nabla\mu-\Pi_K\nabla\mu)\cdot\nabla u_h||_{L^2(K)}\\ &+ \frac{1}{2\sqrt{\lambda_{d,K}}}\sum_{i=1}^{d+1}|||[(\mu-\Pi_{\partial K_i}\mu)\nabla u_h\cdot\mathbf{n}]||_{L^2(\partial K_i)}\Big)\omega_{2,K}(e)\Big).\end{aligned}$$

Using assumption (2.7) and the fact that $\mathbf{r}_{1,K},\dots,\mathbf{r}_{d,K}$ form a basis of $\mathbb{R}^d$, we have

$$\omega_{2,K}^2(e) \le \hat{C}\lambda_{d,K}^2\sum_{j=1}^{d}(\mathbf{r}_{j,K}^T G_K(e)\mathbf{r}_{j,K}) = \hat{C}\lambda_{d,K}^2||\nabla e||_{L^2(\Delta K)}^2.$$

Thus we have

$$\begin{aligned}\int_\Omega \mu|\nabla e|^2 \le \hat{C}\Big(&\sum_{K\in\mathcal{T}_h}\eta_K^2 + \sum_{K\in\mathcal{T}_h}\Big(\lambda_{d,K}||f-\Pi_K f||_{L^2(K)}\\ &+ \lambda_{d,K}||(\nabla\mu-\Pi_K\nabla\mu)\cdot\nabla u_h||_{L^2(K)}\\ &+ \frac{\lambda_{d,K}^{1/2}}{2}\sum_{i=1}^{d+1}|||[(\mu-\Pi_{\partial K_i}\mu)\nabla u_h\cdot\mathbf{n}]||_{L^2(\partial K_i)}\Big)||\nabla e||_{L^2(\Delta K)}\Big)\end{aligned}$$

Using discrete Cauchy-Schwarz and Young's inequality we obtain the result.

□

In order to prove the lower bound, we use the standard bubble functions [9, 73], adapted to the anisotropic case in [62], and modified here to account for the variations of μ.

Proposition 2.1. *Let $e = u - u_h$, there exists a function $\varphi \in H_0^1(\Omega)$ and a constant $\hat{C} > 0$ (that depends only on the reference element $\hat{K}$) such that for any $K \in \mathcal{T}_h$ for*

$i = 1, \dots, d+1$

$$\int_{\partial K_i} [\Pi_{\partial K_i} \mu \nabla u_h \cdot \mathbf{n}] \varphi = \frac{1}{2} \| [\Pi_{\partial K_i} \mu \nabla u_h \cdot \mathbf{n}] \|_{L^2(\partial K_i)} \left(\left(\frac{|\partial K_i|}{\prod_{j=1}^{d} \lambda_{j,K}} \right)^{1/2} \omega_{2,K}(e) + \left(\frac{|\partial K_i|}{\prod_{j=1}^{d} \lambda_{j,K^i}} \right)^{1/2} \omega_{2,K^i}(e) \right) \tag{2.9}$$

$$\int_K (\Pi_K (f + \nabla \cdot (\mu \nabla u_h)) \varphi = \| \Pi_K (f + \nabla \cdot (\mu \nabla u_h)) \|_{L^2(K)} \omega_{2,K}(e), \tag{2.10}$$

$$\left(\sum_{j=1}^{d} \lambda_{j,K}^2 || \nabla \varphi \cdot \mathbf{r}_{j,K} ||_{L^2(K)}^2 \right)^{1/2} \leq \hat{C} \left(\omega_{2,K}(e) + \sum_{i=1}^{d+1} \omega_{2,K^i}(e) \right) \tag{2.11}$$

and

$$\int_K \mu |\nabla \varphi|^2 \leq \hat{C} \left(\Pi_K \mu + \| \mu - \Pi_K \mu \|_{L^\infty(K)} \right) \left(\frac{\omega_{2,K}^2(e)}{\lambda_{d,K}^2} + \sum_{i=1}^{d+1} \frac{\omega_{2,K^i}^2(e)}{\lambda_{d,K^i}^2} \right). \tag{2.12}$$

We denoted for $i = 1, \dots, d+1$, K^i the ith element sharing facet ∂K_i with K (see Figure 2.1).

Proof. We claim that

$$\varphi = \sum_{K \in \mathcal{T}_h} C_K \Psi_K + \frac{1}{2} \sum_{K \in \mathcal{T}_h} \sum_{i=1}^{d+1} C_{\partial K_i} \Psi_{\partial K_i}$$

where $C_K, C_{\partial K_i}$ are constants that need to be computed, and $\Psi_K, \Psi_{\partial K_i}$ are the usual bubble functions over K and a facet element ∂K_i. Note that we set $C_{\partial K_i} = 0$ if $\partial K_i \subset \partial \Omega$. First we compute $C_{\partial K_i}$ for $i = 1, \dots, d+1$. We require that the constants associated to the same facet shared by two elements are equal. Using the fact that $\Psi_K, \Psi_{\partial K_j}$ are zero over ∂K_i for all $j \neq i$, the fact that $[\Pi_{\partial K_i} \mu \nabla u_h \cdot \mathbf{n}]$ is constant over ∂K_i and (2.9), we have

$$C_{\partial K_i} = \pm \frac{1}{2} \left(\left(\frac{|\partial K_i|^2}{\prod_{j=1}^{d} \lambda_{j,K}} \right)^{1/2} \omega_{2,K}(e) + \left(\frac{|\partial K_i|^2}{\prod_{j=1}^{d} \lambda_{j,K^i}} \right)^{1/2} \omega_{2,K^i}(e) \right) \frac{1}{\int_{\partial K_i} \Psi_{\partial K_i}},$$

where the sign is chosen accordingly to the sign of $[\Pi_{\partial K_i} \mu \nabla u_h \cdot \mathbf{n}]$. Moreover using (2.10), the constants $C_{\partial K_i}$ computed and $|K| = \hat{C} \prod_{j=1}^{d} \lambda_{j,K}$, we obtain

$$C_K = \pm \frac{1}{\int_K \Psi_K} \left(\hat{C} \left(\prod_{j=1}^{d} \lambda_{j,K} \right)^{1/2} \omega_{2,K}(e) \right.$$
$$\left. \mp \sum_{i=1}^{d+1} \frac{1}{2} \left(\left(\frac{|\partial K_i|^2}{\prod_{j=1}^{d} \lambda_{j,K}} \right)^{1/2} \omega_{2,K}(e) + \left(\frac{|\partial K_i|^2}{\prod_{j=1}^{d} \lambda_{j,K^i}} \right)^{1/2} \omega_{2,K^i}(e) \right) \frac{\int_K \Psi_{\partial K_i}}{\int_{\partial K_i} \Psi_{\partial K_i}} \right),$$

where the signs are chosen again accordingly to the signs of $[\Pi_{\partial K_i} \mu \nabla u_h \cdot \mathbf{n}]$ and $\Pi_K(f + \nabla \cdot (\mu \nabla u_h))$. Thus φ satisfies equations (2.9) and (2.10). Before proving the remaining inequalities we prove the following bounds on the constants. We have

$$C_{\partial K_i}^2 \leq \hat{C} \left(\frac{\omega_{2,K}^2(e)}{\prod_{j=1}^{d} \lambda_{j,K}} + \frac{\omega_{2,K^i}^2(e)}{\prod_{j=1}^{d} \lambda_{j,K^i}} \right), \tag{2.13}$$

where we used

$$\int_{\partial K_i} \Psi_{\partial K_i} = \hat{C} |\partial K_i|, \quad i = 1, \ldots, d+1. \tag{2.14}$$

In a similar way, using

$$\int_K \Psi_K = \hat{C} \prod_{j=1}^{d} \lambda_{j,K}, \tag{2.15}$$

$$\int_K \Psi_{\partial K_i} = \hat{C} \prod_{j=1}^{d} \lambda_{j,K}, \quad i = 1, \ldots, d+1, \tag{2.16}$$

we have

$$C_K^2 \leq \hat{C} \left(\frac{\omega_{2,K}^2(e)}{\prod_{j=1}^{d} \lambda_{j,K}} + \sum_{i=1}^{d+1} \frac{\omega_{2,K^i}^2(e)}{\prod_{j=1}^{d} \lambda_{j,K^i}} \right). \tag{2.17}$$

To prove (2.12), we note that

$$\int_K \mu |\nabla \varphi|^2 = \int_K \Pi_K \mu |\nabla \varphi|^2 + \int_K (\mu - \Pi_K \mu) |\nabla \varphi|^2$$

and then, using (2.17) and (2.13), we have

$$\int_K |\nabla\varphi|^2 \leq \hat{C}\left(\frac{\omega_{2,K}^2(e)}{\prod_{j=1}^{d}\lambda_{j,K}} + \sum_{i=1}^{d+1}\frac{\omega_{2,K^i}^2(e)}{\prod_{j=1}^{d}\lambda_{j,K^i}}\right)\left(\int_K |\nabla\Psi_K|^2 + \sum_{j=1}^{d+1}\int_K |\nabla\Psi_{\partial K_j}|^2\right).$$

We also recall (1.5)

$$||\nabla\Psi_K||^2_{L^2(K)} \leq \hat{C}\sum_{i=1}^{d}\left(\frac{\prod_{j=1}^{d}\lambda_{j,K}}{\lambda_{i,K}^2}\right)||\hat{\nabla}\hat{\Psi}_{\hat{K}}\cdot\mathbf{p}_{i,K}||^2_{L^2(\hat{K})},$$

which holds also for $\nabla\Psi_{\partial K_i}$ with $i = 1,\ldots,d+1$ and together with the fact that $\lambda_{1,K} \geq \cdots \geq \lambda_{d,K} > 0$ gives

$$\int_K |\nabla\varphi|^2 \leq \hat{C}\left(\frac{\omega_{2,K}^2(e)}{\prod_{j=1}^{d}\lambda_{j,K}} + \sum_{i=1}^{d+1}\frac{\omega_{2,K^i}^2(e)}{\prod_{j=1}^{d}\lambda_{j,K^i}}\right)\left(\frac{\prod_{j=1}^{d-1}\lambda_{j,K}}{\lambda_{d,K}}\right).$$

Using the hypothesis that $\lambda_{i,K}$ vary smoothly around K we conclude. In order to prove (2.11) we proceed similarly. First note that for $i = 1,\ldots,d$

$$\int_K |\nabla\varphi\cdot\mathbf{r}_{i,K}|^2 \leq \hat{C}\left(\frac{\omega_{2,K}^2(e)}{\prod_{j=1}^{d}\lambda_{j,K}} + \sum_{l=1}^{d+1}\frac{\omega_{2,K^l}^2(e)}{\prod_{j=1}^{d}\lambda_{j,K^l}}\right)\Big(\int_K |\nabla\Psi_K\cdot\mathbf{r}_{i,K}|^2 \tag{2.18}$$

$$+\sum_{j=1}^{d+1}\int_K |\nabla\Psi_{\partial K_j}\cdot\mathbf{r}_{i,K}|^2\Big). \tag{2.19}$$

We recall (1.4) proved in Section 1

$$||\hat{\nabla}\hat{\Psi}_{\hat{K}}||^2_{L^2(\hat{K})} = \sum_{i=1}^{d}\left(\frac{\lambda_{i,K}^2}{\prod_{j=1}^{d}\lambda_{j,K}}\right)||\nabla\Psi_K\cdot\mathbf{r}_{i,K}||^2_{L^2(K)}.$$

The same holds for $\nabla\Psi_{\partial K_i}$ with $i = 1,\ldots,d+1$, thus we obtain

$$\sum_{i=1}^{d} \lambda_{i,K}^2 ||\nabla\varphi \cdot \mathbf{r}_{i,K}||^2_{L^2(K)} \leq \hat{C} \left(\omega_{2,K}^2(e) + \sum_{l=1}^{d+1} \omega_{2,K^l}^2(e) \right) \left(||\hat{\nabla}\hat{\Psi}_{\hat{K}}||^2_{L^2(\hat{K})} + \sum_{i=1}^{d+1} ||\hat{\nabla}\hat{\Psi}_{\partial\hat{K}_i}||^2_{L^2(\partial\hat{K}_i)} \right),$$

which gives (2.11). □

We also need the following result.

Proposition 2.2. *For any $K \in \mathcal{T}_h$ and any $v \in H^1(\Omega)$, there exists a constant $\hat{C}$ depending only on the reference element such that for all $i = 1, \ldots, d+1$ we have*

$$\|v - \Pi_K v\|_{L^2(K)} \leq \hat{C} \left(\sum_{j=1}^{d} \lambda_{j,K}^2 ||\nabla v \cdot \mathbf{r}_{j,K}||^2_{L^2(K)} \right)^{1/2},$$

$$\|v - \Pi_{\partial K_i} v\|_{L^2(\partial K_i)} \leq \frac{\hat{C}}{\sqrt{\lambda_{d,K}}} \left(\sum_{j=1}^{d} \lambda_{j,K}^2 ||\nabla v \cdot \mathbf{r}_{j,K}||^2_{L^2(K)} \right)^{1/2}.$$

Proof. Let $\hat{v} \in H^1(\hat{K})$ the function corresponding to v, defined on the reference element. We have

$$\begin{aligned} ||v - \Pi_K v||^2_{L^2(K)} &= \prod_{j=1}^{d} \lambda_{j,K} \int_{\hat{K}} (\hat{v} - \Pi_{\hat{K}} \hat{v})^2 \\ &\leq \hat{C} \prod_{j=1}^{d} \lambda_{j,K} \int_{\hat{K}} |\hat{\nabla}\hat{v}|^2, \end{aligned}$$

where we used Poincaré-Wirtinger inequality. Using again (1.4) we obtain the first relation. For the second, first notice that

$$||v - \Pi_{\partial K_i} v||^2_{L^2(\partial K_i)} \leq ||v - \Pi_K v||^2_{L^2(\partial K_i)}.$$

Then we have, using change of variable and trace inequality

$$\begin{aligned} ||v - \Pi_{\partial K_i} v||^2_{L^2(\partial K_i)} &\leq \hat{C} \prod_{j=1}^{d-1} \lambda_{j,K} ||\hat{v} - \Pi_{\hat{K}} \hat{v}||^2_{L^2(\partial\hat{K}_i)} \\ &\leq \hat{C} \prod_{j=1}^{d-1} \lambda_{j,K} \left(||\hat{v} - \Pi_{\hat{K}} \hat{v}||^2_{L^2(\hat{K})} + ||\hat{\nabla}\hat{v}||^2_{L^2(\hat{K})} \right), \end{aligned}$$

which using again Poincaré-Wirtinger and (1.4) give the desired result. □

We are now in condition to prove the lower bound of Theorem 2.1.

Proof. (Theorem 2.1 : lower bound) Using the definition of η_K^2 and the identities (2.10) and (2.9), one can write

$$\sum_{K\in\mathcal{T}_h}\eta_K^2=\sum_{K\in\mathcal{T}_h}\left(\int_K\left(\Pi_K\left(f+\nabla\cdot(\mu\nabla u_h)\right)\right)\varphi+\frac{1}{2}\sum_{i=1}^{d+1}\int_{\partial K_i}[\Pi_{\partial K_i}\mu\nabla u_h\cdot\mathbf{n}]\varphi\right),$$

where $\varphi\in H_0^1(\Omega)$ is the function given by Proposition 2.1. Therefore, adding and subtracting the correct quantities in the right hand side and using the properties of the L^2 projections Π_K and $\Pi_{\partial K_i}$ we have

$$\begin{aligned}\sum_{K\in\mathcal{T}_h}\eta_K^2=&\sum_{K\in\mathcal{T}_h}\int_K(f+\nabla\cdot(\mu\nabla u_h))\varphi+\frac{1}{2}\sum_{K\in\mathcal{T}_h}\sum_{i=1}^{d+1}\int_{\partial K_i}[\mu\nabla u_h\cdot\mathbf{n}]\varphi\\&+\sum_{K\in\mathcal{T}_h}\int_K(\Pi_K f-f)(\varphi-\Pi_K\varphi)+\sum_{K\in\mathcal{T}_h}\int_K(\Pi_K\nabla\mu-\nabla\mu)\cdot\nabla u_h(\varphi-\Pi_K\varphi)\\&+\frac{1}{2}\sum_{K\in\mathcal{T}_h}\sum_{i=1}^{d+1}\int_{\partial K_i}[(\Pi_{\partial K_i}\mu-\mu)\nabla u_h\cdot\mathbf{n}](\varphi-\Pi_{\partial K_i}\varphi).\end{aligned}$$

Integration by parts over elements $K\in\mathcal{T}_h$, the fact that u solves (2.2) and Cauchy-Schwarz inequality give

$$\begin{aligned}\sum_{K\in\mathcal{T}_h}\eta_K^2\le&\sum_{K\in\mathcal{T}_h}\|\mu^{1/2}\nabla e\|_{L^2(K)}\|\mu^{1/2}\nabla\varphi\|_{L^2(K)}\\&+\sum_{K\in\mathcal{T}_h}\left(\|(\Pi_K f-f)\|_{L^2(K)}+\|(\Pi_K\nabla\mu-\nabla\mu)\cdot\nabla u_h\|_{L^2(K)}\right)\|\varphi-\Pi_K\varphi\|_{L^2(K)}\\&+\frac{1}{2}\sum_{K\in\mathcal{T}_h}\sum_{i=1}^{d+1}\|[(\Pi_{\partial K_i}\mu-\mu)\nabla u_h\cdot\mathbf{n}]\|_{L^2(\partial K_i)}\|\varphi-\Pi_{\partial K_i}\varphi\|_{L^2(\partial K_i)}.\end{aligned}$$

Now, proceeding as in proposition 2.2 we have

$$\begin{aligned}\sum_{K\in\mathcal{T}_h}\eta_K^2\le&\sum_{K\in\mathcal{T}_h}\|\mu^{1/2}\nabla e\|_{L^2(K)}\|\mu^{1/2}\nabla\varphi\|_{L^2(K)}\\&+\hat{C}\sum_{K\in\mathcal{T}_h}\left(\|(\Pi_K f-f)\|_{L^2(K)}+\|(\Pi_K\nabla\mu-\nabla\mu)\cdot\nabla u_h\|_{L^2(K)}\right)\left(\sum_{i=1}^{d}\lambda_{i,K}^2||\nabla\varphi\cdot\mathbf{r}_{i,K}||_{L^2(K)}^2\right)^{1/2}\\&+\frac{\hat{C}}{2}\sum_{K\in\mathcal{T}_h}\sum_{i=1}^{d+1}\|[(\Pi_{\partial K_i}\mu-\mu)\nabla u_h\cdot\mathbf{n}]\|_{L^2(\partial K_i)}\frac{1}{\sqrt{\lambda_{d,K}}}\left(\sum_{j=1}^{d}\lambda_{j,K}^2||\nabla\varphi\cdot\mathbf{r}_{j,K}||_{L^2(K)}^2\right)^{1/2}.\end{aligned}$$

We denote again K^i for $i=1,\dots,d+1$ the element sharing facet ∂K_i with K (see Figure

2.1). Finally, using the two bounds (2.11) and (2.12) and Young's inequality, we obtain

$$\begin{aligned}\sum_{K\in\mathcal{T}_h}\eta_K^2 \leq \hat{C}\Bigg(&\int_\Omega \mu|\nabla e|^2 \\ &+ \sum_{K\in\mathcal{T}_h}\left[\left(\Pi_K\mu + \|\mu-\Pi_K\mu\|_{L^\infty(K)}\right)\left(\frac{\omega_{2,K}^2(e)}{\lambda_{d,K}^2}+\sum_{i=1}^{d+1}\frac{\omega_{2,K^i}^2(e)}{\lambda_{d,K^i}^2}\right)\right] \\ &+ \sum_{K\in\mathcal{T}_h}\Bigg[\Bigg(\|(\nabla\mu-\Pi_K\nabla\mu)\cdot\nabla u_h\|_{L^2(K)} \\ &+ \frac{1}{2\sqrt{\lambda_{d,K}}}\sum_{i=1}^{d+1}\|[(\mu-\Pi_{\partial K_i}\mu)\nabla u_h\cdot\mathbf{n}]]\|_{L^2(\partial K_i)} \\ &+ \|\Pi_K f - f\|_{L^2(K)}\Bigg)\left(\omega_{2,K}(e)+\sum_{i=1}^{d+1}\omega_{2,K^i}(e)\right)\Bigg]\Bigg).\end{aligned} \tag{2.20}$$

Using assumption (2.7) and the fact that $\mathbf{r}_{1,K},\dots,\mathbf{r}_{d,K}$ form a basis of $\mathbb{R}^d$, we have

$$\omega_{2,K}^2(e) \leq \hat{C}\lambda_{d,K}^2\sum_{j=1}^{d}(\mathbf{r}_{j,K}^T G_K(e)\mathbf{r}_{j,K}) = \hat{C}\lambda_{d,K}^2||\nabla e||_{L^2(\Delta K)}^2.$$

In order to conclude the proof we note that

$$\begin{aligned}&\left(\Pi_K\mu + \|\mu-\Pi_K\mu\|_{L^\infty(K)}\right)\left(\frac{\omega_{2,K}^2(e)}{\lambda_{d,K}^2}+\sum_{i=1}^{d+1}\frac{\omega_{2,K^i}^2(e)}{\lambda_{d,K^i}^2}\right) \\ &\leq \hat{C}\left(\Pi_K\mu + \|\mu-\Pi_K\mu\|_{L^\infty(K)}\right)||\nabla e||_{L^2(\mathcal{P}_K)}^2 \\ &\leq \hat{C}\left(||\mu^{1/2}\nabla e||_{L^2(\mathcal{P}_K)}^2 + \frac{||\mu-\Pi_K\mu||_{L^\infty(\mathcal{P}_K)}}{\mu_{\min}}||\mu^{1/2}\nabla e||_{L^2(\mathcal{P}_K)}^2\right),\end{aligned}$$

where we denoted $\mathcal{P}_K = \Delta K \cup (\bigcup_{i=1}^{d+1}\Delta K^i)$. The final result is obtained using assumption 1 of Section 1, Young's inequality, the fact that $\lambda_{i,K}$ vary smoothly around K and inserting the above estimate in (2.20). □

In order to justify equivalence between the error estimator and the numerical error up to higher order terms, we need the following proposition.

Proposition 2.3. *Assume $f \in H^1(\Omega)$ and $\mu \in W^{2,\infty}(\Omega)$. Then we have*

$$||f - \Pi_K f||^2_{L^2(K)} \leq \hat{C} \sum_{i=1}^{d} \lambda_{i,K}^2 ||\nabla f \cdot \mathbf{r}_{i,K}||^2_{L^2(K)},$$

$$||(\nabla\mu - \Pi_K \nabla\mu) \cdot \nabla u_h||^2_{L^2(K)} \leq \hat{C} \left(\sum_{i,j=1}^{d} \frac{\lambda_{i,K}\lambda_{j,K}}{\lambda_{d,K}} ||\mathbf{r}_{i,K}^T H(\mu) \mathbf{r}_{j,K}||_{L^\infty(\partial K)} \right)^2 ||\nabla u_h||^2_{L^2(\partial K)},$$

$$\sum_{i=1}^{d+1} |||[(\mu - \Pi_{\partial K_i}\mu)\nabla u_h \cdot \mathbf{n}]|||^2_{L^2(\partial K_i)} \leq \hat{C} \left(\sum_{i=1}^{d} \lambda_{i,K}^2 ||\nabla\mu \cdot \mathbf{r}_{i,K}||^2_{L^\infty(\partial K)} \right) |||[\nabla u_h \cdot \mathbf{n}]|||^2_{L^2(\partial K)},$$

$$||\mu - \Pi_K \mu||_{L^\infty(K)} \leq \hat{C} \sum_{i=1}^{d} \lambda_{i,K} ||\nabla\mu \cdot \mathbf{r}_{i,K}||_{L^\infty(K)},$$

where $H(\cdot)$ denotes the Hessian matrix.

Remark 2.3. *In the isotropic framework Proposition 2.3 yields a contribution*

$$\sum_{K \in \mathcal{T}_h} \varepsilon_K^2 = O(h^3),$$

which is negligible compared to

$$||(\mu)^{1/2} \nabla(u - u_h)||^2_{L^2(\Omega)} = O(h^2).$$

In the anisotropic setting, for instance if f and μ depend only on x_2 and $\mathbf{r}_{1,K} = (1, 0)$, then

$$\sum_{K \in \mathcal{T}_h} \varepsilon_K^2 = O\left(\left(\max_{K \in \mathcal{T}_h} \lambda_{2,K} \right)^3 \right).$$

Thus in both case, Theorem 2.1 indeed yields (2.4) *up to higher order terms.*

Proof. (Proposition 2.3) The change of variable (1.1) and Poincaré-Wirtinger inequality give

$$||f - \Pi_k f||^2_{L^2(K)} \leq \hat{C} \prod_{j=1}^{d} \lambda_{j,K} \int_{\hat{K}} |\hat{\nabla}\hat{f}|^2.$$

Using (1.4) we obtain the first inequality. We prove now the second inequality. Using again change of variable (1.1) and Poincaré-Wirtinger, we have

$$\begin{aligned} ||\nabla\mu - \Pi_K \nabla\mu||_{L^\infty(K)} &\leq \hat{C} \lim_{p \to \infty} \left(\frac{\prod_{j=1}^{d} \lambda_{j,K}}{\lambda_{d,K}^p} ||\hat{\nabla}\hat{\mu} - \Pi_{\hat{K}} \hat{\nabla}\hat{\mu}||^p_{L^p(\hat{K})} \right)^{1/p} \\ &\leq \frac{1}{\lambda_{d,K}} \hat{C} ||\hat{H}(\hat{\mu})||_{L^\infty(\hat{K})}. \end{aligned}$$

Applying (1.6), we obtain

$$||\nabla\mu - \Pi_K\nabla\mu||_{L^\infty(K)} \leq \frac{\hat{C}}{\lambda_{d,K}} \lim_{p\to\infty} ||\hat{H}(\hat{\mu})||_{L^p(\hat{K})}$$
$$\leq \frac{\hat{C}}{\lambda_{d,K}} \lim_{p\to\infty} d^{1/2-1/p} \sum_{i,j=1}^{d} \frac{\lambda_{i,K}\lambda_{j,K}}{\left(\prod_{l=1}^{d}\lambda_{l,K}\right)^{1/p}} ||\mathbf{r}_{i,K}^T H(v)\mathbf{r}_{j,K}||_{L^p(K)},$$

which concludes the proof. Notice that we explicit the dependence of p of the constant arising from (1.6). For the last inequality, we proceed in the same way : we use change of variable (1.1), Poincaré-Wirtinger and (1.4). We focus on the third inequality. First of all, for $i = 1, \ldots, d+1$ we have

$$||\mu - \Pi_{\partial K_i}\mu||_{L^\infty(\partial K_i)} = \lim_{p\to\infty} \left(\hat{C}|\partial K_i| \int_{\partial\hat{K}_i} (\hat{\mu} - \Pi_{\partial\hat{K}_i}\hat{\mu})^p\right)^{1/p}.$$

We can use Poincaré-Wirtinger again. Thus we have

$$||\mu - \Pi_{\partial K_i}\mu||_{L^\infty(\partial K_i)} \leq \hat{C}||\hat{\nabla}\hat{\mu}||_{L^\infty(\partial\hat{K}_i)}$$

and we conclude as before.

□

2.3 Numerical experiments with non-adapted meshes

The goal of this section is to numerically verify the equivalence between the error estimator presented in Section 2.2 and the true error. We use non-adapted meshes with different mesh size and aspect ratio. We introduce the following notations : the error in H^1 semi-norm

$$e_{H^1} = ||\nabla(u - u_h)||_{L^2(\Omega)},$$

the error in the weighted H^1 semi-norm

$$e_{\mu,H^1} = ||\mu^{1/2}\nabla(u - u_h)||_{L^2(\Omega)},$$

the anisotropic estimator

$$\eta^A = \left(\sum_{K\in\mathcal{T}_h} \eta_K^2\right)^{1/2},$$

the anisotropic effectivity index

$$\mathrm{ei}^A = \frac{\eta^A}{e_{\mu,H^1}},$$

and the ZZ effectivity index

$$\mathrm{ei}^{ZZ} = \frac{||\nabla u_h - \Pi_h^{ZZ} \nabla u_h||_{L^2(\Omega)}}{e_{H^1}}.$$

We aim to verify that these quantities satisfy the following properties :

- ei^A is independent of the solution u,
- ei^A is independent of the variations of μ and of the ratio $\frac{\mu_{\max}}{\mu_{\min}}$,
- ei^A is independent of the mesh size and aspect ratio,
- ei^{ZZ} is close to one (see the discussion in Remark 2.1).

For all $x \in \mathbb{R}$, $\epsilon > 0$, let

$$H_\epsilon(x) = \begin{cases} 0 & x \leq -\epsilon, \\ \frac{x+\epsilon}{2\epsilon} + \frac{1}{2\pi}\sin(\frac{\pi x}{\epsilon}) & -\epsilon \leq x \leq \epsilon, \\ 1 & \epsilon \leq x, \end{cases}$$

be a smoothing of the classical Heavyside function. We consider problem (2.1) in the unit square $\Omega = (0,1)^2$ and choose f so that u is given by

$$u(\mathbf{x}) = \mu_2 \sin(\pi x_1)\sin(\pi x_2) H_\epsilon(x_1 - 0.5) + \mu_1 \sin(\pi x_1)\sin(\pi x_2) H_\epsilon(0.5 - x_1) \tag{2.21}$$

and μ is given by

$$\mu(\mathbf{x}) = \mu_2 H_\epsilon(x_1 - 0.5) + \mu_1(1 - H_\epsilon(x_1 - 0.5)), \tag{2.22}$$

with $\mu_1, \mu_2 > 0$. Thus μ is constant except in a thin boundary layer of width ϵ where a strong gradient can be observed. The results are reported in Table 2.1, where h_1 and h_2 denote the mesh size in direction x_1 and x_2 respectively, see Figures 2.2 and 2.3. We observe that the error estimator is equivalent to the true error uniformly in the mesh size and the ratio $\frac{\mu_{\max}}{\mu_{\min}}$. Moreover the values of ei^{ZZ} show that the Zienkiewicz-Zhu error estimator is asymptotically exact.

TABLE 2.1 : True errors, estimated error and effectivity indices for various non-adapted meshes and various choices of μ_1, μ_2 and ϵ, when u and μ are given by (2.21) and (2.22).

$\mu_1 = 1\ \mu_2 = 2\ \epsilon = 0.1$

h_1-h_2	η^A	e_{μ,H^1}	ei^A	η^{ZZ}	e_{H^1}	ei^{ZZ}
0.05-0.5	8.58	3.25	2.64	1.98	2.54	0.78
0.025-0.25	6.34	2.95	2.37	1.49	1.64	0.91
0.0125-0.125	3.78	1.38	2.74	0.99	1.05	0.95
0.00625-0.0625	2.01	0.73	2.76	0.53	0.55	0.97
0.003125-0.03125	1.02	0.36	2.81	0.27	0.28	0.98
0.0015625-0.015625	0.52	0.19	2.81	0.14	0.14	0.98
0.00078125-0.0078125	0.26	0.095	2.78	0.07	0.07	0.98

$\mu_1 = 1\ \mu_2 = 2\ \epsilon = 0.01$

h_1-h_2	η^A	e_{μ,H^1}	ei^A	η^{ZZ}	e_{H^1}	ei^{ZZ}
0.05-0.5	91.07	36.24	2.51	20.67	29.83	0.69
0.025-0.25	63.39	23.47	2.70	14.44	19.72	0.73
0.0125-0.125	14.20	6.62	2.15	3.50	5.36	0.65
0.00625-0.0625	6.74	2.20	3.07	2.03	1.77	1.15
0.003125-0.03125	3.27	0.99	3.29	0.87	0.81	1.07
0.0015625-0.015625	1.67	0.51	3.28	0.42	0.42	1.02
0.00078125-0.0078125	0.85	0.26	3.30	0.21	0.21	1.00

$\mu_1 = 1\ \mu_2 = 100\ \epsilon = 0.1$

h_1-h_2	η^A	e_{μ,H^1}	ei^A	η^{ZZ}	e_{H^1}	ei^{ZZ}
0.05-0.5	3584.94	1077.18	3.33	123.56	135.07	0.91
0.025-0.25	2395.20	764.94	3.13	85.30	89.35	0.95
0.0125-0.125	1365.70	469.50	2.91	50.27	52.43	0.95
0.00625-0.0625	715.23	246.22	2.90	26.23	26.89	0.98
0.003125-0.03125	359.39	120.49	2.98	12.94	13.13	0.99
0.0015625-0.015625	182.26	61.13	2.98	6.54	6.63	0.99
0.00078125-0.0078125	92.05	31.22	2.95	3.32	3.37	0.99

$\mu_1 = 1\ \mu_2 = 100\ \epsilon = 0.01$

h_1-h_2	η^A	e_{μ,H^1}	ei^A	η^{ZZ}	e_{H^1}	ei^{ZZ}
0.005-0.05	3258.10	1183.14	2.75	162.95	183.48	0.89
0.0025-0.025	1517.05	450.98	3.36	66.70	65.89	1.01
0.00125-0.0125	777.60	231.73	3.36	32.19	32.01	1.01
0.000625-0.00625	375.00	110.71	3.39	15.60	15.61	1.00
0.0006-0.006	360.27	106.08	3.40	14.87	14.90	1.00

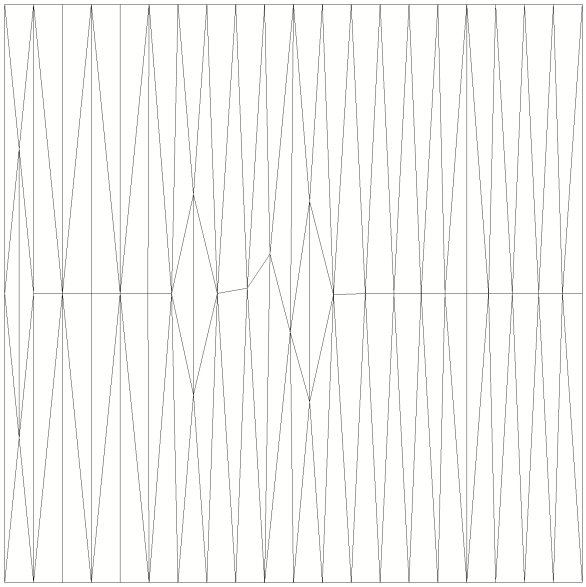

FIGURE 2.2 : Example of non-adapted mesh with $h_1 = 0.05$ and $h_2 = 0.5$.

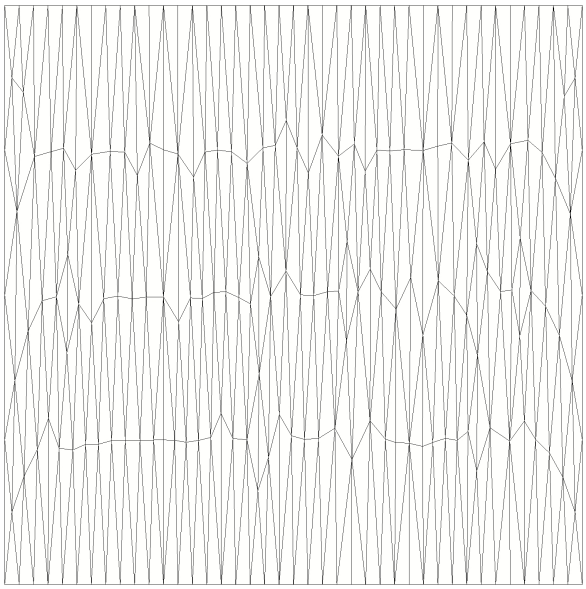

FIGURE 2.3 : Example of non-adapted mesh with $h_1 = 0.025$ and $h_2 = 0.25$.

Consider again problem (2.1) in the unit square $\Omega = (0,1)^2$, with exact solution

$$u(\mathbf{x}) = \mu_2 \sin(\pi x_1) H_\epsilon(x_1 - 0.5) + \mu_1 \sin(\pi x_1) H_\epsilon(0.5 - x_1). \tag{2.23}$$

and μ defined by (2.22). Note that the exact solution is not zero on the boundary anymore, thus in principle an extra-term should be added in the error estimator. However,

numerical results indicate that this is not needed. In Table 2.2 numerical results for different values of μ_1, μ_2, ϵ and mesh sizes h_1, h_2 are reported. We observe again, that the error estimator is equivalent to the true error uniformly in the mesh size, the ratio $\frac{\mu_{\max}}{\mu_{\min}}$ and additionally the mesh aspect ratio. The values of ei^{ZZ} show that the Zienkiewicz-Zhu error estimator is asymptotically exact.

TABLE 2.2 : True error, estimated error and effectivity indices for various non-adapted meshes and various choices of μ_1, μ_2 and ϵ, when u and μ are given by (2.23) and (2.22).

$\mu_1 = 1$ $\mu_2 = 2$ $\epsilon = 0.1$						
h_1-h_2	η^A	e_{μ,H^1}	ei^A	η^{ZZ}	e_{H^1}	ei^{ZZ}
0.05-0.5	1.94	0.67	2.89	0.61	0.53	1.14
0.025-0.25	1.11	0.38	2.92	0.32	0.30	1.08
0.0125-0.125	0.55	0.19	2.89	0.15	0.15	1.02
0.00625-0.0625	0.27	0.096	2.82	0.078	0.077	1.00
0.003125-0.03125	0.13	0.046	2.85	0.037	0.037	1.00
0.005-0.5	0.23	0.068	3.33	0.054	0.054	1.00
0.0025-0.25	0.12	0.037	3.20	0.029	0.029	1.00
0.00125-0.125	0.057	0.019	3.02	0.015	0.015	1.00
$\mu_1 = 1$ $\mu_2 = 2$ $\epsilon = 0.01$						
h_1-h_2	η^A	e_{μ,H^1}	ei^A	η^{ZZ}	e_{H^1}	ei^{ZZ}
0.05-0.5	124.64	51.10	2.44	31.14	42.07	0.74
0.025-0.25	71.61	27.78	2.58	16.72	23.21	0.72
0.0125-0.125	17.34	8.73	1.99	4.82	7.13	0.68
0.00625-0.0625	7.46	2.83	2.64	2.64	2.32	1.14
0.003125-0.03125	3.68	1.33	2.78	1.18	1.10	1.08
0.005-0.5	5.67	1.88	3.02	1.75	1.52	1.15
0.0025-0.25	2.97	1.01	2.95	0.88	0.82	1.06
0.000125-0.125	1.59	0.55	2.92	0.46	0.45	1.03
0.0000625-0.0625	0.80	0.28	2.90	0.23	0.22	1.01
$\mu_1 = 1$ $\mu_2 = 100$ $\epsilon = 0.1$						
h_1-h_2	η^A	e_{μ,H^1}	ei^A	η^{ZZ}	e_{H^1}	ei^{ZZ}
0.05-0.5	1092.93	377.55	2.89	60.08	55.35	1.09
0.025-0.25	643.59	219.28	2.93	31.33	29.50	1.06
0.0125-0.125	311.35	107.36	2.90	15.05	14.88	1.01
0.00625-0.0625	151.81	53.81	2.82	7.59	7.58	1.00
0.003125-0.03125	74.55	26.22	2.84	3.57	3.57	1.00
0.005-0.5	131.94	38.15	3.46	5.31	5.30	1.00
0.0025-0.25	67.29	20.87	3.23	2.87	2.86	1.00
0.00125-0.125	32.51	10.63	3.06	1.48	1.49	1.00
0.000625-0.0625	15.44	5.15	3.00	0.72	0.72	0.99
$\mu_1 = 1$ $\mu_2 = 100$ $\epsilon = 0.01$						
h_1-h_2	η^A	e_{μ,H^1}	ei^A	η^{ZZ}	e_{H^1}	ei^{ZZ}
0.0005-0.5	338.15	109.53	3.09	15.38	15.52	0.99
0.00025-0.25	188.41	60.35	3.12	8.51	8.51	1.00
0.000125-0.125	95.46	31.43	3.04	4.52	4.53	1.00

We aim now to numerically verify predictions of Remark 2.3. Consider numerical experiment of Table 2.1 with $\mu_1 = 1$, $\mu_2 = 2$, $\epsilon = 0.1$, $h = h_1 = \frac{1}{N_x}$ and $h_2 = 2h_1$. In Figure 2.4 we can observe a plot of convergence of $(\eta^A)^2$ and e^2_{μ,H^1}. We observe, as predicted, $(\eta^A)^2 = O(h^2)$ and $e^2_{\mu,H^1} = O(h^2)$. Moreover, in Figure 2.5, we report the convergence of all remaining terms. As theoretically predicted, we have

$$\sum_{K\in\mathcal{T}_h} \lambda^2_{2,K} ||f - \Pi_K f||^2_{L^2(K)} = O(h^4),$$
$$\sum_{K\in\mathcal{T}_h} \lambda^2_{2,K} ||\nabla\mu - \Pi_K \nabla\mu||^2_{L^2(K)} = O(h^4),$$
$$\sum_{K\in\mathcal{T}_h} \lambda_{2,K} \sum_{i=1}^{3} |||[(\mu - \Pi_{l_i}\mu)\nabla u_h \cdot \mathbf{n}]|||^2_{L^2(l_i)} = O(h^5),$$
$$\sum_{K\in\mathcal{T}_h} ||(\mu)^{1/2}\nabla(u - u_h)||^2_{L^2(K)} ||\mu - \Pi_K\mu||_{L^\infty(K)} = O(h^3),$$

which are higher order terms with respect to $(\eta^A)^2$.

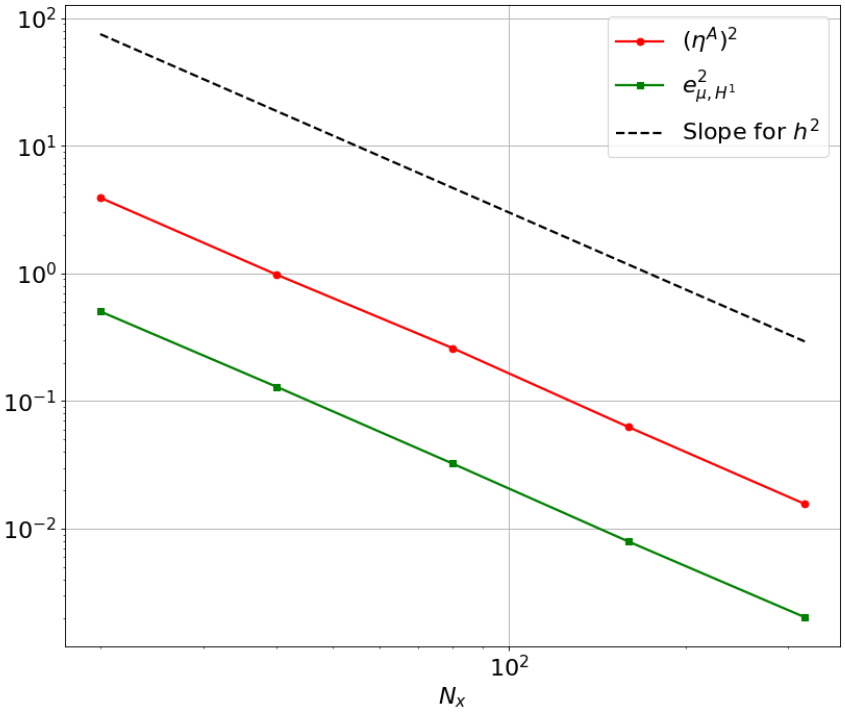

FIGURE 2.4 : Convergence of weighted H^1 semi-norm error and error indicator on fixed meshes, when u and μ are given by (2.21) and (2.22), with $\mu_1 = 1$, $\mu_2 = 2$ and $\epsilon = 0.1$.

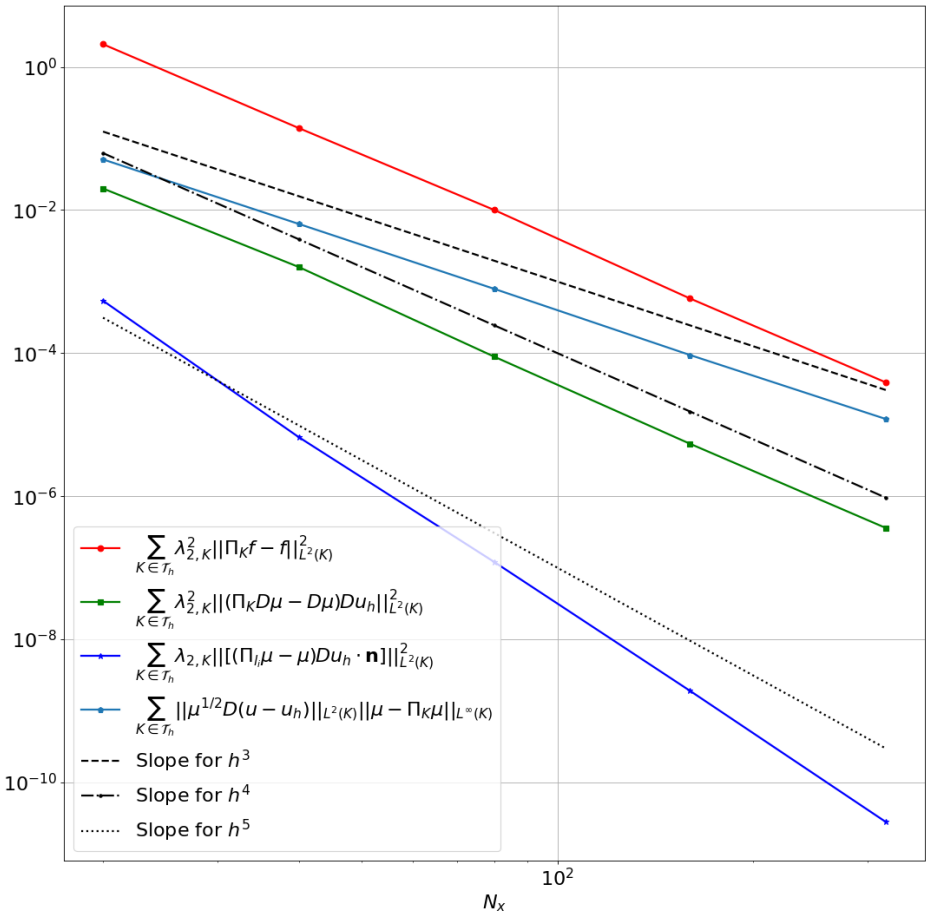

FIGURE 2.5 : Convergence of higher order terms on fixed meshes, when u and μ are given by (2.21) and (2.22), with $\mu_1 = 1$, $\mu_2 = 2$ and $\epsilon = 0.1$.

For a given accuracy, the goal is now to construct adapted meshes to solve problem (2.1) at a reduced computational cost. We thus present an adaptive algorithm based on an a posteriori error estimator.

2.4 Adaptive algorithms

For $\infty > p \geq 2$ and $s = 1, \ldots, d$, let $u \in (W_0^{1,p}(\Omega))^s$ be solution of a generic PDE. Let u_h be the corresponding continuous piecewise linear finite element solution, $||u - u_h||$ represents the error and $\sum_{K\in\mathcal{T}_h} \eta_K^2$ is the corresponding error estimator. For instance, when considering problem (2.1) $s = 1$, $p = 2$, $||u - u_h|| := ||\mu^{1/2}\nabla(u - u_h)||_{L^2(\Omega)}$ and η_K^2

is given by (2.6).

2.4.1 Anisotropic adaptive algorithm

An anisotropic adaptive algorithm in dimension $d = 2, 3$ to solve elliptics PDEs is presented. Presentation and applications of the algorithm can be found in [28, 60, 62, 29, 57]. We define

$$\eta_K^2 = \left(\sum_{i=1}^{d} \eta_{i,K}^4 \right)^{1/2},$$

with

$$\eta_{i,K}^4 = \rho_K^2 \omega_{2,K,i}^2 (u - u_h), \tag{2.24}$$

$$\omega_{2,K,i}^2 (u - u_h) = \lambda_{i,K}^2 \mathbf{r}_{i,K}^T G_K (u - u_h) \mathbf{r}_{i,K} \tag{2.25}$$

and the residual quantity ρ_K depends on the considered PDE. For instance, when considering (2.1)

$$\rho_K = \left(||\Pi_K \left(f + \nabla \cdot (\mu \nabla u_h) \right)||_{L^2(K)} + \frac{1}{2} \sum_{i=1}^{d+1} \left(\frac{|\partial K_i|}{\prod_{j=1}^{d} \lambda_{j,K}} \right)^{1/2} \|[\Pi_{\partial K_i} \mu \nabla u_h \cdot \mathbf{n}]\|_{L^2(\partial K_i)} \right)$$

The quantity $\eta_{i,K}^4$ represents the error in direction $\mathbf{r}_{i,K}$ $i = 1, \ldots, d$. Moreover $G_K(u - u_h)$ still involves the exact solution. In practice post-processing techniques can be applied. We refer to Remark 2.1 for details and we suppose the error indicator as fully computable.

The goal of the adaptive algorithm is to build sequence of meshes, possibly having large aspect ratio, such that the relative estimated error is close to a given tolerance TOL, i.e.

$$0.75\text{TOL} \leq \left(\frac{\sum_{K \in \mathcal{T}_h} \eta_K^2}{||u_h||^m} \right)^{1/m} \leq 1.25\text{TOL}, \tag{2.26}$$

where m is a positive integer (usually $m = 2$). When constructing a mesh satisfying (2.26), the following two main goals have to be kept in mind :

- Align the stretching directions $\mathbf{r}_{i,K}$ to the ith eigenvector of $G_K(u - u_h)$. In Lemma 4.1 of [33] this choice is justified.

- Equidistribute the error in the stretching directions of each element. Numerical experiments performed in [59] suggest this approach. Notice also that in Theorem 2.1 this is equivalent to satisfy hypothesis (2.7) with an equality, which is necessary in order to prove equivalence between the estimated error and the true error. The same occurs in Theorem 4.3.

A sufficient condition for (2.26) to hold is to require that for each $K \in \mathcal{T}_h$

$$\frac{\mathcal{L}}{N_K} \leq \eta_K^2 \leq \frac{\mathcal{R}}{N_K}, \tag{2.27}$$

where we define N_K the number of elements $K \in \mathcal{T}_h$,

$$\mathcal{L} = 0.75^m \mathrm{TOL}^m ||u_h||^m \tag{2.28}$$

and

$$\mathcal{R} = 1.25^m \mathrm{TOL}^m ||u_h||^m. \tag{2.29}$$

Condition (2.27) means that the estimated error is equidistribute over each K. In order to insure (2.27), we require for each $K \in \mathcal{T}_h$ and for $i = 1, \cdots, d$

$$\frac{\mathcal{L}^2}{dN_K^2} \leq \eta_{i,K}^4 \leq \frac{\mathcal{R}^2}{dN_K^2}, \tag{2.30}$$

which correspond to equidistributing the error in each stretching direction. Often, mesh generators require information at the vertices rather than at the elements. Thus we define the error indicator for each vertex P as

$$\eta_P^2 = \sum_{\substack{K \in \mathcal{T}_h \\ P \in K}} \eta_K^2$$

so that

$$\sum_{P \in \mathcal{T}_h} \eta_P^2 = (d+1) \sum_{K \in \mathcal{T}_h} \eta_K^2,$$

and (2.26) can be replaced by

$$0.75\mathrm{TOL} \leq \left(\frac{\sum_{P \in \mathcal{T}_h} \eta_P^2}{(d+1)||u_h||^m} \right)^{1/m} \leq 1.25\mathrm{TOL}.$$

We then equidistribute η_P^2 on each vertex P by adjusting the mesh with the objective to satisfy

$$\frac{(d+1)\mathcal{L}}{N_v} \leq \eta_P^2 \leq \frac{(d+1)\mathcal{R}}{N_v},$$

where N_v is the number of vertices of $\mathcal{T}_h$. As before, we want to equidistribute the error in the directions of stretching. Observing that

$$\eta_P^2 = \sum_{\substack{K \in \mathcal{T}_h \\ P \in K}} (\sum_{i=1}^{d} \eta_{i,K}^4)^{1/2} = \sigma_P^{-1} \sum_{\substack{K \in \mathcal{T}_h \\ P \in K}} \sum_{i=1}^{d} \eta_{i,K}^2,$$

with

$$\sigma_P = \frac{\sum\limits_{\substack{K\in\mathcal{T}_h\\ P\in K}} \sum\limits_{i=1}^{d} \eta_{i,K}^2}{\sum\limits_{\substack{K\in\mathcal{T}_h\\ P\in K}} \Big(\sum\limits_{i=1}^{d} \eta_{i,K}^4\Big)^{1/2}}, \tag{2.31}$$

we require to have for $i = 1, \ldots, d$

$$\frac{(d+1)\sigma_P \mathcal{L}}{dN_v} \leq \sum_{\substack{K\in\mathcal{T}_h\\ P\in K}} \eta_{i,K}^2 \leq \frac{(d+1)\sigma_P \mathcal{R}}{dN_v}. \tag{2.32}$$

Notice that we have $1 \leq \sigma_P \leq \sqrt{d}$.

We are now in position to discuss the update process of the mesh. For each vertex we define the local gradient error matrix

$$G_P = \sum_{\substack{K\in\mathcal{T}_h\\ P\in K}} G_K(u - u_h)$$

and the average stretching values

$$\lambda_{i,P} = \frac{\sum_{\substack{K\in\mathcal{T}_h\\ P\in K}} \lambda_{i,K}}{\sum_{\substack{K\in\mathcal{T}_h\\ P\in K}} 1}, \ i = 1, \ldots, d.$$

For a given tolerance TOL and mesh $\mathcal{T}_h$ we solve the problem and for each $i = 1, \ldots, d$ we do as follows. If

$$\frac{(d+1)\sigma_P \mathcal{L}}{dN_v} \geq \sum_{\substack{K\in\mathcal{T}_h\\ P\in K}} \eta_{i,K}^2,$$

then we set the mesh size in direction x_i to $h_{i,P} = 1.5\lambda_{i,P}$. If instead

$$\sum_{\substack{K\in\mathcal{T}_h\\ P\in K}} \eta_{i,K}^2 \geq \frac{(d+1)\sigma_P \mathcal{R}}{2N_v},$$

then we set $h_{i,P} = \frac{\lambda_{i,P}}{1.5}$. In order to build a new mesh, the mesh generator requires for each point $P \in \mathcal{T}_h$ a symmetric positive defined matrix M_P. We set $M_P = Q^T D Q$, where the columns of Q are given by the eigenvectors of G_P and D is a $d \times d$ diagonal matrix, having entries $(D)_{ii} = \frac{1}{h_{i,P}^2}$ for $i = 1, \ldots, d$.

The algorithm work as follows : Given a tolerance TOL, a starting coarse mesh $\mathcal{T}_h^1$ and an integer $N_{it} > 0$, the problem is solved, the error indicator is computed and a metric is built as previously discussed. Using a mesh generator (BL2D [46] if $d = 2$ and MeshGems [39] if $d = 3$) and the computed metric, a new mesh $\mathcal{T}_h^2$ is constructed. Starting from $\mathcal{T}_h^2$, the process is repeated $N_{it} - 1$ times. The anisotropic adaptive algorithm can be

observed in algorithm 1.

Algorithm 1 $(\mathrm{TOL}, \mathcal{T}_h^1, N_{it})$

for $j = 1, \ldots, N_{it}$ **do**
  Solve problem on $\mathcal{T}_h^j$
  Compute error estimator
  for $l = 1, \ldots, N_v$ **do**
    for $i = 1, \ldots, d$ **do**
      if $\sum_{\substack{K \in \mathcal{T}_h \\ P_l \in K}} \eta_{i,K}^2 \leq \frac{(d+1)\sigma_{P_l}\mathcal{L}}{dN_v}$ **then**
        $h_{i,P_l} \leftarrow 1.5\lambda_{i,P_l}$
      else if $\sum_{\substack{K \in \mathcal{T}_h \\ P_l \in K}} \eta_{i,K}^2 \geq \frac{(d+1)\sigma_{P_l}\mathcal{R}}{dN_v}$ **then**
        $h_{i,P_l} \leftarrow \lambda_{i,P_l}/1.5$
      End
    End
    Compute eigenvectors of G_{P_l}
    Compute Riemannian metric M_{P_l}
  End
  Update the mesh with a mesh generator : $\mathcal{T}_h^{j+1}$
End
$\mathcal{T}_h^{final} \leftarrow \mathcal{T}_h^{j+1}$
Output : Final mesh $\mathcal{T}_h^{final}$ and corresponding solution u_h^{final}

2.4.2 Numerical experiments with adapted meshes

We aim to verify the efficiency of algorithm 1. Consider problem (2.1) in the unit square $\Omega = (0,1)^2$, with exact solution (2.23) and μ defined by (2.22). For $\mu_1 = 1$, $\mu_2 = 2$ and $\epsilon = 0.1$ we choose a starting mesh $\mathcal{T}_h^1$ of size $h_1 = 0.1$ and $h_2 = 0.1$ in direction x_1 and x_2 respectively. We run algorithm 1 with $N_{it} = 40$ for different tolerances TOL. We report the obtained results in Table 2.3. In addition to quantities introduced in Section 2.3, we reported also the number of vertices N_v, the maximum aspect ratio $\mathrm{ar}_{\max} = \max_{K \in \mathcal{T}_h} \frac{\lambda_{1,K}}{\lambda_{2,K}}$ and the average aspect ratio $\mathrm{ar}_{\mathrm{av}}$. We repeat the experiment for $\mu_1 = 1$, $\mu_2 = 100$ and $\epsilon = 0.05$. We choose the same starting mesh $\mathcal{T}_h^1$ and we set $N_{it} = 80$. Results can be observed in Table 2.4. The obtained results suggest that the effectivity index ei^A does not depend on the aspect ratio, the solution u, the variation of μ and the ratio $\frac{\mu_{\max}}{\mu_{\min}}$. The effectivity index ei^{ZZ} is close to one showing the desired properties of the post-processing discussed in Remark 2.1.

TABLE 2.3 : True error, effectivity indices and aspect ratio for different values of the tolerance TOL, when u and μ are given by (2.23) and (2.22), with $\mu_1 = 1$, $\mu_2 = 2$ and $\epsilon = 0.1$. Results are obtained running algorithm 1(TOL,$\mathcal{T}_h^1$,$N_{it} = 40$).

$\mu_1 = 1$ $\mu_2 = 2$ $\epsilon = 0.1$

TOL	N_v	ei^A	e_{μ,H^1}	ei^{ZZ}	$\text{ar}_{\max}$	ar_{av}
0.1	126	3.15	0.14	1.02	317	62
0.05	252	3.09	0.075	1.01	492	108
0.025	481	3.32	0.037	1.01	1015	225
0.0125	1018	3.36	0.0189	1.00	2687	397
0.00625	2252	3.36	0.0093	1.00	3414	704

TABLE 2.4 : True error, effectivity indices and aspect ratio for different values of the tolerance TOL, when u and μ are given by (2.23) and (2.22), with $\mu_1 = 1$, $\mu_2 = 100$ and $\epsilon = 0.05$. Results are obtained running algorithm 1(TOL,$\mathcal{T}_h^1$,$N_{it} = 80$).

$\mu_1 = 1$ $\mu_2 = 100$ $\epsilon = 0.05$

TOL	N_v	ei^A	e_{μ,H^1}	ei^{ZZ}	$\text{ar}_{\max}$	ar_{av}
0.1	123	3.63	78.07	1.02	642	142
0.05	232	3.20	38.74	1.01	1337	305
0.025	464	3.25	20.72	0.99	2326	513
0.0125	882	3.36	10.20	0.99	6651	1131
0.00625	1801	3.34	5.08	1.00	11339	2242

Algorithm 1 give satisfying results, however in order to reduce the computational time, we present now a continuation algorithm for TOL [57].

2.4.3 Continuation anisotropic adaptive algorithm

The idea is to start with a coarse tolerance 2^NTOL_{goal} and finish with a fine one TOL_{goal}, N being an integer reduced by 1 every N_{it} iterations. The continuation anisotropic adaptive algorithm is presented in algorithm 2.

Algorithm 2 ($\text{TOL}_{goal}, N, \mathcal{T}_h^1, N_{it}$)

$\mathcal{T}_h^{final} \leftarrow \mathcal{T}_h^1$
for n=N,...,0 **do**
  $TOL = 2^n \text{TOL}_{goal}$
  $\mathcal{T}_h^{final} \leftarrow$ Algorithm 1(TOL,$\mathcal{T}_h^{final}$, N_{it})
End
Output : Final mesh $\mathcal{T}_h^{final}$ and corresponding solution u_h^{final}

Note that in algorithm 2 at each reduction of TOL the last obtained mesh is used as

starting mesh for algorithm 1.

We present now results obtained using this algorithm. After proving numerical efficiency of algorithm 2 we present numerical results showing the advantages of such a continuation algorithm with respect to algorithm 1. Note that except when differently stated algorithm 2 will be our first choice.

2.4.4 Numerical experiments with adapted meshes using algorithm 2

We aim to verify the efficiency of the adaptive algorithm 2 and to confirm theoretical predictions of Section 2.2 on adapted meshes.

Consider again problem (2.1) in the unit square $\Omega = (0,1)^2$, with exact solution (2.23) and μ defined by (2.22). We consider $\mu_1 = 1$, $\mu_2 = 2$ and $\epsilon = 0.01$. Since the solution is one dimensional, the adapted meshes should have a large aspect ratio. In Table 2.5 results are reported when running the continuation adaptive algorithm (algorithm 2) with $N = 5$, $\text{TOL}_{goal} = 0.003125$ and $N_{it} = 40$. An initial mesh of size $h_1 = 0.1$ and $h_2 = 0.1$ in direction x_1 and x_2 respectively is considered. In addition to quantities previously introduced, we reported also the total CPU time CPU_{tot} and the CPU time spent in the adaptation of the mesh $\text{CPU}_{\text{adapt}}$ (seconds, Intel Core 2.80 GHz). Note that, when running algorithm 2, we always report for $n = N, \ldots, 0$ the results obtained at the last iteration of algorithm 1 for the corresponding $\text{TOL} = 2^n \text{TOL}_{goal}$. Numerical results show the sharpness of our anisotropic error indicator, although the mesh aspect ratio is very large. The anisotropic effectivity index ei^A is independent from the aspect ratio and the ZZ effectivity index ei^{ZZ} is close to one as desired. Moreover, most of the CPU time is spent for building adapted meshes rather than solving the linear systems. To explain this fact, the number of Conjugate Gradient iterations needed to solve the linear system together with the number of vertices are reported for all iterations of the adaptive algorithm in Figure 2.6. Each time the tolerance is halved, first the number of vertices increases and then decreases to a value which is twice the one obtained with the previous tolerance. This is due to the fact that vertices are first added in an isotropic manner and then removed. Moreover, apart from the 40 first mesh iterations, the number of Conjugate Gradient iterations does not increase with the number of vertices, due to the fact that, with mesh iterations, the initial guess of the Conjugate Gradient method is closer and closer to the solution of the linear system. In Figure 2.7, the mesh and solution obtained when $\text{TOL} = 0.025$ are shown.

TABLE 2.5 : True error, effectivity indices and aspect ratio obtained when running algorithm 2($\text{TOL}_{goal} = 0.003125, N = 5, \mathcal{T}_h^1, N_{it} = 40$), when u and μ are given by (2.23) and (2.22), with $\mu_1 = 1$, $\mu_2 = 2$, $\epsilon = 0.01$ and $\mathcal{T}_h^1$ is a starting mesh of size $h_1 = h_2 = 0.1$.

$\mu_1 = 1\ \mu_2 = 2\ \epsilon = 0.01$

TOL	N_v	ei^A	e_{H^1}	ei^{ZZ}	ar_{max}	ar_{av}	CPU_{tot}	$\text{CPU}_{\text{adapt}}$
0.1	169	3.20	0.33	0.95	2989	621	11	8
0.05	323	3.43	0.15	0.99	5436	1243	17	13
0.025	632	3.22	0.075	1.00	15165	2500	25	20
0.0125	1216	3.36	0.038	1.00	27192	5572	36	29
0.00625	2364	3.37	0.019	1.00	84044	11866	54	44
0.003125	4876	3.37	0.009	1.00	131158	22515	88	73

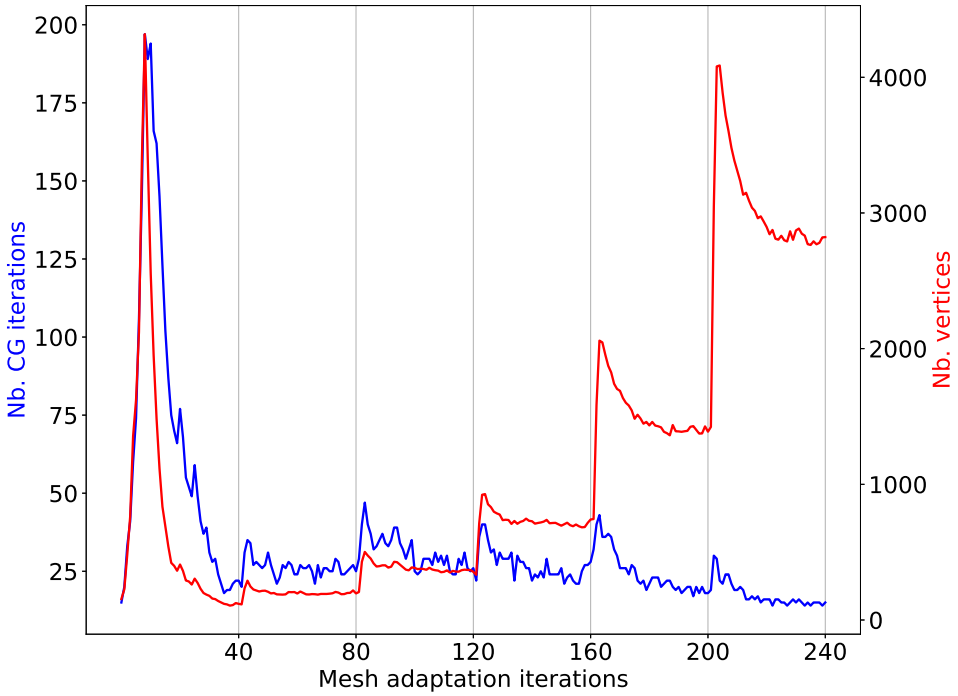

FIGURE 2.6 : Results obtained running algorithm 2($\text{TOL}_{goal} = 0.003125, N = 5, \mathcal{T}_h^1, N_{it} = 40$) with starting mesh $\mathcal{T}_h^1$ of size $h_1 = h_2 = 0.1$. In blue : number of Conjugate Gradient iterations needed to reach a tolerance 10^{-8} for each iteration of the adaptive algorithm. In red : number of vertices of each adapted mesh at each iteration of the adaptive algorithm.

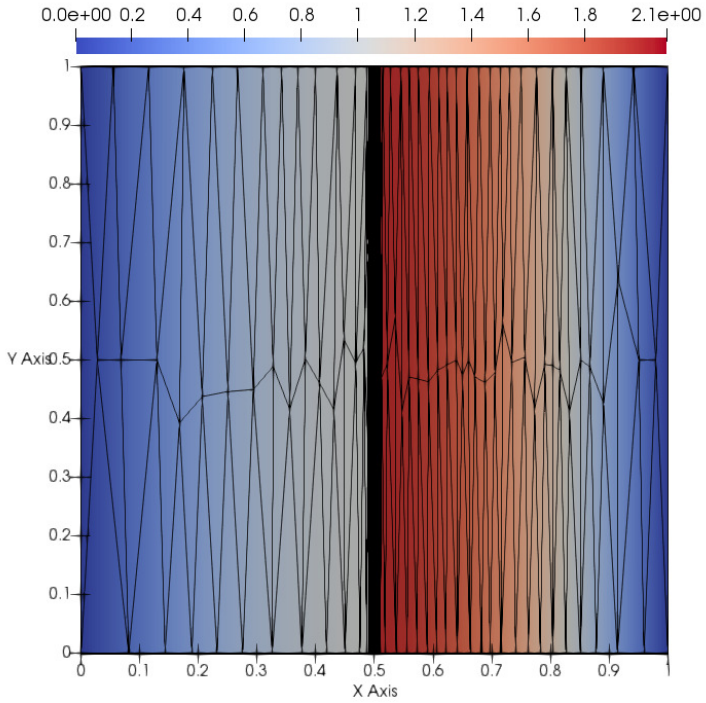

FIGURE 2.7 : Solution on adapted mesh when TOL $= 0.025$, when u and μ are given by (2.23) and (2.22), with $\mu_1 = 1$, $\mu_2 = 2$ and $\epsilon = 0.01$. The Result is obtained running algorithm 2(TOL$_{goal} = 0.003125$,$N = 5$,$\mathcal{T}_h^1$,$N_{it} = 40$) with $\mathcal{T}_h^1$ a starting mesh of size $h_1 = h_2 = 0.1$.

The next experiment has the goal to demonstrate the efficiency of algorithm 2 with respect to algorithm 1. Consider f such that the exact solution is given by (2.23) and μ by (2.22) with $\epsilon = 0.1$, $\mu_1 = 1$ and $\mu_2 = 2$. We choose a starting mesh $\mathcal{T}_h^1$ of size $h_1 = h_2 = 0.1$. We run algorithm 1 with TOL $= 0.0078125$ and $N_{it} = 280$, and algorithm 2 with TOL$_{goal} = 0.0078125$, $N = 6$ and $N_{it} = 40$. We recall that in practice algorithm 2 consists in applying algorithm 1 on a coarse tolerance and, starting from the obtained mesh, reduce by two the tolerance and repeat the process until the desired goal tolerance is reached. In Figure 2.8 we present the obtained results. Both algorithms give similar final meshes, the number of vertices is considerably close and the solutions obtained have comparable accuracy. However algorithm 1 requires an higher number of vertices along first iterations. For this problem we reported the total number of Conjugate Gradient iterations. The first approach increases considerably the CPU time. This is due to the higher refinement of the mesh at initial iterations. Algorithm 2 is clearly the fastest and best option. From now on we will consider only algorithm 2 for our numerical experiments.

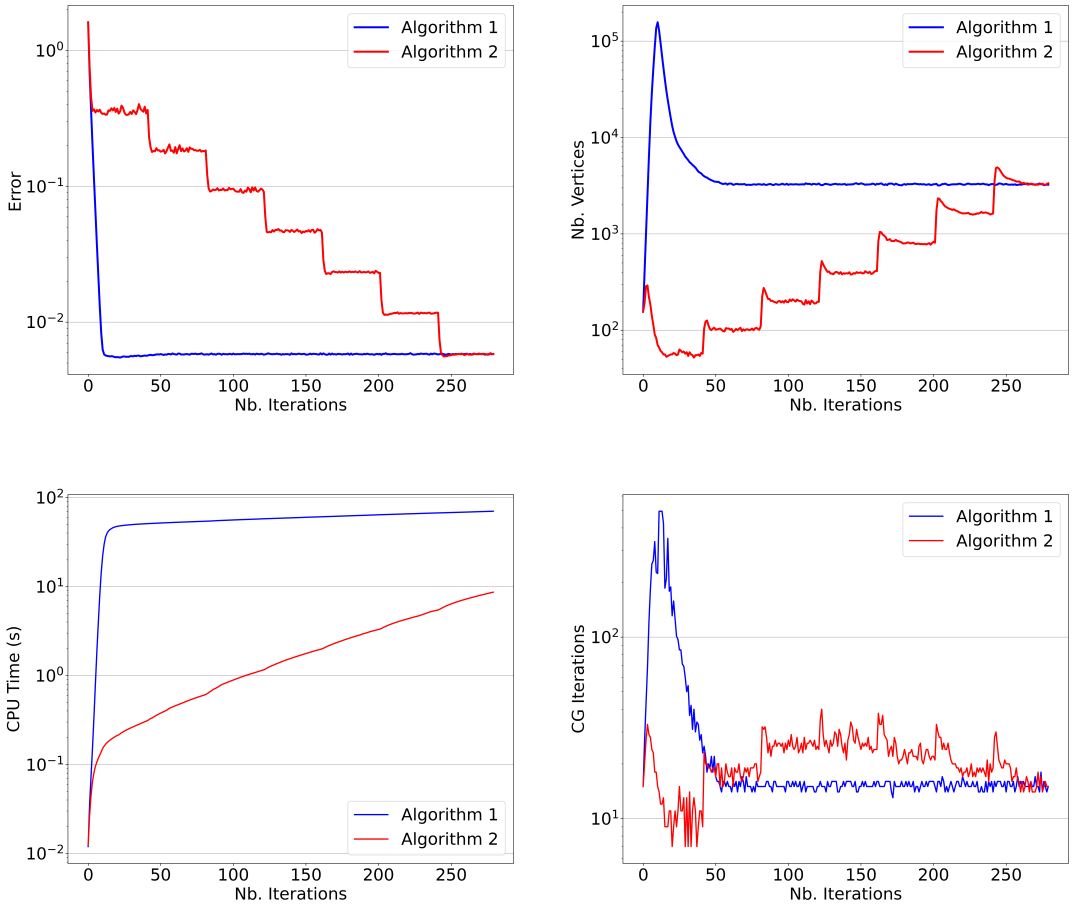

FIGURE 2.8 : Comparison of algorithm 1(TOL $= 0.0078125$,$\mathcal{T}_h^1$,$N_{it} = 280$) and algorithm 2(TOL$_{goal} = 0.0078125$,$N = 6$,$\mathcal{T}_h^1$,$N_{it} = 40$). Top left : error e_{μ,H^1} at each iteration of the corresponding algorithm. Top right : Number of vertices at each iteration of the corresponding algorithm. Bottom left : CPU time at each iteration of the corresponding algorithm. Bottom right : Conjugate Gradient iterations at each iteration of the adaptive algorithm.

In order to check the efficiency of using algorithm 2, we compare the results obtained with algorithm 2 to those obtained when using uniformly refined meshes (isotropic). We set $\epsilon = 0.01$, $\mu_1 = 1$ and $\mu_2 = 100$. We run algorithm 2 with $N = 7$, TOL$_{goal} = 0.00390625$, $N_{it} = 20$ and starting mesh $\mathcal{T}_h^1$ of size $h_1 = 0.2$ and $h_2 = 0.2$. In Figure 2.9 we observe the error e_{μ,H^1} and the corresponding number of vertices of the meshes. In Figure 2.10 we report the error e_{μ,H^1} and the corresponding total CPU time needed to obtain a solution with such an accuracy. In presence of boundary layers or regions where the solution u has strong variations, the use of an adaptive method is thus, clearly necessary to reach a small accuracy. Indeed the number of vertices needed to reach a given precision of the error is considerably reduce when using algorithm 2. Moreover having a solution with a

small error requires a smaller computational time when using the adaptive algorithm.

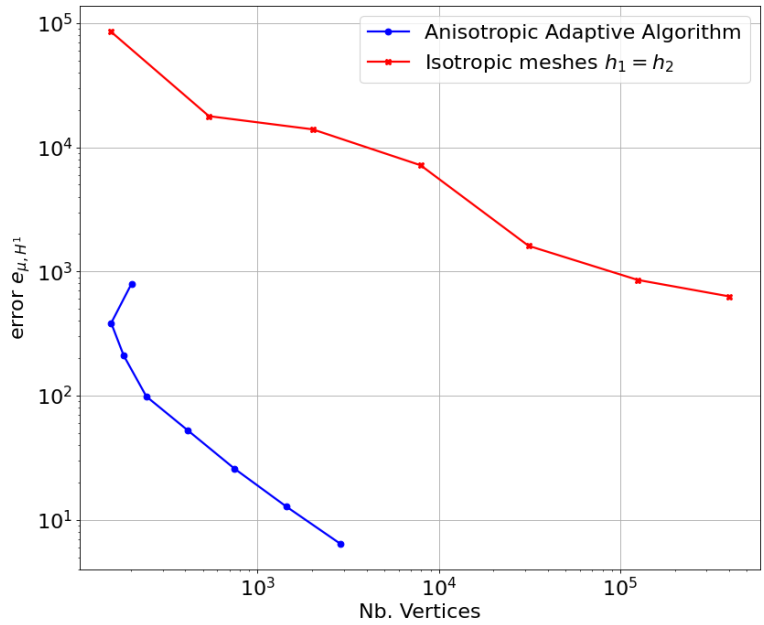

FIGURE 2.9 : Error e_{μ,H^1} and corresponding number of vertices, when solving (2.1) for f such that u, μ are given respectively by (2.23),(2.22) with $\mu_1 = 1$, $\mu_2 = 100$ and $\epsilon = 0.01$. Red : uniformly meshes. Blue : results obtained running algorithm 2($\text{TOL}_{goal} = 0.00390625$,$N = 7$,$\mathcal{T}_h^1$,$N_{it} = 20$).

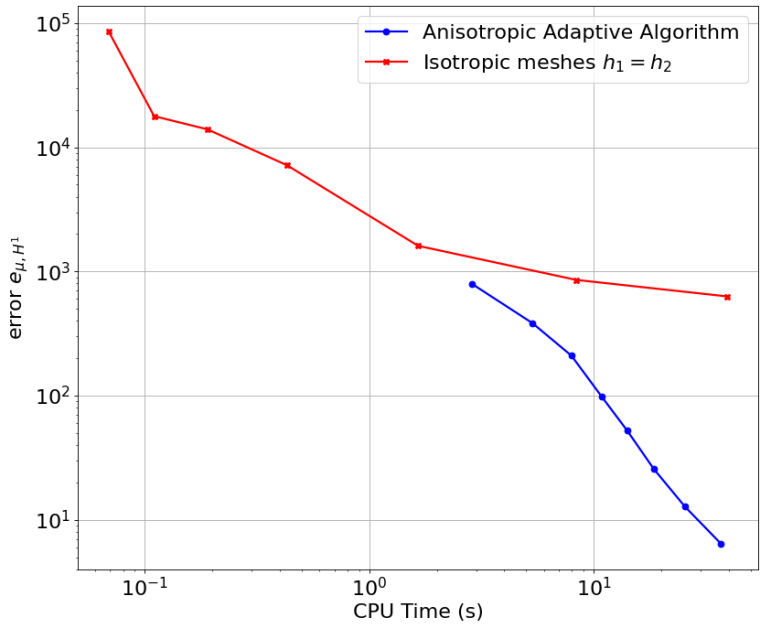

FIGURE 2.10 : Error e_{μ,H^1} and corresponding number of vertices, when solving (2.1) for f such that u, μ are given respectively by (2.23),(2.22) with $\mu_1 = 1$, $\mu_2 = 100$ and $\epsilon = 0.01$. Blue : uniformly meshes. Red : results obtained running algorithm 2($\text{TOL}_{goal} = 0.00390625$,$N = 7$,$\mathcal{T}_h^1$,$N_{it} = 20$).

At this point we numerically verify predictions of the higher order terms presented in Remark 2.3. Consider again $\Omega = (0,1)^2$, f given such that u is given by (2.21) and μ by (2.22) with $\epsilon = 0.1$, $\mu = 1$ and $\mu = 2$. We set $\text{TOL}_{goal} = 0.0625$ and we run algorithm 2 for $N = 4$, $N_{it} = 40$ and a starting mesh of size $h_1 = h_2 = 0.1$. In Figure 2.11 we can observe the convergence of $(\eta^A)^2$ and e^2_{μ,H^1}. We observe, as predicted, $(\eta^A)^2 = O(\text{TOL}^2)$ and $e^2_{\mu,H^1} = O(\text{TOL}^2)$. Moreover, in Figure 2.12, we report the convergence of all remaining terms. As theoretically discussed and observed with non-adapted meshes, we have

$$\sum_{K\in\mathcal{T}_h} \lambda^2_{2,K} ||f - \Pi_K f||^2_{L^2(K)} = O(\text{TOL}^4),$$
$$\sum_{K\in\mathcal{T}_h} \lambda^2_{2,K} ||\nabla\mu - \Pi_K \nabla\mu||^2_{L^2(K)} = O(\text{TOL}^4),$$
$$\sum_{K\in\mathcal{T}_h} \lambda_{2,K} \sum_{i=1}^{3} |||[(\mu - \Pi_{l_i}\mu)\nabla u_h \cdot \mathbf{n}]|||^2_{L^2(l_i)} = O(\text{TOL}^5),$$
$$\sum_{K\in\mathcal{T}_h} ||(\mu)^{1/2}\nabla(u - u_h)||^2_{L^2(K)} ||\mu - \Pi_K\mu||_{L^\infty(K)} = O(\text{TOL}^3),$$

which are negligible with respect to $(\eta^A)^2$.

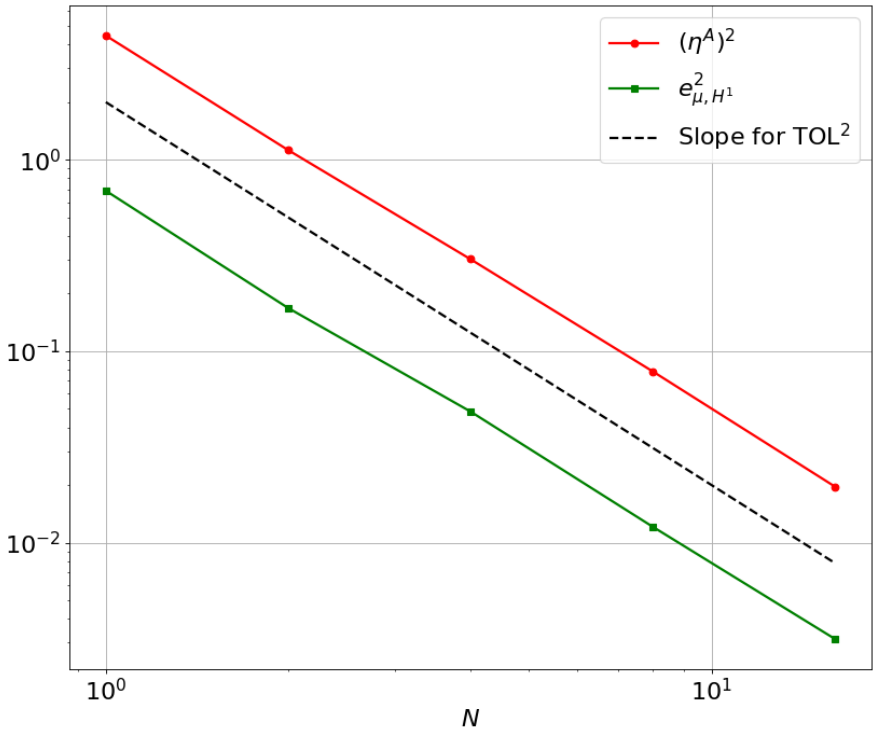

FIGURE 2.11 : Error estimator and true error, when u is given by (2.21) and μ by (2.22) with $\mu_1 = 1$, $\mu_2 = 2$ and $\epsilon = 0.1$. Results obtained running algorithm 2(TOL$_{goal}$ = 0.0625,$N = 4$,$\mathcal{T}_h^1$,$N_{it} = 40$).

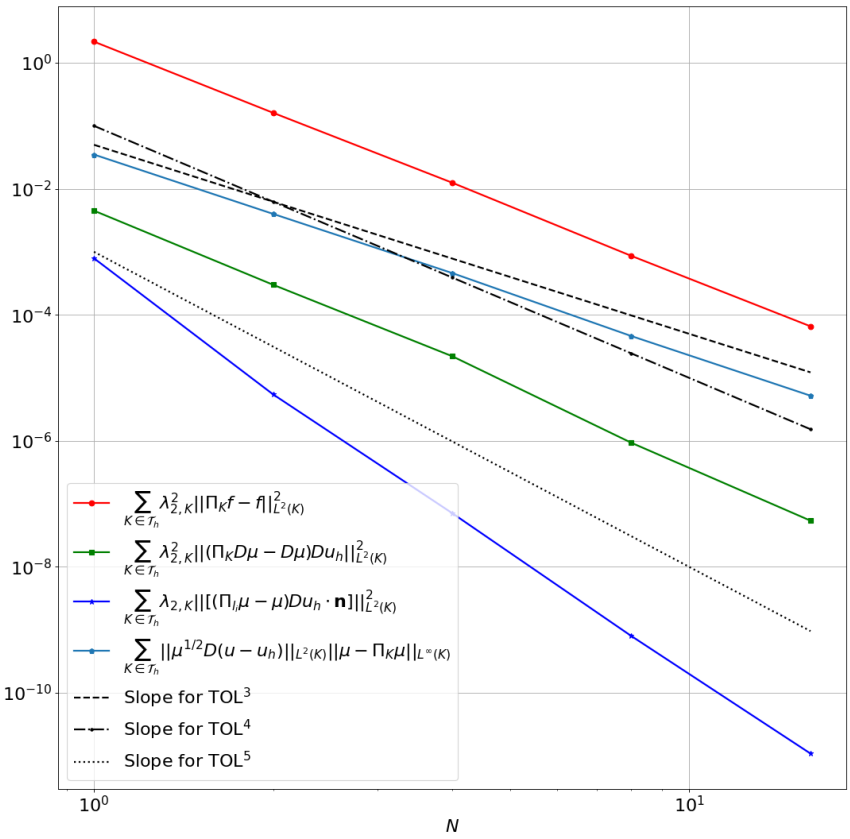

FIGURE 2.12 : Different higher order terms discussed in Remark 2.3, when u is given by (2.21) and μ by (2.22) with $\mu_1 = 1$, $\mu_2 = 2$ and $\epsilon = 0.1$. Results obtained running algorithm 2(TOL$_{goal} = 0.0625$,$N = 4$,$\mathcal{T}_h^1$,$N_{it} = 40$).

We now present a 3D numerical experiment. Let $\Omega = (0,1) \times (0,1) \times (0,0.1)$, we choose f such that μ is given by

$$\mu(\mathbf{x}) = \mu_2 H_\epsilon(x_3 - 0.05) + \mu_1(1 - H_\epsilon(x_3 - 0.05)), \tag{2.33}$$

and u by

$$u(\mathbf{x}) = \mu_2 \sin(\pi x_1) H_\epsilon(x_3 - 0.05) + \mu_1 \sin(\pi x_1) H_\epsilon(0.05 - x_3). \tag{2.34}$$

In Table 2.6 the results are reported when running the algorithm 2 with TOL$_{goal} = 0.03125$, $N = 4$, $N_{it} = 40$ and $\mathcal{T}_h^1$ an initial $10 \times 10 \times 2$ uniform mesh. Several values of μ_1, μ_2 and ϵ are tested. In Figures 2.13 and 2.14, the adapted mesh and solution are shown when TOL $= 0.25$, $\mu_1 = 1$, $\mu = 2$ and $\epsilon = 0.01$.

TABLE 2.6 : True error, effectivity indices and aspect ratio for different values of tolerance TOL, when u and μ are given by (2.34) and (2.33), with various values for and μ_1, μ_2 and ϵ running algorithm 2($\text{TOL}_{goal} = 0.03125$,$N = 4$,$\mathcal{T}_h^1$,$N_{it} = 40$).

$\mu_1 = 1$ $\mu_2 = 2$ $\epsilon = 0.1$

TOL	N_v	ei^A	e_{H^1}	ei^{ZZ}	$\text{ar}_{\max}$	ar_{av}
0.5	93	2.82	0.39	0.88	121	28
0.25	397	3.22	0.18	1.00	476	63
0.125	1525	3.28	0.09	1.00	589	99
0.0625	7511	3.27	0.05	0.99	1028	124
0.03125	39512	3.29	0.02	0.99	1769	166

$\mu_1 = 1$ $\mu_2 = 2$ $\epsilon = 0.01$

TOL	N_v	ei^A	e_{H^1}	ei^{ZZ}	$\text{ar}_{\max}$	ar_{av}
0.5	644	3.61	0.97	1.03	1220	173
0.25	2426	3.65	0.46	0.99	2533	257
0.125	13317	3.67	0.23	0.99	2552	277
0.0625	32479	3.56	0.12	0.98	12101	979
0.03125	214170	3.52	0.07	0.98	33075	1227

$\mu_1 = 1$ $\mu_2 = 100$ $\epsilon = 0.1$

TOL	N_v	ei^A	e_{H^1}	ei^{ZZ}	$\text{ar}_{\max}$	ar_{av}
0.5	107	3.42	32.62	0.99	234	45
0.25	366	3.45	15.67	1.03	377	72
0.125	1570	3.36	8.22	1.01	645	102
0.0625	7250	3.45	3.95	1.00	2024	132
0.03125	39129	3.44	1.96	0.99	1961	184

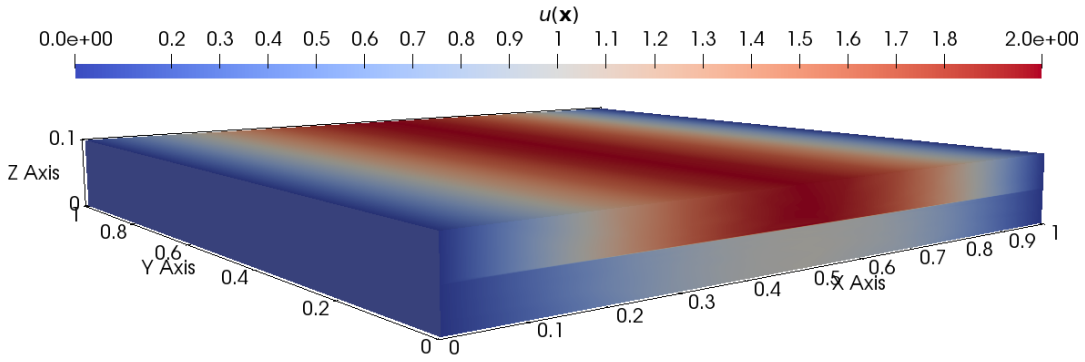

FIGURE 2.13 : Solution on adapted mesh when TOL = 0.25, u and μ are given by (2.34) and (2.33), with $\mu_1 = 1$, $\mu_2 = 2$ and $\epsilon = 0.01$.

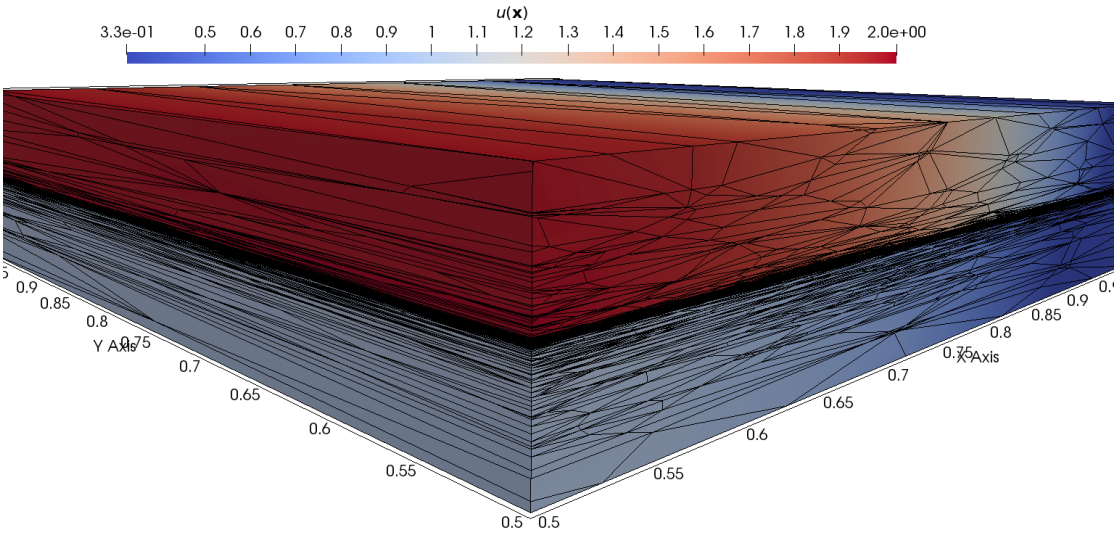

FIGURE 2.14 : Cut at $x = 0.5$ and $y = 0.5$ of the adapted mesh obtained when TOL $= 0.25$, when u and μ are given by (2.34) and (2.33), with $\mu_1 = 1$, $\mu_2 = 2$ and $\epsilon = 0.01$.

In our experiments we observe an anisotropic effectivity index ei^A constant. Thus we can obtain an "exact" error indicator by dividing η_K by ei^A. We divide now η_K by 3.45. the effectivity index should be close to one. We run again algorithm 2 for $\text{TOL}_{goal} = 0.015625$, $N = 4$ and $N_{it} = 40$ when $\mu_1 = 1$, $\mu_2 = 100$ and $\epsilon = 0.01$. The results are reported in Table 2.7. As expected, the effectivity index is now close to one. Again, a non negligible fraction of the CPU time is needed to adapt the mesh.

TABLE 2.7 : True error, effectivity indices and aspect ratio for different values of tolerance TOL, when u and μ are given by (2.34) and (2.33), with $\mu_1 = 1$, $\mu_2 = 100$ and $\epsilon = 0.01$. Results obtained running algorithm 2($\text{TOL}_{goal} = 0.01562$,$N = 4$,$\mathcal{T}_h^1$,$N_{it} = 40$).

TOL	N_v	ei^A	e_{H^1}	ei^{ZZ}	$\text{ar}_{\max}$	ar_{av}	CPU_{tot}	$\text{CPU}_{\text{adapt}}$
0.25	191	1.06	195.85	1.01	864	143	23	19
0.125	452	1.09	85.17	1.04	4542	310	46	39
0.0625	1283	1.03	47.37	1.01	6684	694	94	78
0.03125	6426	1.01	26.36	0.99	15832	1098	292	237
0.015625	33745	1.10	13.60	0.99	117521	1588	2298	1402

2.4.5 An anisotropic adaptive algorithm based on the number of vertices

We propose another adaptive algorithm, which can be of interest for industrial applications. The goal of the algorithm is to obtain a mesh such that the number of vertices is close to a number M and the vertices are distributed according to the error estimator. Let M be the goal number of vertices, $\alpha > 0$ a positive constant and let N be the number

of vertices of the actual mesh. All other notations are as in the rest of Section 2.4. The objective will be to construct a mesh such that

$$\frac{1}{1+\alpha}M \leq N \leq \frac{1}{1-\alpha}M \tag{2.35}$$

is satisfied. If, for all vertices $P_i \in \mathcal{T}_h$, $i = 1, \ldots, N$ we have

$$(1-\alpha)\frac{1}{M}\sum_{j=1}^{N}\eta_{P_j}^2 \leq \eta_{P_i}^2 \leq (1+\alpha)\frac{1}{M}\sum_{j=1}^{N}\eta_{P_j}^2, \tag{2.36}$$

then relation (2.35) is satisfied. Thus we will require that for all $i = 1, \ldots, N$ and $j = 1, \ldots, d$ the following is satisfied

$$\frac{\sigma_{P_i}}{d}(1-\alpha)\frac{1}{M}\sum_{l=1}^{N}\eta_{P_l}^2 \leq \sum_{K\in\mathcal{T}_h, P_i\in K}\eta_{j,K}^2 \leq \frac{\sigma_{P_i}}{d}(1+\alpha)\frac{1}{M}\sum_{l=1}^{N}\eta_{P_l}^2. \tag{2.37}$$

The adaptation procedure is the same as explained in section 2.4.1 replacing (2.32) by (2.37). We consider thus the new algorithm 3.

Algorithm 3 $(M_{goal}, N, N_{it}, \alpha, \mathcal{T}_h^1)$

$\mathcal{T}_h^{final} \leftarrow \mathcal{T}_h^1$
for n=N,. . .,0 **do**
  $M = 2^{-n}\mathrm{M}_{goal}$
  $\mathcal{T}_h^{final} \leftarrow$ Algorithm 1(TOL,$\mathcal{T}_h^{final}$,N_{it}) replacing (2.32) by (2.37)
End
Output : Final mesh $\mathcal{T}_h^{final}$ and corresponding solution u_h^{final}

Consider problem (2.1) with $\Omega = (0,1)^2$, f such that u is given by (2.23) with $\epsilon = 0.01$ and μ by (2.22) with $\mu_1 = 1$ and $\mu_2 = 2$. We set $\alpha = 10/M$, $M_{goal} = 3200$, $N = 6$, $N_{it} = 40$ and we run the Algorithm 3 , starting by a mesh of size $h_1 = h_2 = 0.1$. Obtained results are reported in Table 2.8.

TABLE 2.8 : True error, effectivity indices and aspect ratio for different values of tolerance TOL, when u and μ are given by (2.34) and (2.33), with $\mu_1 = 1$, $\mu_2 = 100$ and $\epsilon = 0.01$. Results obtained running algorithm 3($M_{goal} = 3200$,$N = 6$,$N_{it} = 40$,$\alpha = 10/M$,$\mathcal{T}_h^1$).

M	N_v	ei^A	e_{H^1}	ei^{ZZ}	$\mathrm{ar}_{\max}$	$\mathrm{ar}_{\mathrm{av}}$
100	102	1.24	27.33	0.53	8	3
200	213	3.11	0.21	0.99	3358	736
400	408	3.06	0.11	1.00	8721	1629
800	802	3.24	0.053	1.00	16119	3336
1600	1563	3.33	0.028	1.00	43189	6553
3200	3067	3.30	0.014	1.00	85052	12178

As we can observe the algorithm performs as expected, a mesh with the desired number of vertices is built. The considered problem is essential one dimensional, thus to reduce the error, vertices should be added only on the direction x_1. When multiplying by two the number of vertices the error e_{H^1} is divided by two.

3 Anisotropic adaptive finite elements for steady Stokes problem

In this section we present an error indicator for the Steady Stokes equation. Numerical experiments showing the sharpness of the error indicator are presented. Applications of the adaptive algorithms introduced in Sections 2.4.3 and 2.4.5 are discussed.

3.1 Problem statement and numerical method

Given $\mathbf{f} : \Omega \to \mathbb{R}^d$ and a constant $\mu > 0$, we are looking for $u : \Omega \to \mathbb{R}^d$, $p : \Omega \to \mathbb{R}$ such that

$$\left\{ \begin{array}{rl} -\operatorname{div}(\mu \nabla \mathbf{u}) + \nabla p = \mathbf{f} & \text{in } \Omega, \\ \operatorname{div}(\mathbf{u}) = 0 & \text{in } \Omega, \\ \mathbf{u} = 0 & \text{on } \partial\Omega, \end{array} \right. \tag{3.1}$$

Suppose $\mathbf{f} \in \left(L^2(\Omega)\right)^d$, the weak formulation of problem (3.1) reads : find $(\mathbf{u}, p) \in V \times Q = (H_0^1(\Omega))^d \times L_0^2(\Omega)$ such that

$$\left\{ \begin{array}{rl} a(\mathbf{u}, \mathbf{v}) + b(\mathbf{v}, p) & = F(\mathbf{v}), \\ b(\mathbf{u}, q) & = 0, \end{array} \right. \tag{3.2}$$

for all $(\mathbf{v}, q) \in V \times Q$, where we have defined

$$a(\mathbf{u}, \mathbf{v}) = \int_\Omega \mu \nabla \mathbf{u} : \nabla \mathbf{v}, \quad b(\mathbf{v}, q) = -\int_\Omega q \operatorname{div}(\mathbf{v}) \quad \text{and} \quad F(\mathbf{v}) = \int_\Omega \mathbf{f} \cdot \mathbf{v}.$$

A robust piecewise continuous finite element procedure to solve the problem has been presented for instance in [42, 35] for the isotropic case. Following what has been presented in [54] for the anisotropic case, we discretize the problem using a stabilized method. The

discrete problem reads : find $(\mathbf{u}_h, p_h) \in V_h \times Q_h$ such that

$$\left\{ \begin{array}{rl} a(\mathbf{u}_h, \mathbf{v}_h) + b(\mathbf{v}_h, p_h) & = F(\mathbf{v}_h), \\ b(\mathbf{u}_h, q_h) - \sum_{K\in\mathcal{T}_h} \int_K s_K \left(-\mu\Delta\mathbf{u}_h + \nabla p_h - \mathbf{f}\right) \cdot \left(-\mu\Delta\mathbf{v}_h + \nabla q_h\right) & = 0, \end{array} \right. \tag{3.3}$$

for all $(\mathbf{v}_h, q_h) \in V_h \times Q_h$, where $V_h \times Q_h \subset V \times Q$ is the approximation space for velocity and pressure involving continuous affine functions over $\mathcal{T}_h$. For $\alpha > 0$, we set the stability coefficient $s_K = \alpha \frac{\lambda_{d,K}^2}{\mu}$, see Theorem 4.1 in [54] for a convergence study.

3.2 Anisotropic error estimator

We present an error indicator for the previous Stokes problem. In order to state the theorem we need to introduce as in [17, 61] the following dual problem. Given p solution of (3.1) and p_h solution of (3.3), we are looking for $(\mathbf{w}, r) \in V \times Q$ weak solution of

$$\left\{ \begin{array}{rl} -\operatorname{div}(\mu\nabla\mathbf{w}) + \nabla r = 0 & \text{in } \Omega, \\ \operatorname{div}(\mathbf{w}) = p - p_h & \text{in } \Omega. \end{array} \right. \tag{3.4}$$

A slight modification of the following theorem is presented in [54]

Theorem 3.1. *Let $(\mathbf{u}, p)$, $(\mathbf{u}_h, p_h)$ and $(\mathbf{w}, r)$ be weak solutions of (3.2), (3.3) and (3.4) respectively. There exists a constant C depending only on Ω and a constant $\hat{C}$ depending only on the reference element $\hat{K}$ such that*

$$\begin{aligned} ||\nabla(\mathbf{u} - \mathbf{u}_h)||^2_{L^2(\Omega)} + \frac{C}{\mu^2}||p - p_h||^2_{L^2(\Omega} \leq \hat{C} \sum_{K\in\mathcal{T}_h} \sqrt{d} \left(\sum_{i,j=1}^{d} \rho_K^i \omega_{2,K,j}^2 (u_i - (u_h)_i) \right)^{1/2} \\ + \hat{C} \sum_{K\in\mathcal{T}_h} \frac{\sqrt{d}}{C\mu} \left(\sum_{i,j=1}^{d} \rho_K^i \omega_{2,K,j}^2 (w_i) \right)^{1/2} \\ + C \sum_{K\in\mathcal{T}_h} ||\operatorname{div} \mathbf{u}_h||^2_{L^2(K)}, \end{aligned}$$

where

$$\rho_K^i = || \left(\frac{1}{\mu} \left(\mathbf{f} - \nabla p_h \right) \right) + \Delta \mathbf{u}_h \Big)_i ||_{L^2(K)} + \frac{1}{2} \sum_{l=1}^{d+1} \left(\frac{|\partial K_l|}{\prod_{j=1}^{d} \lambda_{j,K}} \right)^{1/2} || \left([\nabla \mathbf{u}_h \mathbf{n}] \right)_i ||_{L^2(\partial K_l)}.$$

We denote as usual $[\cdot]$ the jump across an internal boundary element ∂K_i with $i = 1, \ldots, d+1$ ($[\cdot] = 0$ on $\partial\Omega$), $\mathbf{n}$ the outer unit normal to K, $\nabla \mathbf{u}_h \mathbf{n}$ is a matrix vector multiplication and $\omega_{2,K,j}(\cdot)$ is defined in (2.25) for $j = 1, \ldots, d$.

Proof. (proof Theorem 3.1) First, as in [61] using (3.2) and (3.3) we obtain for any $(\mathbf{v}_h, q_h) \in V_h \times Q_h$

$$\begin{aligned}\mu||\nabla(\mathbf{u}-\mathbf{u}_h)||^2_{L^2(\Omega)} &= \int_\Omega \mathbf{f}\cdot(\mathbf{u}-\mathbf{u}_h-\mathbf{v}_h) - \int_\Omega \mu\nabla\mathbf{u}_h : \nabla(\mathbf{u}-\mathbf{u}_h-\mathbf{v}_h)\\ &+ \int_\Omega p_h\nabla\cdot(\mathbf{u}-\mathbf{u}_h-\mathbf{v}_h) - \int_\Omega (p-p_h-q_h)\nabla\cdot\mathbf{u}_h\\ &- \sum_{K\in\mathcal{T}_h} s_K\int_K(-\mu\Delta\mathbf{u}_h+\nabla p_h-\mathbf{f})\cdot(-\mu\Delta\mathbf{v}_h+\nabla q_h).\end{aligned}$$

Setting $\mathbf{v}_h = R_h(\mathbf{u}-\mathbf{u}_h)$ and $q_h = 0$, integrating by parts and applying Cauchy-Schwarz we have

$$\begin{aligned}||\nabla(\mathbf{u}-\mathbf{u}_h)||^2_{L^2(\Omega)} \le \sum_{K\in\mathcal{T}_h}\sum_{i=1}^d ||(\frac{1}{\mu}(\mathbf{f}-\nabla p_h)+\Delta\mathbf{u}_h)_i||_{L^2(K)}||(\mathbf{u}-\mathbf{u}_h-R_h(\mathbf{u}-\mathbf{u}_h))_i||_{L^2(K)}\\ + \frac{1}{2}\sum_{K\in\mathcal{T}_h}\sum_{i=1}^d ||([\nabla\mathbf{u}_h\mathbf{n}])_i||_{L^2(\partial K)}||(\mathbf{u}-\mathbf{u}_h-R_h(\mathbf{u}-\mathbf{u}_h))_i||_{L^2(\partial K)}\\ + \sum_{K\in\mathcal{T}_h}||\nabla\cdot\mathbf{u}_h||_{L^2(K)}||\frac{1}{\mu}(p-p_h)||_{L^2(K)}.\end{aligned}$$

Using Proposition 1.1 and Young's inequality we have, for a constant $\hat{C} > 0$ and a constant $\gamma > 0$ to be chosen,

$$\begin{aligned}||\nabla(\mathbf{u}-\mathbf{u}_h)||^2_{L^2(\Omega)} \le \hat{C}\sum_{K\in\mathcal{T}_h}\sum_{i=1}^d \rho_K^i\omega_{2,K}(u_i-(u_h)_i) + \frac{\gamma}{2}\sum_{K\in\mathcal{T}_h}||\nabla\cdot\mathbf{u}_h||^2_{L^2(K)}\\ + \frac{1}{2\mu^2\gamma}\sum_{K\in\mathcal{T}_h}||p-p_h||^2_{L^2(K)}.\end{aligned} \tag{3.5}$$

Using (3.4) and again (3.2) and (3.3), we can write

$$\begin{aligned}||p-p_h||^2_{L^2(\Omega)} &= -\int_\Omega \mathbf{f}\cdot(\mathbf{w}-\mathbf{v}_h) + \mu\int_\Omega \nabla\mathbf{u}_h : \nabla(\mathbf{w}-\mathbf{v}_h)\\ &- \int_\Omega p_h\nabla\cdot(\mathbf{w}-v_h) + \mu\int_\Omega\nabla(\mathbf{u}-\mathbf{u}_h):\nabla\mathbf{w}\\ &- \sum_{K\in\mathcal{T}_h} s_K\int_K(-\mu\Delta\mathbf{u}_h+\nabla p_h-\mathbf{f})\cdot(-\mu\Delta\mathbf{v}_h+\nabla q_h)\end{aligned}$$

for any $(\mathbf{v}_h, q_h) \in V_h \times Q_h$. Proceeding as before, we obtain

$$||p-p_h||^2_{L^2(\Omega)} \le \hat{C}\sum_{K\in\mathcal{T}_h}\sum_{i=1}^d \rho_K^i\omega_{2,K}(w_i) + \int_\Omega \mu\nabla(\mathbf{u}-\mathbf{u}_h):\nabla\mathbf{w}.$$

As explained in [61], as a consequence of inf-sup condition, one have

$$||\nabla \mathbf{w}||_{L^2(\Omega)} + \frac{1}{\mu}||r||_{L^2(\Omega)} \leq C||p - p_h||_{L^2(\Omega)}.$$

Thus, using again Cauchy-Schwarz and Young's inequality, we obtain

$$||p - p_h||^2_{L^2(\Omega)} \leq 2\hat{C}\mu \sum_{K\in\mathcal{T}_h} \sum_{i=1}^{d} \rho_K^i \omega_{2,K}(w_i) + C\mu^2 ||\nabla(\mathbf{u} - \mathbf{u}_h)||^2_{L^2(\Omega)}. \tag{3.6}$$

All together, using definition (2.25), the fact that

$$\sum_{i=1}^{d} \sqrt{a_i} \leq \sqrt{d} \left(\sum_{i=1}^{d} a_i \right)^{1/2}$$

for any $a_i \geq 0$ and summing up (3.5) and $\frac{1}{2C^2\mu^2}$ times (3.6) we conclude. □

Remark 3.1. *Observe that the presented estimator involves the exact solution* $\mathbf{u}$ *and* $\mathbf{w}$*. The term* $\omega_{2,K}(u_i - (u_h)_i)$ *can be efficiently approximated by ZZ post-processing as explained in Remark 2.1. While in [61] a method to approximate* $\omega_{2,K}(w_i)$ *is presented.*

In what follows, we are mainly interested in controlling the H^1 semi-norm of the velocity thus, extrapolating from the previous theorem, we introduce the error indicator $\sum_{K\in\mathcal{T}_h} \eta_K^2$ to control $\mu||\nabla(\mathbf{u} - \mathbf{u}_h)||_{L^2(\Omega)}$, where we defined

$$\eta_K^2 = \left(\sum_{j=1}^{d} \eta_{j,K}^4 \right)^{1/2} \tag{3.7}$$

and

$$\eta_{j,K}^4 = \sum_{i=1}^{d} (\rho_K^i)^2 \omega_{2,K,j}^2 (u_i - (u_i)_h) \tag{3.8}$$

We numerically verify the sharpness of the error indicator, which is heuristic since the pressure term is not taken into account. In the next Section we present numerical results on non-adapted meshes for $\mu = 1$.

3.3 Numerical experiments with non-adapted meshes

Similarly to what presented in 2.3, we introduce the following quantities : the H^1 semi-norm error

$$e_{H^1} = ||\nabla(\mathbf{u} - \mathbf{u}_h)||_{L^2(\Omega)},$$

the L^2 pressure error

$$e_p = ||p - p_h||_{L^2(\Omega)},$$

the anisotropic estimator

$$\eta^A = \left(\sum_{K \in \mathcal{T}_h} \eta_K^2 \right)^{1/2},$$

the anisotropic effectivity index

$$\mathrm{ei}^A = \frac{\eta^A}{e_{H^1}}$$

and the ZZ effectivity index

$$\mathrm{ei}^{ZZ} = \frac{||\nabla \mathbf{u}_h - \Pi_h^{ZZ} \nabla \mathbf{u}_h||_{L^2(\Omega)}}{||\nabla(\mathbf{u} - \mathbf{u}_h)||_{L^2(\Omega)}}.$$

Where we noted for any $\mathbf{v} \in V$ with v_i the ith component

$$||\nabla \mathbf{v}||^2_{L^2(\Omega)} = \sum_{i=1}^{d} ||\nabla v_i||^2_{L^2(\Omega)}$$

and $\Pi_h^{ZZ} \nabla \mathbf{v}$ has components $\Pi_h^{ZZ} \nabla v_i$. We aim to verify that these quantities satisfy the following properties :

- ei^A is independent of the solution u.
- ei^A is independent of the mesh size and aspect ratio,
- ei^{ZZ} is close to one (see discussion Remark 2.1).

Consider problem (3.1), let $\Omega = (0,1)^3$, $\mu = 1$ and choose $\mathbf{f}$ so that, for $\epsilon > 0$, $\mathbf{u}$ and p are given by

$$\mathbf{u}(\mathbf{x}) = [\tanh(\frac{x_2 - 0.5}{\epsilon}), 0, 0], \quad p(\mathbf{x}) = x_1 + x_2 + x_3 - \frac{3}{2}. \tag{3.9}$$

We denote h_1, h_2 and h_3 the mesh sizes in directions x_1, x_2 and x_3 respectively. In Table 3.1 results for different mesh sizes are reported. The true errors e_{H^1}, e_p and the error indicator η^A, are converging as expected. Moreover the effectivity index ei^{ZZ} is near to one as desired, showing the well behaviour of the post-processing. The effectivity index ei^A seems to be constant, independent of the solution and of the aspect ratio.

TABLE 3.1 : Estimated error, True error, and effectivity indices for various non-adapted meshes and various choices of ϵ, when $\mu = 1$ and $\mathbf{u}$ and p are given by (3.9).

$\epsilon = 0.1$

h_1-h_2-h_3	η^A	e_{H^1}	ei^A	e_p	ei^{ZZ}
0.1-0.1-0.1	2.734	0.926	2.95	0.40	1.14
0.05-0.05-0.05	1.424	0.448	3.18	0.19	1.12
0.025-0.025-0.025	0.691	0.219	3.16	0.063	1.03
0.0125-0.0125-0.0125	0.342	0.108	3.16	0.039	1.01
0.2-0.02-0.2	0.541	0.158	3.42	0.296	1.02
0.1-0.01-0.1	0.275	0.074	3.73	0.068	1.01
0.05-0.005-0.05	0.137	0.035	3.87	0.022	1.00

$\epsilon = 0.05$

h_1-h_2-h_3	η^A	e_{H^1}	ei^A	e_p	ei^{ZZ}
0.05-0.05-0.05	3.98	1.308	3.04	0.407	1.17
0.025-0.025-0.025	2.046	0.631	3.24	0.187	1.13
0.0125-0.0125	0.983	0.308	3.19	0.061	1.04
0.2-0.02-0.2	1.562	0.450	3.47	0.611	1.11
0.1-0.01-0.1	0.776	0.209	3.71	0.208	1.03
0.05-0.005-0.05	0.386	0.100	3.86	0.059	1.00

3.4 Numerical experiments with adapted meshes

For a given accuracy, the goal is now to build adapted meshes to solve problem (3.1) at a reduced computational cost. We aim thus to apply algorithm 2 presented in Section 2.4.3. We consider (3.7) as indicator of the adaptive strategy in order to control H^1 semi-norm. Notice that when considering algorithm 2, the definition (2.24) introduced in Section 2.4.1 has to be modified as in (3.8).

Consider problem (3.1) with $\Omega = (0,1)^3$, where $\mathbf{f}$ is such that exact solutions are again given by (3.9). We choose a starting mesh of size $h_1 = h_2 = h_3 = 0.1$ and we run algorithm 2 with $\text{TOL}_{goal} = 0.015625$, $N = 6$ and $N_{it} = 20$. In Table 3.2 results are reported for each tolerance and for different values of ϵ. Similar results as for non-adapted meshes are obtained. The true error e_{H^1} converge as expected. The effectivity index ei^{ZZ} stays close to 1, as desired, and the effectivity index ei^A is constant, independent of the aspect ratio and independent of the solution. The pressure error e_p tends to decrease, but with some oscillations.

TABLE 3.2 : Number of vertices, effectivity indices, true error and aspect ratio for different values of tolerance TOL, when $\mathbf{u}$ and p are given by (3.9) with $\mu = 1$. Results obtained running algorithm 2($\text{TOL}_{goal} = 0.015625$,$N = 6$,$\mathcal{T}_h^1$,$N_{it} = 20$).

$\epsilon = 0.1$

TOL	Vertices	ei^A	e_{H^1}	e_p	ei^{ZZ}	$\text{ar}_{\max}$	ar_{av}
0.5	85	3.17	0.563	2.925	1.04	82	20
0.25	115	3.36	0.280	0.57	0.98	137	36
0.125	213	3.27	0.14	0.929	0.98	779	77
0.0625	355	3.38	0.0691	0.564	0.98	902	171
0.03125	738	3.35	0.0345	0.42	0.98	2198	307
0.015625	1519	3.39	0.017	0.402	0.98	7361	654

$\epsilon = 0.01$

TOL	Vertices	ei^A	e_{H^1}	e_p	ei^{ZZ}	$\text{ar}_{\max}$	ar_{av}
0.5	309	3.52	1.68	1.14	1.02	472	84
0.25	234	3.47	0.84	0.57	0.99	1460	259
0.125	334	3.43	0.435	0.377	0.97	3959	618
0.0625	518	3.40	0.214	0.260	0.98	12362	1258
0.03125	1246	3.38	0.110	0.53	0.98	37400	2386
0.015625	9830	3.55	0.053	0.056	0.98	34920	1988

Here the considered pressure was linear and without strong variations. Thus, we run another experiment. The pressure is chosen nonlinear and with a different direction with respect of the velocity. The following numerical experiment is considered. Let $\Omega = (0,1)^3$ and consider $\mathbf{f}$ such that, for $\epsilon > 0$, the exact solution is given by

$$\mathbf{u}(\mathbf{x}) = \left[\tanh(\frac{x_2 - 0.5}{\epsilon}), 0, 0\right], \quad p(\mathbf{x}) = \tanh(\frac{x_3 - 0.5}{\epsilon}). \tag{3.10}$$

We run again algorithm 2 with the same parameters as the previous test. Results are reported in Table 3.3. For the velocity component, results are similar to the previous numerical experiment. Even-thought, we have no control of the error e_p, it is still diminishing.

TABLE 3.3 : Number of vertices, effectivity indices, true error and aspect ratio for different values of tolerance TOL, when $\mathbf{u}$ and p are given by (3.10) with $\mu = 1$. Results obtained running algorithm 2($\text{TOL}_{goal} = 0.015625$,$N = 6$,$\mathcal{T}_h^1$,$N_{it} = 20$).

$\epsilon = 0.1$

TOL	Vertices	ei^A	e_{H^1}	e_p	ei^{ZZ}	$\text{ar}_{\max}$	ar_{av}
0.5	68	3.25	0.636	2.187	0.99	72	18
0.25	136	3.26	0.274	1.774	0.97	140	37
0.125	248	3.28	0.141	1.091	0.97	457	72
0.0625	549	3.27	0.073	0.709	0.96	918	128
0.03125	1231	3.46	0.0377	0.694	0.96	3286	270
0.015625	3444	3.51	0.0175	0.344	0.97	19316	404

In Figure 3.1 a cut of the mesh obtained at the last iteration of algorithm 2 when TOL = 0.03125 running experiment presented in Table 3.2, can be observed. On the right a cut of the obtained mesh at the last iteration when TOL = 0.03125 for the last experiment is shown. Even-though, the adaptation is run with respect to the same velocity, the obtained meshes are different. On the right, an additional refinement around a layer in the z direction can be observed. The pressure plays thus, a role in the adaptation process, even when only an indicator for the velocity is considered.

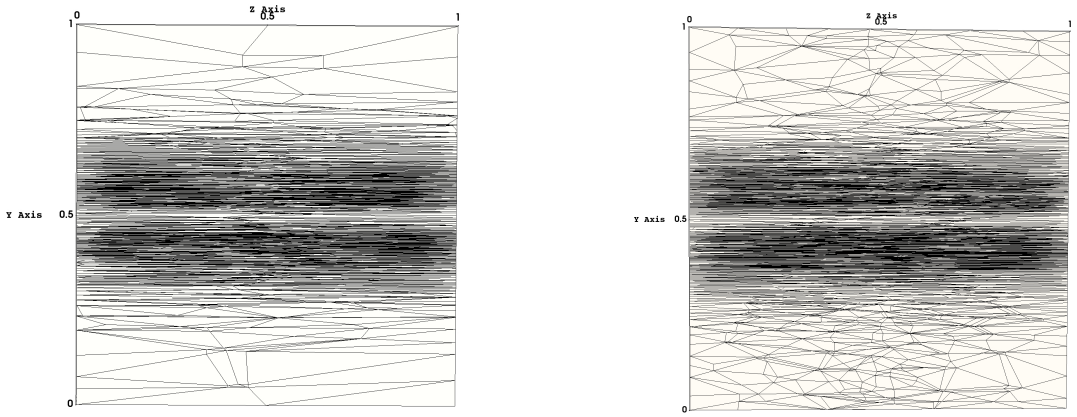

FIGURE 3.1 : Cut of mesh at $x = 0.5$. Left : adapted mesh at TOL=0.03125 when $\mathbf{u}$, p are given by (3.9). Right : adapted mesh at TOL=0.03125 when $\mathbf{u}$, p are given by (3.10).

In Chapter 5, an application to aluminium electrolysis is presented. Aluminium electrolysis involves some multi-scale features (from meters to millimeters). In particular a domain composed by long thin channels will be considered. We thus test our algorithm on a simplified flat domain. Consider problem (3.1) and $\Omega = (0,1)^2 \times (0, 0.02)$. Let $\mathbf{f}$ be

such that

$$\begin{aligned} \mathbf{u}(\mathbf{x}) &= \left[4(y-1)y(x-1)^2x^2(y-0.5), -4(x-0.5)xy^2(y-1)^2(x-1), 0\right], \\ p(\mathbf{x}) &= x_1 + x_2 + x_2 - \frac{3}{2}. \end{aligned} \tag{3.11}$$

Starting with a mesh $\mathcal{T}_h^1$ of size $h_1 = 0.1$, $h_2 = 0.1$ and $h_3 = 0.01$, we set $\text{TOL}_{goal} = 0.125$, $N = 4$ and $N_{it} = 20$ and we run algorithm 2. Results are reported in Table 3.4. Even with thin domains, the algorithm manages to build adapted meshes with large aspect ratio having the velocity error under control. The true error e_{H^1} converges as expected, the effectivity index ei^A is constant and does not depend on the aspect ratio, while ei^{ZZ} is closed to one, as desired.

TABLE 3.4 : Number of vertices, effectivity indices, true error and aspect ratio for different values of tolerance TOL, when solving (3.1) with $\mathbf{u}$ and p given by (3.11). Results obtained running algorithm 2($\text{TOL}_{goal} = 0.125$,$N = 4$,$\mathcal{T}_h^1$,$N_{it} = 20$).

TOL	Vertices	ei^A	e_{H^1}	e_p	ei^{ZZ}	$\text{ar}_{\max}$	ar_{av}
1.0	139	3.03	0.0186	0.0034	1.03	63	12
0.5	560	3.21	0.0092	0.0093	1.03	144	21
0.25	1999	3.19	0.00475	0.0110	1.00	290	39
0.125	8661	3.15	0.00241	0.00219	0.99	1198	72

For a future application to aluminium electrolysis, we test algorithm 3. We set $M_{goal} = 1600$, $N = 5$, $N_{it} = 20$ and $\alpha = 0.1$. We report obtained results in Table 3.5. The number of vertices of the obtained meshes are close to the desired one. The error e_{H^1} goes to zero together with the error e_p.

TABLE 3.5 : Number of vertices, effectivity indices, true error and aspect ratio for different values of M goal of vertices, when solving (3.1) with $\mu = 1$, $\mathbf{u}$ and p are given by (3.11). Results obtained running algorithm 3($M_{goal} = 1600$,$N = 5$,$N_{it} = 20$,$\alpha = 0.1$,$\mathcal{T}_h^1$).

M	Vertices	ei^A	e_{H^1}	e_p	ei^{ZZ}	$\text{ar}_{\max}$	ar_{av}
100	118	2.96	0.017	0.20	0.90	101	30
200	186	3.03	0.013	0.22	0.92	153	29
400	369	2.87	0.0083	0.11	0.91	136	26
800	653	2.83	0.0056	0.043	0.91	121	22
1600	1348	2.79	0.0036	0.029	0.91	111	20

In Figure 3.2 a cut at $x = 0.5$ of the obtained mesh with corresponding solution, when $M = 1600$ is reported.

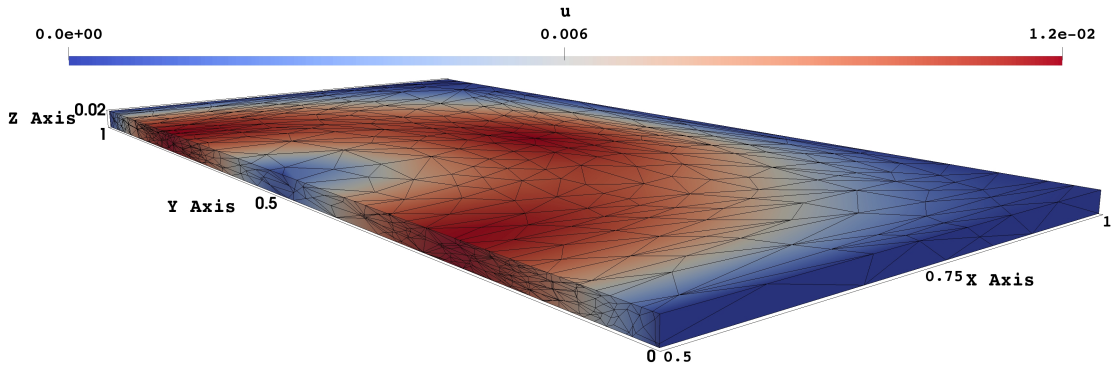

FIGURE 3.2 : Cut of mesh at $x = 0.5$. Adapted mesh at $M = 1600$ when $\mathbf{u}$, p are given by (3.11).

Finally the next numerical experiment has the goal to demonstrate, the efficiency of the continuation algorithm 2 over algorithm 1 for Stokes problem as already demonstrated in Section 2.4.4 for an elliptic problem. Consider problem (3.1) and let $\Omega = (0,1) \times (0,1) \times (0,0.1)$ and $\mathbf{f}$ be such that

$$\begin{aligned} \mathbf{u}(x,y,z) &= \left[x^3(1-x)^3y^2(1-y)^2(1-2y), -x^2(1-x)^2y^3(1-y)^3(1-2x), 0\right]^T, \\ p(x,y,z) &= xy - 0.25. \end{aligned} \tag{3.12}$$

For algorithm 1 we set TOL $= 0.125$, $N_{it} = 80$ and $\mathcal{T}_h^1$ an initial mesh of size $h_1 = h_2 = 0.1$ and $h_3 = 0.05$. When testing algorithm 2 we choose $\text{TOL}_{goal} = 0.125$, $N_{it} = 20$, $N = 4$ and the same starting mesh $\mathcal{T}_h^1$. In Figure 3.3 the obtained results can be observed.

As for the elliptic problem, the benefits of the continuation algorithm on the preset tolerance parameter are clear. The CPU time required is reduced.

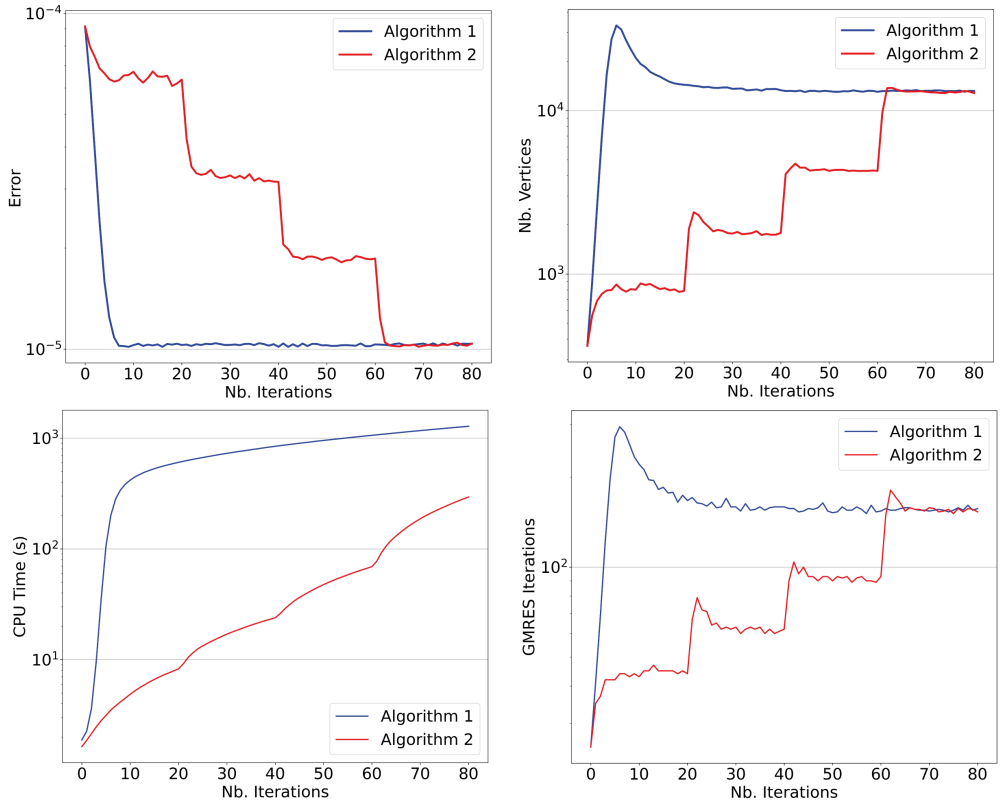

FIGURE 3.3 : Comparison of algorithm 1(TOL $= 0.125$,$\mathcal{T}_h^1$,$N_{it} = 80$) and algorithm 2(TOL$_{goal} = 0.125$,$N = 4$,$\mathcal{T}_h^1$,$N_{it} = 20$), when solving problem (3.1) when $\mathbf{u}$ and p are given by (3.12). Top left : error at each iteration. Top right : Number of vertices at each iteration. Bottom left : CPU time at each iteration. Bottom right : GMRES iterations at each iteration of the adaptive algorithm.

4 Anisotropic adaptive finite elements for a p-Laplacian problem

We are interested in the p-Laplace problem $-\nabla \cdot ((\mu + |\nabla u|^{p-2})\nabla u) = f$ in $\Omega \subset \mathbb{R}^d$, where $\mu \geq 0$ and $p \geq 2$. This problem can be seen as a simplification of Navier-Stokes equation with the so-called Smagorinsky turbulence model [64], which will be considered in the context of aluminium electrolysis in Chapter 5. A posteriori error estimates for the p-Laplacian problem were proposed in [21, 11, 48, 20, 13, 26] for isotropic finite elements. The goal of this chapter is to derive a posteriori error estimates for large aspect ratio finite elements. In particular a theoretical and numerical study of the equivalence between the error estimator and different numerical errors $u - u_h$ is presented, the involved constants being independent of the aspect ratio. Finally, an application of adaptive algorithm 2 is discussed.

4.1 Problem statement and numerical method

Given $f : \Omega \to \mathbb{R}$ we search for $u : \Omega \to \mathbb{R}$ such that

$$\begin{cases} -\nabla \cdot ((\mu + |\nabla u|^{p-2})\nabla u) = f & \text{in } \Omega, \\ \\ u = 0 & \text{on } \partial\Omega, \end{cases} \tag{4.1}$$

where $\mu \geq 0$ is a constant and $p \geq 2$. We assume throughout this chapter that $f \in L^2(\Omega)$. The weak formulation of problem (4.1) consists in finding $u \in W_0^{1,p}(\Omega)$ such that

$$\int_\Omega (\mu + |\nabla u|^{p-2})\nabla u \cdot \nabla v = \int_\Omega fv, \qquad \forall\ v \in W_0^{1,p}(\Omega). \tag{4.2}$$

When $\mu = 0$ existence and uniqueness of a solution $u \in W_0^{1,p}(\Omega)$ has been proved in [47, 36]. The case $\mu > 0$ can be proved in a similar way. To approximate the solution of

(4.2), we are looking for $u_h \in V_h$ such that

$$\int_\Omega (\mu + |\nabla u_h|^{p-2}) \nabla u_h \cdot \nabla v_h = \int_\Omega f v_h, \ \forall \ v_h \in V_h. \tag{4.3}$$

Existence and uniqueness of $u_h \in V_h$ can be again proved similarly as in [47, 36]. To solve this nonlinear problem, the Newton's method is advocated. We define the functional $F : W_0^{1,p}(\Omega) \to \mathbb{R}$ by

$$_{(W_0^{1,p}(\Omega))'} < F(u), v >_{W_0^{1,p}(\Omega)} = \int_\Omega (\mu + |\nabla u|^{p-2}) \nabla u \cdot \nabla v - fv,$$

where $_{(W_0^{1,p}(\Omega))'} < \cdot, \cdot >_{W_0^{1,p}(\Omega)}$ is the duality product, noted simply $< \cdot, \cdot >$ in next proposition.

Proposition 4.1. *The Gâteau derivative of F in u in direction w for any $v \in V$ is given by*

$$< DF(u)w, v >= (p-2) \int_\Omega \frac{|\nabla u|^{p-3} \nabla u \cdot \nabla w}{|\nabla u|} \nabla u \cdot \nabla v + \int_\Omega (\mu + |\nabla u|^{p-2}) \nabla w \cdot \nabla v.$$

Proof. By definition we have

$$\begin{aligned} < DF(u)w, v > &= \lim_{\epsilon \to 0} \frac{< F(u + \epsilon w), v > - < F(u), v >}{\epsilon} \\ &= \lim_{\epsilon \to 0} \int_\Omega \frac{|\nabla u + \epsilon \nabla w|^{p-2} - |\nabla u|^{p-2}}{\epsilon} \nabla u \cdot \nabla v \\ &+ \lim_{\epsilon \to 0} \int_\Omega (\mu + |\nabla u + \epsilon \nabla w|^{p-2} \nabla w \cdot \nabla v). \end{aligned}$$

By computing

$$\lim_{\epsilon \to 0} \int_\Omega \frac{|\nabla u + \epsilon \nabla w|^{p-2} - |\nabla u|^{p-2}}{\epsilon} = (p-2) \int_\Omega \frac{|\nabla u|^{p-3} \nabla u \cdot \nabla w}{|\nabla u|}$$

we conclude the proof. □

The Newton's method works as follows, if $u_h^n \in V_h$ is known, we need to find $w_h \in V_h$ such that

$$< DF(u_h^n) w_h, v_h >=< F(u_h^n), v_h >$$

for all $v_h \in V_h$, we set $u_h^{n+1} = u_h^n - w_h$ and we go on until convergence is reached.

4.2 An anisotropic error estimator

Let $u \in W_0^{1,p}(\Omega)$ be the weak solution of (4.2) and $u_h \in V_h$ the solution of the finite elements approximation (4.3). We can derive a family of estimators for the error in the

norm :

$$\mu||\nabla(u-u_h)||^2_{L^2(\Omega)} + ||\nabla(u-u_h)||^p_{L^p(\Omega)}$$

and also in the quasi-norm :

$$\int_\Omega |\nabla(u-u_h)|^2(\mu + (|\nabla(u-u_h)| + |\nabla u|)^{p-2}).$$

We first focus on the quasi-norm. Note that by quasi-norm we mean that all properties of a norm are satisfied except homogeneity.

Proposition 4.2. *Let $\mu \geq 0$, for $w \in W_0^{1,p}(\Omega)$ and $v \in W_0^{1,p}(\Omega)$ let*

$$||v||^p_{(w)} = \int_\Omega |\nabla v|^2(\mu + (|\nabla w| + |\nabla v|)^{p-2}).$$

Then $||\cdot||_{(w)}$ is a quasi-norm on $W_0^{1,p}(\Omega)$.

The proof is as in [11]. We now state and prove a slight modification of Lemma 2.1. in [50], where we set $\alpha_1 = \alpha_2 = 0$, $\delta = 0$ and μ has been added.

Lemma 4.1. *Let $\mu \geq 0$, $p \geq 2$, $d = 2, 3$ and $k \in \mathcal{C}^1(0,\infty) \cap \mathcal{C}[0,\infty[$ be defined by $k(t) = \mu + t^{p-2}$. Then there exists two constants $C, M > 0$ such that for all $\mu \geq 0$ for all $\mathbf{x}, \mathbf{y} \in \mathbb{R}^d$ we have*

$$|k(|\mathbf{x}|)\mathbf{x} - k(|\mathbf{y}|)\mathbf{y}| \leq C|\mathbf{x}-\mathbf{y}|(\mu + (|\mathbf{x}| + |\mathbf{y}|)^{p-2}) \tag{4.4}$$

and

$$(k(|\mathbf{x}|)\mathbf{x} - k(|\mathbf{y}|)\mathbf{y}) \cdot (\mathbf{x}-\mathbf{y}) \geq M|\mathbf{x}-\mathbf{y}|^2(\mu + (|\mathbf{x}| + |\mathbf{y}|)^{p-2}). \tag{4.5}$$

Proof. We start by proving (4.4). First, observe that for all $s, t > 0$

$$|k(t)t - k(s)s| \leq C|t-s|(\mu + (t+s)^{p-2}). \tag{4.6}$$

Indeed, assume for instance $0 \leq s \leq t$, by mean value theorem there exists $s \leq x \leq t$ such that

$$\begin{aligned} k(t)t - k(s)s &= (t-s)((p-2)x^{p-3}x + (\mu + x^{p-2})) \\ &\leq (t-s)(p-1)(\mu + x^{p-2}) \end{aligned}$$

and (4.6) follows directly. Proceeding as in Lemma 2.1. in [50] we can obtain (4.4). To prove (4.5), we observe that there exists $M > 0$ for all $t \geq s \geq 0$ such that

$$k(t)t - k(s)s \geq M(t-s)(\mu + (t+s)^{p-2}).$$

Indeed, we have

$$\begin{aligned}(t-s)(\mu+(t+s)^{p-2}) &= (t-s)\mu + t\exp\left((p-2)\ln(t+s)\right) - s\exp\left((p-2)\ln(t+s)\right)\\ &\leq (t-s)\mu + 2^{p-2}\left(t\exp\left((p-2)\ln(t)\right) - s\exp\left((p-2)\ln(s)\right)\right)\\ &\leq 2^{p-2}\left(t(\mu+t^{p-2}) - s(\mu+s^{p-2})\right).\end{aligned}$$

Again following the idea of Lemma 2.1 in [50], we prove (4.5). □

We now recall lemma 5.2 of [48], when $\theta = 1$.

Lemma 4.2. *For all $\sigma_1, \sigma_2, \sigma_3 \geq 0$ we have*

$$(\sigma_3+\sigma_1)^{p-2}\sigma_1\sigma_2 \leq (\sigma_3+\sigma_1)^{p-2}\sigma_1^2 + (\sigma_3+\sigma_2)^{p-2}\sigma_2^2.$$

As in [49], we set

$$a(u,v) = \int_\Omega (\mu + |\nabla u|^{p-2})\nabla u\cdot\nabla v.$$

Following [48] and [11] we can prove next proposition.

Proposition 4.3. *Let C and M be the constants of Lemma 4.1. Let $u \in W_0^{1,p}(\Omega)$, then for all $v, w \in W_0^{1,p}(\Omega)$ we have*

$$a(u,u-v) - a(v,u-v) \geq \frac{M}{2}||u-v||_{(u)}^p \tag{4.7}$$

and

$$|a(u,w) - a(v,w)| \leq C\left(||u-v||_{(u)}^p + ||w||_{(u)}^p\right). \tag{4.8}$$

Proof. First we prove equation (4.7), using relation (4.5) of Lemma 4.1. We have

$$\begin{aligned}a(u,u-v) - a(v,u-v) &= \int_\Omega ((\mu+|\nabla u|^{p-2})\nabla u - (\mu+|\nabla v|^{p-2})\nabla v)\nabla(u-v)\\ &\geq M\int_\Omega |\nabla(u-v)|^2(\mu + (|\nabla u| + |\nabla v|)^{p-2}),\end{aligned}$$

Using the fact that for all $\mathbf{x}, \mathbf{y} \in \mathbb{R}^d$ we have

$$2(|\mathbf{x}| + |\mathbf{y}|) \geq |\mathbf{x}| + |\mathbf{x}-\mathbf{y}|,$$

we obtain

$$\begin{aligned}a(u,u-v) - a(v,u-v) &\geq \frac{M}{2}\int_\Omega |\nabla(u-v)|^2(\mu + (|\nabla u| + |\nabla(u-v)|)^{p-2})\\ &= \frac{M}{2}||u-v||_{(u)}^p.\end{aligned}$$

We now prove (4.8). We have

$$|a(u,w)-a(v,w)| \leq \int_\Omega |((\mu+|\nabla u|^{p-2})\nabla u-(\mu+|\nabla v|^{p-2})\nabla v)||\nabla w|$$

We apply (4.4) of Lemma 4.1 and the fact that for all $\mathbf{x},\mathbf{y}\in\mathbb{R}^d$ we have

$$\frac{|\mathbf{x}|+|\mathbf{y}|}{2} \leq |\mathbf{x}|+|\mathbf{x}-\mathbf{y}|$$

to obtain

$$|a(u,w)-a(v,w)| \leq C\int_\Omega |\nabla(u-v)|(\mu+(|\nabla u|+|\nabla(u-v)|)^{p-2})|\nabla w|.$$

Using Lemma 4.2 we obtain

$$\begin{aligned}|a(u,w)-a(v,w)| \leq C\Bigg(&\int_\Omega (|\nabla(u-v)|^2(\mu+(|\nabla u|+|\nabla(u-v)|)^{p-2}))\\ &+\int_\Omega ((\mu+(|\nabla u|+|\nabla w|)^{p-2})|\nabla w|^2)\Bigg),\end{aligned}$$

which concludes the proof. □

The next result follows directly taking $w=u-v$ in (4.7)-(4.8)

Proposition 4.4. *Let $u\in W_0^{1,p}(\Omega)$ and $v\in W_0^{1,p}(\Omega)$. Then there exist two constants $M,C>0$ independent of μ, u, v such that*

$$\frac{1}{2C}(a(u,u-v)-a(v,u-v)) \leq ||u-v||^p_{(u)} \leq \frac{2}{M}(a(u,u-v)-a(v,u-v)). \tag{4.9}$$

We can also prove the following proposition.

Proposition 4.5. *There exists $\alpha>0$ such that for all $\mu\geq 0$ and $u,v\in W_0^{1,p}(\Omega)$ we have*

$$\alpha(\mu||\nabla(u-v)||^2_{L^2(\Omega)}+||\nabla(u-v)||^p_{L^p(\Omega)}) \leq a(u,u-v)-a(v,u-v). \tag{4.10}$$

Proof. It suffices to prove that there exists α such that for all $\mathbf{x},\mathbf{y}\in\mathbb{R}^d$ we have

$$\Big((\mu+|\mathbf{x}|^{p-2})\mathbf{x}-(\mu+|\mathbf{y}|^{p-2})\mathbf{y}\Big)\cdot(\mathbf{x}-\mathbf{y}) \geq \alpha(\mu|\mathbf{x}-\mathbf{y}|^2+|\mathbf{x}-\mathbf{y}|^p). \tag{4.11}$$

Indeed, we have

$$\Big((\mu+|\mathbf{x}|^{p-2})\mathbf{x}-(\mu+|\mathbf{y}|^{p-2})\mathbf{y}\Big)\cdot(\mathbf{x}-\mathbf{y}) \geq \mu|\mathbf{x}-\mathbf{y}|^2+(|\mathbf{x}|^{p-2}\mathbf{x}-|\mathbf{y}|^{p-2}\mathbf{y})\cdot(\mathbf{x}-\mathbf{y})$$

so that (4.11) follows using Lemma 5.1 in [36]. □

We can now state the main result of the section.

Theorem 4.3. *Let $u \in W_0^{1,p}(\Omega)$ be solution of (4.2) and $u_h \in V_h$ solution of (4.3). Let $p \geq 2$. Then there exists $\hat{C}_1 > 0$ independent of μ, u, the mesh size and the aspect ratio such that*

$$\mu||\nabla(u-u_h)||^2_{L^2(\Omega)} + ||\nabla(u-u_h)||^p_{L^p(\Omega)} + ||u-u_h||^p_{(u)} \leq \hat{C}_1\left(\sum_{K\in\mathcal{T}_h}\eta_{2,K} + \epsilon_1\right) \quad (4.12)$$

Moreover if there exists a constant $\hat{C}$, dependent only on the reference triangle $\hat{K}$, such that for all $K \in \mathcal{T}_h$ for $i = 1, \ldots, d-1$

$$\lambda^2_{i,K}(\mathbf{r}^T_{i,K}G_K(u-u_h)\mathbf{r}_{i,K}) \leq \hat{C}\lambda^2_{d,K}(\mathbf{r}^T_{d,K}G_K(u-u_h)\mathbf{r}_{d,K}) \quad (4.13)$$

and assuming $\lambda_{i,K}$ vary smoothly around K for $i = 1, \ldots, d$, then there exists a constant $\hat{C}_2 > 0$ independent of μ, u, the mesh size and the aspect ratio such that

$$\sum_{K\in\mathcal{T}_h}\eta_{2,K} \leq \hat{C}_2\left(||u-u_h||^p_{(u)} + \sum_{j=1}^{4}\epsilon_j\right). \quad (4.14)$$

Here

$$\begin{aligned}\eta_{2,K} = \Bigg(&||\nabla\cdot\left((\mu+|\nabla u_h|^{p-2})\nabla u_h\right) + \Pi_K f||_{L^2(K)} \\ &+ \frac{1}{2}\sum_{i=1}^{d+1}\left(\frac{|\partial K_i|}{\prod_{j=1}^{d}\lambda_{j,K}}\right)^{1/2} |||[(\mu+|\nabla u_h|^{p-2})\nabla u_h\cdot\mathbf{n}]|||_{L^2(\partial K_i)}\Bigg)\omega_{2,K}(u-u_h),\end{aligned} \quad (4.15)$$

$$\epsilon_1 = \sum_{K\in\mathcal{T}_h}||f-\Pi_K f||_{L^2(K)}\omega_{2,K}(u-u_h),$$

$$\epsilon_2 = \sum_{K\in\mathcal{T}_h}\lambda_{d,K}||f-\Pi_K f||^2_{L^2(K)},$$

$$\epsilon_3 = \sum_{K\in\mathcal{T}_h}\sum_{K'\in\mathcal{P}_K}\int_{K'}|\left(\mu+|\nabla u_h|^{p-2}\right)_{|K} - \left(\mu+|\nabla u_h|^{p-2}\right)_{|K'}|\ |\nabla(u-u_h)|^2$$

and

$$\epsilon_4 = \sum_{K\in\mathcal{T}_h}\lambda_{d,K}||\nabla(u-u_h)||^2_{L^2(\Delta K)}$$

Here $\omega_{2,K}(\cdot)$ is defined in (1.3), $\mathbf{n}$ stands for the unit outer normal to element K, $[\cdot]$ denotes the jump across boundary element ∂K_i of K for $i = 1, \ldots, d+1$ ($[\cdot] = 0$ if $\partial K \subset \partial\Omega$) and for all $K \in \mathcal{T}_h$, we define $\Pi_K f$ as in (2.5). Moreover we denoted

$$\mathcal{P}_K = \Delta K \cup (\bigcup_{i=1}^{d+1}\Delta K^i)$$

with K^i the ith element sharing a facet ∂K_i with K (see Figure 2.1).

Remark 4.1. *Let $2 \leq p' \leq p$ and q' the Hölder conjugate of p'. Then the upper bound* (4.12) *can be generalized by*

$$\hat{C}_1 \left(\sum_{K \in \mathcal{T}_h} \eta_{p',K} + \sum_{K \in \mathcal{T}_h} ||f - \Pi_K f||_{L^{q'}(K)} \omega_{p',K}(u - u_h) \right),$$

where

$$\eta_{p',K} = \Bigg(||\nabla \cdot \left((\mu + |\nabla u_h|^{p-2}) \nabla u_h \right) + \Pi_K f||_{L^{q'}(K)} + \frac{1}{2} \sum_{i=1}^{d+1} \left(\frac{|\partial K_i|}{\prod_{j=1}^{d} \lambda_{j,K}} \right)^{1/p'} ||[(\mu + |\nabla u_h|^{p-2}) \nabla u_h \cdot \mathbf{n}]||_{L^{q'}(\partial K_i)} \Bigg) \omega_{p',K}(u - u_h).$$

Remark 4.2. *Assume $f \in H^1(\Omega)$ then we have*

$$||f - \Pi_K f||^2_{L^2(K)} \leq \hat{C} \sum_{i=1}^{d} \lambda^2_{i,K} ||\nabla f \cdot \mathbf{r}_{i,K}||^2_{L^2(K)}.$$

In the isotropic case this yields $\epsilon_1, \epsilon_2, \epsilon_4 = O(h^3)$, that are higher order terms compared to $||u - u_h||^p_{(u)}$ which should be according to [11], $O(h^2)$. In the anisotropic context if, for instance f depends only on x_2, $d = 2$ and $\mathbf{r}_{1,K} = (1, 0)$, then $\epsilon_1, \epsilon_2, \epsilon_4 = O\left(\left(\max_{K \in \mathcal{T}_h} \lambda_{2,K} \right)^3 \right)$. Numerical experiments performed in Sections 4.3 and 4.4 confirm previous predictions and show that ϵ_3 is also of higher order with respect to $||u - u_h||^p_{(u)}$, see Figures 4.1,4.2, 4.3 and 4.4. Thus when $\max_{K \in \mathcal{T}_h} \lambda_{d,K} \to 0$, then $||u - u_h||^p_{(u)}$ and $\sum_{K \in \mathcal{T}_h} \eta_{2,K}$ are equivalent up to higher order terms.

Remark 4.3. *Observe that local error estimator* (4.15) *is not standard since the exact solution is present in the term $\omega_{2,K}(u - u_h)$. In practice Zienkiewicz-Zhu (ZZ) post-processing can be applied as explained in Remark 2.1.*

Proof. (Upper bound (4.12) of Theorem 4.3) For all $v \in W^{1,p}_0(\Omega)$ and $v_h \in V_h$ we have

using (4.2) and (4.3) :

$$\begin{aligned} a(u,v) - a(u_h,v) &= \int_\Omega f(v-v_h) - \int_\Omega (\mu + |\nabla u_h|^{p-2})\nabla u_h \cdot \nabla (v-v_h) \\ &= \sum_{K\in\mathcal{T}_h} \Bigg(\int_K (f + \nabla\cdot(\mu + |\nabla u_h|^{p-2})\nabla u_h)(v-v_h) \\ &\quad + \frac{1}{2}\int_{\partial K} [(\mu + |\nabla u_h|^{p-2})\nabla u_h \cdot \mathbf{n}](v-v_h)\Bigg), \end{aligned}$$

where we integrated by parts. We set $v = u - u_h$ and $v_h = R_h(u-u_h)$, adding and subtracting $\Pi_K f$, using Hölder inequality and proposition 1.1 we obtain

$$\begin{aligned} &|a(u,v) - a(u_h,v)| \\ &\leq \sum_{K\in\mathcal{T}_h} \Big(||\Pi_K f + \nabla\cdot\Big((\mu + |\nabla u_h|^{p-2})\nabla u_h\Big)||_{L^2(K)} \\ &+ ||f - \Pi_K f||_{L^2(K)}\Big)\, ||u - u_h - R_h(u-u_h)||_{L^2(K)} \\ &+ \frac{1}{2}\sum_{K\in\mathcal{T}_h} |||[(\mu + |\nabla u_h|^{p-2})\nabla u_h\cdot\mathbf{n}]||_{L^2(\partial K)} ||u - u_h - R_h(u-u_h)||_{L^2(\partial K)} \\ &\leq C \sum_{K\in\mathcal{T}_h} \Bigg(||\Pi_K f + \nabla\cdot\Big((\mu + |\nabla u_h|^{p-2})\nabla u_h\Big)||_{L^2(K)} \\ &+ \frac{1}{2}\sum_{i=1}^{d+1} \left(\frac{|\partial K_i|}{\prod_{j=1}^{d}\lambda_{j,K}} \right)^{1/2} |||[(\mu + |\nabla u_h|^{p-2})\nabla u_h\cdot\mathbf{n}]||_{L^2(\partial K_i)} \\ &+ ||f - \Pi_K f||_{L^2(K)}\Bigg)\omega_{2,K}(u-u_h), \end{aligned}$$

which, together with proposition 4.4, yields (4.12). □

We now aim to prove the lower bound (4.14). The classical standard bubble functions [9, 73], adapted to the anistropic case [62, 29] and modified to take into account the nonlinearity, are involved. Next Proposition is an extension of proposition 2.1.

Proposition 4.6. *Let $e = u - u_h$, under the same assumptions of Theorem 4.3 there exists a function $\varphi \in W_0^{1,p}(\Omega)$ and a constant $\hat{C} > 0$ (that depends only on the reference*

triangle $\hat{K}$ and on p) such that for any $K \in \mathcal{T}_h$ and $i = 1, \dots, d+1$

$$\begin{aligned}\int_{\partial K_i} [(\mu + |\nabla u_h|^{p-2})\nabla u_h \cdot \mathbf{n}]\varphi = \frac{1}{2}\Bigg(& \frac{|\partial K_i|^{1/2}}{\left(\prod_{j=1}^{d} \lambda_{j,K}\right)^{1/2}} \omega_{2,K}(e) \\ + & \frac{|\partial K_i|^{1/2}}{\left(\prod_{j=1}^{d} \lambda_{j,K^i}\right)^{1/2}} \omega_{2,K^i}(e)\Bigg) \|[(\mu + |\nabla u_h|^{p-2})\nabla u_h \cdot \mathbf{n}]\|_{L^2(\partial K_i)}\end{aligned} \tag{4.16}$$

$$\begin{aligned}&\int_K (\Pi_K f + \nabla \cdot ((\mu + |\nabla u_h|^{p-2})\nabla u_h))\varphi \\ &= \|\Pi_k f + \nabla \cdot ((\mu + |\nabla u_h|^{p-2})\nabla u_h)\|_{L^2(K)} \omega_{2,K}(e),\end{aligned} \tag{4.17}$$

$$\left(\sum_{j=1}^{d} \lambda_{j,K}^2 ||\nabla\varphi \cdot \mathbf{r}_{j,K}||_{L^2(K)}^2\right)^{1/2} \leq \hat{C}\left(\omega_{2,K}(e) + \sum_{i=1}^{d+1} \omega_{2,K^i}(e)\right), \tag{4.18}$$

$$\int_K |\nabla\varphi|^2 \leq \hat{C}\left(\frac{\omega_{2,K}^2(e)}{\lambda_{d,K}^2} + \sum_{i=1}^{d+1} \frac{\omega_{2,K^i}^2(e)}{\lambda_{d,K^i}^2}\right), \tag{4.19}$$

$$\int_K |\nabla\varphi|^p \leq \hat{C}||\nabla e||_{L^p(\mathcal{P}_K)}^p. \tag{4.20}$$

We denoted for $i = 1, \dots, d+1$, K^i the ith element sharing facet ∂K_i with K (see Figure 2.1).

Proof. Following the proof of [62] and Proposition 2.1 we claim that

$$\varphi = \sum_{K \in \mathcal{T}_h} C_K \Psi_K + \frac{1}{2} \sum_{K \in \mathcal{T}_h} \sum_{i=1}^{d+1} C_{\partial K_i} \Psi_{\partial K_i},$$

where $C_K, C_{\partial K_i}$ are constants, $\Psi_K, \Psi_{\partial K_i}$ are the usual bubble function over K and its facets ∂K_i $i = 1, \dots, d+1$. We set $\partial K_i = 0$ if $\partial K_i \subset \partial\Omega$. First we compute $C_{\partial K_i}$ for $i = 1, \dots, d+1$. We require that the constants associated to the same facet shared by two elements are equal. Using the fact that $\Psi_K, \Psi_{\partial K_i}$ are zero over ∂K_i for all $i \neq j$, the fact that $(\Pi_K f + \nabla \cdot ((\mu + |\nabla u_h|^{p-2})\nabla u_h)$ and $[(\mu + |\nabla u_h|^{p-2})\nabla u_h \cdot \mathbf{n}]$ are constants over K and ∂K_i respectively, $|K| = \hat{C} \prod_{j=1}^{d} \lambda_{j,K}$ and (4.17) and (4.16) we obtain, as in

Proposition 2.1

$$C_{\partial K_i} = \pm\frac{1}{2}\left(\left(\frac{|\partial K_i|^2}{\prod_{j=1}^{d}\lambda_{j,K}}\right)^{1/2}\omega_{2,K}(e) + \left(\frac{|\partial K_i|^2}{\prod_{j=1}^{d}\lambda_{j,K^i}}\right)^{1/2}\omega_{2,K^i}(e)\right)\frac{1}{\int_{\partial K_i}\Psi_{\partial K_i}}.$$

and

$$C_K = \pm\frac{1}{\int_K \Psi_K}\left(\hat{C}\left(\prod_{j=1}^{d}\lambda_{j,K}\right)^{1/2}\omega_{2,K}(e)\right.$$
$$\left.\mp\sum_{i=1}^{d+1}\frac{1}{2}\left(\left(\frac{|\partial K_i|^2}{\prod_{j=1}^{d}\lambda_{j,K}}\right)^{1/2}\omega_{2,K}(e) + \left(\frac{|\partial K_i|^2}{\prod_{j=1}^{d}\lambda_{j,K^i}}\right)^{1/2}\omega_{2,K^i}(e)\right)\frac{\int_K\Psi_{\partial K_i}}{\int_{\partial K_i}\Psi_{\partial K_i}}\right).$$

We proceed as in Proposition 2.1 to prove (4.19) and (4.18). We now prove (4.20). We have

$$\int_K |\nabla\varphi|^p \le \hat{C}\int_K\left(|C_K|^p|\nabla\Psi_K|^p + \sum_{i=1}^{d}|C_{\partial K_i}|^p|\nabla\Psi_{\partial K_i}|^p\right).$$

Proceeding as in (2.13) and (2.17) we obtain the following bounds

$$|C_{\partial K_i}|^p \le \hat{C}\left(\frac{\omega_{2,K}^p(e)}{\left(\prod_{j=1}^{d}\lambda_{j,K}\right)^{p/2}} + \frac{\omega_{2,K^i}^p(e)}{\left(\prod_{j=1}^{d}\lambda_{j,K^i}\right)^{p/2}}\right),$$

$$|C_K|^p \le \hat{C}\left(\frac{\omega_{2,K}^p(e)}{\left(\prod_{j=1}^{d}\lambda_{j,K}\right)^{p/2}} + \sum_{i=1}^{d+1}\frac{\omega_{2,K^i}^p(e)}{\left(\prod_{j=1}^{d}\lambda_{j,K^i}\right)^{p/2}}\right).$$

Thus we obtain

$$\int_K |\nabla\varphi|^p \leq \hat{C}\left(\frac{\omega_{2,K}^p(e)}{\left(\prod_{j=1}^d \lambda_{j,K}\right)^{p/2}} + \sum_{i=1}^{d+1} \frac{\omega_{2,K^i}^p(e)}{\left(\prod_{j=1}^d \lambda_{j,K^i}\right)^{p/2}}\right)\left(\int_K |\nabla\Psi_K|^p + \sum_{j=1}^{d+1}\int_K |\nabla\Psi_{\partial K_j}|^p\right)$$

Using assumption (4.13) we have

$$\omega_{2,K}^p(e) \leq \hat{C}\left(\lambda_{d,K}^2 ||\nabla e||_{L^2(\Delta K)}^2\right)^{p/2}.$$

Using (1.5) and the fact that $\lambda_{1,K} \geq \cdots \geq \lambda_{d,K} > 0$, we obtain

$$||\nabla\Psi_K||_{L^p(K)}^p \leq \frac{\prod_{j=1}^d \lambda_{j,K}}{\lambda_{d,K}^p} ||\hat{\nabla}\hat{\Psi}_{\hat{K}}||_{L^p(\hat{K})}^p$$

and the same occurs for $\nabla\Psi_{\partial K_i}$. All together using the hypothesis that $\lambda_{i,K}$ vary smoothly around K for $i = 1, \ldots, d$ we have

$$\int_K |\nabla\varphi|^p \leq \hat{C}\left(\prod_{j=1}^d \lambda_{j,K}\right)^{(2-p)/2}\left(\left(\int_{\Delta K} |\nabla e|^2\right)^{p/2} + \sum_{i=1}^{d+1}\left(\int_{\Delta K^i} |\nabla e|^2\right)^{p/2}\right).$$

using Hölder's inequality we have

$$\int_K |\nabla\varphi|^p \leq \hat{C}\left(\prod_{j=1}^d \lambda_{j,K}\right)^{(2-p)/2}\left(|\Delta K|^{(p-2)/2}\int_{\Delta K} |\nabla e|^p + \sum_{i=1}^{d+1} |\Delta K^i|^{(p-2)/2}\int_{\Delta K^i} |\nabla e|^p\right),$$

and using assumption 1 of Chapter 1 and the fact that $\lambda_{i,K}$ vary smoothly around K we obtain (4.20). □

We are now ready to prove (4.14) of Theorem 4.3.

Proof. (Lower bound (4.14) of Theorem 4.3) Using definition of $\eta_{2,K}$ and identities (4.17)-(4.16), one can write

$$\begin{aligned}\sum_{K\in\mathcal{T}_h} \eta_{2,K} = &\sum_{K\in\mathcal{T}_h}\int_K \left(\Pi_K f + \nabla\cdot\left((\mu + |\nabla u_h|^{p-2})\nabla u_h\right)\varphi\right) \\ &+ \frac{1}{2}\int_{\partial K}[(\mu + |\nabla u_h|^{p-2})\nabla u_h\cdot\mathbf{n}]\varphi,\end{aligned}$$

where φ is the bubble function introduced in Proposition 4.6. Using (4.2) and integration

by parts we obtain

$$\begin{aligned}\sum_{K\in\mathcal{T}_h}\eta_{2,K} &= \int_K \left(\left(\mu+|\nabla u|^{p-2}\right)\nabla u-\left(\mu+|\nabla u_h|^{p-2}\right)\nabla u_h\right)\nabla\varphi\\ &\quad-\sum_{K\in\mathcal{T}_h}\int_K (f-\Pi_K f)(\varphi-\Pi_K\varphi)\\ &\leq |a(u,\varphi)-a(u_h,\varphi)|+\sum_{K\in\mathcal{T}_h}\int_K |f-\Pi_K f|\ |\varphi-\Pi_K\varphi|.\end{aligned}$$

Using Proposition 4.3 and Cauchy-Schwarz inequality we obtain

$$\sum_{K\in\mathcal{T}_h}\eta_{2,K}\leq \hat{C}\left(||e||^p_{(u_h)}+||\varphi||^p_{(u_h)}\right)+\sum_{K\in\mathcal{T}_h}||f-\Pi_K f||_{L^2(K)}||\varphi-\Pi_K\varphi||_{L^2(K)}. \quad (4.21)$$

Using Proposition 2.2 we have

$$||\varphi-\Pi_K\varphi||^2_{L^2(K)}\leq \hat{C}\sum_{j=1}^{d}\lambda^2_{j,K}||\nabla\varphi\cdot\mathbf{r}_{j,K}||^2_{L^2(K)},$$

which together with (4.18) gives

$$||\varphi-\Pi_K\varphi||_{L^2(K)}\leq \hat{C}\left(\omega_{2,K}(e)+\sum_{i=1}^{d+1}\omega_{2,K^i}(e)\right).$$

Using assumption (4.13) and Young's inequality we obtain

$$\begin{aligned}\sum_{K\in\mathcal{T}_h}||f-\Pi_K f||_{L^2(K)}||\varphi-\Pi_K\varphi||_{L^2(K)} &\leq \hat{C}\left(\sum_{K\in\mathcal{T}_h}||f-\Pi_K f||_{L^2(K)}\omega_{2,K}(e)+\sum_{i=1}^{d+1}\omega_{2,K^i}(e)\right)\\ &\leq \hat{C}\left(\epsilon_1+\sum_{K\in\mathcal{T}_h}\lambda_{d,K}||f-\Pi_K f||_{L^2(K)}\sum_{i=1}^{d+1}||\nabla e||_{L^2(\Delta K^i)}\right)\\ &\leq \hat{C}\left(\epsilon_1+\epsilon_2+\epsilon_4\right).\end{aligned}$$

We have

$$\begin{aligned}||\varphi||^p_{(u_h)} &= \sum_{K\in\mathcal{T}_h}\int_K(\mu+(|\nabla u_h|+|\nabla\varphi|)^{p-2})|\nabla\varphi|^2\\ &\leq \hat{C}\sum_{K\in\mathcal{T}_h}\int_K(\mu+|\nabla u_h|^{p-2})|\nabla\varphi|^2+\hat{C}\int_K|\nabla\varphi|^p\\ &\leq \hat{C}\sum_{K\in\mathcal{T}_h}\int_{\mathcal{P}_K}\left(\mu+|\nabla u_h|^{p-2}\right)_{|K}|\nabla e|^2+|\nabla e|^p,\end{aligned}$$

where we used (4.19)-(4.20). We have

$$\begin{aligned}
&\sum_{K\in\mathcal{T}_h}\int_{\mathcal{P}_K}\left(\mu+|\nabla u_h|^{p-2}\right)_{|K}|\nabla e|^2\\
&=\sum_{K\in\mathcal{T}_h}\sum_{K'\in\mathcal{P}_K}\int_{K'}\left(\left(\mu+|\nabla u_h|^{p-2}\right)_{|K}-\left(\mu+|\nabla u_h|^{p-2}\right)_{|K'}\right)|\nabla e|^2\\
&+\sum_{K\in\mathcal{T}_h}\int_{\mathcal{P}_K}\left(\mu+|\nabla u_h|^{p-2}\right)|\nabla e|^2.
\end{aligned}$$

All together we have

$$\begin{aligned}
\sum_{K\in\mathcal{T}_h}\eta_{2,K}\leq\hat{C}||e||^p_{(u_h)}+\hat{C}\sum_{K\in\mathcal{T}_h}\lambda^2_{d,K}||f-\Pi_K f||^2_{L^2(K)}\\
+\hat{C}\sum_{K\in\mathcal{T}_h}\sum_{K'\in\mathcal{P}_K}\int_{K'}\left(\left(\mu+|\nabla u_h|^{p-2}\right)_{|K}-\left(\mu+|\nabla u_h|^{p-2}\right)_{|K'}\right)|\nabla e|^2,
\end{aligned}$$

therefore, applying the triangle inequality $||e||^p_{(u_h)}\leq\hat{C}||e||^p_{(u)}$, we get the desired result. □

4.3 Numerical experiments with non-adapted meshes

The goal of this section is to numerically check the sharpness of the error estimator presented in Theorem 4.3. We are interested by the case $p=3$, since it corresponds to the so called Smagorinsky model [67, 64] discussed in Chapter 5. We will study error estimator (4.15). The following notations are introduced : the quasi-norm error

$$e_{QN}=||u-u_h||^3_{(u)},$$

the $W^{1,3}_0$ semi-norm error

$$e_3=||\nabla(u-u_h)||^3_{L^3(\Omega)},$$

and the weighted $W^{1,2}_0$ semi-norm error

$$e_2=\mu||\nabla(u-u_h)||^2_{L^2(\Omega)}.$$

We also define the following anisotropic effectivity indices :

$$\mathrm{ei}^N=\frac{\sum_{K\in\mathcal{T}_h}\eta_{2,K}}{e_2+e_3},\tag{4.22}$$

$$\mathrm{ei}^{QN}=\frac{\sum_{K\in\mathcal{T}_h}\eta_{2,K}}{e_{QN}},\tag{4.23}$$

and the ZZ effectivity index

$$\mathrm{ei}_{L^2}^{ZZ} = \frac{||\nabla u_h - \Pi_h^{ZZ} \nabla u_h||_{L^2(\Omega)}}{||\nabla (u - u_h)||_{L^2(\Omega)}}.$$

We aim to verify if these quantities satisfy the following properties :

- ei^{QN} and ei^{N} are independent of the solution u,
- ei^{QN} and ei^{N} are independent of the choice of μ,
- ei^{QN} and ei^{N} are independent of the mesh size and aspect ratio,
- $\mathrm{ei}_{L^2}^{ZZ}$ is close to one (see the discussion in Remark 2.1 in Chapter 2).

Let $\Omega = (0,1)^2$ and consider problem (4.1). Results with various meshes sizes (h_1-h_2 being the mesh size in directions x_1 and x_2) and various values of μ are reported in Table 4.1 for the exact solution

$$u(x,y) = 4(1 - e^{-\alpha x} - (1 - e^{-\alpha})x)y(1-y) \tag{4.24}$$

as in [34] with $\alpha = 50$. Similarly, in Tables 4.2 and 4.3 results are reported for the exact solution

$$u(x,y) = \tanh(\frac{x - 0.5}{\epsilon}) \tag{4.25}$$

with $\epsilon = 0.1$ and $\epsilon = 0.05$ respectively. Note that u defined by (4.25) is not zero on the boundary, thus the theory does not apply as is anymore. Nevertheless, numerical results indicate that the error estimator is still sharp.

The ZZ effectivity index is close to one as desired. We observe that the derived error estimator is accurate for both the $W_0^{1,3}$ norm and the quasi-norm when μ is large. When μ is large the effectivity indices are around 9 which corresponds to the linear elliptic problem [29, 62] discussed in Chapter 2. When μ is small, only the quasi-norm should be considered. Indeed, when h is small enough, the corresponding effectivity indices remain between 11 and 18 uniformly with respect to μ and h. We therefore can conclude that the upper bound (4.12) seems to be sharp with $p = 3$.

TABLE 4.1 : True errors and effectivity indices for various non-adapted meshes and various choices of μ when solving problem (4.1) with f given such that the exact solution is given by (4.24), with $\alpha = 50$.

h_1-h_2	ei^N	ei^{QN}	e_{QN}	e_3	e_2	$ei_{L^2}^{ZZ}$
			$\mu = 0$			
0.025 0.025	8.43	2.78	81.50	26.21	0	0.59
0.0125 0.0125	20.08	6.14	15.32	3.11	0	0.82
0.00625 0.00625	85.17	9.66	3.12	3.53e-01	0	0.93
0.003125 0.003125	208.47	11.99	7.11e-01	4.07e-02	0	0.98
0.01 0.1	55.12	10.07	7.75	1.40	0	0.96
0.005 0.05	111.62	12.10	1.86	2.02e-01	0	0.98
0.0025 0.025	235.82	13.89	4.60e-01	2.70e-02	0	0.99
0.00125 0.0125	510.447	15.33	1.02e-01	3.05e-03	0	0.99
			$\mu = 1$			
0.025 0.025	8.13	2.72	82.71	26.06	1.64	0.59
0.0125 0.0125	27.28	6.13	15.70	3.12	4.02e-01	0.82
0.00625 0.00625	68.39	9.57	3.21	3.54e-01	9.60e-02	0.93
0.003125 0.003125	134.81	11.84	7.34e-01	4.09e-02	2.36e-02	0.98
0.01 0.1	44.00	9.94	8.17	1.40	4.42e-01	0.97
0.005 0.05	73.06	11.83	1.98	2.01e-01	1.20e-01	0.98
0.0025 0.025	111.91	13.48	4.92e-01	2.70e-02	3.22e-02	
0.00125 0.0125	148.42	14.78	1.10e-01	3.07e-03	7.91e-03	0.99
			$\mu = 100$			
0.025 0.025	4.16	3.23	222.81	23.33	149.50	0.63
0.0125 0.0125	7.22	5.65	53.55	3.00	38.89	0.84
0.00625 0.00625	9.40	7.36	12.54	3.51e-01	9.47	0.94
0.003125 0.003125	10.69	8.36	3.05	4.09e-02	2.35	0.98
0.01 0.1	8.66	7.60	51.04	1.37	43.42	0.97
0.005 0.05	9.08	7.99	13.72	1.99e-01	11.87	0.98
0.0025 0.025	9.45	8.34	3.67	2.69e-02	3.21	0.99
0.00125 0.0125	9.66	8.58	8.92e-01	3.06e-03	7.90e-01	0.99

TABLE 4.2 : True errors and effectivity indices for various non-adapted meshes and various choices of μ when solving problem (4.1) with f given such that the exact solution is given by (4.25), with $\epsilon = 0.1$.

h_1-h_2	ei^N	ei^{QN}	e_{QN}	e_3	e_2	$ei_{L^2}^{ZZ}$
			$\mu = 0$			
0.05 0.05	85.12	11.59	1.30	1.77e-01	0	1.04
0.025 0.025	159.87	13.17	2.73e-01	2.25e-02	0	1.02
0.0125 0.0125	309.63	13.82	6.11e-02	2.73e-03	0	1.00
0.00625 0.00625	643.61	14.22	1.51e-02	3.33e-04	0	1.00
0.003125 0.003125	1280.79	14.34	3.74e-03	4.19e-05	0	1.00
0.005 0.05	772.78	15.81	8.26e-03	1.69e-04	0	0.99
0.0025 0.025	1547.62	15.57	1.92e-03	1.94e-05	0	1.00
0.00125 0.0125	3098.95	15.62	4.79e.04	2.41e-06	0	1.00
0.002 0.2	2574.62	18.56	1.25e-03	9.02e-06	0	1.00
0.001 0.1	4704.70	17.58	3.16e.04	1.18e-06	0	0.99
0.0005 0.05	8910.96	17.36	7.57e-05	1.47e-07	0	0.99
			$\mu = 1$			
0.05 0.05	45.73	11.27	1.47	1.73e-01	1.88e-01	1.06
0.025 0.025	59.82	12.46	3.15e-01	2.24e-02	4.33e-02	1.02
0.0125 0.0125	71.31	12.95	7.12e-02	2.73e-03	1.02e-02	1.01
0.00625 0.00625	80.49	13.29	1.76e-02	3.33e-04	2.57e-03	1.00
0.003125 0.003125	85.29	13.39	4.39e-03	4.10e-05	6.47e-04	1.00
0.005 0.05	88.81	14.67	9.68e-02	1.69e-04	1.43e-03	1.00
0.0025 0.025	91.69	14.42	2.26e-03	1.94e-05	3.36e-04	1.00
0.00125 0.0125	95.00	14.46	5.61e-04	2.41e-06	8.30e-05	1.00
0.002 0.2	111.81	17.23	1.47e-03	9.03e-06	2.17e-04	1.00
0.001 0.1	108.85	16.32	3.70e-04	1.18e-06	5.44e-05	0.99
0.0005 0.05	107.82	16.09	8.88e-05	1.47e-07	1.31e-05	0.99
			$\mu = 100$			
0.05 0.05	8.82	8.33	18.90	1.63e-01	17.70	1.08
0.025 0.025	8.66	8.19	4.56	2.22e-02	4.29	1.03
0.0125 0.0125	8.55	8.09	1.08	2.73e-03	1.02	1.01
0.00625 0.00625	8.65	8.19	2.73e-01	3.34e-04	2.58e-01	1.00
0.003125 0.003125	8.64	8.17	6.83e-02	4.21e-05	6.46e-02	1.00
0.005 0.05	8.92	8.44	1.51e-01	1.79e-04	1.42e-01	1.00
0.0025 0.025	8.69	8.22	3.55e-02	1.94e-05	3.36e-02	1.00
0.00125 0.0125	8.68	8.21	8.78e-03	2.42e-06	8.30e-03	1.00
0.001 0.1	10.07	9.52	5.74e-03	1.17e.06	5.42e-03	0.99
0.0005 0.05	9.75	9.22	1.38e-03	1.46e-07	1.31e-03	0.99

TABLE 4.3 : True errors and effectivity indices for various non-adapted meshes and various choices of μ when solving problem (4.1) with f given such that the exact solution is given by (4.25), with $\epsilon = 0.05$.

h_1-h_2	ei^N	ei^{QN}	e_{QN}	e_{L^3}	e_{L^2}	$ei_{L^2}^{ZZ}$
			$\mu = 0$			
0.025 0.025	74.61	11.67	4.93	7.70e-01	0	1.06
0.0125 0.0125	153.99	13.08	1.05	8.89e-02	0	1.00
0.00625 0.00625	324.70	13.90	2.50e-01	1.07e-02	0	1.01
0.003125 0.003125	650.11	14.17	6.12e-02	1.33e-03	0	1.00
0.005 0.05	384.54	14.91	1.38e-01	5.36e-03	0	0.89
0.0025 0.025	766.47	15.20	3.13e-02	6.22e-04	0	0.99
0.00125 0.0125	1544.29	15.53	7.71e-03	7.76e-05	0	1.00
0.002 0.2	1184.92	17.28	2.01e-02	2.93e-04	0	1.00
0.001 0.1	2189.84	17.27	5.26e-03	4.14e-05	0	1.00
0.0005 0.05	4364.82	17.12	2.21e-03	4.77e-06	0	1.00
			$\mu = 1$			
0.025 0.025	53.56	11.46	5.25	7.64e-01	3.58e-01	1.08
0.0125 0.0125	83.35	12.73	1.13	8.85e-02	8.33e-02	1.02
0.00625 0.00625	115.70	13.44	2.70e-01	1.07e-02	2.07e-02	1.01
0.003125 0.003125	138.78	13.68	6.64e-02	1.33e-03	5.21e-03	1.00
0.005 0.05	121.83	14.53	1.48e-01	5.23e-03	1.24e-02	0.95
0.0025 0.025	150.69	14.62	3.40e-02	6,22e-04	2.68e-03	1.00
0.00125 0.0125	167.63	14.92	8.39e-03	7.76e-05	6.68e-04	1.00
0.002 0.2	179.26	16.61	2.18e-02	2.94e-04	1.73e-03	1.00
0.001 0.1	191.54	16.58	5.71e-03	4.14e-05	4.53e-05	1.00
0.0005 0.05	196.31	16.44	1.32e-03	4.77e-06	1.06e-05	1.00
			$\mu = 100$			
0.025 0.025	9.29	8.34	38.88	7.36e-01	34.19	1.09
0.0125 0.0125	9.35	8.39	9.16	8.78e-02	8.14	1.03
0.00625 0.00625	9.47	8.50	2.31	1.07e-02	2.06	1.01
0.003125 0.003125	9.47	8.50	5.80e-01	1.34e-03	5.19e-01	1.00
0.005 0.05	9.76	8.77	1.24	5.16e-03	1.11	1.00
0.0025 0.025	9.51	8.53	2.98e-01	6.22e-04	2.67e-01	1.00
0.00125 0.0125	9.58	8.60	7.45e-02	7.77e-05	6.68e-02	1.00
0.002 0.2	10.91	9.79	1.93e-01	2.93e-04	1.73e-01	1.00
0.001 0.1	10.72	9.61	5.05e-02	4.12e-05	4.52e-02	1.00
0.0005 0.05	10.58	9.49	1.18e-02	4.75e-06	1.06e-02	0.99

Consider the higher order terms of the upper and lower bounds ϵ_1, ϵ_2 and ϵ_3 (see Theorem 4.3). Consider again the first numerical experiment when $\mu = 0$ and u is given by (4.24) with $\alpha = 50$, let $h_1 = \frac{1}{N_x}$ and $h_2 = 10h_1$. In Figure 4.1 we can observe the order of convergence of the error estimator $\sum_{K\in\mathcal{T}_h} \eta_{2,K} = O(h^2)$, the quasi-norm error $e_{QN} = O(h^2)$ and the $W_0^{1,3}$ error $e_3 = O(h^3)$. Moreover in Figure 4.2 we observe $\epsilon_1, \epsilon_2, \epsilon_4 = O(h^3)$ and $\epsilon_3 = O(h^5)$, which are higher order terms with respect to e_{QN} as discussed in Remark 4.2.

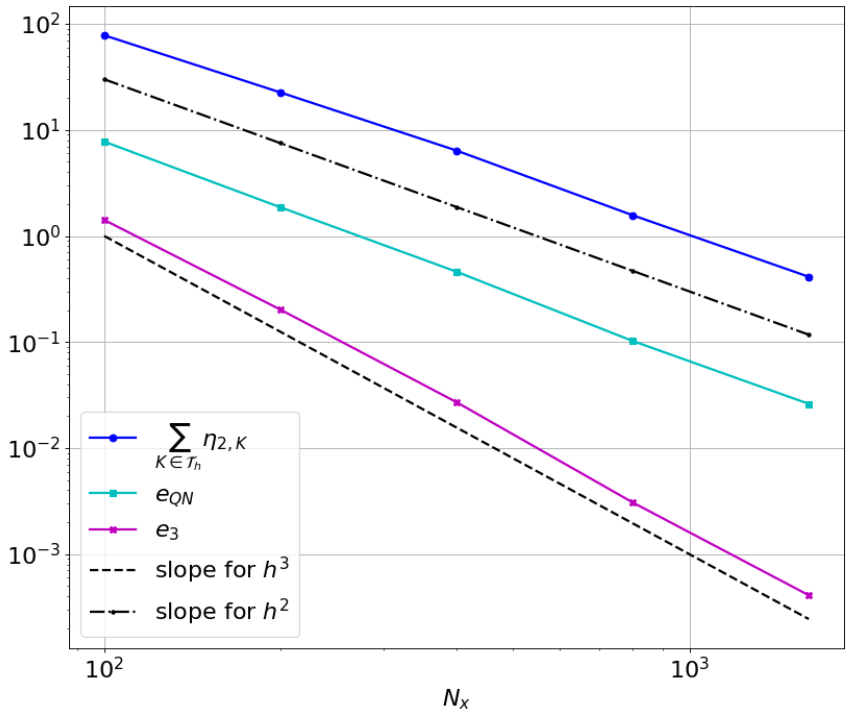

FIGURE 4.1 : Error estimator, quasi-norm error, $W_0^{1,3}$ semi-norm error with corresponding slopes, when u is given by (4.24), $\mu = 0$ and $\alpha = 50$.

Considering again experiment of Table 4.1, we compare the error estimator $\eta_2 = \sum_{K\in\mathcal{T}_h} \eta_{2,K}$ with the error estimator $\eta_3 = \sum_{K\in\mathcal{T}_h} \eta_{3,K}$ discussed in Remark 4.1. In Table 4.4 we report a comparison of the two estimators and a comparison of $\text{ei}_{L^2}^{ZZ}$ with

$$\text{ei}_{L^3}^{ZZ} = \frac{||\nabla u_h - \Pi_h^{ZZ}\nabla u_h||_{L^3(\Omega)}}{||\nabla(u - u_h)||_{L^3(\Omega)}}.$$

Both estimators give similar results and show similar behaviours. For practical reasons only η_2 will be considered.

In the next section we use the derived error estimator (4.15) as indicator for our

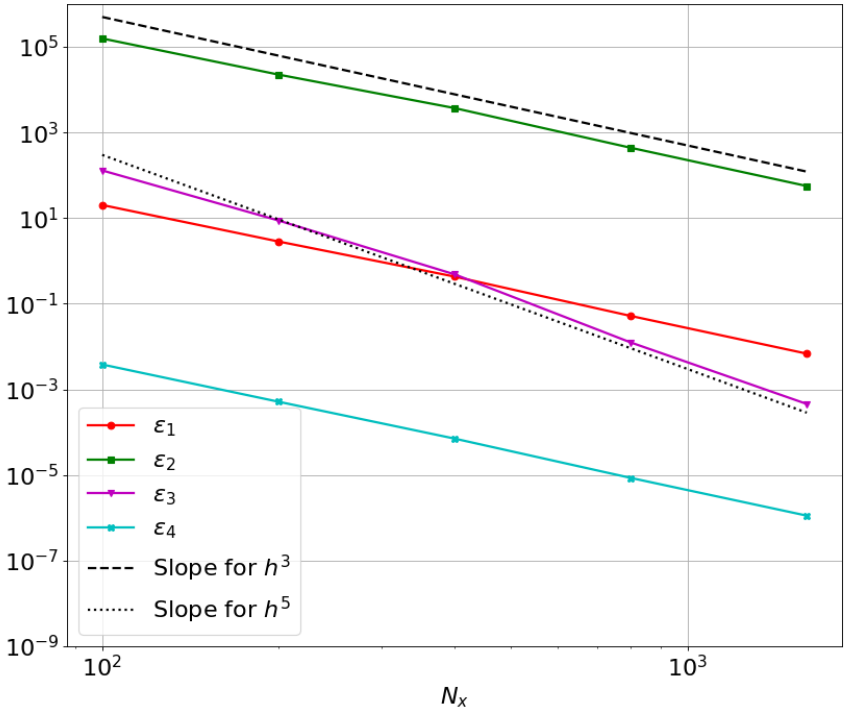

FIGURE 4.2 : Higher order terms ϵ_1, ϵ_2, ϵ_3, ϵ_4 with corresponding slopes, when u is given by (4.24), $\mu = 0$ and $\alpha = 50$.

adaptive strategy. Given an accuracy, the goal will be again to construct adapted meshes able to solve problem (4.1) at a reduced computational cost.

TABLE 4.4 : Error estimators η_2, η_3 and ZZ-effectivity indices for various non-adapted meshes and various choices of μ when solving problem (4.1) with f given such that the exact solution is given by (4.24), with $\alpha = 50$.

h_1-h_2	η_2	η_3	$ei_{L^2}^{ZZ}$	$ei_{L^3}^{ZZ}$
	$\mu = 0$			
0.025 0.025	221.00	226.93	0.59	0.47
0.0125 0.0125	99.57	94.12	0.82	0.71
0.00625 0.00625	30.12	32.74	0.93	0.86
0.003125 0.003125	8.52	9.39	0.98	0.93
0.01 0.1	78.03	81.95	0.96	0.93
0.005 0.05	22.56	24.19	0.98	0.97
0.0025 0.025	6.39	6.93	0.98	0.99
0.00125 0.0125	1.57	1.70	0.99	0.99
	$\mu = 1$			
0.025 0.025	225.36	231.57	0.47	0.59
0.0125 0.0125	96.16	101.77	0.82	0.71
0.00625 0.00625	30.74	33.42	0.93	0.86
0.003125 0.003125	8.69	9.58	0.98	0.93
0.01 0.1	81.14	85.41	0.97	0.93
0.005 0.05	23.43	25.17	0.98	0.97
0.0025 0.025	6.63	7.21	0.99	0.98
0.00125 0.0125	1.63	1.77	0.99	0.99
	$\mu = 100$			
0.025 0.025	719.56	753.04	0.63	0.50
0.0125 0.0125	302.41	323.81	0.84	0.73
0.00625 0.00625	92.35	101.24	0.94	0.86
0.003125 0.003125	25.52	28.30	0.98	0.93
0.01 0.1	387.99	426.65	0.97	0.94
0.005 0.05	109.57	121.53	0.98	0.97
0.0025 0.025	30.57	34.18	0.99	0.99
0.00125 0.0125	7.65	8.57	0.99	0.99

4.4 Numerical experiments with adapted meshes

We consider now algorithm 2 described in Section 2.4.3. Error indicator noted η_K^2 in Section 2.4.3 is replaced by $\eta_{2,K}$, we aim to control the quasi-norm error $||u - u_h||_{(u)}^{3/2}$ and set $m = 2$ in (2.26).

Let $\Omega = (0,1)^2$ and consider again problem (4.1) with exact solution (4.24) with

$\alpha = 100$. We apply algorithm 2 with a starting mesh of size $h_1 = 0.1$ and $h_2 = 0.1$ in directions x_1 and x_2 respectively. We choose $\text{TOL}_{goal} = 0.015625$, $N = 6$ and $N_{it} = 40$. In Table 4.5 obtained results are reported for different values of μ. We observe that, for any choice of μ, the value of ei^{QN} does not increase together with the average aspect ratio av_{ar} and the maximum aspect ratio $\max_{\text{ar}}$. Consider the same experiment with $\alpha = 50$,

TABLE 4.5 : True errors, effectivity indices, number of vertices and aspect ratio for different values of tolerance TOL and μ, when solving problem (4.1) with f such that the exact solution is given by (4.24) with $\alpha = 100$. Results obtained running algorithm 2($\text{TOL}_{goal} = 0.015625$,$N = 6$,$\mathcal{T}_h^1$,$N_{it} = 40$).

TOL	ei^N	ei^{QN}	e_{QN}	ei^{ZZ}	N_v	av_{ar}	$\max_{\text{ar}}$
			$\mu = 0$				
0.5	33.52	10.25	20.50	0.97	89	25	116
0.25	70.84	12.97	3.48	0.98	249	32	272
0.125	98.70	13.67	8.17e-01	0.97	838	33	239
0.0625	338.71	17.13	1.61e-01	1.01	2975	36	421
0.03125	756.82	18.82	3.63e-02	1.01	11582	37	825
0.015625	1539.65	18.33	9.43e-03	1.00	44454	39	962
			$\mu = 1$				
0.5	38.02	11.01	14.23	0.99	95	26	131
0.25	61.19	13.65	3.38	0.99	254	29	305
0.125	83.56	15.21	7.28e-01	0.99	863	33	257
0.0625	112.37	16.89	1.58e-01	1.01	3182	36	607
0.03125	135.67	17.64	3.93e-02	1.00	11936	37	695
0.015625	150.25	17.90	9.84e-03	1.00	46032	41	670
			$\mu = 100$				
0.5	9.94	8.37	40.89	0.93	171	18	202
0.25	10.39	8.91	10.16	0.95	502	23	225
0.125	10.65	9.18	2.42	0.95	1713	26	253
0.0625	11.85	10.15	5.23e-01	0.99	6649	26	436
0.03125	12.44	10.63	1.26e-02	1.00	25536	27	635
0.015625	13.07	11.13	3.02e-02	1.00	98424	29	1064

we run again algorithm 2 with the same parameters of before. In Figure 4.3 we observe the order of convergence of the error estimator $\sum_{K\in\mathcal{T}_h} \eta_{2,K} = O(\text{TOL}^2)$, the quasi-norm error $e_{QN} = O(\text{TOL}^2)$, the $W_0^{1,3}$ semi-norm $e_3 = O(\text{TOL}^3)$ and the $W_0^{1,2}$ semi-norm $e_2 = O(\text{TOL}^2)$. In Figure 4.4 we observe the following convergences : $\epsilon_1, \epsilon_2, \epsilon_4 = O(\text{TOL}^3)$ and $\epsilon_3 = O(\text{TOL}^5)$. Theoretical predictions of Remark 4.2 are again numerically verified. Thus also when working with adapted meshes ϵ_1, ϵ_2, ϵ_3 and ϵ_4 are of higher order with respect to error estimator $\sum_{K\in\mathcal{T}_h} \eta_{2,K}$.

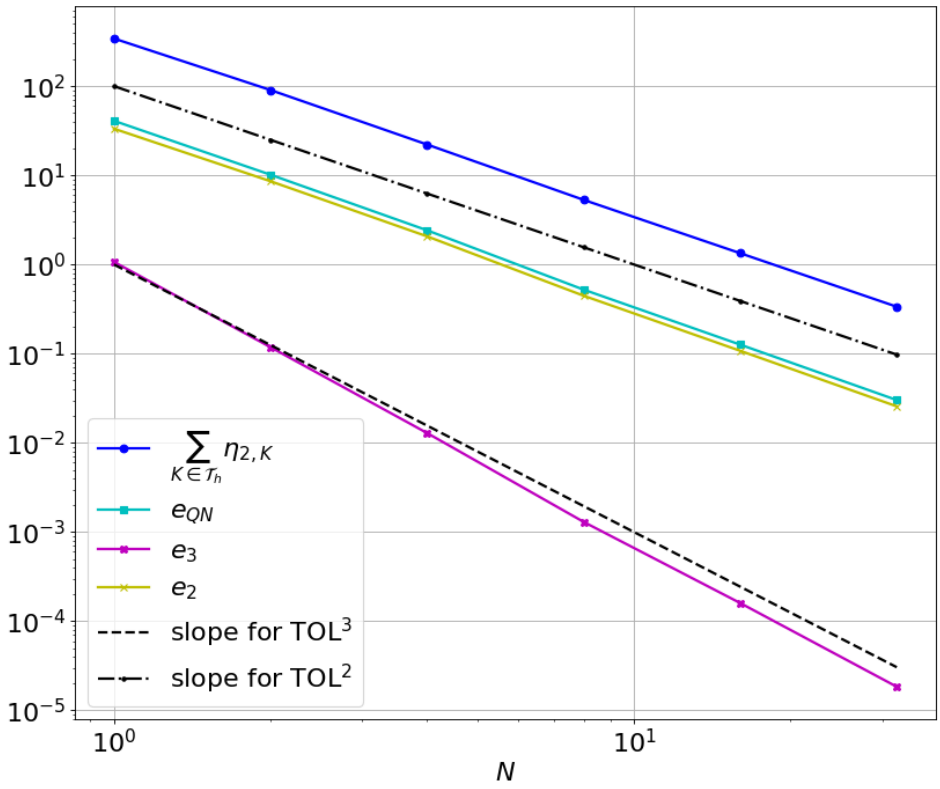

FIGURE 4.3 : Error estimator, quasi-norm error, $W_0^{1,3}$ and $W_0^{1,2}$ semi-norm errors with corresponding slope, when u is given by (4.24), $\mu = 100$ and $\alpha = 100$. Results obtained running algorithm 2(TOL$_{goal} = 0.015625$,$N = 6$,$\mathcal{T}_h^1$,$N_{it} = 40$) and reported for TOL $= 0.5 \times 2^{-N}$.

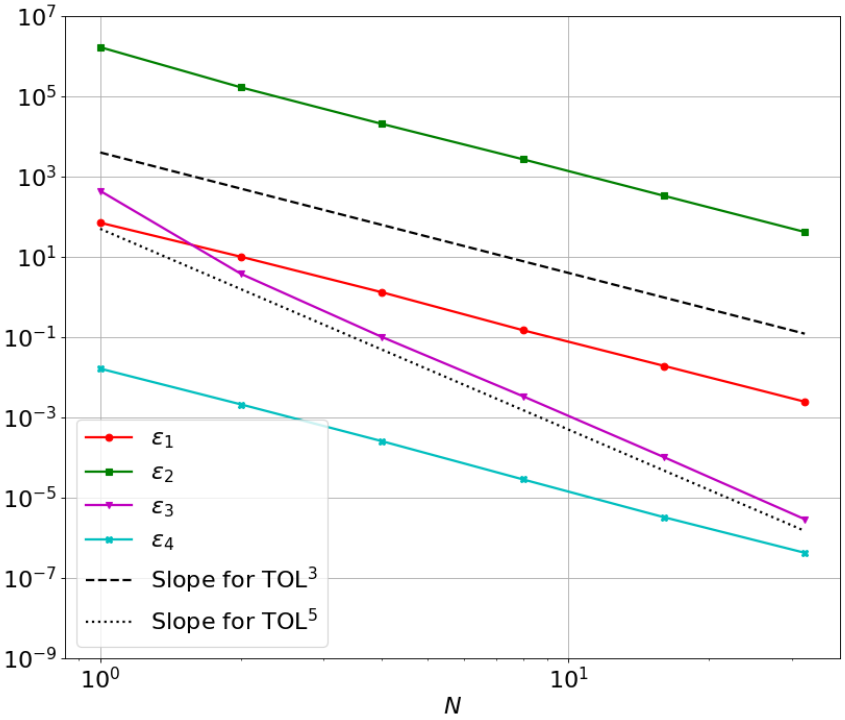

FIGURE 4.4 : Higher order terms ϵ_1, ϵ_2, ϵ_3, ϵ_4 with corresponding slopes, when u is given by (4.24), $\mu = 100$ and $\alpha = 100$. Results obtained running algorithm 2(TOL$_{goal}$ = 0.015625,$N = 6$,$\mathcal{T}_h^1$,$N_{it} = 40$) and reported for TOL $= 0.5 \times 2^{-N}$.

Consider again problem (4.1) with exact solution (4.25) with $\epsilon = 0.05$ and $\Omega = (0,1)^2$. In Table 4.6 we can observe the results for different values of μ obtained applying algorithm 2. The starting mesh is again of size $h_1 = h_2 = 0.1$ in each directions, we set TOL$_{goal}$ = 0.000976562, $N = 10$ and $N_{it} = 40$.

TABLE 4.6 : True errors, effectivity indices, number of vertices and aspect ratio for different values of tolerance TOL and μ, when solving problem (4.1) with f given such that the exact solution is given by (4.25) with $\epsilon = 0.05$. Results obtained running algorithm 2($\text{TOL}_{goal} = 0.000976562$,$N = 10$,$\mathcal{T}_h^1$,$N_{it} = 40$).

TOL	ei^N	ei^{QN}	e_{QN}	ei^{ZZ}	N_v	av_{ar}	$\max_{\text{ar}}$
			$\mu = 0$				
0.5	58.15	11.68	3.34	0.91	52	20	61
0.25	139.26	18.36	6.68e-01	0.97	70	47	142
0.125	225.39	17.53	1.64e-01	0.96	150	88	325
0.0625	412.32	20.95	4.00e-02	0.99	246	189	865
0.03125	558.11	20.95	9.93e-03	0.97	492	351	1365
0.015625	1282.96	22.44	2.34e-03	0.98	863	845	4025
0.0078125	2426.23	23.76	5.73e-04	0.99	1703	1661	6348
0.00390625	3384.70	22.91	1.45e-04	0.98	3434	3286	16889
0.00195312	7852.33	23.20	3.61e-05	0.99	6821	6640	38352
0.000976562	14905.10	23.23	9.12e-06	0.99	13510	13250	61063
			$\mu = 1$				
0.5	51.02	12.56	2.88	0.93	80	14	46
0.25	72.59	15.53	6.46e-01	0.96	76	51	171
0.125	104.87	19.87	1.50-01	0.99	137	104	359
0.0625	95.51	19.04	4.37e-02	0.98	272	166	575
0.03125	108.03	20.36	1.11e-02	0.99	488	367	1444
0.015625	107.27	20.01	2.63e-03	0.99	967	788	3325
0.0078125	104.77	20.58	6.76e-04	0.97	1828	1644	7717
0.00390625	120.28	21.25	1.66e-04	1.00	3520	3315	15048
0.00195312	116.67	20.94	4.10e-05	0.99	7169	6587	40360
0.000976562	119.16	21.27	1.03e-05	1.00	14026	13530	66011
			$\mu = 100$				
0.5	13.03	12.03	17.13	0.97	59	23	90
0.25	10.08	9.42	6.18	0.91	105	45	131
0.125	11.39	10.53	1.18	0.97	210	92	364
0.0625	13.48	12.51	2.91e-01	0.97	401	180	971
0.03125	12.51	11.61	6.89e-02	0.99	732	424	2046
0.015625	13.04	12.07	1.79e-02	1.00	1354	872	4121
0.0078125	13.14	12.15	4.50e-03	0.99	2622	1735	7951
0.00390625	13.48	12.45	1.10e-03	1.00	5080	3770	17808
0.00195312	13.54	12.48	6.82e-05	1.00	9976	15286	77916
0.000976562	13.60	12.54	7.01e-05	1.00	19640	14987	71481

Results confirm that the effectivity index ei^{QN} does not increase along with the aspect ratio, but slightly depend on μ, when μ is small. Moreover when μ is small ei^N goes to

infinity along with the aspect ratio. In Figure 4.5 an example of the obtained adapted mesh is reported.

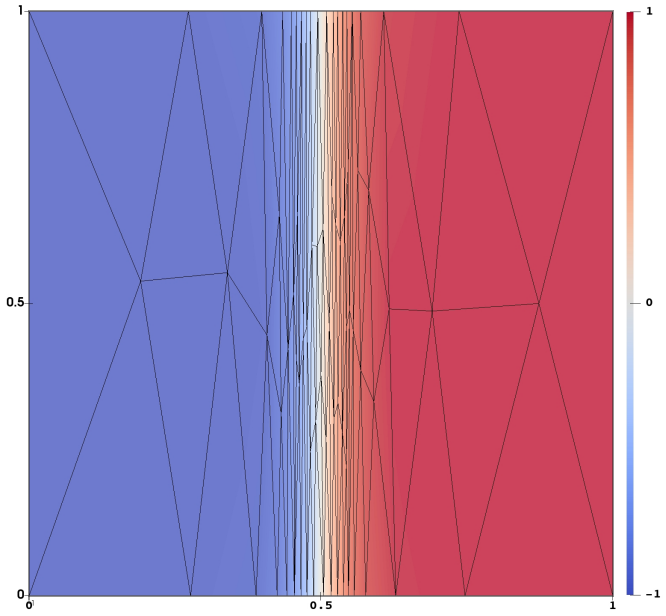

FIGURE 4.5 : Adapted mesh obtained when TOL = 0.25, when u is given by (4.25) and $\mu = 1$. Result obtained running algorithm 2(TOL$_{goal}$ = 0.000976562,$N = 10$,$\mathcal{T}_h^1$,$N_{it} = 40$).

Finally, we aim to test again the efficiency of the continuation algorithm 2 with respect to algorithm 1. Consider problem (4.1), $\Omega = (0,1)^2$ and let f be such that the exact solution is given by (4.25) with $\mu = 0$ and $\epsilon = 0.1$. For algorithm 1 we set TOL = 0.0078125, $N_{it} = 140$, for algorithm 2 we set TOL$_{goal}$ = 0.0078125, $N = 5$ and $N_{it} = 20$. Both start with a mesh of size $h_1 = h_2 = 0.1$. In Figure 4.6 we present the obtained results. Both algorithms give similar final meshes, the number of vertices is considerably close and the solution obtained have comparable accuracy. However algorithm 1 requires an higher number of vertices along first iterations. For this nonlinear problem we reported the total number of Conjugate Gradient iterations (sum for each Newton method step). The first approach increases considerably the CPU time. This is due to the higher refinement of the mesh at initial iterations. Algorithm 2 is clearly the fastest and best option. Numerical experiments show, once more, clearly benefits of a continuation algorithm on the preset tolerance parameter.

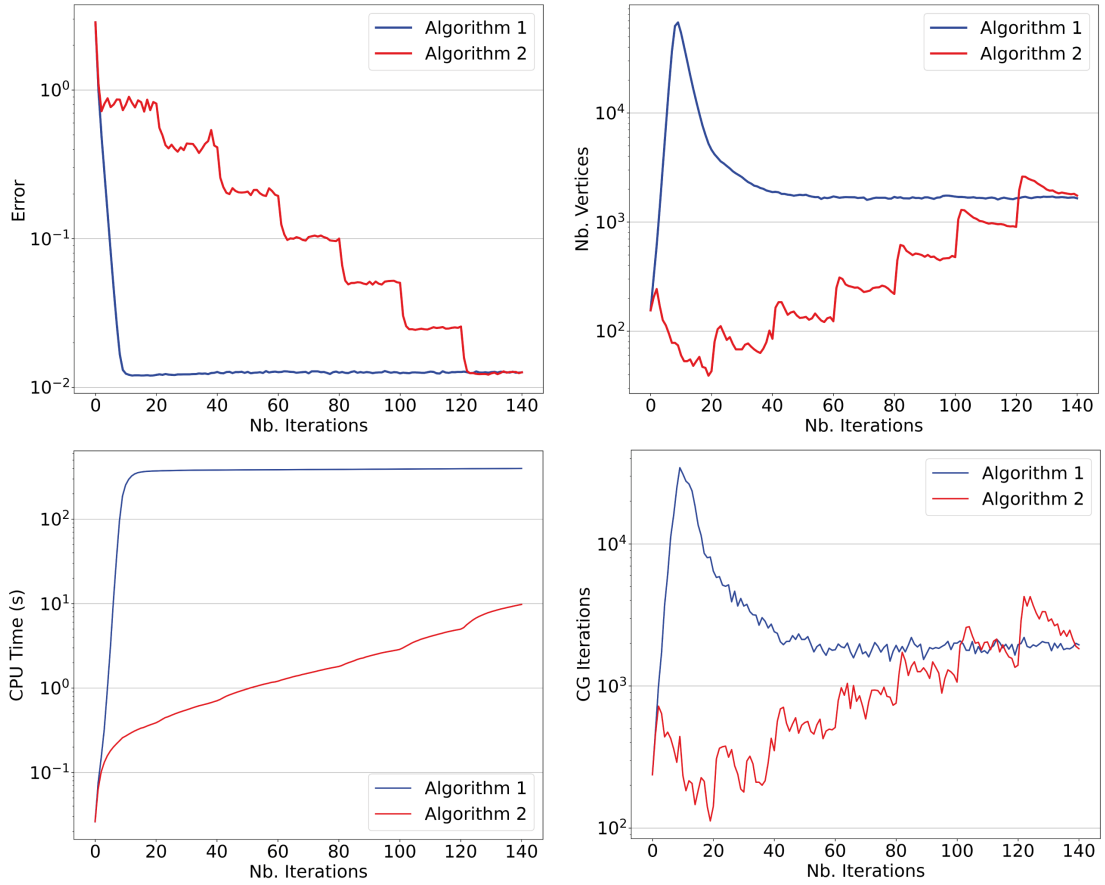

FIGURE 4.6 : Comparison of algorithm 1(TOL $= 0.0078125$,$\mathcal{T}_h^1$,$N_{it} = 140$) and algorithm 2(TOL$_{goal} = 0.0078125$,$N = 5$,$\mathcal{T}_h^1$,$N_{it} = 20$), solving problem (4.1) when u is given by (4.25) with $\mu = 0$ and $\epsilon = 0.1$. Top left : quasi-norm error at each iteration. Top right : Number of vertices at each iteration. Bottom left : CPU time at each iteration. Bottom right : sum of conjugate gradient iterations for Newton method at each iteration of the adaptive algorithm.

For a future application to an industrial problem we aim now to present a simplified error indicator for problem (4.1). Moreover we present also an additional adaptive strategy that will be considered for the future industrial application.

4.5 A simplified error indicator for a p-Laplace problem

In [45] it is proven, up to higher order terms, that edge residuals dominate for the Poisson problem and linear finite elements method on anisotropic meshes. The goal of this section is to numerically compare now, error estimator (4.15) with a simplified error indicator, where only edge residuals are considered :

$$\tilde{\eta}_{2,K} = \left(\frac{1}{2} \sum_{i=1}^{d+1} \left(\frac{|\partial K_i|}{\prod_{j=1}^{d} \lambda_{j,K}} \right)^{1/2} ||[(\mu_0 + |\nabla u_h|^{p-2}) \nabla u_h \cdot \mathbf{n}]||_{L^2(\partial K_i)} \right) \omega_{2,K}(u - u_h). \quad (4.26)$$

Let $\Omega = (0,1)^2$ and consider problem (4.1) with exact solution (4.25) with $\epsilon = 0.05$ and $\mu = 0$. We apply adaptive algorithm 2 of Section 2.4.3 with a starting mesh $\mathcal{T}_h$ of size $h_1 = 0.1$ and $h_2 = 0.1$ in directions x_1 and x_2 respectively. We set $\text{TOL}_{goal} = 0.000976562$, $N = 9$ and $N_{it} = 40$. We define as in (4.22)-(4.23) the effectivity index of the modified error indicator

$$\tilde{\text{ei}}^{QN} = \frac{\sum_{K \in \mathcal{T}_h} \tilde{\eta}_{2,K}}{e_{QN}}.$$

In Table 4.7 results obtained for both error indicators $\eta_{2,K}$ and $\tilde{\eta}_{2,K}$ are reported. Both error indicators give similar results, in particular the effectivity index ei^{QN} is around 23 while $\tilde{\text{ei}}^{QN}$ is around 9. In Figure 4.7 two adapted meshes with their respective solution can be observed. Error indicators $\eta_{2,K}$ and $\tilde{\eta}_{2,K}$ seem to be equivalent with different magnitudes.

TABLE 4.7 : True errors, effectivity indices for different values of tolerance TOL, when solving problem (4.1) with f such that the exact solution is given by (4.25) with $\epsilon = 0.05$ and $\mu = 0$. Left : Adapting with respect to the local error estimator (4.15). Right : Adapting with respect to the local error indicator (4.26). Results obtained running algorithm 2($\text{TOL}_{goal} = 0.000976562$,$N = 9$,$\mathcal{T}_h^1$,$N_{it} = 40$) .

TOL	ei^{QN}	e_{QN}	N_v	av_{ar}	$\tilde{\text{ei}}^{QN}$	e_{QN}	N_v	av_{ar}
0.03125	20.95	9.93e-03	492	350	8.24	2.47e-02	306	241
0.015625	22.45	2.34e-03	863	844	8.80	5.90e-03	587	491
0.0078125	23.76	5.73e-04	1703	1661	9.03	1.49e-03	1133	1008
0.00390625	22.91	1.46e-04	3425	3286	9.37	3.68-04	2220	2040

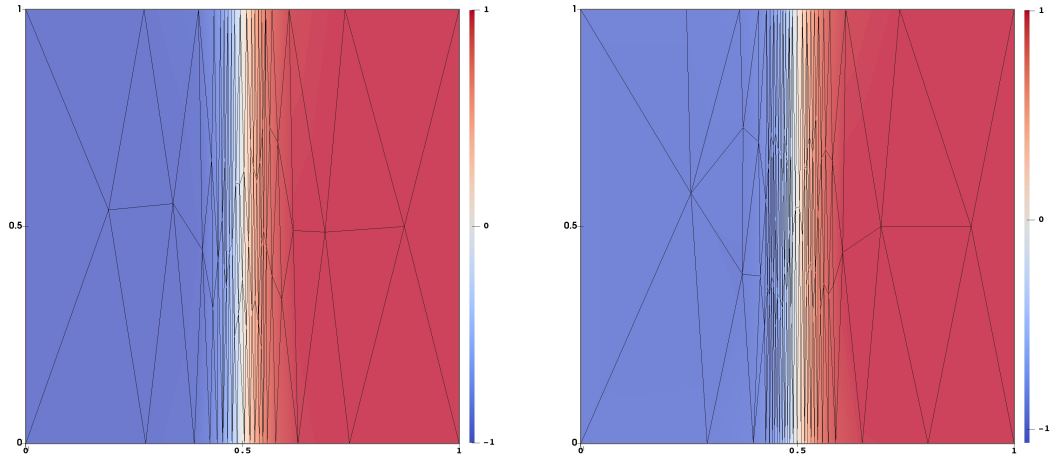

FIGURE 4.7 : Results obtained running algorithm 2(TOL$_{goal}$ = 0.000976562,N = 9,$\mathcal{T}_h^1$,N_{it} = 40), when u is given by (4.25) with $\epsilon = 0.05$ and $\mu = 0$. Left : adapted mesh obtained when TOL = 0.25 using the local error estimator (4.15). Right : adapted mesh obtained when TOL = 0.125 using the local error indicator (4.26).

4.6 A numerical zoom approach

An interest for industrial application, is to refine a specific area of the mesh domain. We present a slightly modification of algorithm 3 having the goal of refining specific areas of the domain. Let Ω be the domain of definition of a PDE. Let $\Omega_1, \Omega_2 \subset \Omega$ such that $\Omega = \Omega_1 \cup \Omega_2$ and $\Omega_1 \cap \Omega_2 = \emptyset$. We aim to build a sequences of meshes, possibly having large aspect ratio, such that the total number of vertices is close to a given number M. Additionally we would like one of the two domains to have more vertices than the other.

We recall some definitions introduced in section 2.4.1. Consider an error estimator $\sum_{K\in\mathcal{T}_h} \eta_K^2$ and a numerical error $||u-u_h||$. Definitions of $\eta_{i,K}^4$, $\mathcal{L}$, $\mathcal{R}$ and σ_P can be found in (2.24), (2.27) and (2.31). Moreover, for each vertex $P \in \mathcal{T}_h$, we defined the local error indicator

$$\eta_P^2 = \sum_{\substack{K\in\mathcal{T}_h \\ P\in K}} \eta_K^2.$$

Given a goal number of vertices M and $\alpha \in (0,1)$, the objective of the adaptive algorithm is to construct a sequences of meshes such that

$$\frac{1}{1+\alpha}M \leq N \leq \frac{1}{1-\alpha}M, \tag{4.27}$$

where N is the number of vertices of the mesh. Let N_1 and N_2 be the number of vertices of the mesh in domain Ω_1 and Ω_2 respectively. Let $w \in (0,1)$, if we have

$$\frac{(1-w)M}{1+\alpha} \leq N_1 \leq \frac{(1-w)M}{1-\alpha} \tag{4.28}$$

and

$$\frac{wM}{1+\alpha} \leq N_2 \leq \frac{wM}{1-\alpha}, \tag{4.29}$$

then (4.27) is satisfied. Consequently the mesh will have approximately N_1 vertices in domain Ω_1 and N_2 in Ω_2. Let $P_1, \ldots, P_{N_1} \in \mathcal{T}_h \cap \Omega_1$ and $P_{N_1+1}, \ldots, P_N \in \mathcal{T}_h \cap \Omega_2$, in order to satisfy (4.28)-(4.29), and consequently (4.27), we require for all $i = 1, \ldots, N_1$, $k = N_1 + 1, \ldots, N$ and $j = 1, \ldots, d$ that

$$\frac{\sigma_{P_i}(1-\alpha)}{(1-w)(d+1)} \frac{1}{M} \sum_{l=1}^{N_1} \eta_{P_l}^2 \leq \sum_{K \in \mathcal{T}_h, P_i \in K} \eta_{j,K}^2 \leq \frac{\sigma_{P_i}(1+\alpha)}{(1-w)(d+1)} \frac{1}{M} \sum_{l=1}^{N_1} \eta_{P_l}^2, \tag{4.30}$$

$$\frac{\sigma_{P_k}(1-\alpha)}{w(d+1)} \frac{1}{M} \sum_{l=N_1+1}^{N} \eta_{P_l}^2 \leq \sum_{K \in \mathcal{T}_h, P_k \in K} \eta_{j,K}^2 \leq \frac{\sigma_{P_k}(1+\alpha)}{w(d+1)} \frac{1}{M} \sum_{l=N_1+1}^{N} \eta_{P_l}^2. \tag{4.31}$$

The algorithm then follows exactly the same strategy as discussed in Section 2.4.1.

Consider problem (4.1) with $\Omega = (0,5) \times (0,1)$ and $p = 3$. Suppose f such that the exact solution is

$$u(\mathbf{x}) = \exp(-400((x_1-0.5)^2+(x_2-0.5)^2)) + \exp(-400((x_1-1.5)^2+(x_2-0.5)^2)) \tag{4.32}$$

and $\mu = 0$. We consider the algorithm introduced here above, where η_K^2 is defined by $\eta_{2,K}$ as in (4.15) and the numerical error is defined by the quasi-norm defined in Proposition 4.2 $||u - u_h||_{(u)}$. We choose a starting mesh $\mathcal{T}_h^1$ of size $h_1 = 0.1$, $h_2 = 0.1$ in direction x_1 and x_2 respectively. We set $\Omega_1 = (0,1) \times (0,1)$ and $\Omega_2 = (1,5) \times (0,1)$, We run 40 iterations of the adaptive algorithm starting from $M = 200$, the number of desired vertices is then doubled and the process is repeat until $M = 3200$ is reached. In Table 4.8 we report for different choices of w, the quasi-norm error e_{QN}, the number of vertices in domain Ω_1 and Ω_2, noted N_1 and N_2 respectively. Moreover we report the quasi-norm error committed in each domain. We noted for $i = 1, 2$

$$e_{\Omega_i} = \int_{\Omega_i} |\nabla(u-u_h)|^2(\mu + |\nabla u| + |\nabla(u-u_h)|)$$

and numerically e_{Ω_1} includes all triangles crossing the boundary between Ω_1 and Ω_2, while e_{Ω_2} includes only triangles in domain Ω_2.

TABLE 4.8 : Quasi-norm error, local errors, number of vertices of domain Ω_1 and Ω_2 for different values of M and w, when solving problem (4.1) with f given such that the exact solution is given by (4.32) with $\mu = 0$.

M	e_{QN}	N_1	N_2	e_{Ω_1}	e_{Ω_2}
		$w = 0.5$			
200	17.91	96	100	10.09	7.61
400	8.23	193	205	4.38	3.85
800	1.44	401	390	0.89	0.56
1600	0.60	808	769	0.20	0.40
3200	0.19	1538	1552	0.093	0.0952
		$w = 0.25$			
200	44.40	137	58	4.62	39.78
400	18.01	303	112	1.01	16.99
800	2.93	576	219	0.45	2.49
1600	0.74	1231	398	0.19	0.55
3200	0.40	2393	788	0.07	0.32
		$w = 0.1$			
200	794.93	179	30	2.77	792.16
400	45.09	349	53	1.11	43.98
800	21.42	713	87	0.70	20.72
1600	5.83	1371	168	0.12	5.71
3200	2.35	2904	325	0.076	2.27

In Figure 4.8 we observe the obtained mesh when $M = 800$ and $w = 0.1$. As we can observe domain Ω_1 is more refined than Ω_2 as desired.

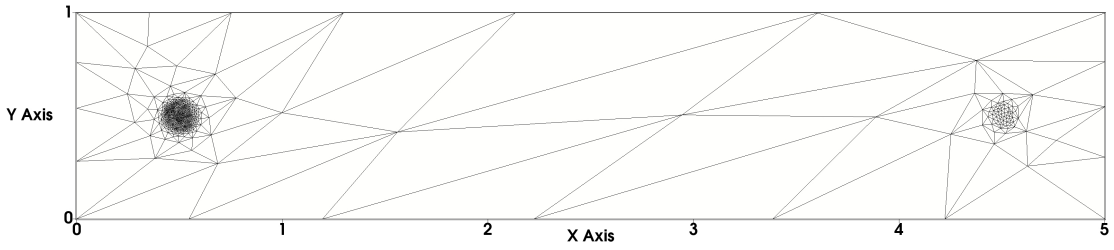

FIGURE 4.8 : Obtained mesh, when $M = 800$ and $w = 0.1$, running algorithm described in Section 4.6 with $\alpha = 10/M$, when solving problem (4.1) with f such that u is given by (4.32) and $\mu = 0$.

5 Application to aluminium electrolysis

We aim now to study an industrial application of adaptive finite elements with large aspect ratio. We focus on numerical simulation of aluminium electrolysis.

5.1 The Hall-Héroult electrolysis process

The goal of this section is to give a brief introduction of the aluminium electrolysis process.

The Hall-Héroult process has the goal to produce aluminium (Al) from alumina (Al_2O_3). The production occurs in huge cells, see Figure 5.1 for an example. In Figure 5.2 a schematic representation of a single cell is shown, it is made of anodes (blue), liquid (electrolyte, red and aluminium, green) and cathodes (purple). Entering the anodes, an electrical current crosses the cell and thus the fluid domain. Electrolyte is liquid due to the high temperature (950 C°) induced by the electrical current. Alumina is injected into the electrolyte bath and, if the temperature is high enough, dissolves into aluminium's ion and oxygen's ion

$$Al_2O_3 \rightarrow 2Al^{3+} + 3O^{2-}.$$

Because anodes are composed by carbon, the following reduction occurs

$$6O^{2-} + 3C \rightarrow 3CO_2 + 12e^-$$

and finally, aluminium is produced

$$2Al^{3+} + 6e^- \rightarrow 2Al.$$

Again, because of high temperature, aluminium is liquid and it separates from electrolyte due to different densities. We have indeed an interface between the two fluids (see Figure 5.2).

Electrical current give rise to an induction magnetic field, which interacts with the

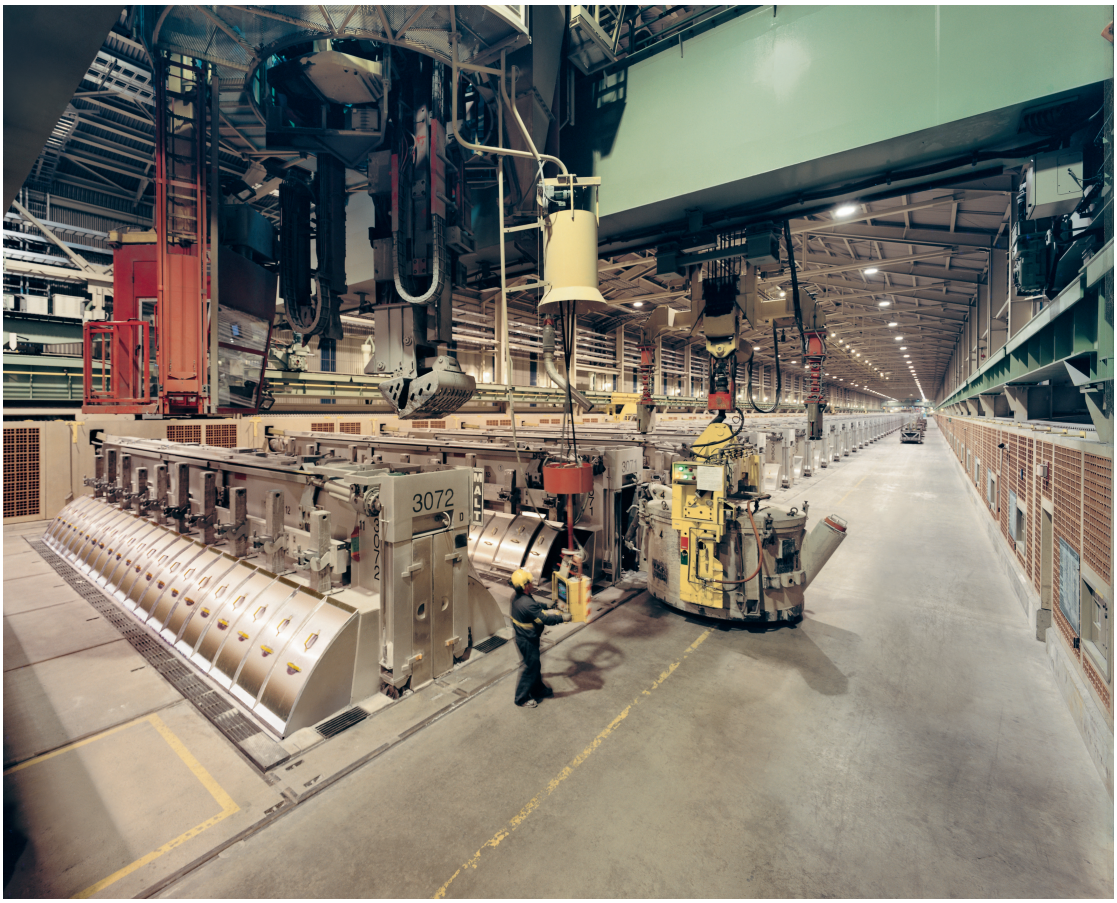

FIGURE 5.1 : View of different aluminium cells. CopyRight : Rio Tinto Aluminium

current density producing a Lorentz force. As explained in [67], the complex geometry of the cells together with a variable current in the fluids, contribute to variations of the force in the whole domain. As a consequence, liquid aluminium and electrolyte are moving, and turbulence occurs.

Three principal possible instabilities need to be considered [67, 66]. First, instabilities due to strong movements of the interface between electrolyte and liquid aluminium. Second, strong or weak concentration of alumina in the bath domain. Last, loss of thermal equilibrium. When the interface moves too much, the risk of shortcut increases. If the concentration of alumina is too elevated, sediments of alumina on the cathode form and the electrical current perturbation increases. On the contrary, if the concentration of alumina decreases considerably, the electrolysis process could stop and several sources of pollution would occur. Finally, if thermal equilibrium disappears, corrosion is a high risk. To avoid all these situations a strong knowledge of the fluids dynamics is essential. Since experimental measure are difficult due to high temperatures, numerical simulations are unavoidable.

Numerical experiments are conducted using Alucell software [70], which implements

algorithms pertaining to the numerical modelling of aluminium electrolysis. Alucell is owned by EPFL and Rio Tinto Aluminium and maintained by YcoorSystems SA (Sierre, Switzerland) and EPFL. The collaboration between Rio Tinto Aluminium, EPFL and YcoorSystems SA has resulted in many PhD thesis. For instance, in [70] Magneto-hydrodynamics equations have been considered ; models of turbulence for the fluid-flow problem have been studied in [67]. In [31, 68] thermal effects are presented, in [41, 40] the aluminium transport and dissolution is studied and in [69] a mixture model to take into account diluted gas in the liquid flow is discussed.

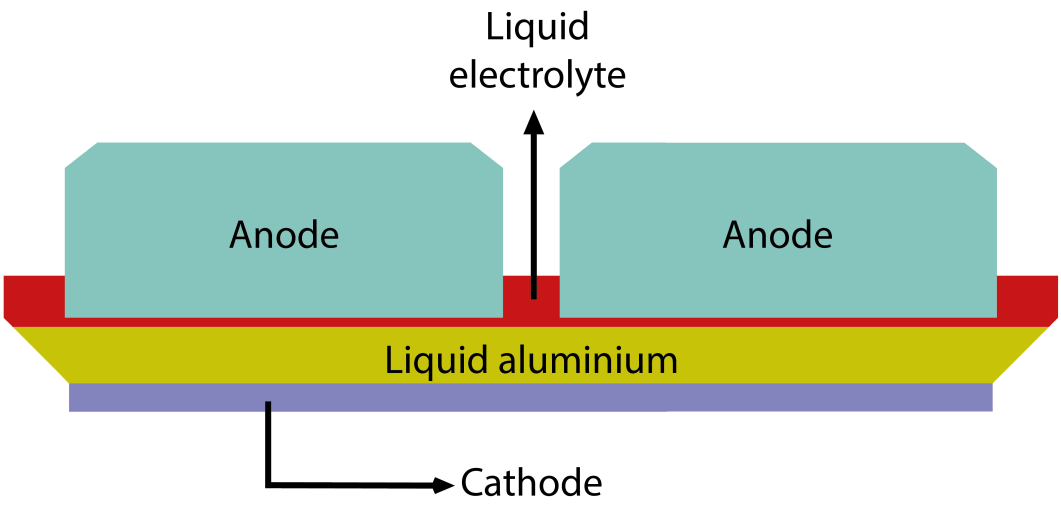

FIGURE 5.2 : Schematic representation of Aluminium Electrolysis' cell

5.2 The fluid-flow problem without gas

This section is dedicated to a brief introduction to the fluid-flow problem related to aluminium electrolysis. For a complete presentation we refer to [67]. Gas is not taken into account in this model.

Let $D \subset \mathbb{R}^3$ be a bounded domain representing an aluminium electrolysis cell, see Figure 5.3. Consider $\Omega \subset D$ as the fluid domain composed by the electrolyte bath Ω_{el} and the liquid aluminium domain Ω_{al}, see Figure 5.2. Let $\Gamma = \Omega_{al} \cap \Omega_{el}$ be the interface between the two fluids. Let $\rho_{al}, \mu_{al}, \rho_{el}, \mu_{el}$ be constants representing the density and the viscosity of the liquid aluminium domain and the electrolyte bath respectively. We define

$$\rho(\mathbf{x}) = \begin{cases} \rho_{al} & \text{if} \quad \mathbf{x} \in \Omega_{al} \\ \rho_{el} & \text{if} \quad \mathbf{x} \in \Omega_{el} \end{cases}$$

The following Navier-Stokes equations are considered. We are looking for velocity $\mathbf{u} : \Omega \to \mathbb{R}^3$, pressure $p : \Omega \to \mathbb{R}$ such that

$$\begin{cases} -\nabla \cdot (\tau(\mathbf{u}, p)) + \rho(\mathbf{u} \cdot \nabla)\mathbf{u} &= \rho\mathbf{g} + \mathbf{j} \wedge \mathbf{B} & \text{in } \Omega, \\ \nabla \cdot \mathbf{u} &= 0 & \text{in } \Omega, \\ \mathbf{u} &= 0 & \text{on } \partial\Omega. \end{cases} \tag{5.1}$$

Here we note $\mathbf{g}$ the gravity and $\mathbf{j}$ and $\mathbf{B}$ the electrical current and the magnetic field obtained by solving equations described in [70]. From now on we consider $\mathbf{f} = \rho\mathbf{g} + \mathbf{j} \wedge \mathbf{B}$ known. Problem (5.1) is completed with the following conditions on the interface between electrolyte and aluminium

$$\begin{cases} [(\tau\mathbf{n}) \cdot \mathbf{t}_i] &= 0 \quad \text{on } \Gamma \quad i = 1, 2, \\ \mathbf{u} \cdot \mathbf{n} &= 0 \quad \text{on } \Gamma. \end{cases} \tag{5.2}$$

We noted $(\mathbf{t}_1, \mathbf{t}_2, \mathbf{n})$ a local orthonormal frame on Γ and $[\cdot]$ the jump over Γ. We define the tensor

$$\tau_{ij}(\mathbf{u}, p) = -p\delta_{ij} + 2\mu\epsilon_{ij}(\mathbf{u}) \quad i, j = 1, 2, 3,$$

where

$$\epsilon_{i,j}(\mathbf{u}) = \frac{1}{2}\left(\frac{\partial u_i}{\partial x_j} + \frac{\partial u_j}{\partial x_i}\right) \quad i, j = 1, 2, 3.$$

The Smagorisnky turbulence model [64], as described in [67], is considered. We set

$$\mu = \mu(\epsilon(\mathbf{u})) := \mu_L + C_T|\epsilon(\mathbf{u})|, \tag{5.3}$$

where $C_T > 0$ is a constant and $\mu_L = \mu_{el}$ in Ω_{el} and $\mu_L = \mu_{al}$ in Ω_{al}.

An equilibrium solution of problem (5.1)-(5.2) has to additionally satisfy,

$$[(\tau\mathbf{n}) \cdot \mathbf{n}] = 0 \text{ on } \Gamma, \tag{5.4}$$

that is to say that the jump of normal forces on the interface Γ is zero. In order to find such an equilibrium solution, a stationary algorithm based on [25], and described for turbulent Smagorinsky model in [67], is considered. Given Γ, we solve (5.1)-(5.2), then update Γ with (5.4). In order to solve (5.1)-(5.2) the classical mini element [30] is used.

Our primary goal is to reduce the computational cost, of solving (5.1)-(5.2) for a given accuracy. The approach consists in using adaptive finite elements with large aspect ratio. In Figure 5.3 a representation of an industrial aluminium cell mesh is shown. In particular, in Figure 5.4 the fluid domain mesh is reported. The domain is approximately long 14 meters, large 3 meters and high 0.38 meters. The top domain is composed by long thin channels and thus the use of large aspect ratio elements could be beneficial for such a geometry.

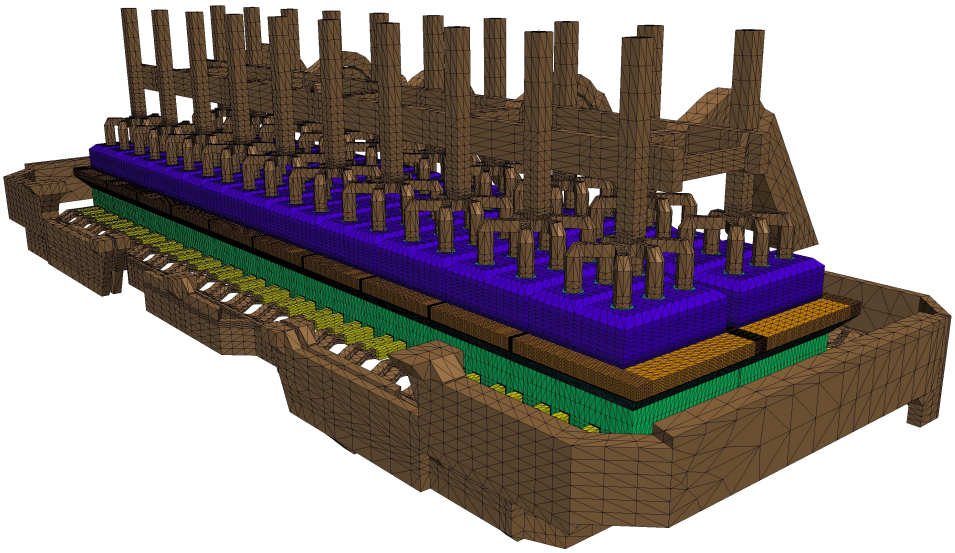

FIGURE 5.3 : Side view of a mesh of the numerical aluminium electrolysis cell.

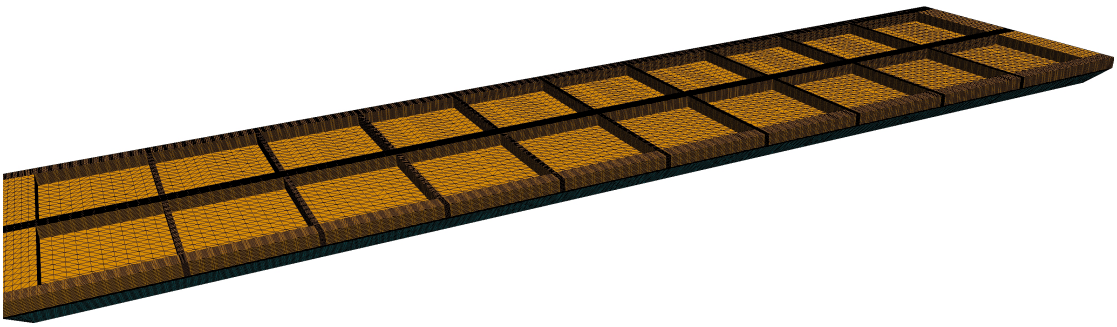

FIGURE 5.4 : View of a mesh of the fluid domain.

5.3 Error indicators and adaptive strategy for the fluid-flow problem

We aim to construct an adapted mesh of the fluid domain in order to reduce the computational time to solve (5.1)-(5.2). We have two possibilities to build an adapted mesh. First we can build adapted meshes solving (5.1)-(5.2). A second possibility is to consider a simplified Stokes problem.

Consider the same definitions and notations introduced above, we introduce Stokes version of problem (5.1)-(5.2). Given an interface Γ, we are looking for $\mathbf{u} : \Omega \to \mathbb{R}^3$ and

$p : \Omega \to \mathbb{R}$ such that

$$\begin{cases} -2\nabla \cdot (\mu\epsilon(\mathbf{u})) + \nabla p &= \mathbf{f} \quad \text{in } \Omega, \\ \nabla \cdot \mathbf{u} &= 0 \quad \text{in } \Omega, \\ \mathbf{u} &= 0 \quad \text{on } \partial\Omega, \end{cases} \tag{5.5}$$

with

$$\begin{cases} [(\epsilon(\mathbf{u})\mathbf{n}) \cdot \mathbf{t}_i] &= 0 \quad \text{on } \Gamma, \\ \mathbf{u} \cdot \mathbf{n} &= 0 \quad \text{on } \Gamma \end{cases} \tag{5.6}$$

and where $\mu(|\epsilon(\mathbf{u})|)$ is given by (5.3). The adaptive algorithms previously introduced in Section 2.4 are considered. The adaptive criteria is based on an heuristic error indicator. A motivation of such a choice is discussed in the following Section.

5.3.1 P-Laplace inspired error indicator

Recall that in problems (5.1)-(5.2) and (5.5)-(5.6) the following turbulent viscosity is considered

$$\mu = \mu_L + C_T|\epsilon(\mathbf{u})|,$$

where $C_T > 0$ is a constant, $\mu_L = \mu_{al}$ in Ω_{al} and $\mu_L = \mu_{el}$ in Ω_{el} with μ_{al} and μ_{el} two constants. Problem (5.5)-(5.6) can be seen as an extension of the p-Laplace model described in Section 4

$$-\nabla \cdot (\mu\nabla u) = f,$$

where the following viscosity was considered

$$\mu = \mu_0 + |\nabla u|^{p-2}$$

for $\mu_0 \geq 0$ and $p \geq 2$. When choosing $p = 3$, viscosity of the nonlinear p-Laplace problem corresponds to the one of both problems (5.1)-(5.2) and (5.5)-(5.6). Our approach consists thus in using error indicator (4.26) as indicator for an adaptive strategy, when solving (5.5)-(5.6) or (5.1)-(5.2). We recall error indicator (4.26)

$$\tilde{\eta}_{2,K} = \left(\frac{1}{2} \sum_{i=1}^{d+1} \left(\frac{|\partial K_i|}{\prod_{j=1}^{d} \lambda_{j,K}} \right)^{1/2} ||[(\mu_0 + |\nabla u_h|^{p-2})\nabla u_h \cdot \mathbf{n}]||_{L^2(\partial K_i)} \right) \omega_{2,K}(u - u_h), \tag{5.7}$$

where $\omega_{2,K}(\cdot)$ is defined by (1.3), $\mathbf{n}$ is the outer normal of boundary element ∂K_i, $i = 1, \ldots, d+1$ and $[\cdot]$ is the jump over ∂K_i ($[\cdot] = 0$ if $\partial K_i \subset \Omega$). In Section 4.5 we presented a comparison between error indicator involving only the edge residuals (4.26) and the full estimator (4.15) for the p-laplace problem. As error indicator for the industrial problem we consider only the edge residual part of the error indicator which

will read

$$\sum_{K\in\mathcal{T}_h}\left(\sum_{l,m=1}^{3}\frac{1}{4}\sum_{i=1}^{4}\left(\frac{|\partial K_i|}{\prod_{j=1}^{3}\lambda_{j,K}}\right)||([\mu\epsilon(\mathbf{u}_h)\mathbf{n}])_l||^2_{L^2(\partial K_i)}\omega^2_{2,K,m}(u_l-(u_h)_l)\right)^{1/2}. \tag{5.8}$$

We focus again on the industrial problem. We present now results using this adaptive criteria when solving first turbulent Stokes problem and successively turbulent Navier-Stokes problem.

5.3.2 Adaptive results solving turbulent Stokes problem

The adaptation process works as follow. Consider Γ given and flat, $\mathbf{f}$ is previously computed on a fixed industrial mesh, named fine reference mesh. We choose a starting triangulation $\mathcal{T}_h^1$ of the fluid domain Ω, the forces are interpolated and problem (5.5)-(5.6) is solved on the new fluid mesh. Note that the starting mesh is chosen particularly coarse (9552 vertices) with the goal to speed up adaptation. We then run an adaptation algorithm, We choose a tolerance, run 20 iterations and then we repeat the process reducing the tolerance. Note that the interface is fixed along the process. The idea is then to use the obtained meshes to update the interface and find a stationary solution (see Section 5.3.4), i.e. a solution satisfying also (5.4). The obtained results will be compared with reference industrial meshes of Table 5.1.

Table 5.1 : Reference meshes

Fine reference mesh	326099 Vertices
Coarse reference meshes	177631 Vertices

In Table 5.2 we report the obtained number of vertices for the chosen tolerance, when building adapted meshes.

Table 5.2 : Adaptation with respect to error indicator (5.8) of the fluid domain, when solving problem (5.5)-(5.6) with Smagorinsky turbulent model.

TOL	Number of Vertices
0.5	24083
0.375	94078
0.25	604149

In Figure 5.5, we report a cut at $x = -6$ of the fine reference mesh and the obtained adapted mesh with TOL= 0.5. In Figure 5.6 we report a cut at $x = -6$ of adapted meshes with TOL= 0.375 and TOL= 0.25. In Figure 5.7 a zoom can be observed. Additionally, in Figure 5.8 the meshes of the interface for the fine reference mesh and the obtained

adapted meshes are reported.

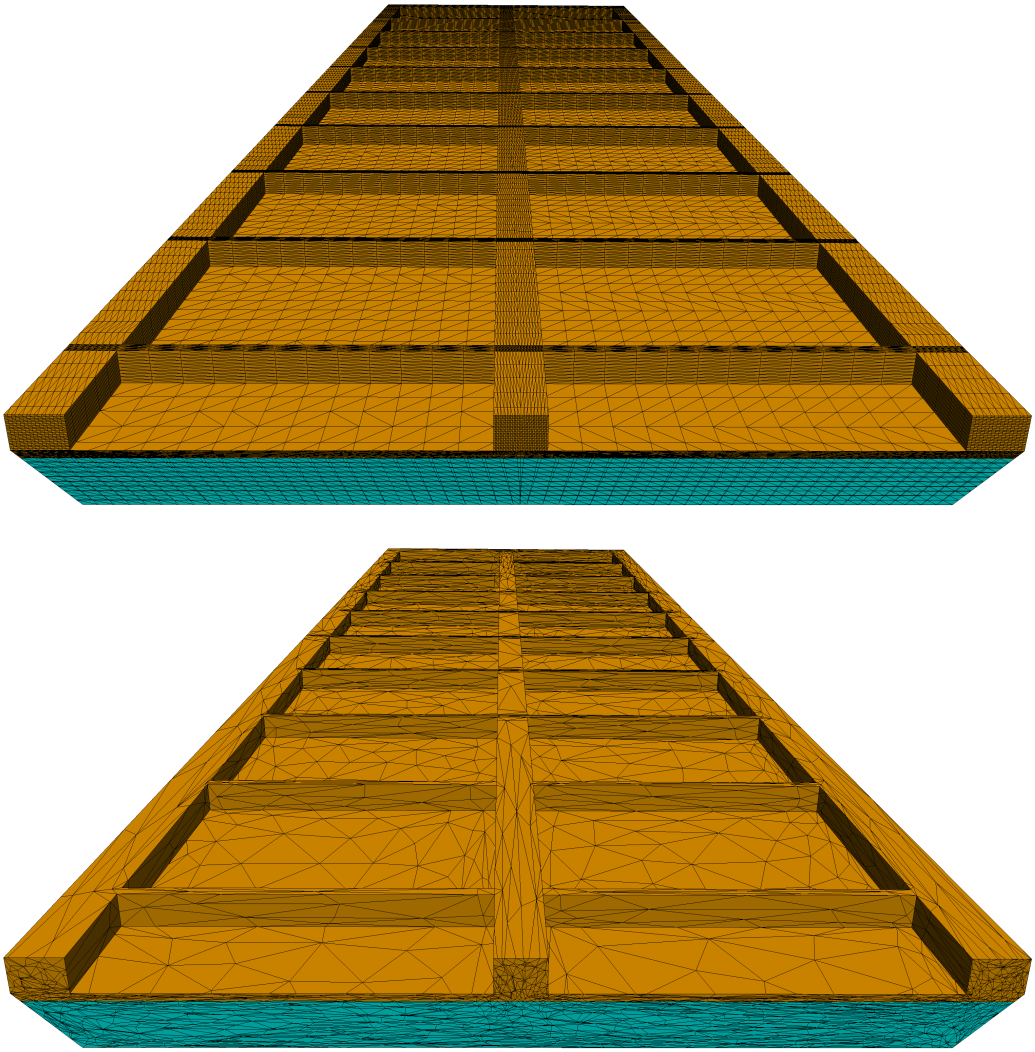

FIGURE 5.5 : Fine reference mesh (Top) and adapted mesh TOL= 0.5 (Bottom) obtained using error indicator (5.8), when solving Stokes problem (5.5)-(5.6).

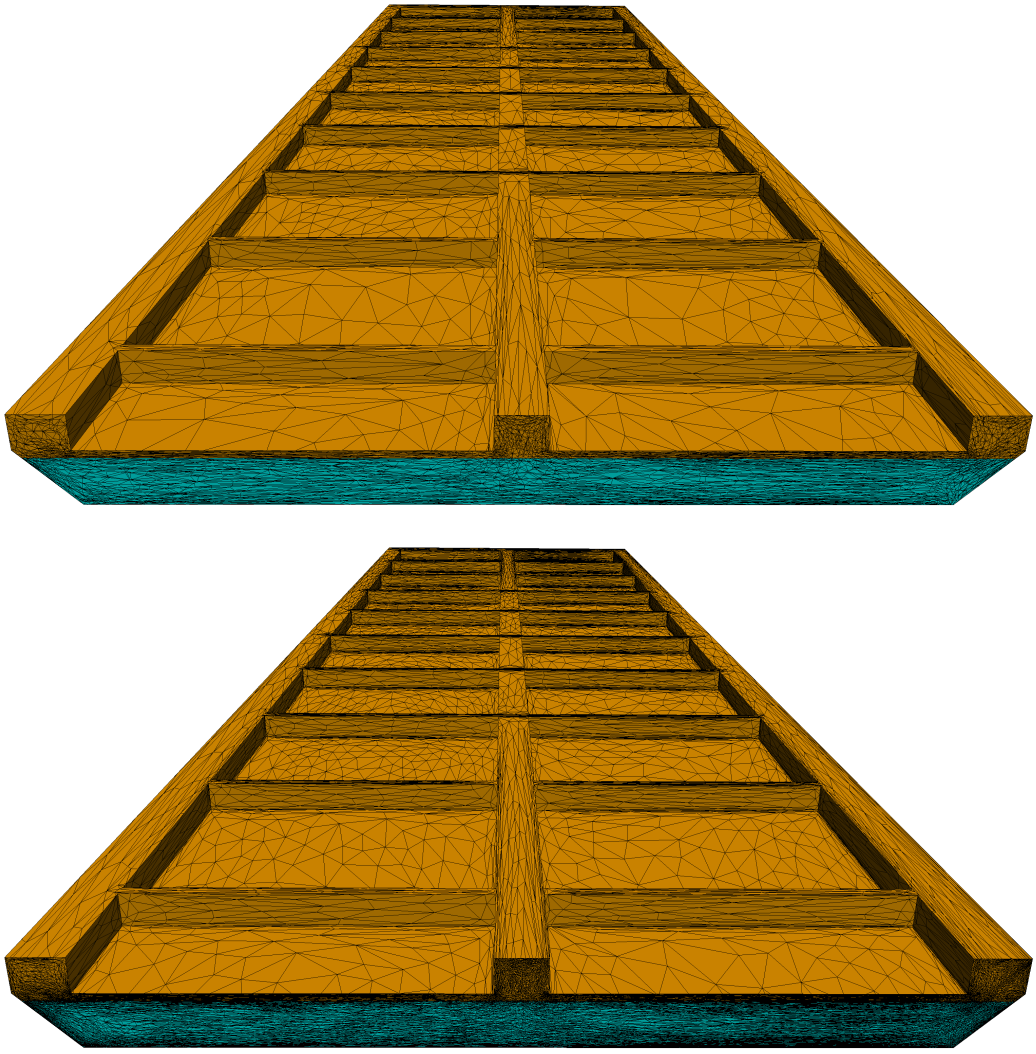

FIGURE 5.6 : Adapted meshes TOL= 0.375 (Top) and TOL= 0.25 (Bottom) obtained using error indicator (5.8), when solving Stokes problem (5.5)-(5.6).

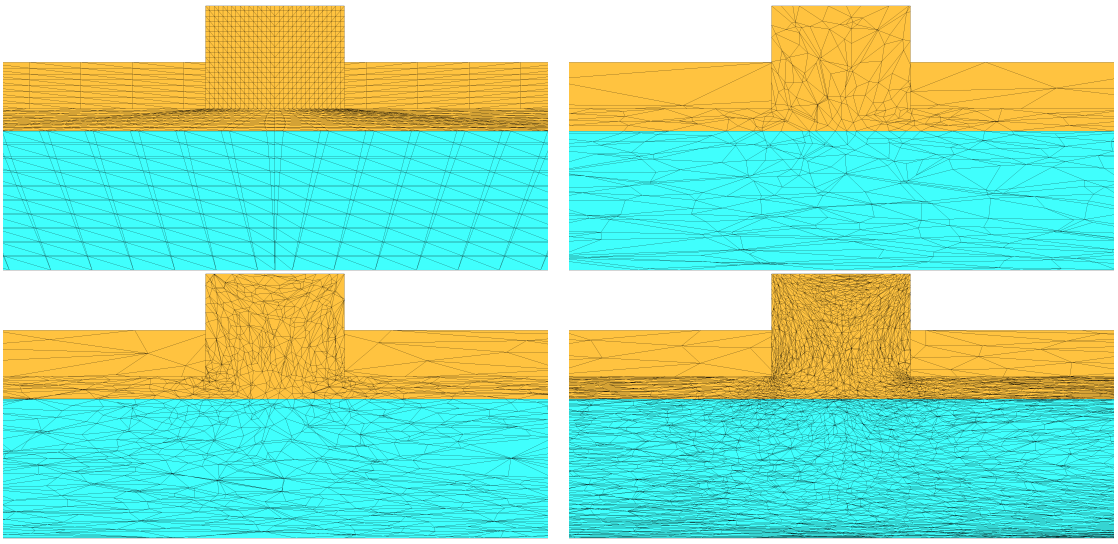

FIGURE 5.7 : Zoom of fine reference mesh (Top left), adapted mesh with TOL= 0.5 (Top right), adapted mesh with TOL= 0.375 (Bottom left) and adapted mesh with TOL= 0.25 (Bottom right) obtained using error indicator (5.8), when solving Stokes problem (5.5)-(5.6).

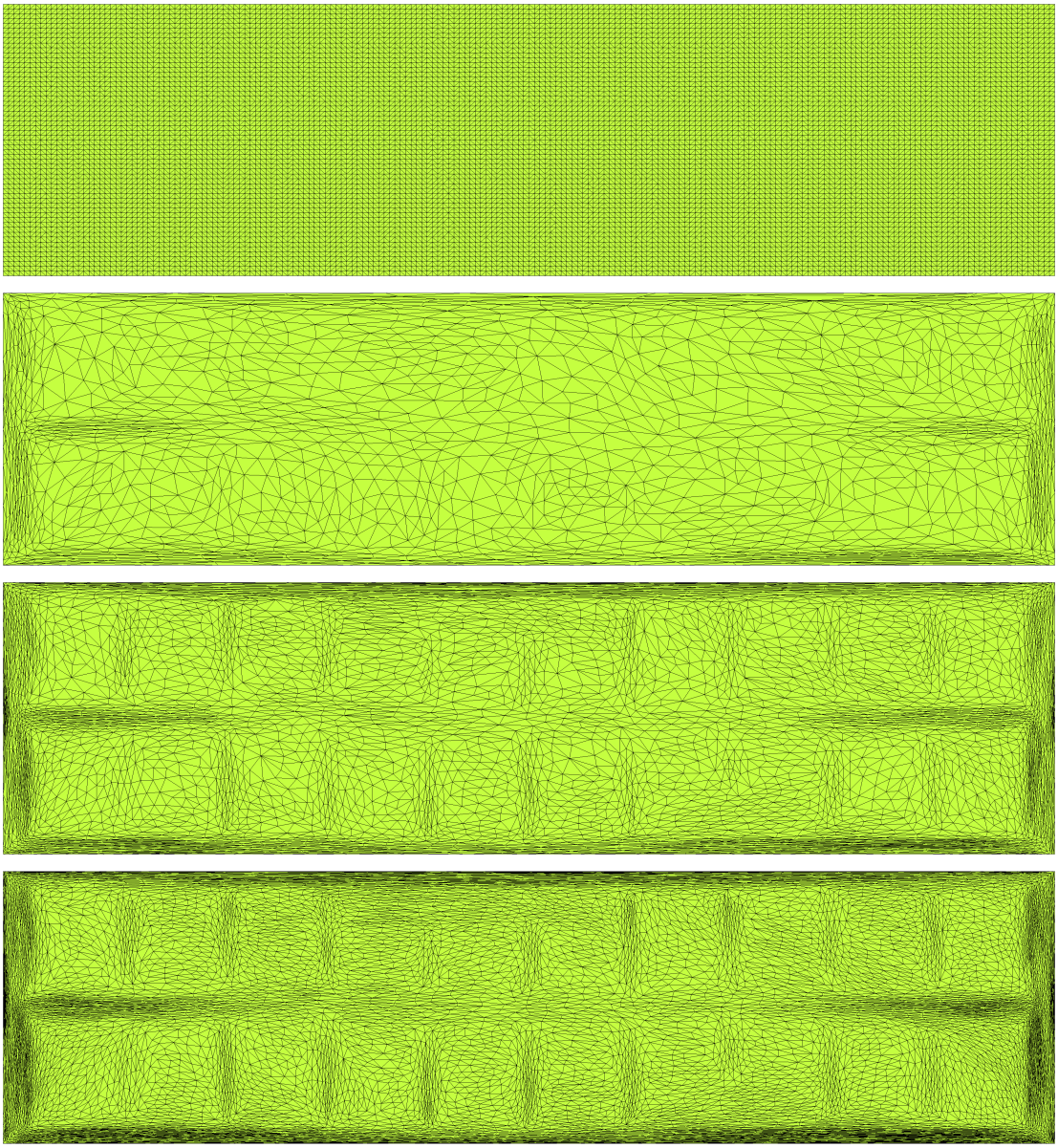

FIGURE 5.8 : From Top to Bottom : interface of fine reference mesh, adapted mesh with TOL= 0.5, adapted mesh with TOL= 0.375 and adapted mesh with TOL= 0.25 obtained using error indicator (5.8), when solving Stokes problem (5.5)-(5.6).

5.3.3 Adaptive results solving turbulent Navier-Stokes problem

The second approach consists in building adapted meshes, using again error indicator (5.8), when solving problem (5.1)-(5.2) for a given flat interface. As before the force $\mathbf{f}$ is previously computed on the fine reference mesh. The same starting mesh $\mathcal{T}_h^1$ of the fluid domain is considered. The forces are interpolated and problem (5.1)-(5.2) is solved. Error indicator (5.8) is then use to run algorithm 2 of Section 2.4.1. In Table 5.3 we report the number of vertices for the corresponding tolerance for each obtained adapted mesh. In Figures 5.9 and 5.10 a cut at $x = -6$ of the fine reference mesh and the obtained

TABLE 5.3 : Adaptation with respect to error indicator (5.8) of the fluid domain, when solving problem (5.1)-(5.2) with Smagorinsky turbulent model. Vertices of obtained meshes.

TOL	Number of Vertices
0.5	24613
0.375	98326
0.25	602684

adapted meshes is reported. In Figure 5.11 the corresponding zoom can be observed. The mesh of the interface of the fine reference mesh and the obtained adapted meshes can be observed in Figure 5.12. As before, the obtained meshes will be used to update the interface and find a stationary solution (see Section 5.3.4).

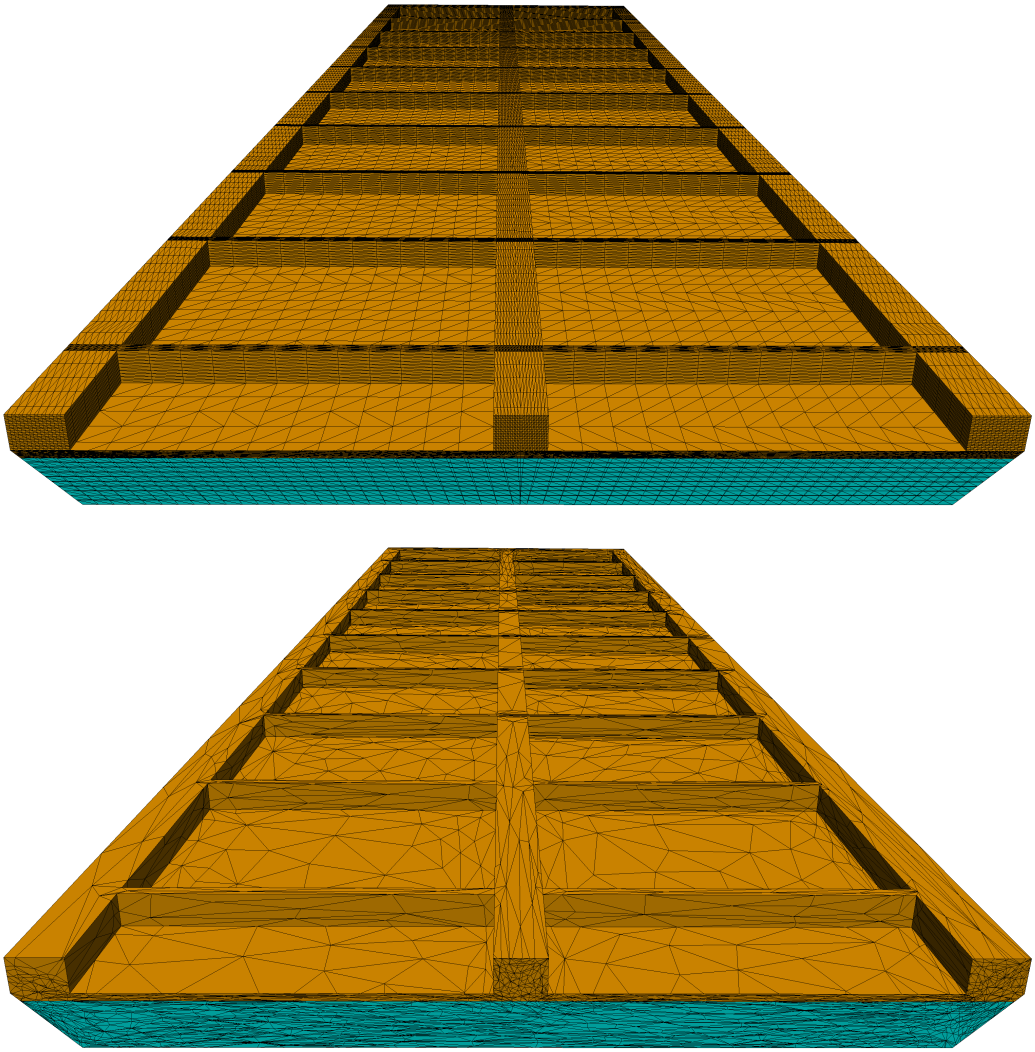

FIGURE 5.9 : Fine reference mesh (Top) and adapted mesh TOL= 0.5 (Bottom) obtained using error indicator (5.8), when solving Navier-Stokes problem (5.1)-(5.2).

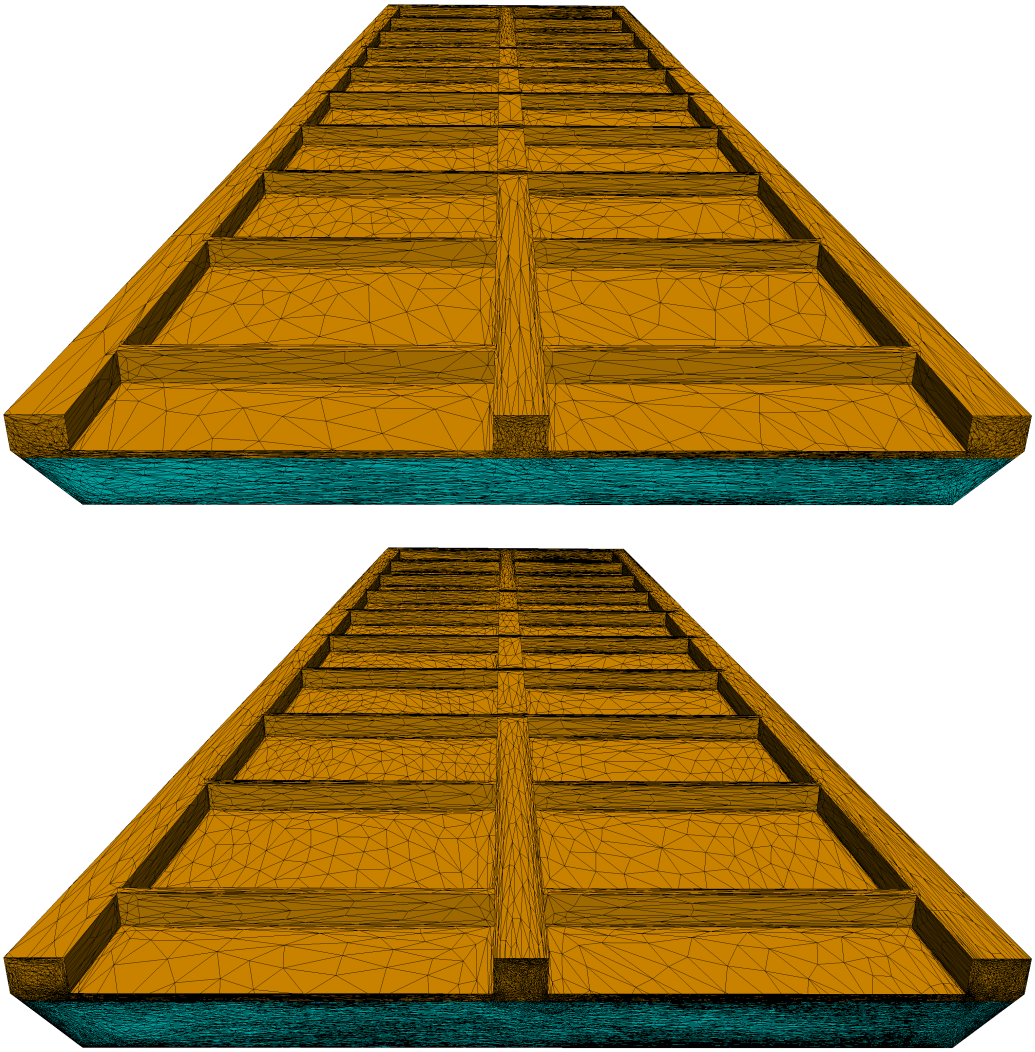

FIGURE 5.10 : Adapted meshes TOL= 0.375 (Top) and TOL= 0.25 (Bottom) obtained using error indicator (5.8), when solving Navier-Stokes problem (5.1)-(5.2).

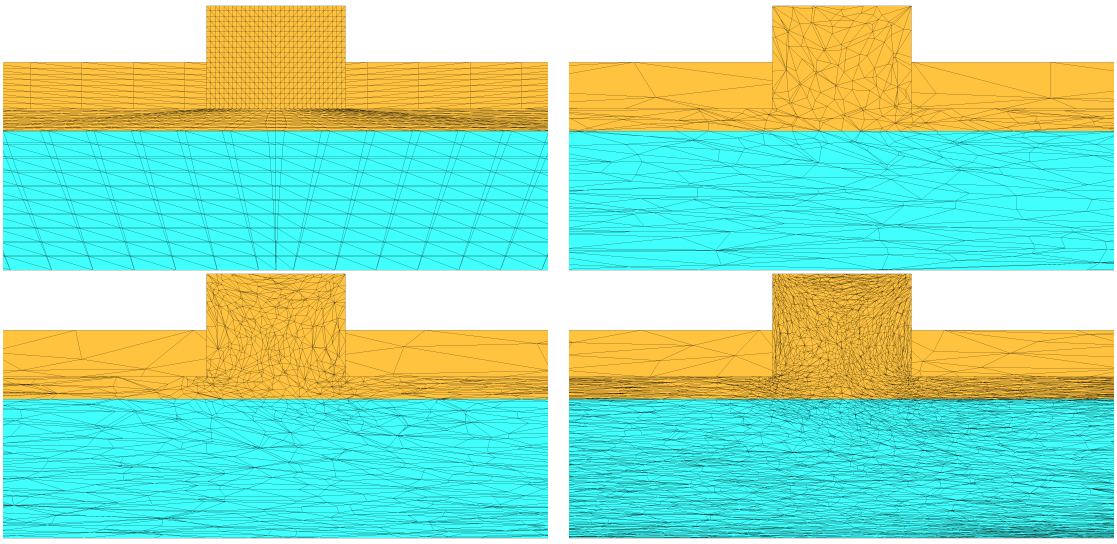

FIGURE 5.11 : Zoom of fine reference mesh (Top left), adapted mesh with TOL= 0.5 (Top right), adapted mesh with TOL= 0.375 (Bottom left) and adapted mesh with TOL= 0.25 (Bottom right) obtained using error indicator (5.8), when solving Navier-Stokes problem (5.1)-(5.2).

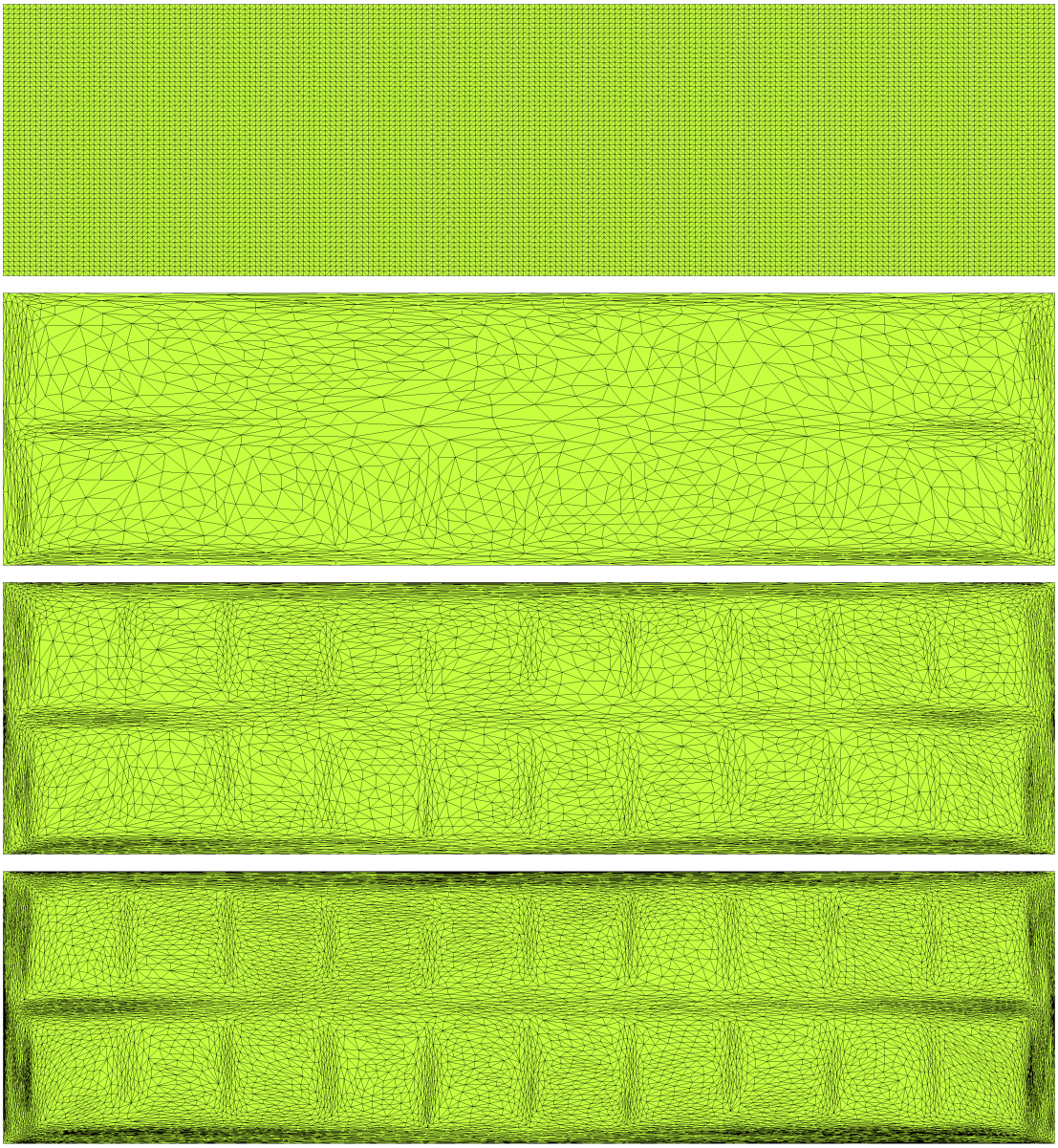

FIGURE 5.12 : From Top to bottom : interface of fine reference mesh, adapted mesh with TOL= 0.5, adapted mesh with TOL= 0.375 and adapted mesh with TOL= 0.25 obtained using error indicator (5.8), when solving Navier-Stokes problem (5.1)-(5.2).

5.3.4 Interface update

We recall that in [67] an update interface algorithm is presented. Problem (5.1)-(5.2) is iteratively solved and at each step the bath-metal interface Γ is updated to satisfy (5.4). The goal of this section is to present results obtained running the interface update algorithm with adapted meshes previously computed. In particular, we start by comparing results obtained with adapted meshes built with strategy of Section 5.3.2 together with results obtained with the industrial reference meshes of Table 5.1. Similarly we compare results obtained with adapted meshes built with strategy presented in Section 5.3.3 together with the reference industrial meshes. Finally we discuss which strategy should be considered.

Interface update for adapted meshes built with strategy 5.3.2

We run 10 iterations of update interface algorithm when solving (5.1)-(5.2). The starting interface is flat. We consider the three adapted meshes of Table 5.2 and the two reference industrial meshes of Table 5.1. In Figure 5.13 we observe the convergence of L^2 discrepancy of the velocity along with the iterations of the update interface algorithm. In Figure 5.14 we report the L^2 relative height discrepancy of the interface along with interface iterations.

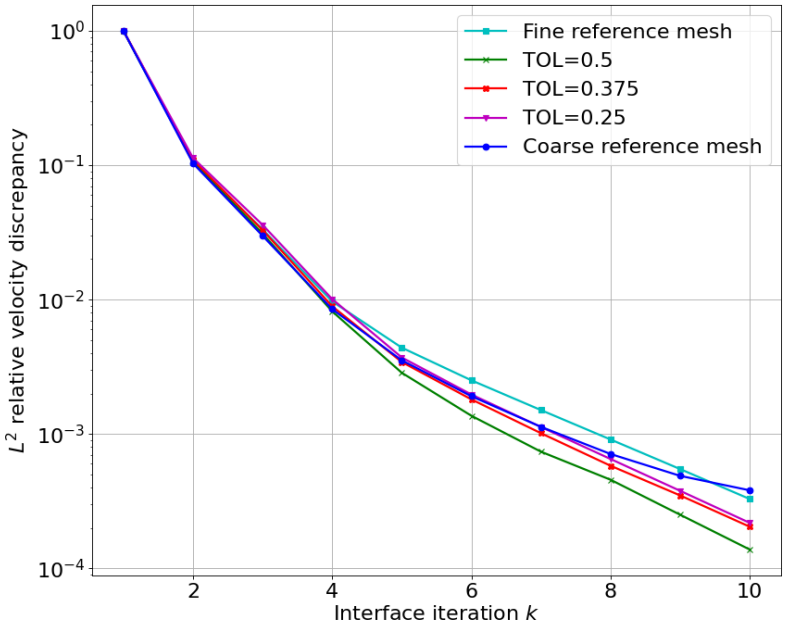

FIGURE 5.13 : L^2 relative discrepancy of velocity along with interface iterations for adapted meshes of Table 5.2 and references meshes of Table 5.1.

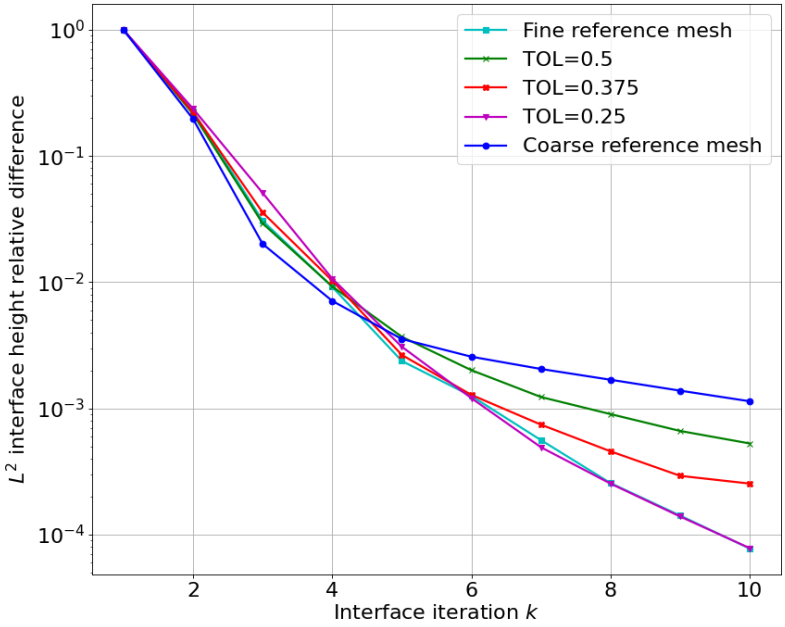

FIGURE 5.14 : L^2 relative discrepancy of interface height along with interface iterations for adapted meshes of Table 5.2 and references meshes of Table 5.1.

In Figure 5.15 we can observe velocity fields obtained with the fine reference mesh and the adapted meshes.

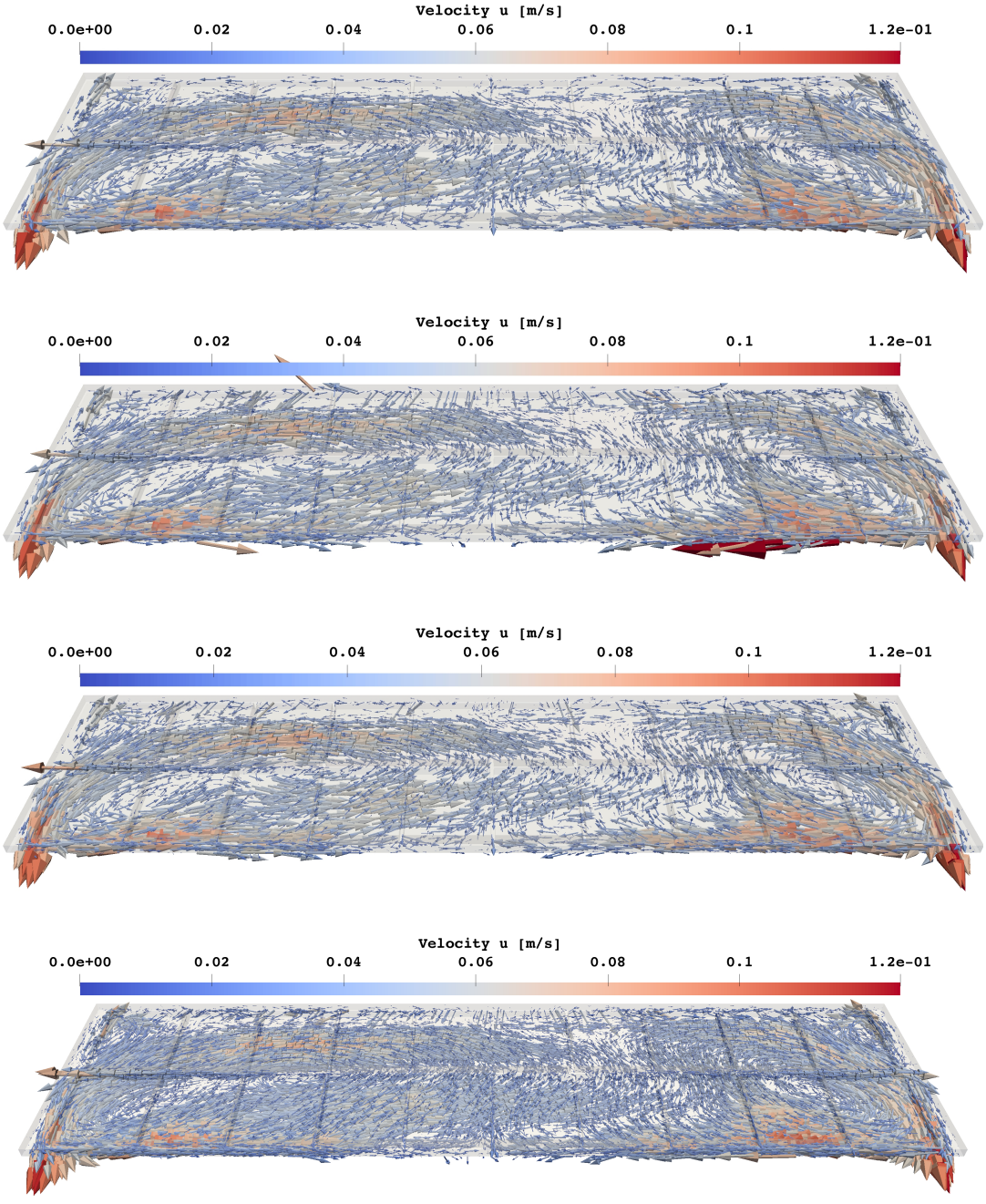

FIGURE 5.15 : Velocity fields obtained at iteration 10, when updating interface solving (5.1)-(5.2). From Top to bottom : fine reference mesh, adapted mesh TOL= 0.5, adapted mesh with TOL= 0.375 and adapted mesh with TOL= 0.25.

In Figure 5.16 we present plot over lines of the velocity magnitude for different regions of the fluid domain and different meshes. As we can observe even with the adapted mesh obtained with tolerance $TOL = 0.5$, similar results to the fine reference mesh are obtained.

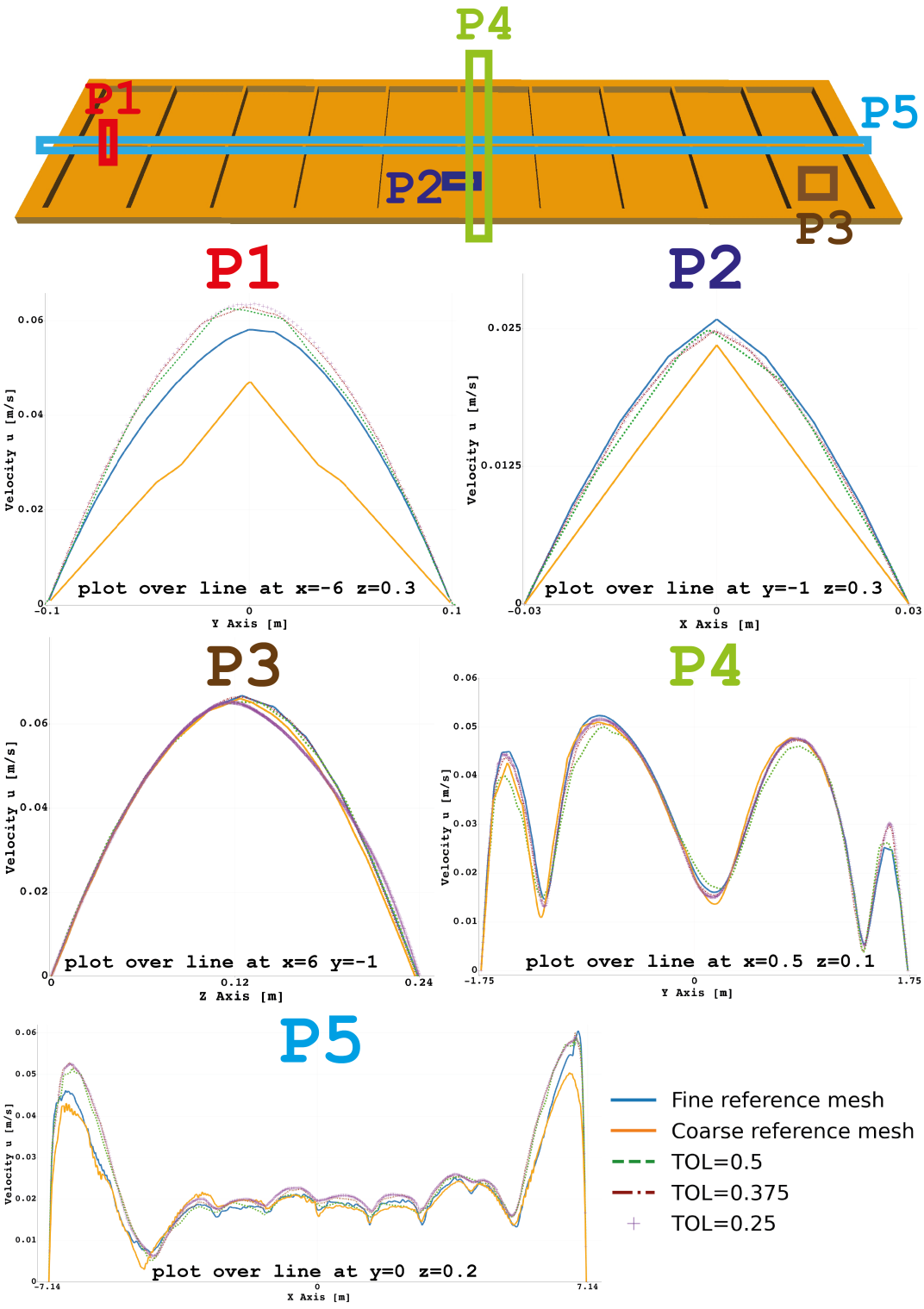

FIGURE 5.16 : Results obtained at iteration 10 of update interface algorithm. Plot over lines of velocity magnitude in different zones. Results obtained with reference meshes of Table 5.1 and 3 adapted meshes of Table 5.2.

In Figure 5.17 we show a cut at $x = -6$ of the fine reference mesh of Table 5.1 and the three adapted meshes of Table 5.2. We observe in particular the new interfaces. Finally in Figure 5.18 the obtained interface height of the fine reference mesh and the adapted meshes is reported. In conclusion the convergence of the update interface algorithm seems to work similarly for the adapted meshes and the reference one. In particular the use of adapted meshes does not perturb the algorithm and gives velocity with similar accuracy of the fine reference mesh. Similar interface deformation is obtained for the adapted and reference meshes. The CPU time required to run 10 iterations of the update interface algorithm with the adapted mesh obtained with TOL=0.5 is 46.56 minutes, while the time required by the fine reference mesh is about 5.21 hours. A considerable CPU time is saved, when using the adapted mesh.

TABLE 5.4 : CPU time to perform 10 iterations of the interface algorithm on (5.1)-(5.2). Fine reference mesh and adapted meshes obtained with strategy 5.3.2

Mesh	CPU time
Fine reference mesh	5.21 hours
Adapted mesh TOL=0.5	0.776 hours
Adapted mesh TOL=0.375	2.88 hours

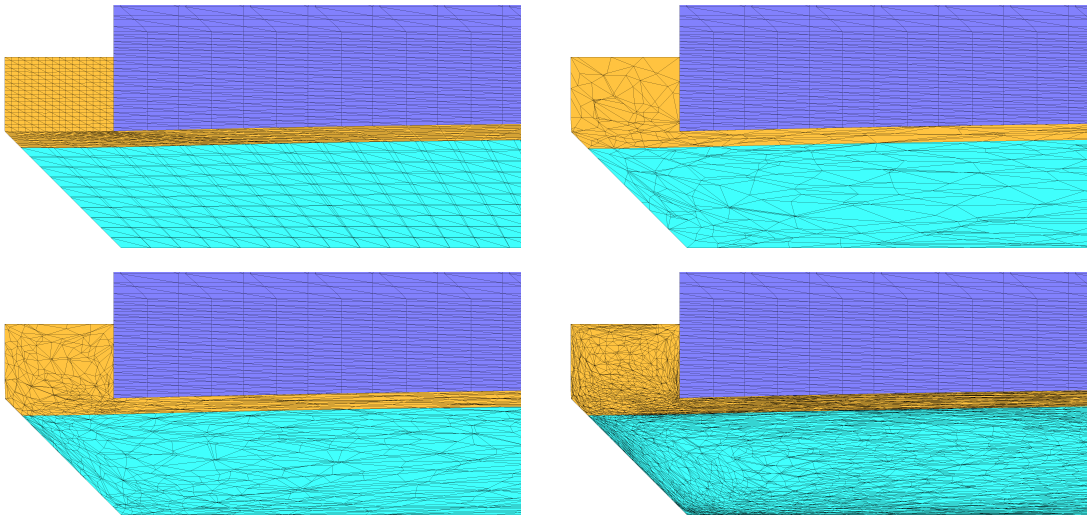

FIGURE 5.17 : Interface deformation at iteration 10. Zoom of fine reference mesh (Top left), adapted mesh with TOL= 0.5 (Top right), adapted mesh with TOL= 0.375 (Bottom left) and adapted mesh with TOL= 0.25 (Bottom right). Adapted meshes of Table 5.2.

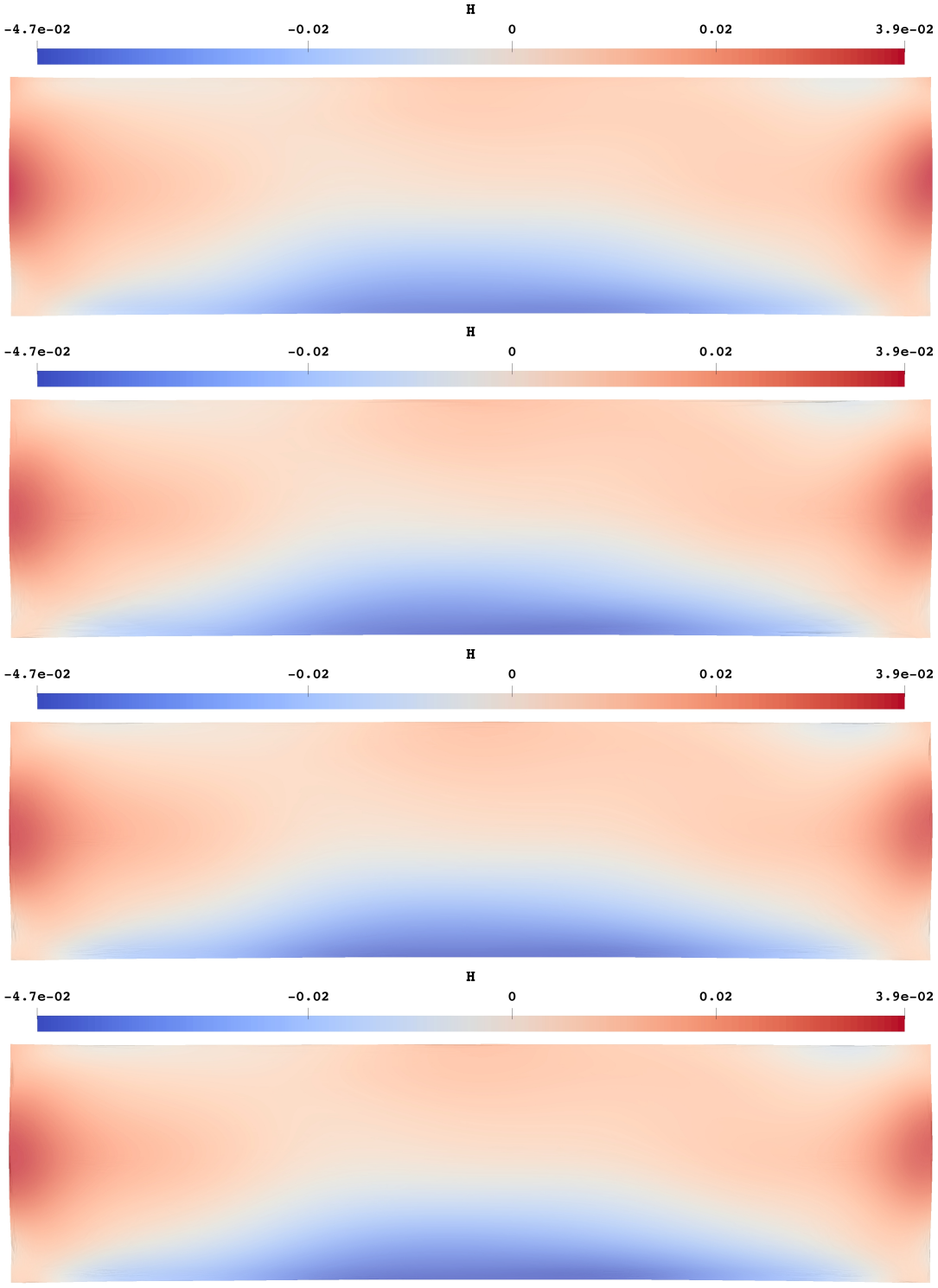

FIGURE 5.18 : Interface height H. From Top to Bottom : interface of fine reference mesh, adapted mesh TOL= 0.5, adapted mesh with TOL= 0.375 and adapted mesh with TOL= 0.25. Adapted meshes of Table 5.2.

Interface update for adapted meshes built with strategy 5.3.3

We run again 10 iterations of the update interface algorithm when solving (5.1)-(5.2). We consider the three adapted meshes of Table 5.3 and two reference industrial meshes (Table 5.1). In Figure 5.19, we observe the L^2 relative discrepancy of the velocity along with the iterations of the update algorithm, while in Figure 5.20 we observe the L^2 relative discrepancy of the interface height along with interface iterations. Globally, there is no relevant difference with the previous strategy.

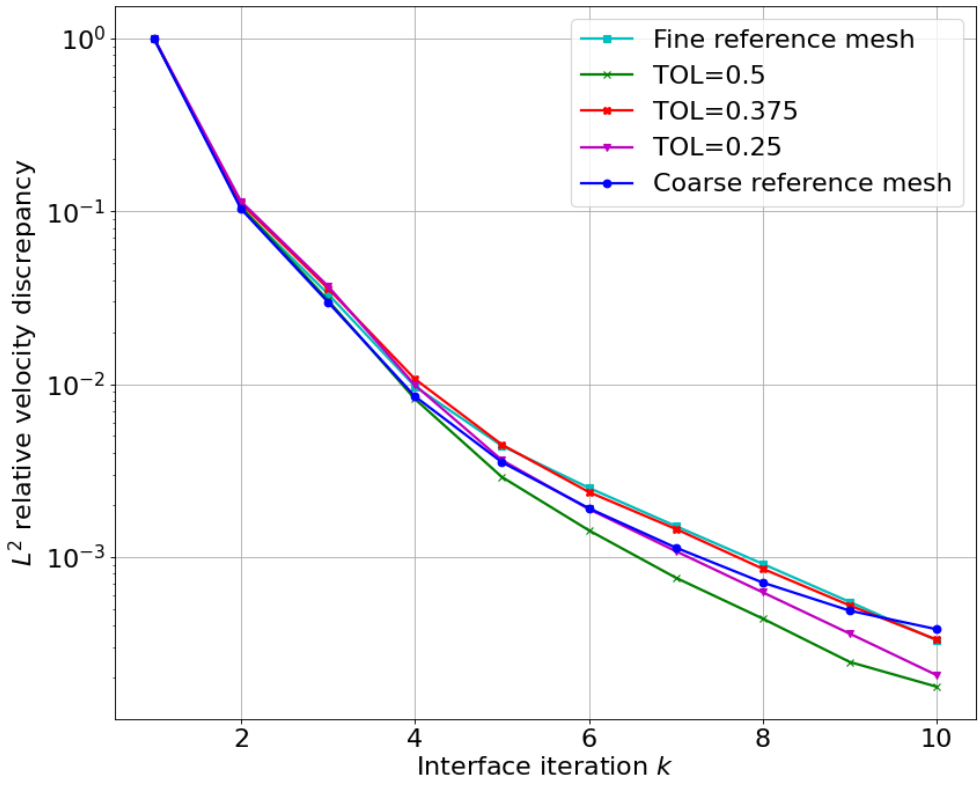

FIGURE 5.19 : L^2 relative discrepancy of velocity along with interface iterations for adapted meshes of Table 5.3 and references meshes of Table 5.1.

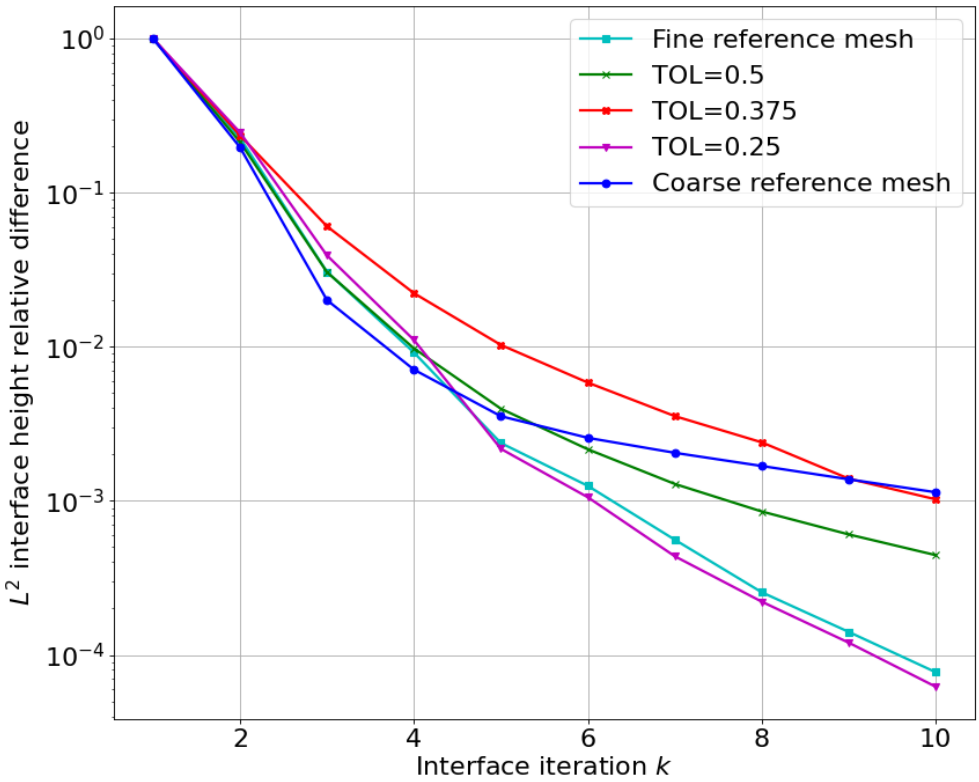

FIGURE 5.20 : L^2 relative discrepancy of interface height along with interface iterations for adapted meshes of Table 5.3 and references meshes of Table 5.1.

In Figure 5.21 we can observe velocity fields obtained with the fine reference mesh and the adapted meshes.

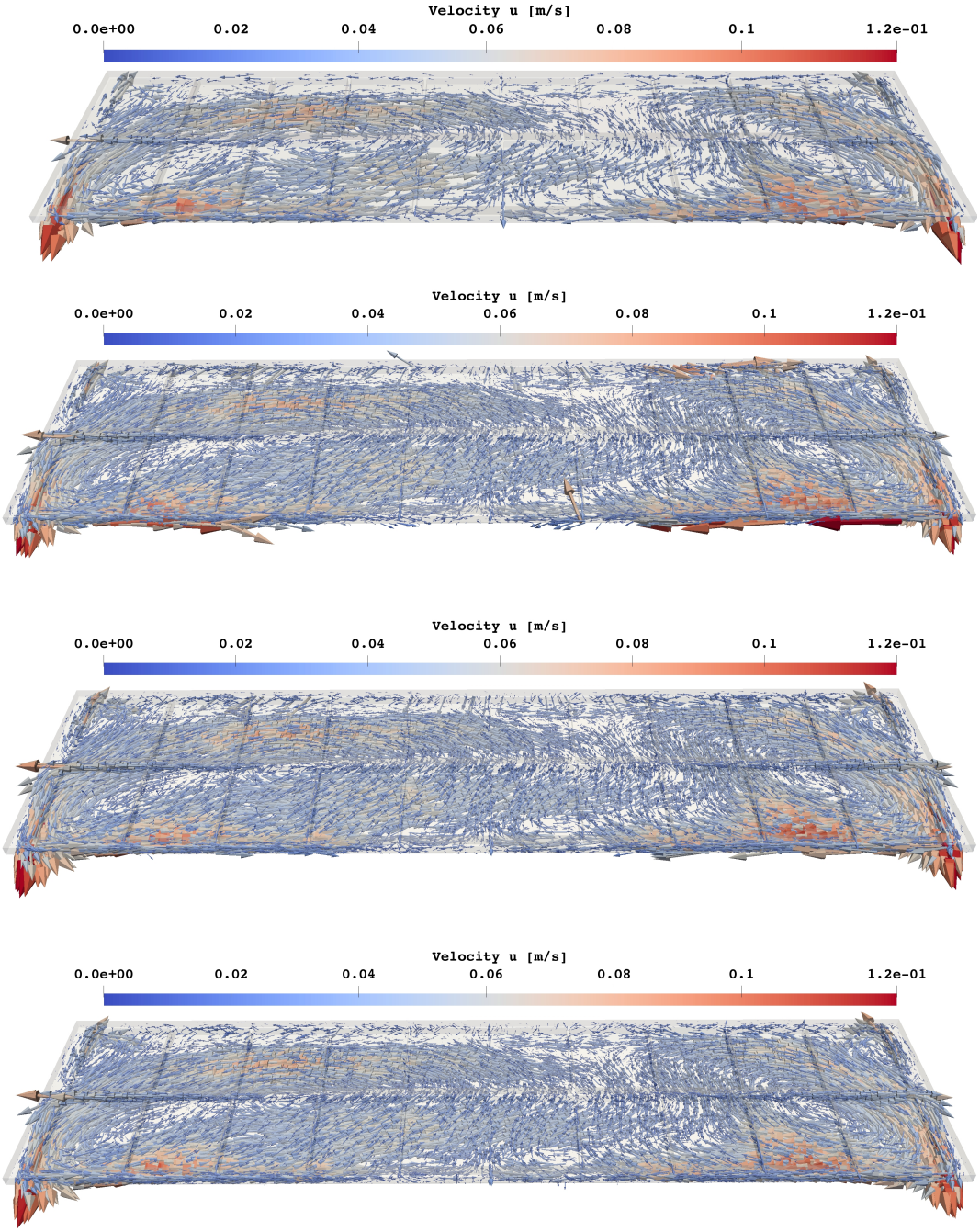

FIGURE 5.21 : Velocity fields obtained at iteration 10, when updating interface solving (5.1)-(5.2). From Top to Bottom : fine reference mesh, adapted mesh TOL= 0.5, adapted mesh with TOL= 0.375 and adapted mesh with TOL= 0.25.

In Figure 5.22 we show plot over lines of the velocity magnitude for different regions of the fluid domain and different meshes. Again we observe that with the adapted mesh obtained with tolerance $TOL = 0.5$, similar results as the one obtained with the fine reference mesh are obtained.

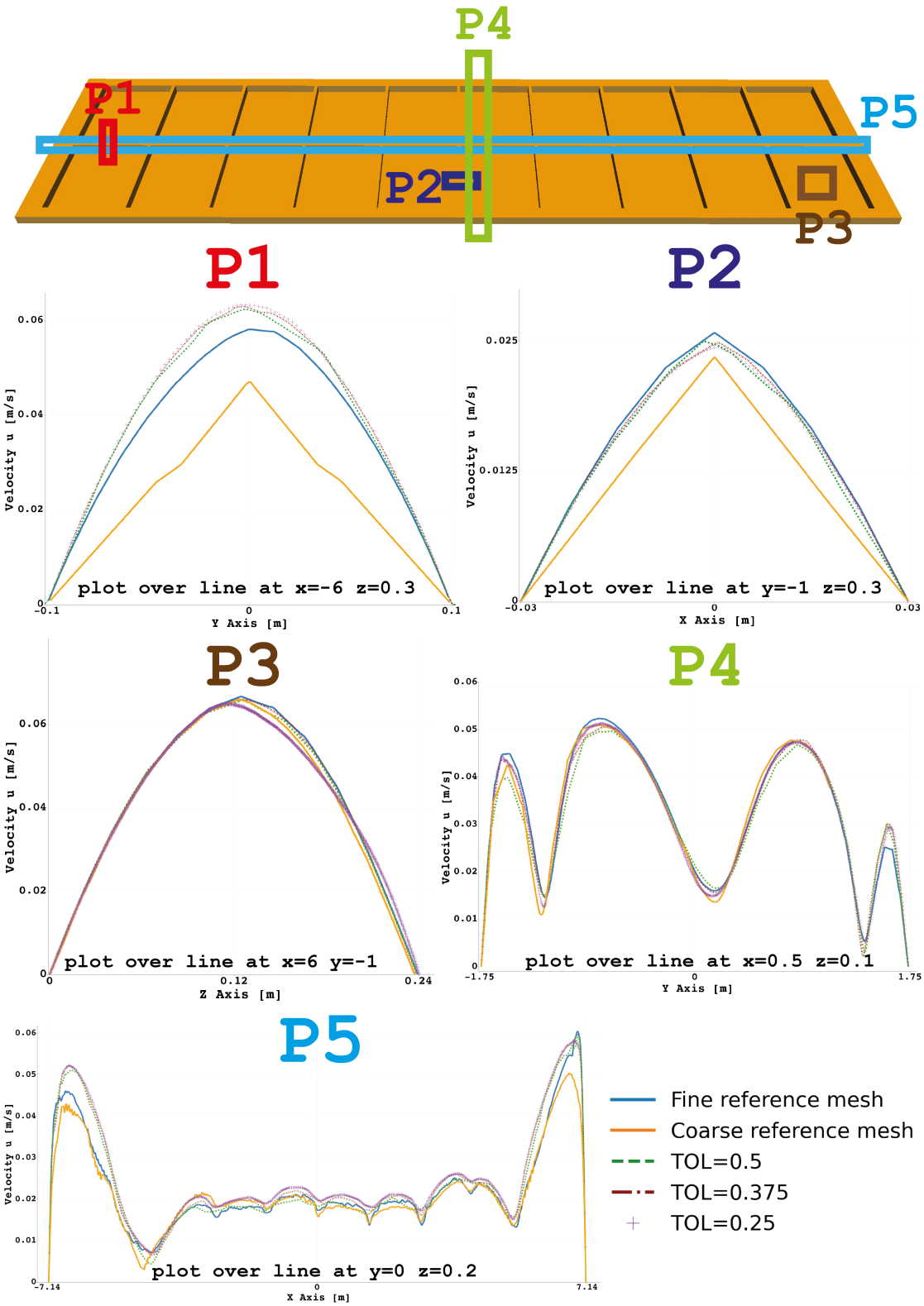

FIGURE 5.22 : Results obtained at iteration 10 of update interface algorithm. Plot over lines of velocity magnitude in different zones. Results obtained with reference meshes of Table 5.1 and 3 adapted meshes of Table 5.3.

In Figure 5.23 a cut at $x = -6$ of the fine reference mesh of Table 5.1 and the three adapted meshes of Table 5.3 can be observed. The new interface can be seen. Finally in Figure 5.24 the interface height obtained of the fine reference mesh and the adapted meshes is reported. The use of adapted meshes give similar results as the fine reference mesh, but reducing the CPU time of the update interface algorithm as can be observed in Table 5.5. To conclude both strategies give similar results and similar computational times, both reducing the computational time with respect to the fine reference mesh.

TABLE 5.5 : CPU time to perform 10 iterations of the interface algorithm on (5.1)-(5.2). Fine reference mesh and adapted meshes obtained with strategy 5.3.3

Mesh	CPU time
Fine reference mesh	5.21 hours
Adapted mesh TOL=0.5	0.799hours
Adapted mesh TOL=0.375	2.92 hours

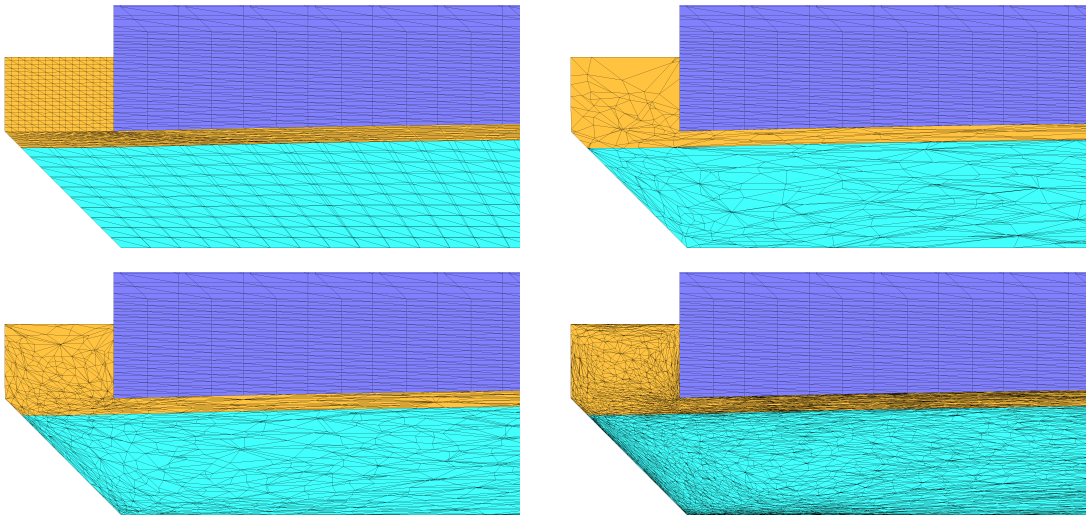

FIGURE 5.23 : Interface deformation at iteration 10. Zoom of fine reference mesh (Top left), adapted mesh with TOL= 0.5 (Top right), adapted mesh with TOL= 0.375 (Bottom left) and adapted mesh with TOL= 0.25 (Bottom right). Adapted meshes of Table 5.3.

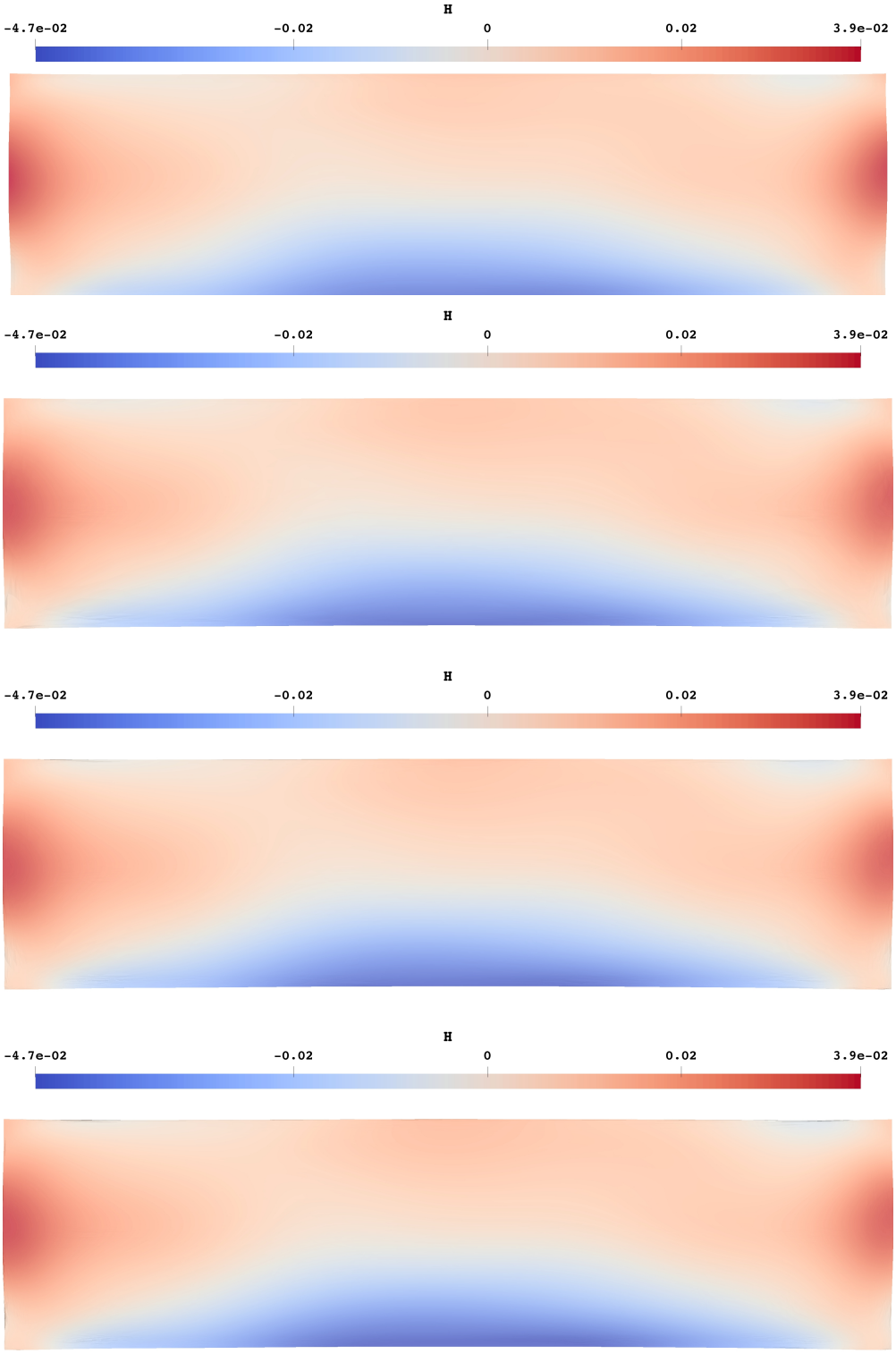

FIGURE 5.24 : Interface height H. From Top to Bottom : interface of fine reference mesh, adapted mesh TOL= 0.5, adapted mesh with TOL= 0.375 and adapted mesh with TOL= 0.25. Adapted mesh of Table 5.3.

In [69] a model to take into account diluted gas in numerical magneto-hydrodynamics simulations is presented. The goal is to evaluate how the liquid flow is modified by the density composed of a mixture of gas and liquid. The objective of our work is to apply an adaptation strategy to reduce the computational cost of such a computation. We briefly introduce equations considered. For an extensive analysis and description we refer to [69].

5.4 The gas model

The goal of this section is to give an insight in the fluid-flow problem coupled with a mixed model to take into account diluted gas. Suppose D, Ω, Ω_{el}, Ω_{al} and Γ are given and defined as in Section 5.2. Moreover we have $\Gamma_{out} \subset \partial\Omega_{el}$ the outflow boundary of electrolyte domain.

We are looking for $\mathbf{u} : \Omega \to \mathbb{R}^3$, $p : \Omega \to \mathbb{R}$, $\mathbf{u}_g : \Omega_{el} \to \mathbb{R}^3$ and $\alpha_g : \Omega_{el} \to \mathbb{R}$ such that

$$\begin{aligned}
\nabla \cdot (\rho \mathbf{u} \otimes \mathbf{u}) - \nabla \cdot (\tau(\mathbf{u}, p)) &= \rho \mathbf{g} + \mathbf{j} \wedge \mathbf{B} && \text{in } \Omega && (5.9)\\
\nabla \cdot (\rho \mathbf{u}) &= 0 && \text{in } \Omega && (5.10)\\
\nabla \cdot (\alpha_g \rho_g \mathbf{u}_g \otimes \mathbf{u}_g) + D\alpha_g \frac{\rho}{\rho_l} \mathbf{u}_g - \nabla \cdot (\tau_g(\mathbf{u}_g, p)) &= \mathbf{F}_g && \text{in } \Omega_{el} && (5.11)\\
\frac{\partial \alpha_g}{\partial t} + \nabla \cdot (\alpha_g \mathbf{u}_g - K \nabla \alpha_g) &= \dot{\alpha}_{source} && \text{in } \Omega_{el} && (5.12)
\end{aligned}$$

with the following buondary conditions

$$\begin{aligned}
\mathbf{u} &= 0 && \text{on } \partial\Omega, && (5.13)\\
\mathbf{u} \cdot \mathbf{n} &= 0 && \text{on } \Gamma, && (5.14)\\
[(\tau \mathbf{n}) \cdot \mathbf{t}_i] &= 0 && \text{on } \Gamma,\ i = 1, 2 && (5.15)\\
\mathbf{u}_g \cdot \mathbf{n} &= 0 && \text{on } \partial\Omega_{el} \backslash \Gamma_{out}, && (5.16)\\
(\tau_g \mathbf{n}) \cdot \mathbf{t}_i &= 0 && \text{on } \partial\Omega_{el},\ i = 1, 2 && (5.17)\\
(\tau_g \mathbf{n}) \cdot \mathbf{n} &= \alpha_g p_0 && \text{on } \Gamma_{out}, && (5.18)\\
K \nabla \alpha_g \cdot \mathbf{n} &= 0 && \text{on } \partial\Omega_{el}. && (5.19)
\end{aligned}$$

Here we denoted

$$\mathbf{F}_g = -p \nabla \alpha_g + \alpha_g \rho_g \mathbf{g} + D\alpha_g \frac{\rho}{\rho_l} \mathbf{u}$$

and

$$\rho(\mathbf{x}) = \begin{cases} \rho_{al} & \text{if} \quad \mathbf{x} \in \Omega_{al}, \\ \alpha_g \rho_g + (1 - \alpha_g) \rho_{el} & \text{if} \quad \mathbf{x} \in \Omega_{el}. \end{cases}$$

The following constants are known ρ_{al}, ρ_{el}, μ_{al}, ρ_g and μ_g, so as D the drag force (see Section 1.6 of [69]). As for section 5.2, $\mathbf{j}$ is the density of current and $\mathbf{B}$ the magnetic

field, which we suppose as known. Moreover we define the tensors

$$\tau_{ij}(\mathbf{u},p) = -p\delta_{ij} - \frac{2}{3}\mu\nabla\cdot(\mathbf{u})\delta_{ij} + 2\mu\epsilon_{ij}(\mathbf{u}) \quad i,j=1,2,3,$$

$$(\tau_g)_{ij}(\mathbf{u}_g,p) = -p\alpha_g\delta_{ij} - \frac{2}{3}\mu_g\nabla\cdot(\mathbf{u}_g)\delta_{ij} + 2\mu_g\epsilon_{ij}(\mathbf{u}_g) \quad i,j=1,2,3,$$

where ϵ is the symmetric tensor. The diffusion coefficient K is given by

$$K = K_L + K_T|\epsilon(u_g)|$$

with K_L and K_T known constants. As for previous section Smagorinsky turbulent model is considered

$$\mu(\mathbf{x}) = \mu_L + C_T|\epsilon(\mathbf{u})|$$

with $\mu_L = \mu_{al}$ if $\mathbf{x} \in \Omega_{al}$ and $\mu_L = \mu_{el}$ if $\mathbf{x} \in \Omega_{el}$. Finally p_0 is a given constant and $\dot{\alpha}_{source}$ is the volumetric internal source term.

In [69] an iterative algorithm to find solution of (5.9)-(5.12) with (5.13)-(5.19) is presented. The goal of the algorithm is to find the liquid velocity $\mathbf{u}$, the pressure p, the gas velocity $\mathbf{u}_g$ and the volumetric fraction of gas α_g satisfying (5.9)-(5.12) with (5.13)-(5.19) and also to modify the interface Γ in order to have $[(\tau\mathbf{n})\cdot\mathbf{n}] = 0$.

We present an adaptation strategy to build adapted meshes when solving (5.9)-(5.12) with (5.13)-(5.19).

5.4.1 P-Laplace error indicator solving the Gas problem

The approach consists in solving (5.9)-(5.12) with (5.13)-(5.19) for a given flat interface. The force $\mathbf{f} = \rho\mathbf{g} + \mathbf{j}\wedge\mathbf{B}$ is previously computed on the fine reference mesh (Table 5.1) and interpolated when solving the problem on adapted meshes. Starting from a mesh $\mathcal{T}_h^1$ three iterations of problem (5.9)-(5.19) are computed. Using the obtained mixture liquid velocity $\mathbf{u}$ and error indicator (5.8) the mesh is adapted with algorithm 1. Note that there is a clear dependence between solutions $\mathbf{u}$, $\mathbf{u}_g$ and α_g, thus to observe the influence of gas on $\mathbf{u}$ we choose to run three iterations before adapting the mesh. The obtained mesh is then used to repeat the process 10 times. The Tolerance is reduced and everything repeated until reaching the desired goal tolerance. Note that we are applying the continuation reduction on the parameter TOL on the spirit of algorithm 2. In Table 5.6, for each tolerance, we report the obtained number of vertices at the last iteration.

TABLE 5.6 : Adaptation with respect to error indicator (5.8) of the fluid domain, when solving problem (5.9)-(5.19) with Smagorinsky turbulent model.

TOL	Number of Vertices
0.5	67500
0.4125	110044
0.375	229699

In Figure 5.25 we report a cut at $x = -6$ of the fine reference mesh and the obtained mesh with TOL= 0.5. Similarly in Figure 5.26 we report a cut at $x = -6$ of the obtained adapted meshes with TOL= 0.4125 and TOL= 0.375. In Figure 5.27 a zoom is reported.

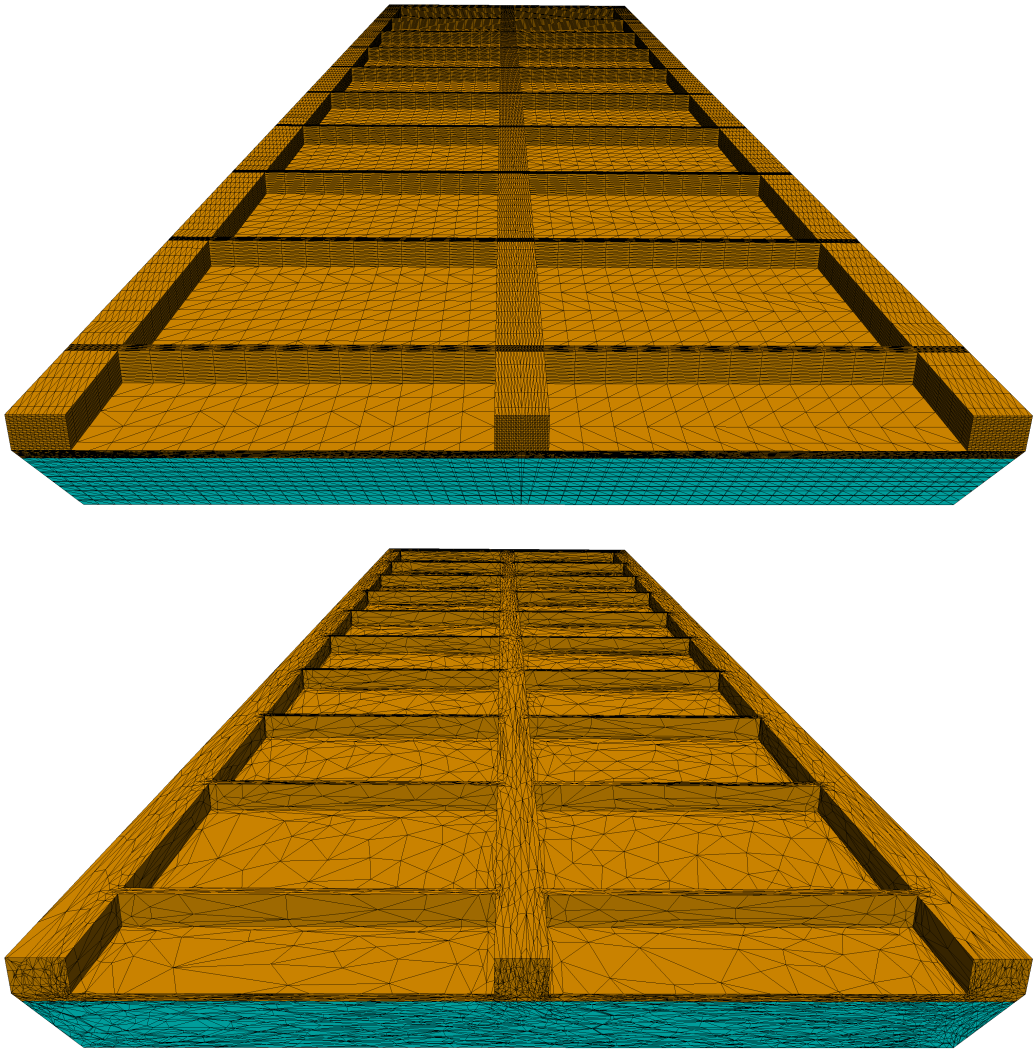

FIGURE 5.25 : Fine reference mesh (Top) and adapted mesh TOL= 0.5 (Bottom) obtained using error indicator (5.8), when solving problem (5.9)-(5.19).

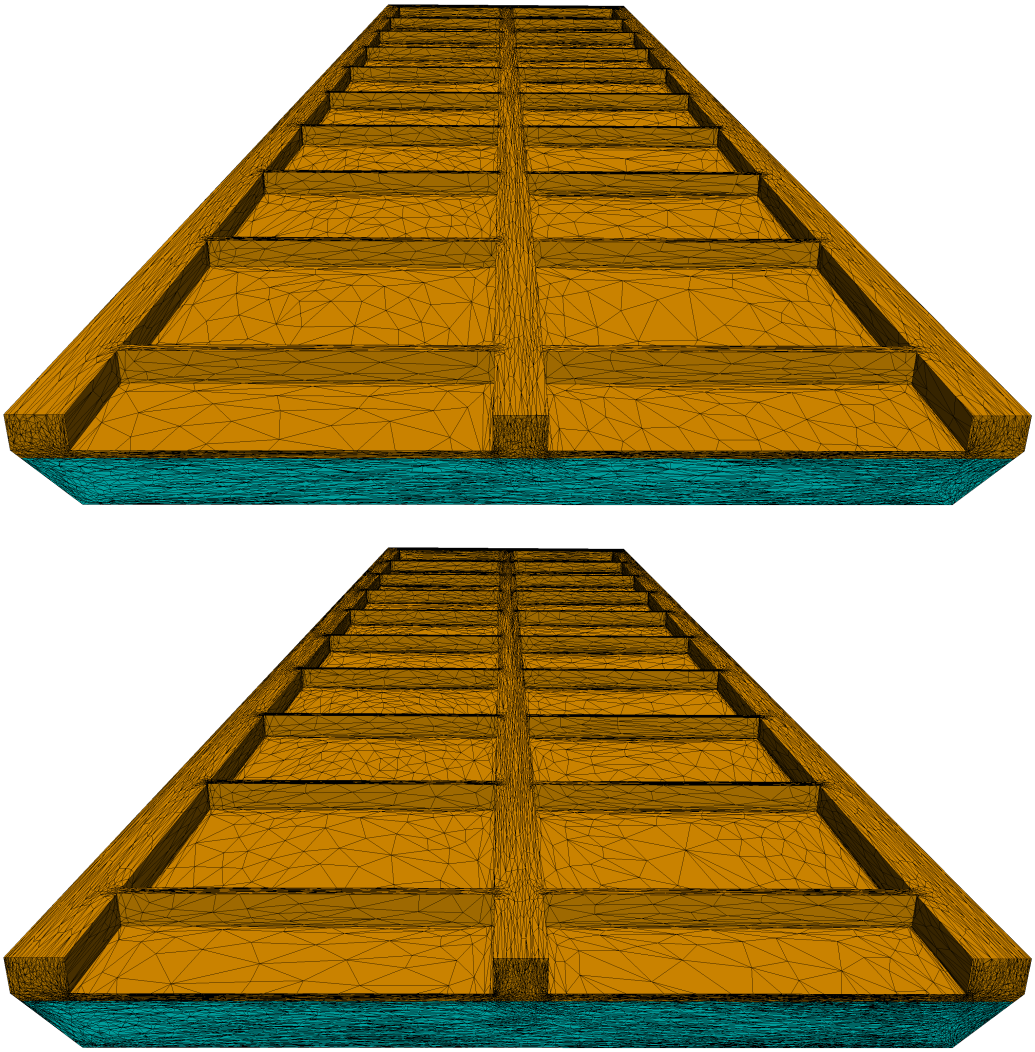

FIGURE 5.26 : Adapted meshes TOL= 0.4125 (Top) and TOL= 0.375 (Bottom) obtained using error indicator (5.8), when solving problem (5.9)-(5.19).

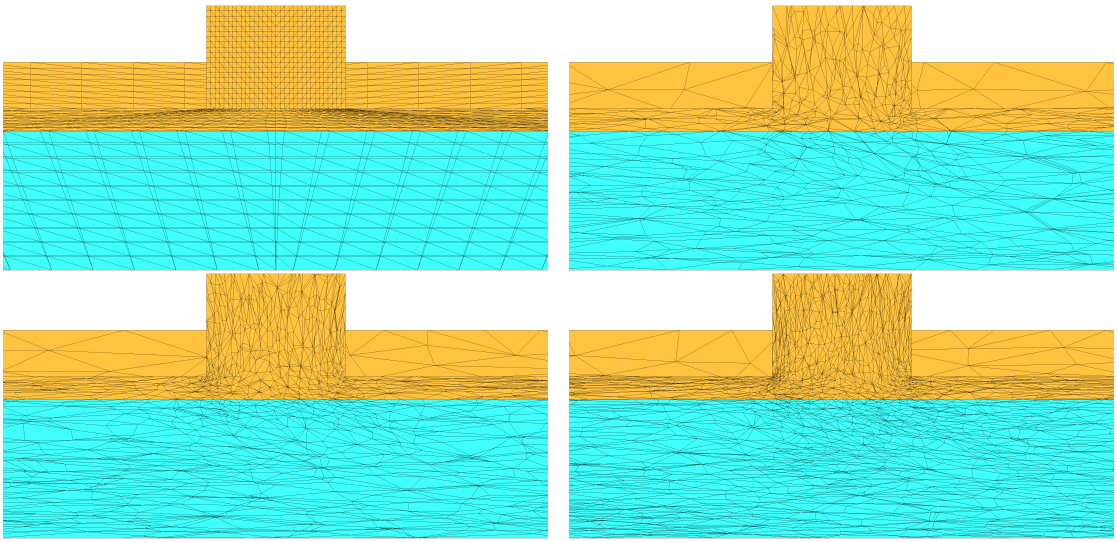

FIGURE 5.27 : Zoom of fine reference mesh (Top left), adapted mesh with TOL= 0.5 (Top right), adapted mesh with TOL= 0.4125 (Bottom left) and adapted mesh with TOL= 0.375 (Bottom right) obtained using error indicator (5.8), when solving problem (5.9)-(5.19).

For the given flat interface and the given adapted meshes we solve 10 iterations of problem (5.9)-(5.19). In Figure 5.28 (Top) we observe convergence of the L^2 discrepancy of the velocity $\mathbf{u}$, while in Figure 5.28 (Bottom) we observe the convergence of the L^2 discrepancy of the gas velocity $\mathbf{u}_g$. In Figure 5.29 we observe convergence of L^2 discrepancy of α_g. No relevant difference between the adapted meshes and the fine reference mesh can be observed. In Figure 5.30 plots over lines of the velocity $\mathbf{u}$ magnitude for different regions of the fluid domain and different meshes are reported. In Figures 5.31 and 5.32 a plot of gas velocity $\mathbf{u}_g$ magnitude and α_g respectively over a line at $x = -6$ $z = 0.3$ can be observed for the different meshes. The solution computed on the refined meshes seem to converge. Except from plot on P5, no relevant difference can be observed between adapted meshes solutions and the fine reference one. Nevertheless the CPU time required is considerably reduce when using for example the adapted mesh obtained with TOL=0.5 (see Table 5.7).

TABLE 5.7 : 10 iterations solving problem (5.9)-(5.19) for a given interface.

Mesh	CPU time
Fine reference mesh	4.89 hours
Adapted mesh TOL=0.5	1.94 hours
Adapted mesh TOL=0.4125	3.17 hours
Adapted mesh TOL=0.375	6.87 hours

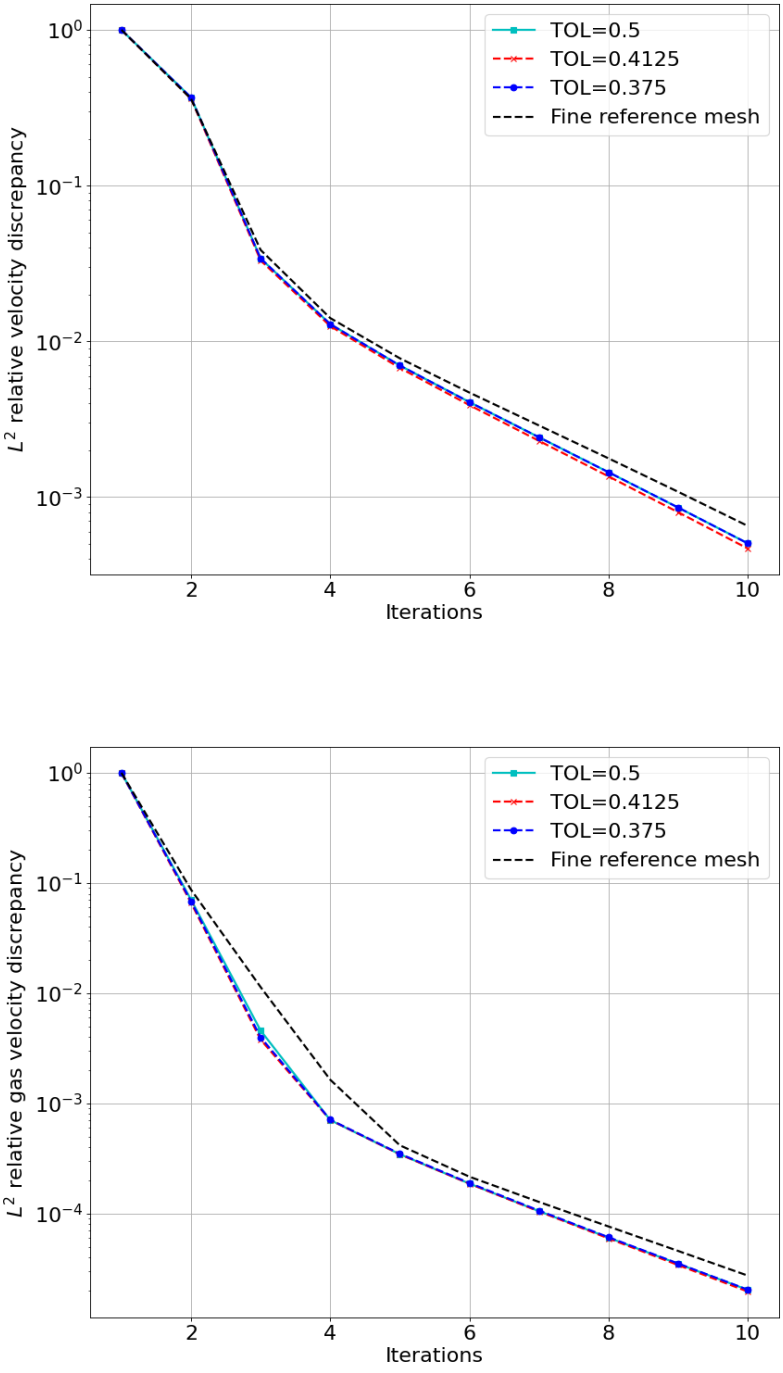

FIGURE 5.28 : Top : L^2 relative discrepancy of velocity $\mathbf{u}$, when iteratively solve problem (5.9)-(5.19) with flat interface for adapted meshes of Table 5.6 and fine reference mesh. Bottom : L^2 relative discrepancy of gas velocity $\mathbf{u}_g$, when iteratively solve problem (5.9)-(5.19) with flat interface for adapted meshes of Table 5.6 and fine reference mesh.

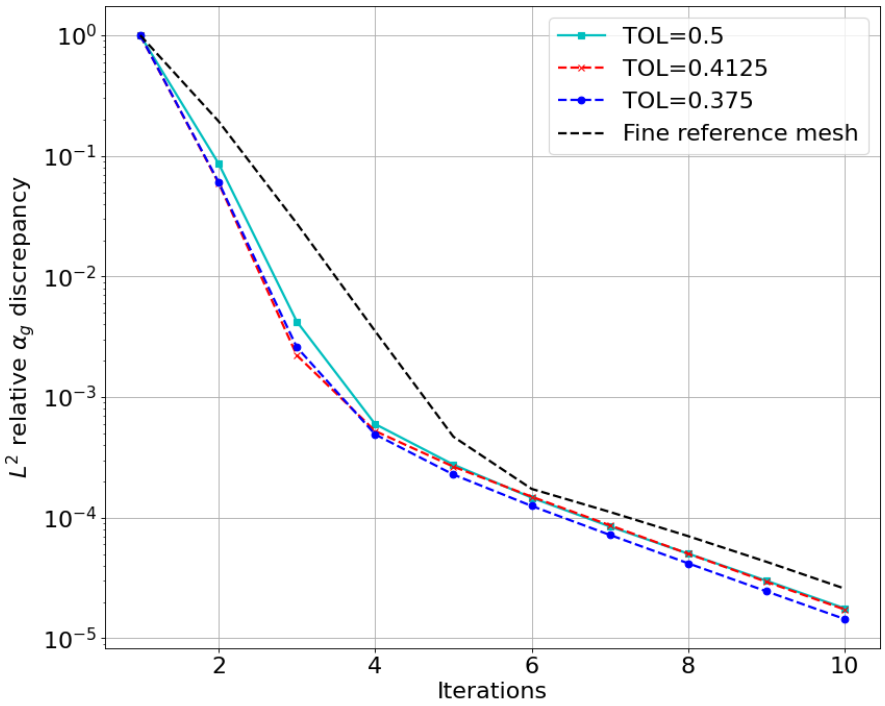

FIGURE 5.29 : L^2 relative discrepancy of α_g, when iteratively solve problem (5.9)-(5.19) with flat interface for adapted meshes of Table 5.6 and fine reference mesh.

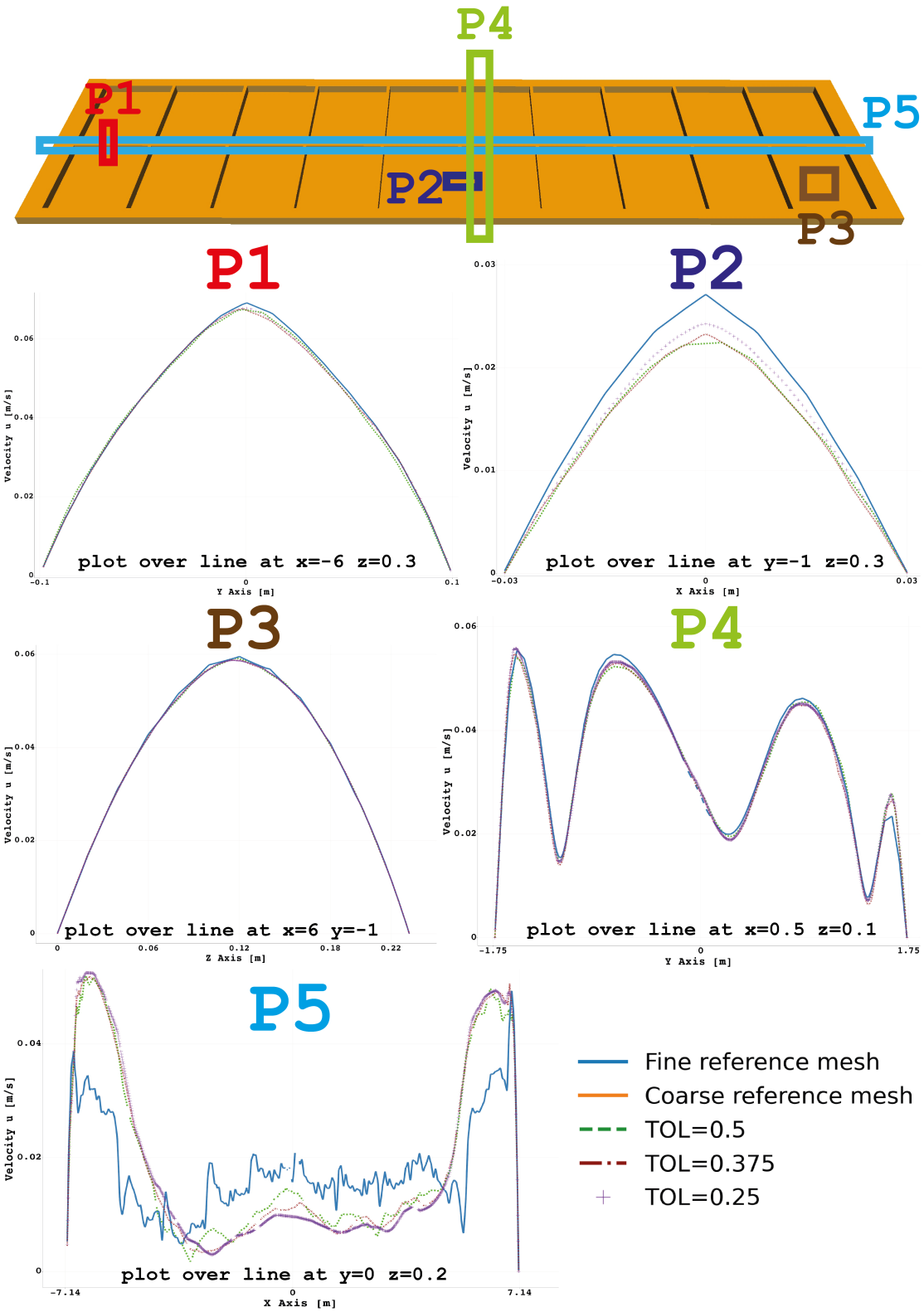

FIGURE 5.30 : Results obtained at iteration 10 solving (5.9)-(5.19) for a given flat interface Γ. Plot over lines of velocity $\mathbf{u}$ magnitude in different zones.

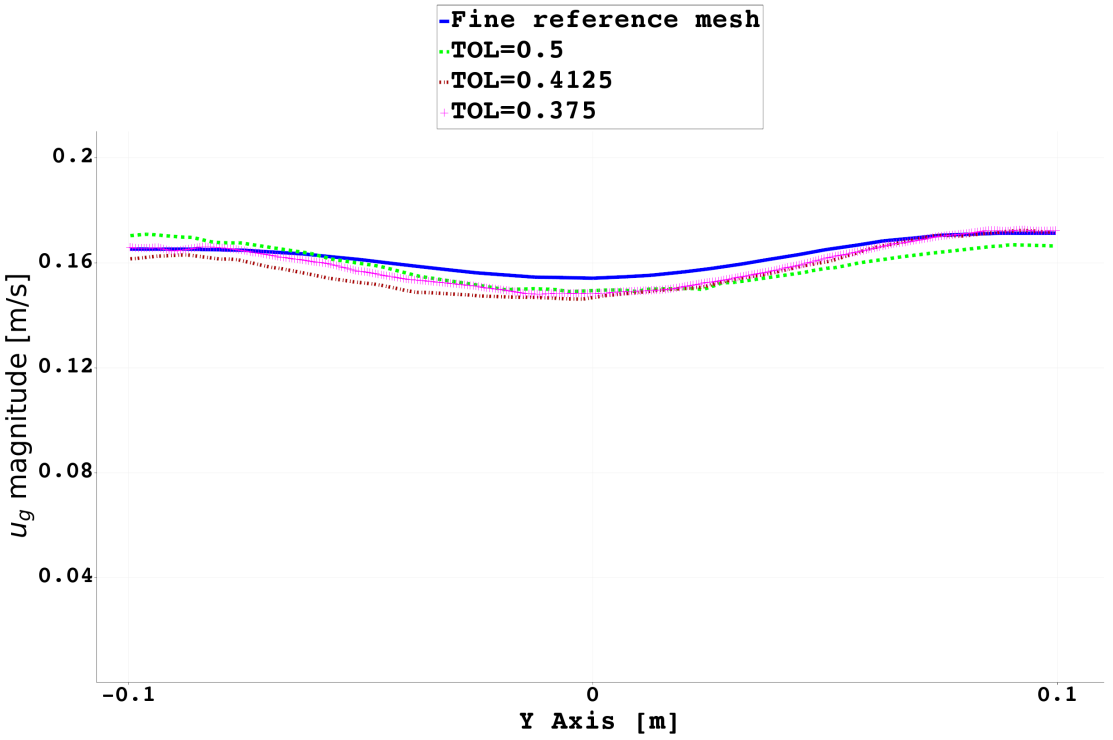

FIGURE 5.31 : Results obtained at iteration 10 solving (5.9)-(5.19) for a given flat interface Γ. Plot over a line at $x = -6$ and $z = 0.3$ (P1 in Figure 5.30) of gas velocity $\mathbf{u}_g$ magnitude.

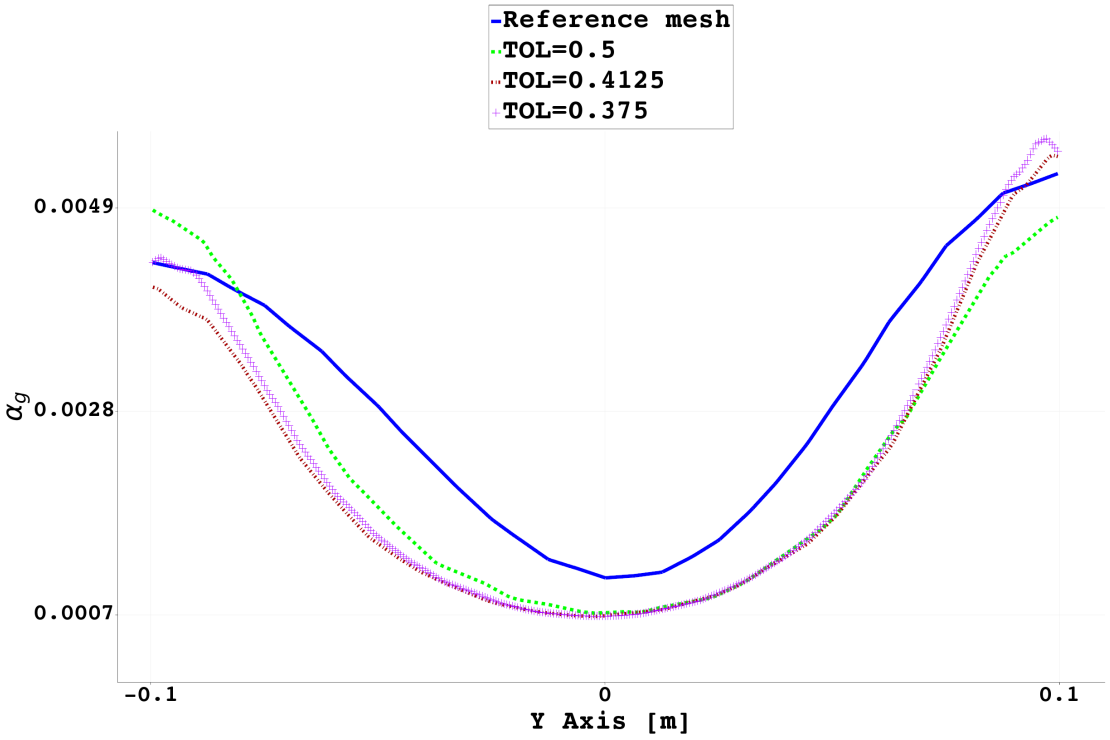

FIGURE 5.32 : Results obtained at iteration 10 solving (5.9)-(5.19) for a given flat interface Γ. Plot over a line at $x = -6$ and $z = 0.3$ (P1 in Figure 5.30) of α_g.

The obtained adapted mesh TOL= 0.5 is now used to solve problem (5.9)-(5.19) updating the interface with the goal to have $[(\tau \mathbf{n}) \cdot \mathbf{n}] = 0$ and thus a stationary solution [69].

5.4.2 Interface update

We perform 10 iterations of the interface algorithm on (5.9)-(5.19). The starting interface is flat. We present results obtained with the fine reference mesh and the adapted mesh obtained with TOL= 0.5 (see Table 5.6). In Figure 5.33, we observe the L^2 relative discrepancy of the velocity $\mathbf{u}$ along with the iterations of the update algorithm, while in Figure 5.34 (Top) we can see the L^2 relative discrepancy of the gas velocity $\mathbf{u}_g$ along with the interface iterations. In Figure 5.34 (Bottom) we observe the L^2 relative discrepancy of α_g and in Figure 5.35 the L^2 relative discrepancy of interface height. In Figure 5.36 we report plots over lines of the velocity $\mathbf{u}$ magnitude for different regions of the fluid domain. In Figures 5.37 and 5.38 a plot over a line at $x = -6$ and $z = 0.3$ of the gas velocity $\mathbf{u}_g$ magnitude and α_g respectively can be observed. In Figure 5.39 we report the obtained interface with the corresponding height. Using adapted mesh of TOL= 0.5 we obtain similar results as the one obtained with the fine reference mesh, reducing the computational time (see Table 5.8).

TABLE 5.8 : CPU time to perform 10 iterations of the interface algorithm on (5.9)-(5.19).

Mesh	CPU time
Fine reference mesh	4.96 hours
Adapted mesh TOL=0.5	2.06 hours

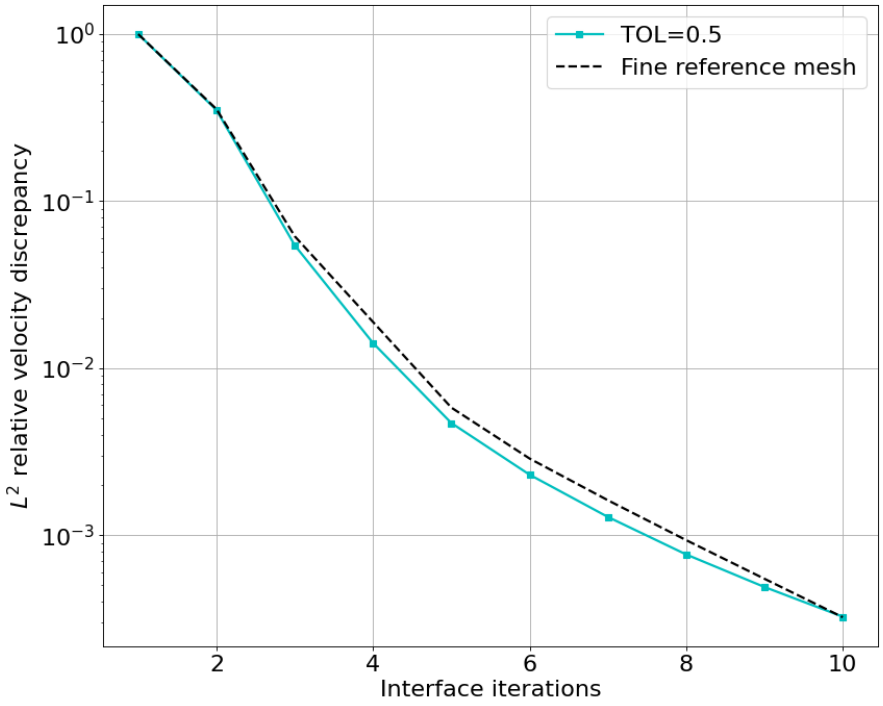

FIGURE 5.33 : L^2 relative discrepancy of velocity $\mathbf{u}$ along with interface iterations for adapted mesh with TOL= 0.5 and the fine reference mesh.

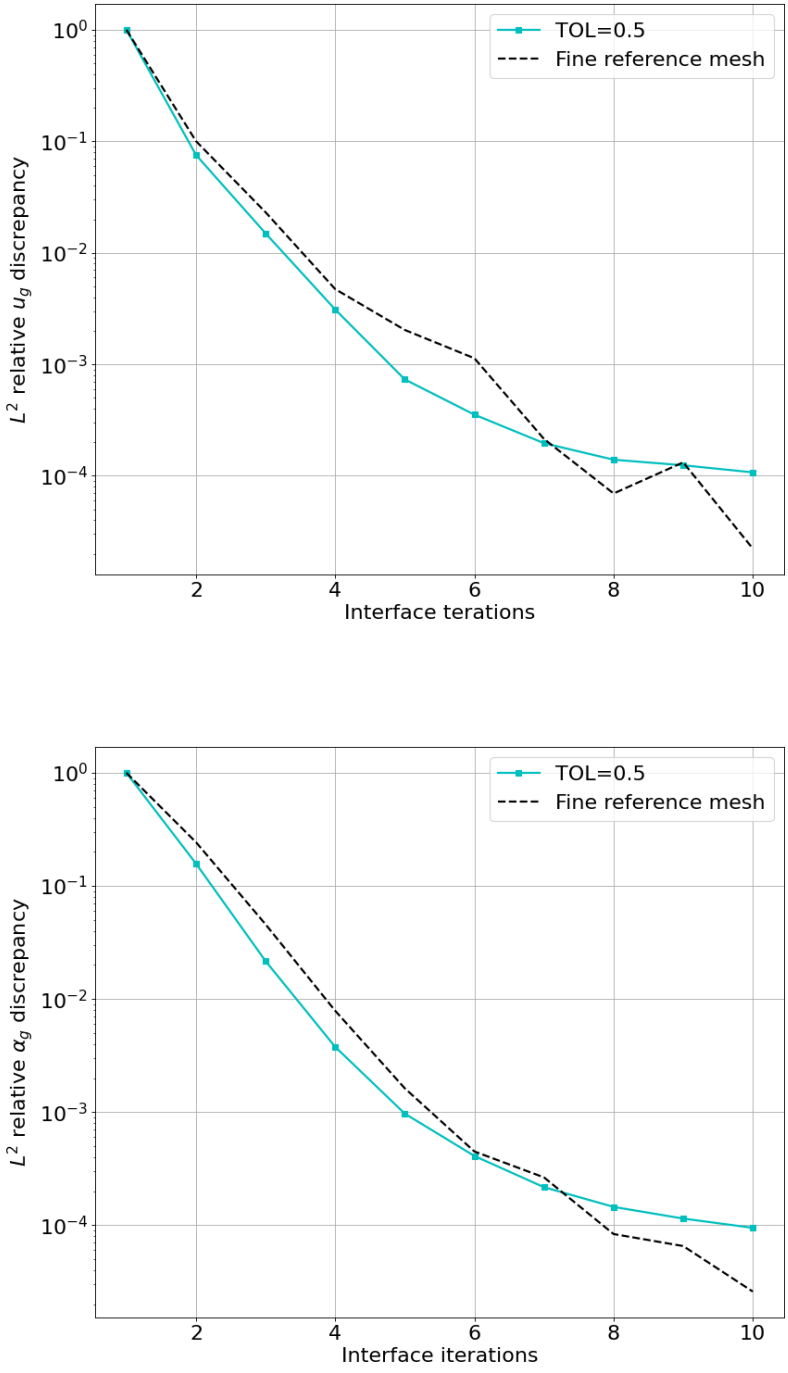

FIGURE 5.34 : Top : L^2 relative discrepancy of the gas velocity $\mathbf{u}_g$ along with the interface iterations for adapted mesh with TOL= 0.5 and the fine reference mesh. Bottom : L^2 relative discrepancy of α_g along with interface iterations for adapted mesh with TOL= 0.5 and the fine reference mesh.

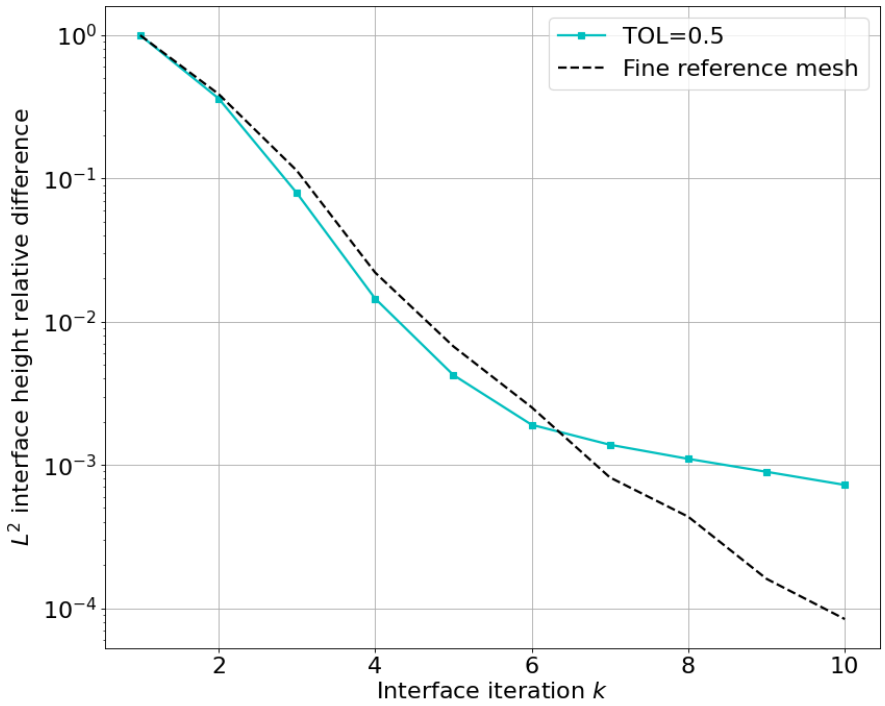

FIGURE 5.35 : L^2 relative discrepancy of interface height along with interface iterations for adapted mesh with TOL= 0.5 and the fine reference mesh.

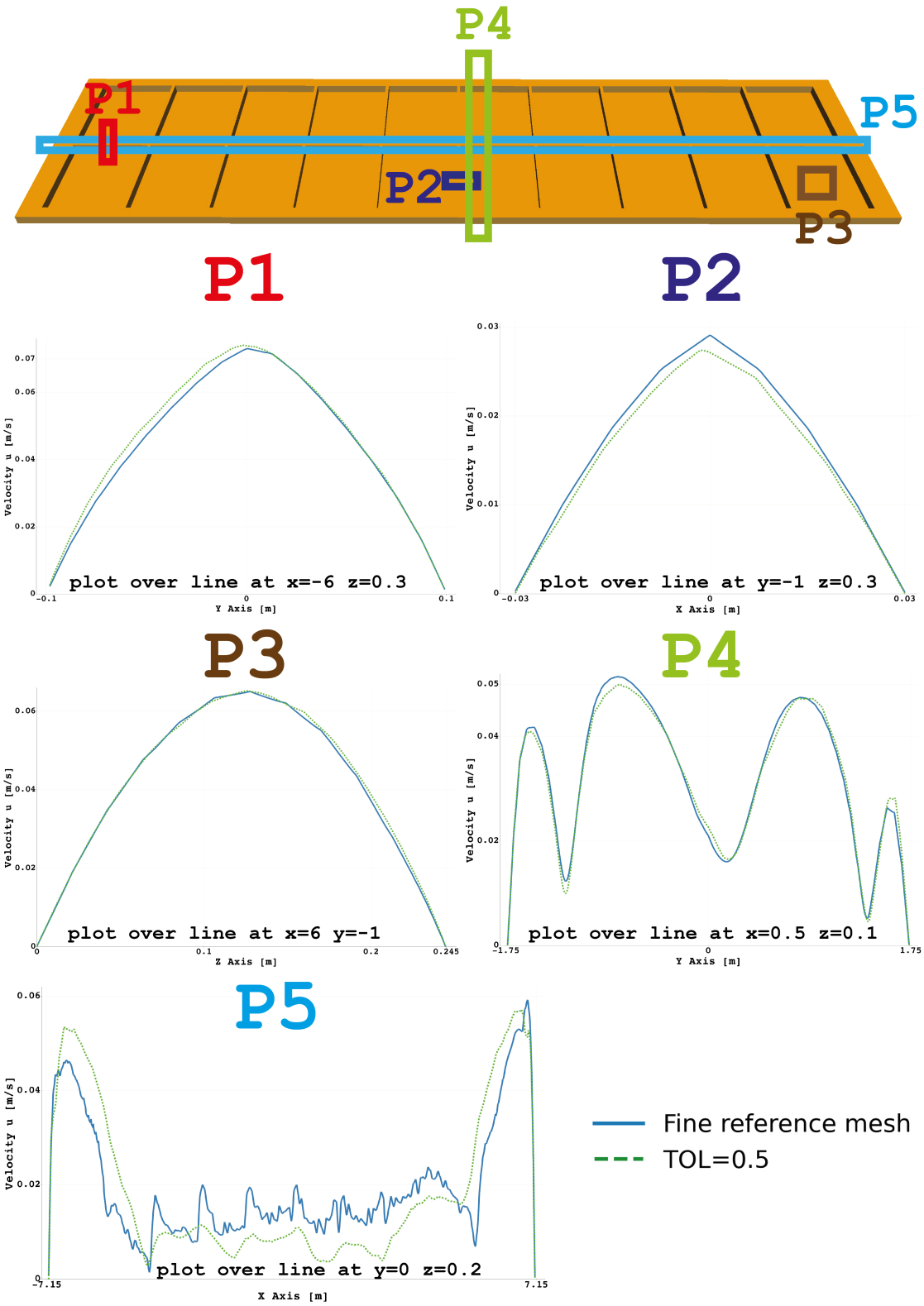

FIGURE 5.36 : Results obtained at iteration 10 of update interface algorithm. Plot over lines of velocity magnitude **u** in different zones.

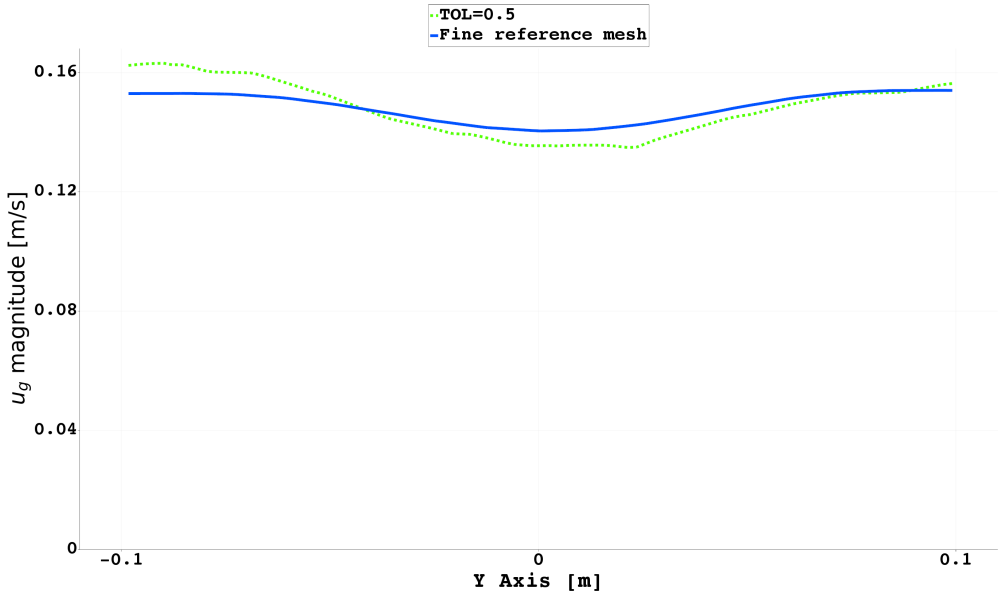

FIGURE 5.37 : Results obtained at iteration 10 of update interface algorithm. Plot over a line at $x = -6$ and $z = 0.3$ (P1 in Figure 5.36) of gas velocity $\mathbf{u}_g$ magnitude.

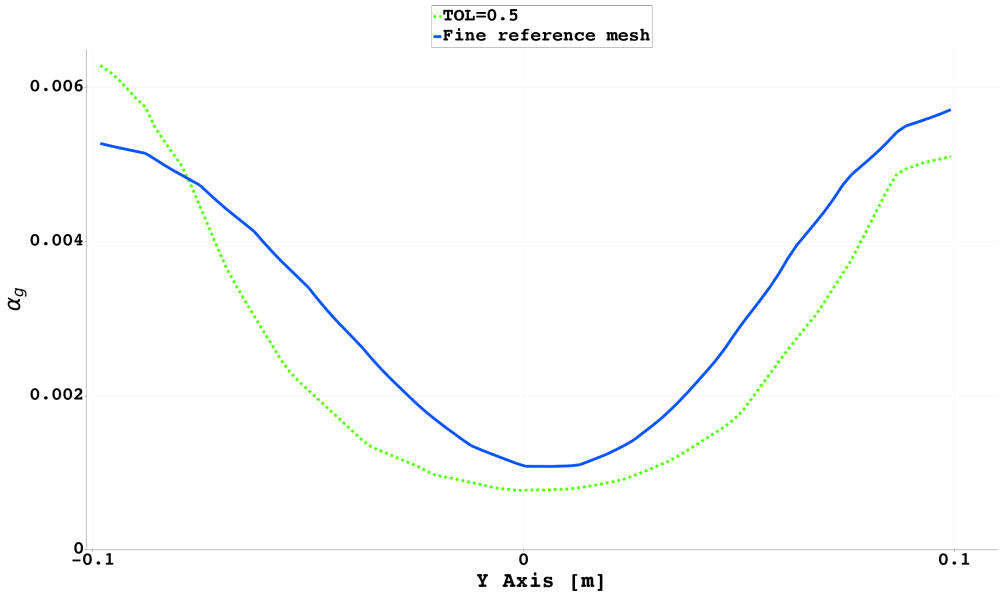

FIGURE 5.38 : Results obtained at iteration 10 of update interface algorithm. Plot over a line at $x = -6$ and $z = 0.3$ (P1 in Figure 5.36) of α_g.

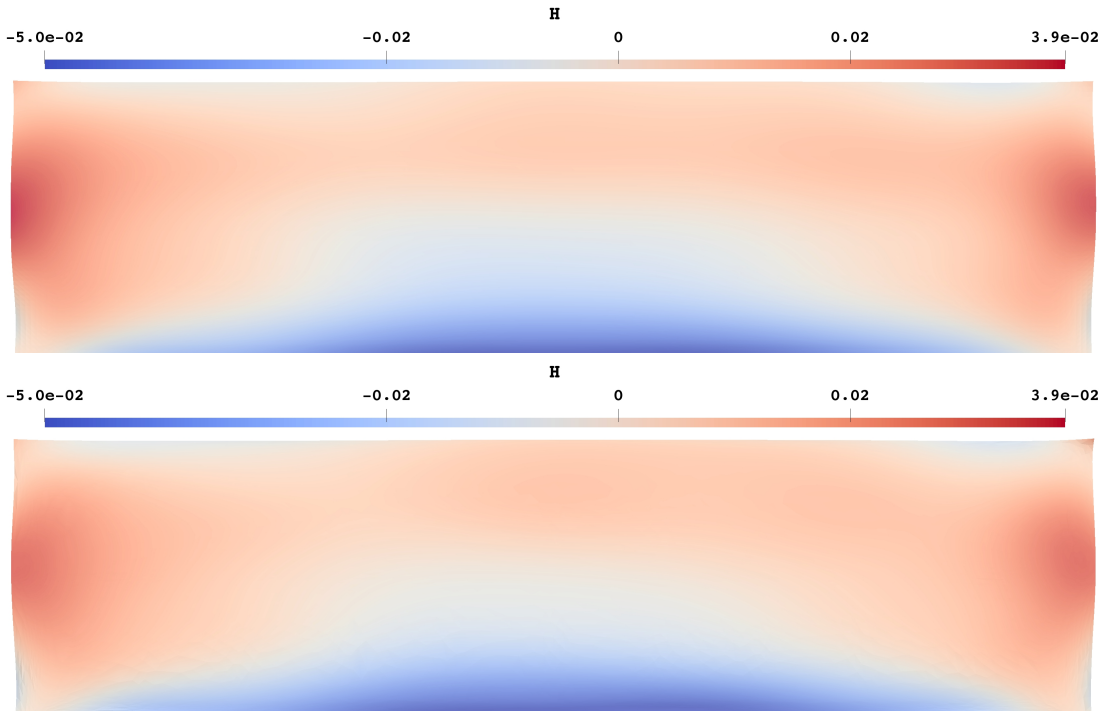

FIGURE 5.39 : Interface height obtained at iteration 10 of the update interface algorithm. Interface of fine reference mesh (Top) and interface of the adapted mesh with TOL= 0.5 (Bottom).

5.5 Aluminium cell with slots

5.5.1 Aluminium cell with slots

In Chapter 5.4 a model taking into account gas produced by aluminium electrolysis is introduced. The fluid domain geometry considered in our previous computations is a simplification of a real fluid domain of a cell. Additionally to small channels of Figure 5.4 each of the twenty squares which represents an anode's block should be divided in two smaller anodes. An additional channel between the two small anodes should be considered. Moreover in order to let the gas produced easily escape, in each small anode two slots are considered. We refer to Figure 5.40 for an example. We aim to use adaptive finite element with large aspect ratio in order to add these geometrical components and build meshes with a reasonable number of vertices. Domain of Figure 5.41 is now considered, each anode's block is divided in two smaller anodes and slots are considered only in four small anodes.

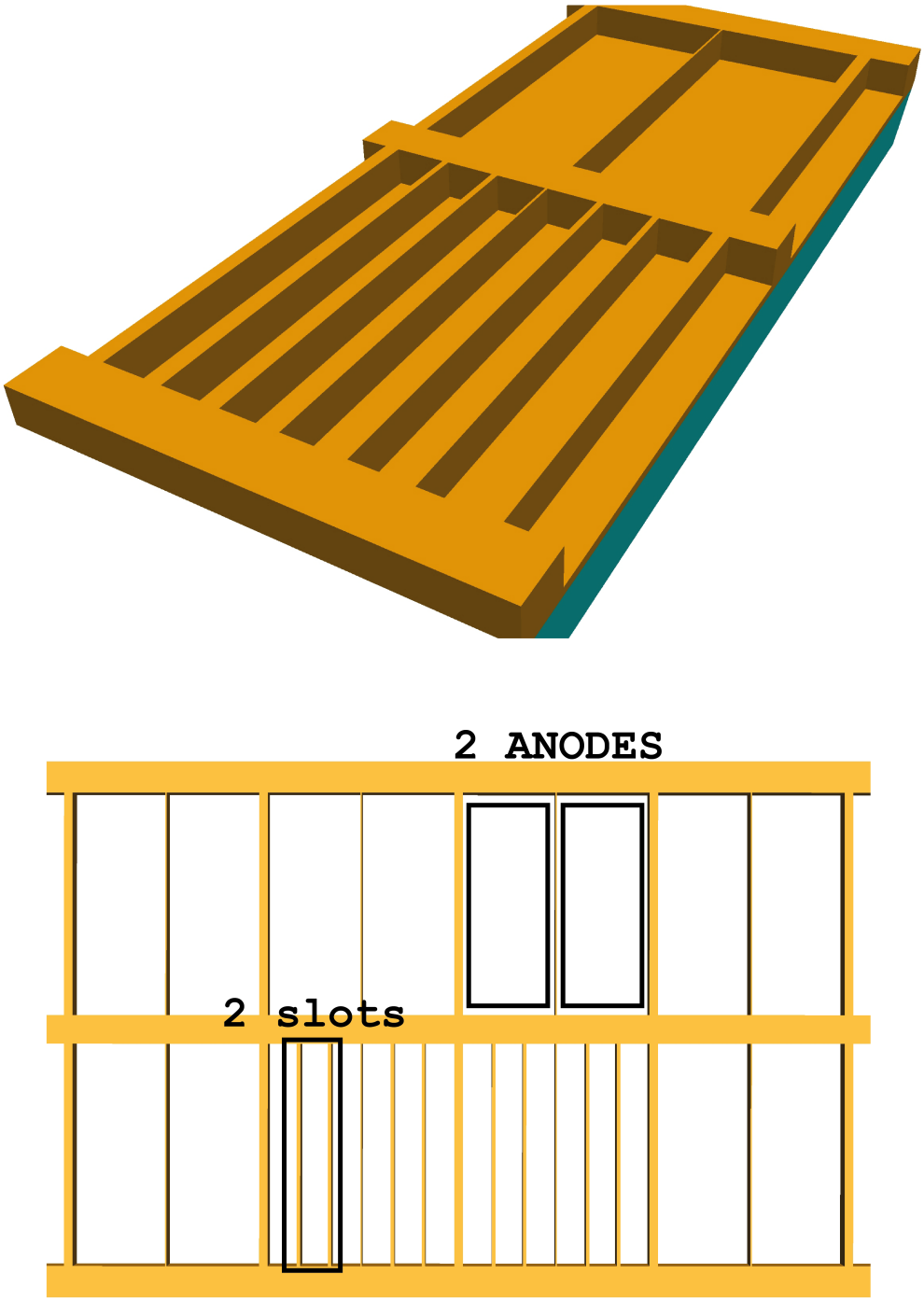

FIGURE 5.40 : Zoom of new fluid domain.

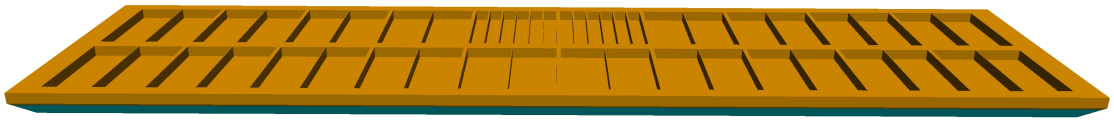

FIGURE 5.41 : Realistic fluid domain with slots on four anodes.

Our approach consists now in building adapted meshes for the new fluid domain, when solving problem (5.9)-(5.19) and using strategy described in Section 5.4.1.

An interest for industrial application, is to refine a specific area of the mesh domain, for instance the slots of an anode. This could be done manually. We propose a different approach using the adaptive strategy presented in Section 4.6.

5.5.2 The gas model with slots

We consider now the new geometry introduced in Section 5.5.1. The gas model discussed in Section 5.4 is considered. Using the same adaptive strategy of Section 5.4.1. Being the goal to build adapted mesh taking into account slots, we use technique discussed in Section 4.6 to build adapted mesh refined in the slots region. Keeping the same notations, we define Ω the fluid domain, $\Omega_1 = (-1.5, 1.5) \times (0.1, 2.1) \times (0.235, 0.38)$ and $\Omega_2 = \Omega \backslash \Omega_1$. We set $M = 150000$ and different values of w. Given a flat interface we solve three iterations of problem (5.9)-(5.19) and adapt the mesh. The process is repeated 10 times. In Table 5.9 the obtained results are reported.

TABLE 5.9 : Adaptation with respect to error indicator (5.8) of the fluid domain with slots when considering fluid velocity, when solving problem (5.9)-(5.19) with Smagorinsky turbulent model

w	Number of vertices Ω_1	Number of vertices Ω_2
0.995	949	171395
0.91	7341	166740
0.82	13926	160192
0.64	26045	146650

In Figure 5.43 a zoom of a cut at $y = 1$ of the obtained meshes can be observed. While in Figure 5.42 a cut at $y = 1$ of the considered fine reference mesh is reported.

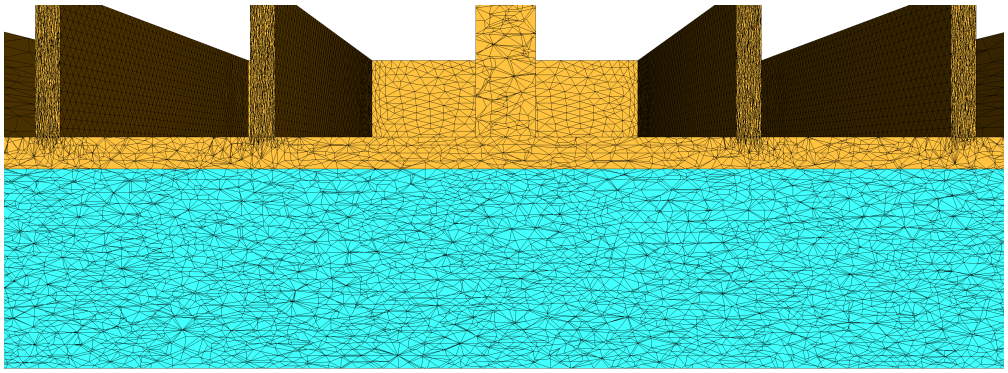

FIGURE 5.42 : Zoom of fine reference mesh.

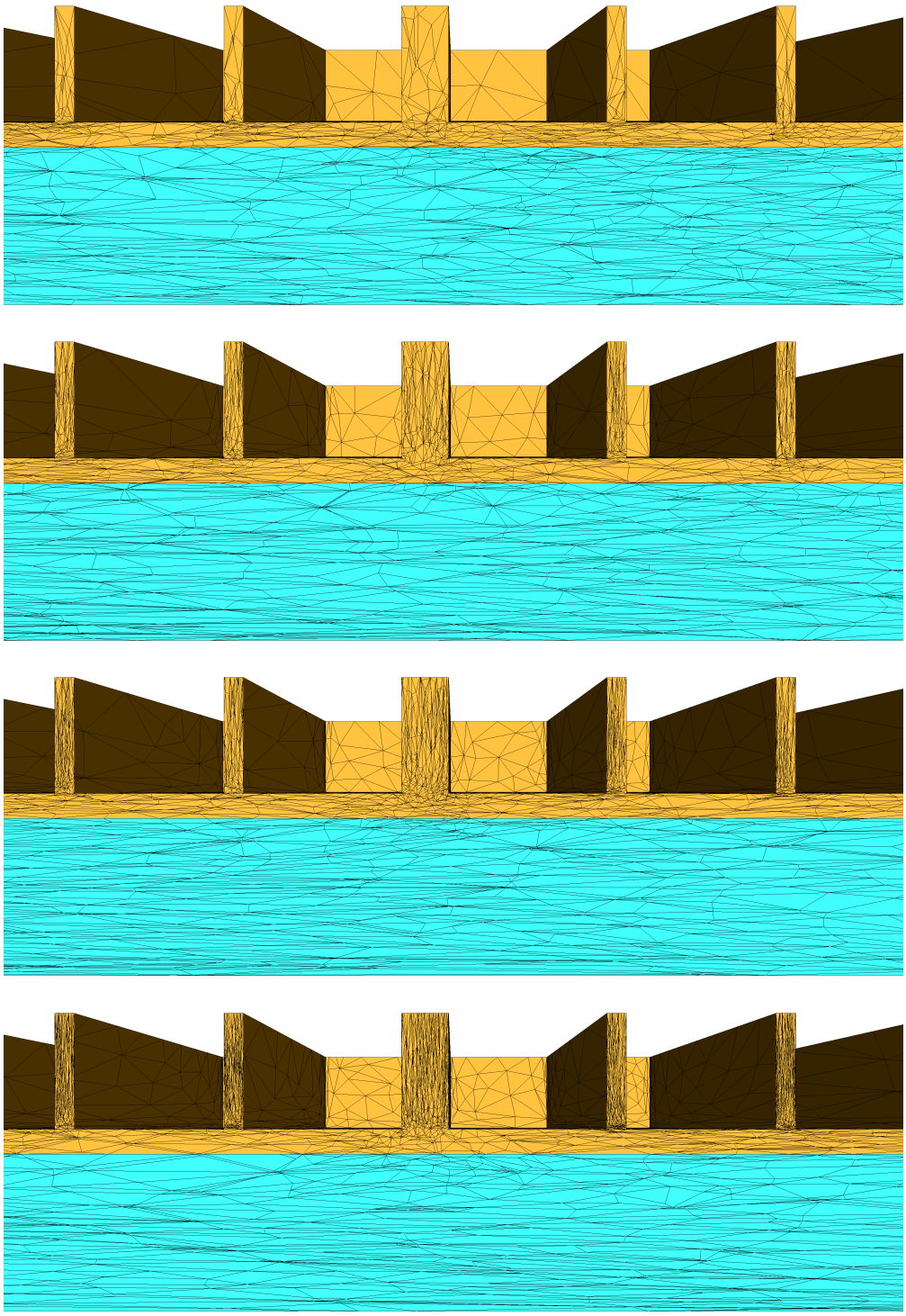

FIGURE 5.43 : Zoom of obtained adapted meshes from Top to Bottom with $w = 0.995$, $w = 0.91$, $w = 0.82$ and $w = 0.64$ obtained using error indicator (5.8), when solving (5.9)-(5.19).

We solve then 10 iterations for a given fixed interface of problem (5.9)-(5.19) on the reference mesh and the obtained adapted meshes. In Figures 5.44 and 5.45 the L^2 relative discrepancy of the velocity $\mathbf{u}$, of the gas velocity $\mathbf{u}_g$ and α_g along with the iterations are reported. In Figures 5.46, 5.47 and 5.48 we report a plot over a line of the velocity $\mathbf{u}$ magnitude, the gas velocity $\mathbf{u}_g$ magnitude and α_g at $y = 1$ $z = 0.3$ respectively along one slot for the different adapted meshes and for the fine reference mesh. A convergence of the solutions and similar results for the adapted and reference meshes can be observed. Additionally in Figure 5.49 we report a view from below of the electrolyte bath and the corresponding value of α_g. From Top to Bottom we observe results obtained using the fine reference mesh with slots, the adapted mesh with slots of Table 5.9 with $w = 0.64$, the fine reference mesh without slots and the adapted mesh without slots of Table 5.6 with TOL=0.375. When considering slots a clear reduction of α_g can be noted. Results presented show that slots allow the gas mixture to leave the domain more easily. The use of adaptive finite elements allows accurate computations with a reasonable number of vertices. With our approach it is now affordable to add more slots in the geometry and to study numerical results on a more realistic domain.

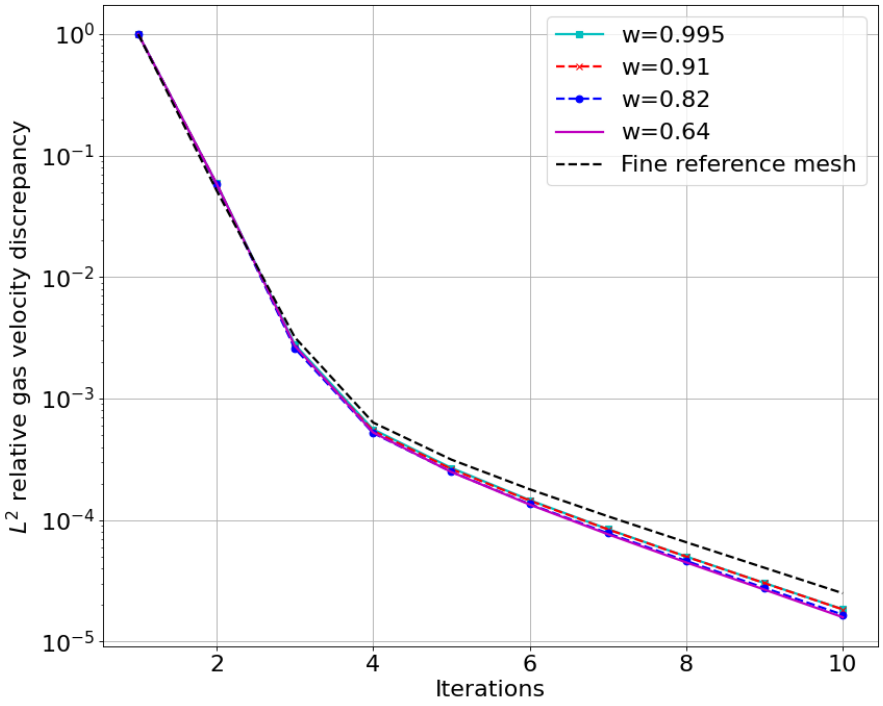

FIGURE 5.44 : L^2 relative discrepancy of velocity $\mathbf{u}$ along with iterations for adapted meshes obtained with different w and the fine reference mesh.

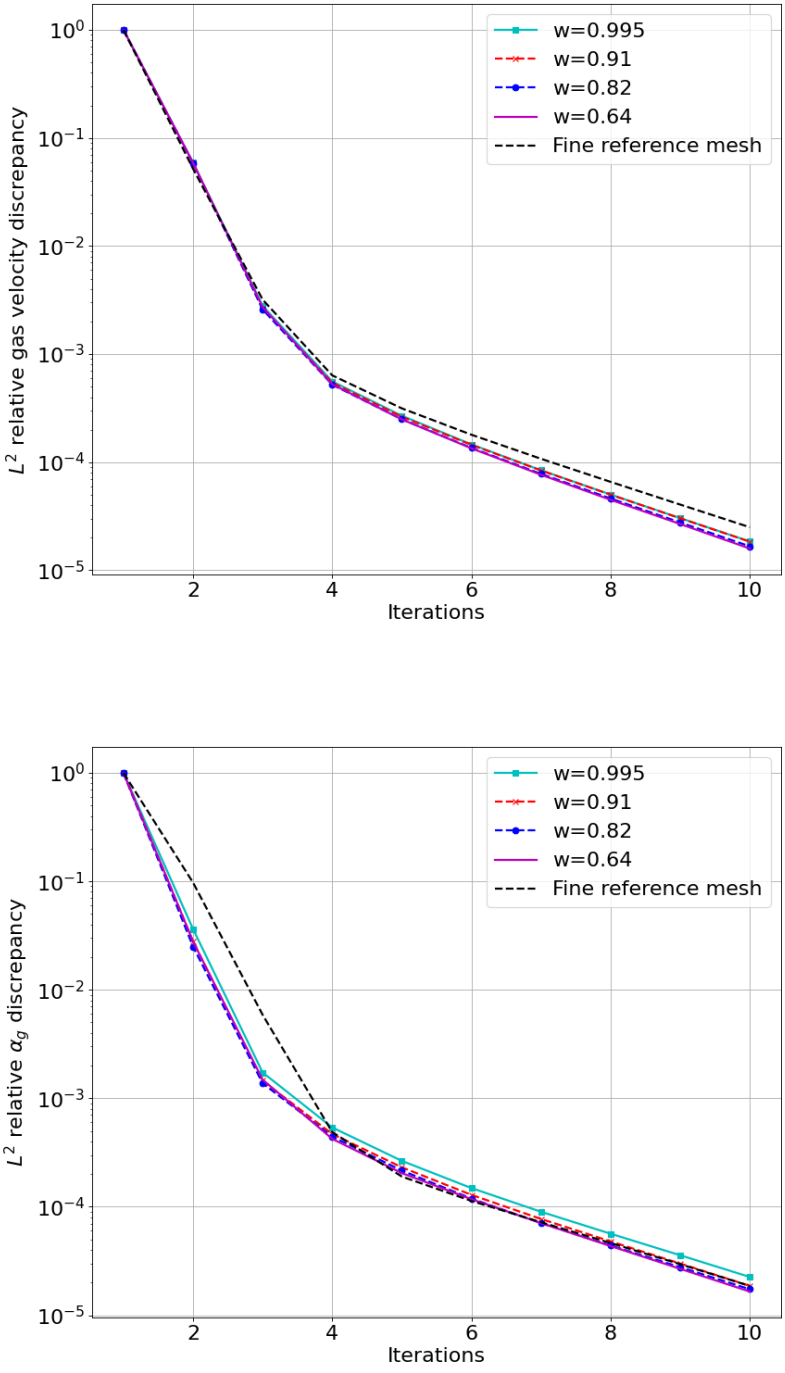

FIGURE 5.45 : Top : L^2 relative discrepancy of the gas velocity $\mathbf{u}_g$ along with the iterations for adapted meshes obtained with different w and the fine reference mesh. Bottom : L^2 relative discrepancy of α_g along with iterations for adapted meshes obtained with different w and the fine reference mesh.

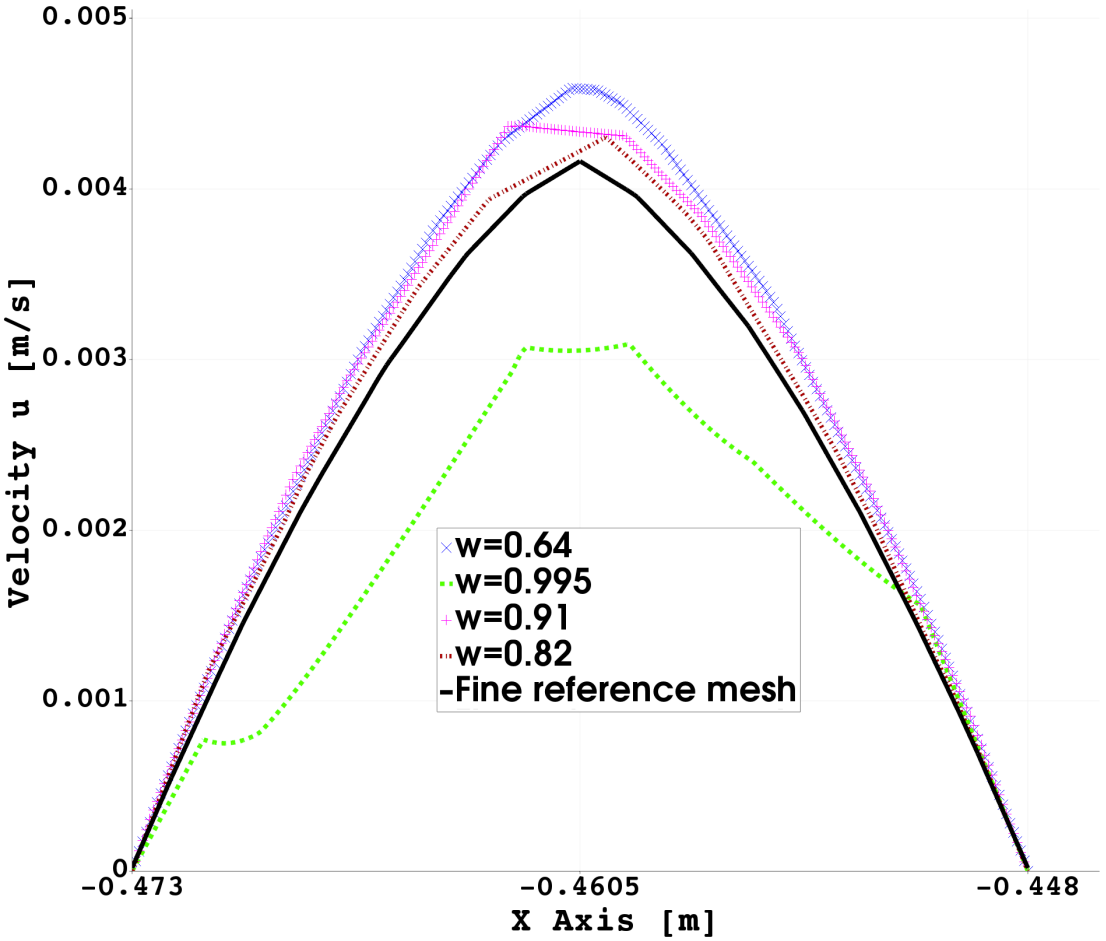

FIGURE 5.46 : Velocity magnitude $\mathbf{u}$, plot over a line at $y = 1$ and $z = 0.3$ for different adapted meshes.

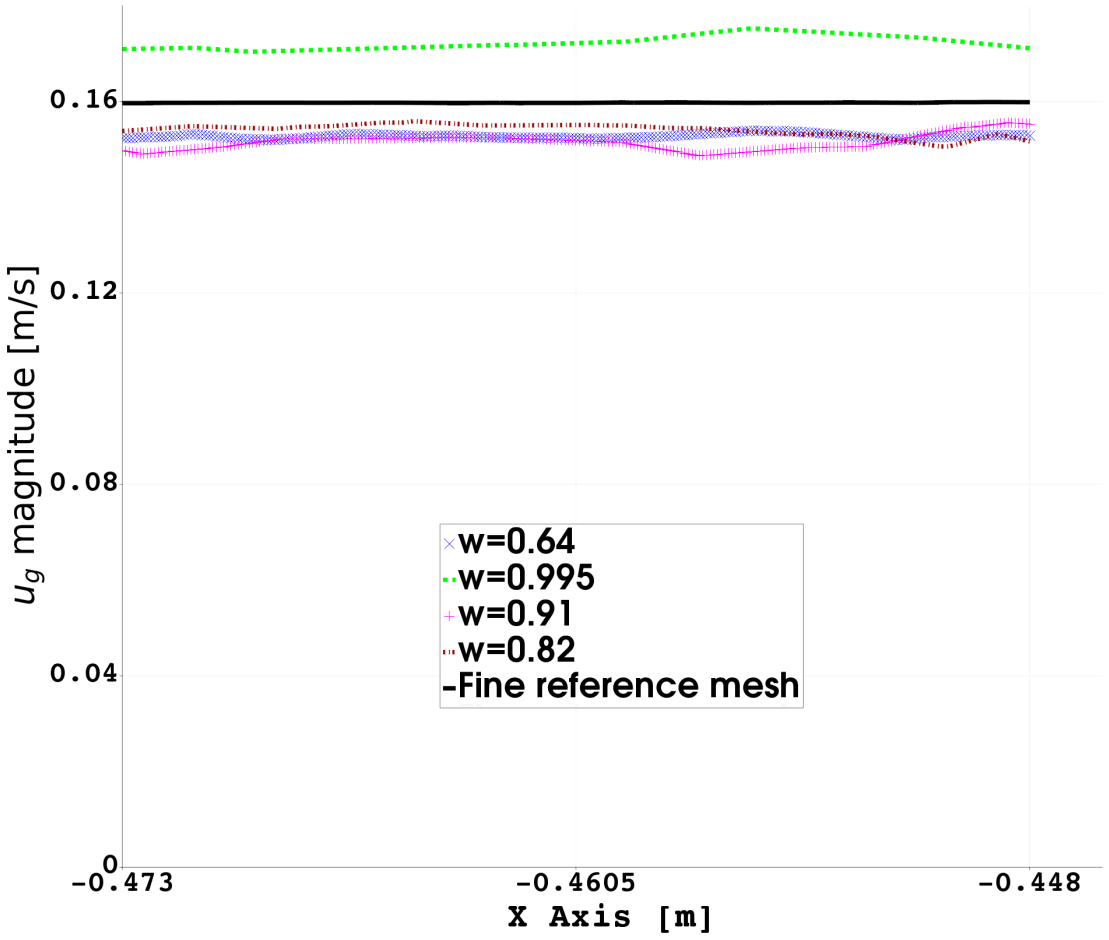

FIGURE 5.47 : Gas velocity magnitude $\mathbf{u}_g$, plot over a line at $y = 1$ and $z = 0.3$ for different adapted meshes.

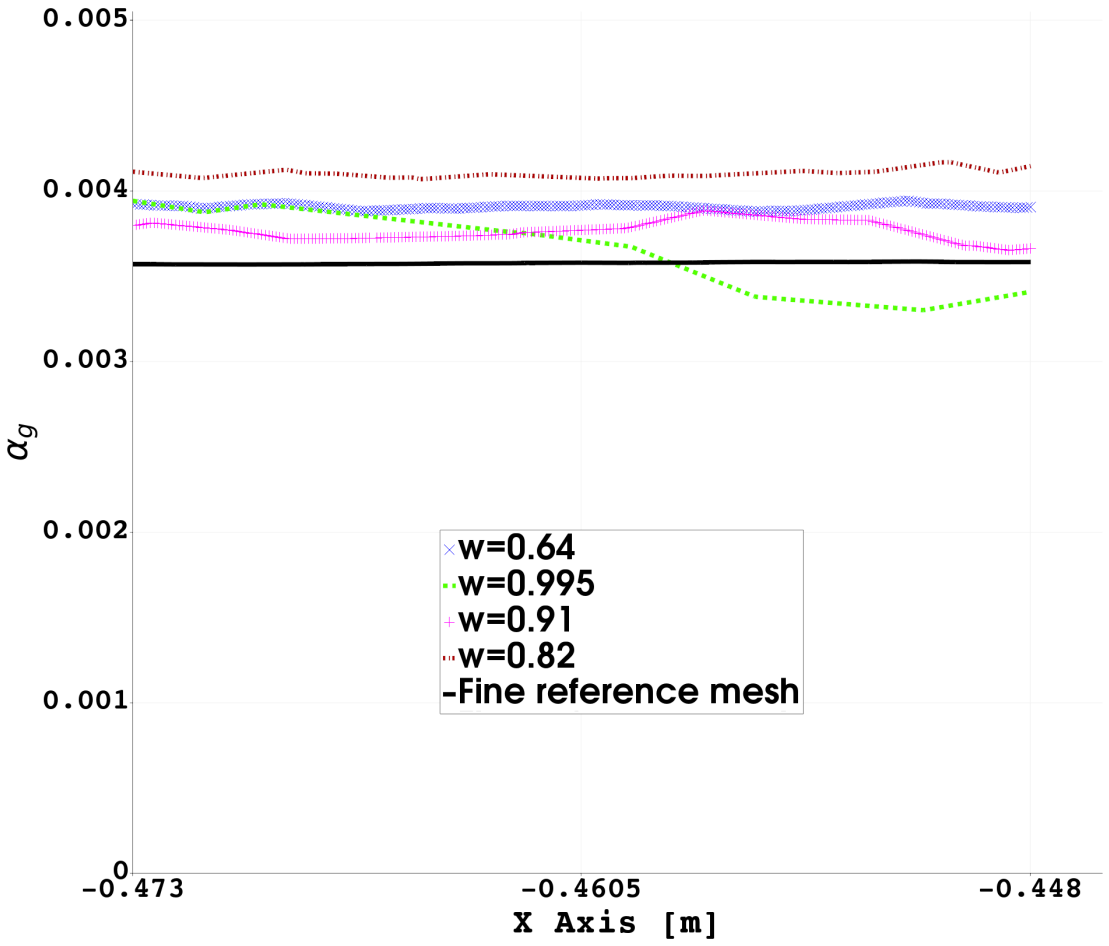

FIGURE 5.48 : α_g, plot over a line at $y = 1$ and $z = 0.3$ for different adapted meshes.

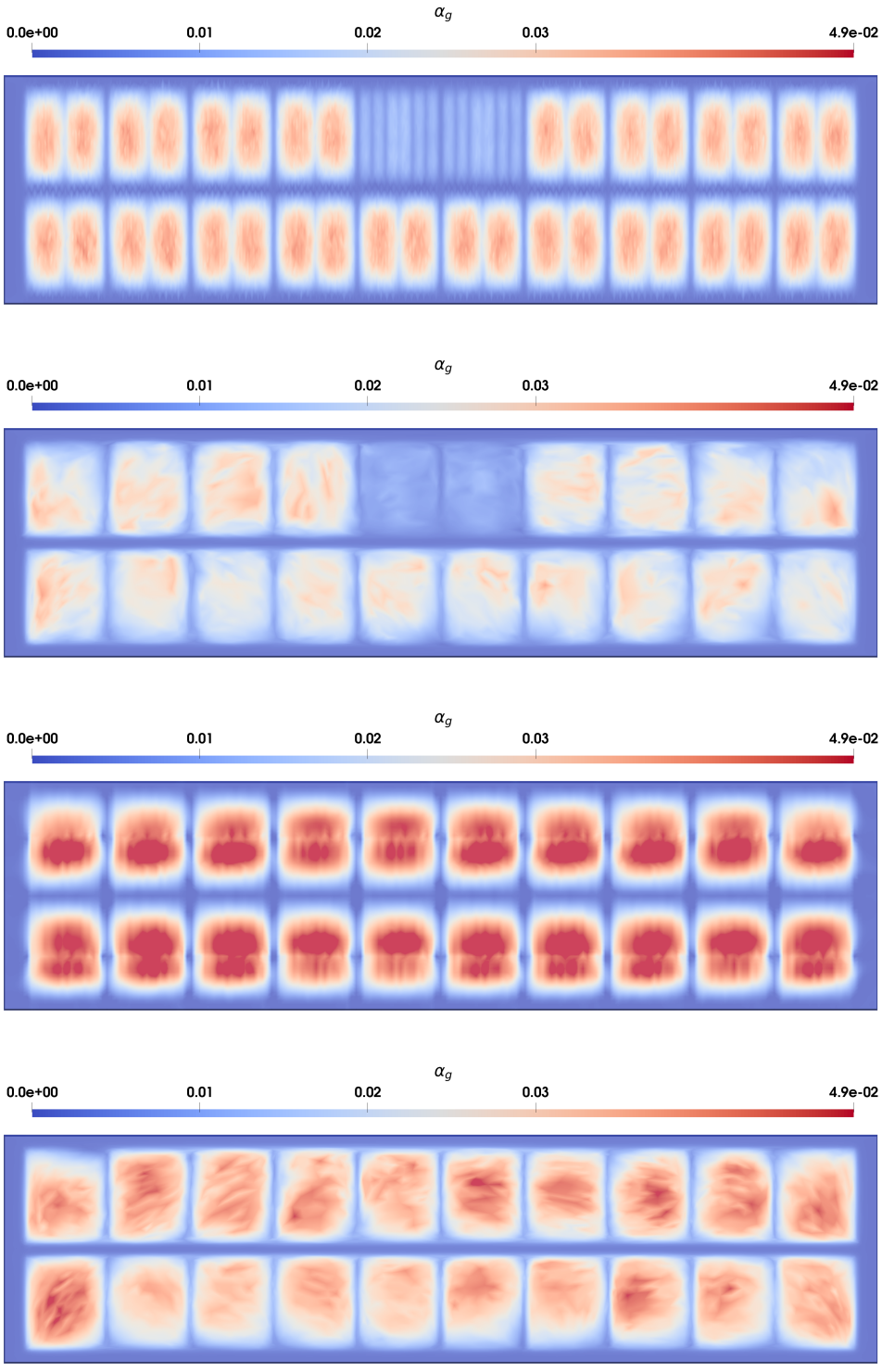

FIGURE 5.49 : View from below of the electrolyte bath and the corresponding α_g. From Top to Bottom : fine reference mesh with slots, adapted mesh with slots of Table 5.9 with $w = 0.64$, fine reference mesh without slots and adapted mesh without slots of Table 5.6 with TOL=0.375.

Conclusion and perspectives

The goal of this thesis was to apply adaptive finite elements with large aspect ratio for the numerical simulation of aluminium electrolysis. We derived a strategy to build adapted meshes with goal to reduce the computational time for a given accuracy. The adaptive criteria is based on a posteriori error estimates derived for simplified problems.

In **Chapter 1** the anisotropic framework is introduced. We proved interpolation estimates error for a general L^p norm and for $\Omega \subset \mathbb{R}^d$, that are used along the whole work.

In **Chapter 2** an error estimator for the approximation of elliptic problems with smooth strongly varying diffusion coefficient is presented. An equivalence with the true error, up to higher order terms, is shown. Moreover, various adaptive algorithms have been presented and their efficiency and accuracy numerically verified.

In **Chapter 3** we discussed an error indicator for the Steady Stokes problem. In this part sharpness of the error indicator is numerically demonstrated. Additionally, applications via adaptive algorithms are presented.

Chapter 4 is devoted to the nonlinear p-Laplace problem $-\nabla((\mu+|\nabla u|^{p-2})\nabla u) = f$. We studied error estimates for the $W_0^{1,p}(\Omega)$ norm and then a quasi-norm. When μ is large the estimator is sharp for both norms, while when μ is small only the quasi-norm should be considered. For the quasi-norm a lower bound is shown. An equivalence between the error estimator and the quasi-norm error, up to higher order terms, is demonstrated. Numerical results confirm these theoretical predictions. Adaptive algorithms are then applied with the new error estimator and their efficiency is numerically verified.

In **Chapter 5** the simulation of aluminium electrolysis is presented. Based on results obtained in previous model problems a strategy to build adapted meshes is presented. In Section 5.3 we presented numerical results obtained for the fluid-flow problem. Given a horizontal bath-metal interface, adapted meshes are produced to compute the velocity with accuracy. These adapted meshes are then used to solve the interface problem. Adapted meshes allow a reduction of the computational time up to 85% for a reference mesh with similar accuracy. In section 5.4 a model to take into account diluted gas in the fluid-flow problem is introduced. Given a flat interface, we use again our adaptive strategy to build adapted meshes for this problem. The adapted meshes are then used to solve an interface problem between the two fluids. As before, the accuracy obtained

using adapted meshes is comparable to the one obtained with a reference industrial mesh, while reducing the computational time. Finally in Section 5.5 a more complex geometry is presented, new features, namely slots, are introduced. An algorithm to refine the mesh in a small region containing the slots is proposed. Numerical results show that indeed, slots allow the gas mixture to leave the domain more easily. It should be noted that the introduction of adaptive finite elements with large aspect ratio allows to check convergence of the simulations.

Several interesting perspectives could be considered. First, as explained in [67, 69], different boundary conditions are sometimes used for the velocity of the fluid-flow problem. In particular the homogeneous Dirichlet boundary condition

$$\mathbf{u} = 0 \qquad \text{on } \partial\Omega,$$

of problem (5.1) or (5.13) can be relaxed with a friction parameter α_f obtaining

$$\begin{aligned} \mathbf{u} \cdot \mathbf{n} &= 0 && \text{on } \partial\Omega, \\ (\tau \mathbf{n}) \cdot \mathbf{t}_i &= \alpha_f (\mathbf{u} \cdot \mathbf{t}_i) && i = 1, 2 \text{ on } \partial\Omega, \end{aligned}$$

where $(\mathbf{t}_1, \mathbf{t}_2, \mathbf{n})$ is a local orthonormal frame on $\partial\Omega$. Thus a numerical study to introduce adaptive finite elements with large aspect ratio, when considering such boundary conditions should be conducted. Second we presented an adaptive strategy for the gas problem (5.9)-(5.19). The adaptive criteria was based on an error indicator on velocity $\mathbf{u}$. A different indicator defined by combinations of the velocity $\mathbf{u}$, the gas velocity $\mathbf{u}_g$ and the gas volumetric ratio α_g, should also be investigated. Finally, adaptive finite elements with large aspect ratio should be introduced in the Magneto-hydrodynamics-thermal problem [68, 31].

Bibliographie

[1] M. Ainsworth and J. T. Oden. A posteriori error estimation in finite element analysis. *Comput. Methods Appl. Mech. Engrg.*, 142(1-2) :1–88, 1997.

[2] M. Ainsworth, J. Z. Zhu, A. W. Craig, and O. C. Zienkiewicz. Analysis of the Zienkiewicz-Zhu a posteriori error estimator in the finite element method. *Internat. J. Numer. Methods Engrg.*, 28(9) :2161–2174, 1989.

[3] F. Alauzet, P. Frey, and P. George. Anisotropic mesh adaptation for Rayleigh-Taylor instabilities. In *European Congress on Computational Methods in Applied Sciences and Engineering (ECCOMAS)*, 2004.

[4] F. Alauzet and A. Loseille. A decade of progress on anisotropic mesh adaptation for computational fluid dynamics. *Comput.-Aided Des.*, 72 :13–39, 2016.

[5] R. C. Almeida, R. A. Feijóo, A. C. Galeão, C. Padra, and R. S. Silva. Adaptive finite element computational fluid dynamics using an anisotropic error estimator. volume 182, pages 379–400. 2000. IV WCCM (Buenos Aires, 1998).

[6] T. Apel. *Anisotropic finite elements : local estimates and applications*. B. G. Teubner Stuttgart, 1999.

[7] I. Babushka, J. Chandra, and J. E. Flaherty. *Adaptive methods for partial differential equations*, volume 39. Siam, 1989.

[8] I. Babuška and W. C. Rheinboldt. A-posteriori error estimates for the finite element method. *International journal for numerical methods in engineering*, 12(10) :1597–1615, 1978.

[9] I. Babuška, R. Durán, and R. Rodríguez. Analysis of the efficiency of an a posteriori error estimator for linear triangular finite elements. *SIAM J. Numer. Anal.*, 29(4) :947–964, 1992.

[10] W. Bangerth and R. Rannacher. *Adaptive finite element methods for differential equations*. Springer Science & Business Media, 2003.

[11] J. W. Barrett and W. B. Liu. Quasi-norm error bounds for the finite element approximation of a non-Newtonian flow. *Numer. Math.*, 68(4) :437–456, 1994.

[12] T. Barth and H. Deconinck. *Error estimation and adaptive discretization methods in computational fluid dynamics*. Lecture Notes in Computational Science and Engineering. Springer Berlin Heidelberg, 2002.

[13] L. Belenki, L. Diening, and C. Kreuzer. Optimality of an adaptive finite element method for the p-Laplacian equation. *IMA J. Numer. Anal.*, 32(2) :484–510, 2012.

[14] E. Boey, Y. Bourgault, and T. Giordano. Anisotropic space-time adaptation for reaction-diffusion problems. *arXiv preprint arXiv :1707.04787*, 2017.

[15] A. Boisneault, S. Dubuis, and M. Picasso. An adaptive space-time algorithm for the incompressible Navier-Stokes equations. *J. Comput. Phys.*, 493 :Paper No. 112457, 22, 2023.

[16] Y. Bourgault and M. Picasso. Anisotropic error estimates and space adaptivity for a semidiscrete finite element approximation of the transient transport equation. *SIAM J. Sci. Comput.*, 35(2) :A1192–A1211, 2013.

[17] F. Brezzi and J. Douglas, Jr. Stabilized mixed methods for the Stokes problem. *Numer. Math.*, 53(1-2) :225–235, 1988.

[18] W. Cao. Superconvergence analysis of the linear finite element method and a gradient recovery postprocessing on anisotropic meshes. *Math. Comput.*, 84 :89–117, 2014.

[19] C. Carstensen. All first-order averaging techniques for a posteriori finite element error control on unstructured grids are efficient and reliable. *Math. Comp.*, 73(247) :1153–1165, 2004.

[20] C. Carstensen and R. Klose. A posteriori finite element error control for the p-Laplace problem. *SIAM J. Sci. Comput.*, 25(3) :792–814, 2003.

[21] C. Carstensen, W. Liu, and N. Yan. A posteriori FE error control for p-Laplacian by gradient recovery in quasi-norm. *Math. Comp.*, 75(256) :1599–1616, 2006.

[22] P. Clément. Approximation by finite element functions using local regularization. *Rev. Française Automat. Informat. Recherche Opérationnelle Sér. Rouge Anal. Numér.*, 9 :77–84, 1975.

[23] T. Coupez. Metric construction by length distribution tensor and edge based error for anisotropic adaptive meshing. *J. Comput. Phys.*, 230(7) :2391–2405, 2011.

[24] S. Das. Achieving carbon neutrality in the global aluminum industry. *JOM*, 64(2) :285–290, 2012.

[25] J. Descloux, R. Frosio, and M. Flück. A two fluids stationary free boundary problem. *Comput. Methods Appl. Mech. Engrg.*, 77(3) :215–226, 1989.

[26] L. Diening and C. Kreuzer. Linear convergence of an adaptive finite element method for the p-Laplacian equation. *SIAM J. Numer. Anal.*, 46(2) :614–638, 2008.

[27] W. Dörfler. A convergent adaptive algorithm for Poisson's equation. *SIAM J. Numer. Anal.*, 33(3) :1106–1124, 1996.

[28] S. Dubuis. Adaptive algorithms for two fluids flows with anisotropic finite elements and order two time discretizations. Technical report, EPFL, 2020.

[29] S. Dubuis, P. Passelli, and M. Picasso. Anisotropic adaptive finite elements for an elliptic problem with strongly varying diffusion coefficient. *Comput. Methods Appl. Math.*, 22(3) :529–543, 2022.

[30] A. Ern and J.-L. Guermond. *Éléments finis : théorie, applications, mise en œuvre*, volume 36 of *Mathématiques & Applications (Berlin) [Mathematics & Applications]*. Springer-Verlag, Berlin, 2002.

[31] S. Flotron. Simulations numériques de phénomènes mhd-thermiques avec interface libre dans l'électrolyse de l'aluminium. Technical report, EPFL, 2013.

[32] L. Formaggia, S. Micheletti, and S. Perotto. Anisotropic mesh adaption in computational fluid dynamics : application to the advection-diffusion-reaction and the Stokes problems. *Appl. Numer. Math.*, 51(4) :511–533, 2004.

[33] L. Formaggia and S. Perotto. New anisotropic a priori error estimates. *Numer. Math.*, 89(4) :641–667, 2001.

[34] L. Formaggia and S. Perotto. Anisotropic error estimates for elliptic problems. *Numer. Math.*, 94(1) :67–92, 2003.

[35] L. P. Franca and R. Stenberg. Error analysis of Galerkin least squares methods for the elasticity equations. *SIAM J. Numer. Anal.*, 28(6) :1680–1697, 1991.

[36] R. Glowinski and A. Marrocco. Sur l'approximation, par éléments finis d'ordre un, et la résolution, par pénalisation-dualité, d'une classe de problèmes de Dirichlet non linéaires. *Rev. Française Automat. Informat. Recherche Opérationnelle Sér. Rouge Anal. Numér.*, 9 :41–76, 1975.

[37] P. Grisvard. *Elliptic problems in nonsmooth domains*, volume 69 of *Classics in Applied Mathematics*. Society for Industrial and Applied Mathematics (SIAM), Philadelphia, PA, 2011. Reprint of the 1985 original [MR0775683], With a foreword by Susanne C. Brenner.

[38] W. G. Habashi, M. Fortin, J. Dompierre, M.-G. Vallet, and Y. Bourgault. Anisotropic mesh adaptation : a step towards a mesh-independent and user-independent CFD. In *Barriers and challenges in computational fluid dynamics (Hampton, VA, 1996)*, volume 6 of *ICASE/LaRC Interdiscip. Ser. Sci. Eng.*, pages 99–117. Kluwer Acad. Publ., Dordrecht, 1998.

[39] S. C. Headquarters. *3d precise mesh.* Broomfield, 222.3ds.com.

[40] T. F. Hilke. Méthodes numériques liées à la distribution d'alumine dans une cuve d'électrolyse d'aluminium. Technical report, EPFL, 2019.

[41] T. Hofer. Numerical simulation and optimization of the alumina distribution in an aluminium electrolysis pot. Technical report, EPFL, 2011.

[42] T. J. R. Hughes, L. P. Franca, and M. Balestra. A new finite element formulation for computational fluid dynamics. V. Circumventing the Babuška-Brezzi condition : a stable Petrov-Galerkin formulation of the Stokes problem accommodating equal-order interpolations. *Comput. Methods Appl. Mech. Engrg.*, 59(1) :85–99, 1986.

[43] G. Kunert. An a posteriori residual error estimator for the finite element method on anisotropic tetrahedral meshes. *Numer. Math.*, 86(3) :471–490, 2000.

[44] G. Kunert and S. Nicaise. Zienkiewicz-Zhu error estimators on anisotropic tetrahedral and triangular finite element meshes. *M2AN Math. Model. Numer. Anal.*, 37(6) :1013–1043, 2003.

[45] G. Kunert and R. Verfürth. Edge residuals dominate a posteriori error estimates for linear finite element methods on anisotropic triangular and tetrahedral meshes. *Numer. Math.*, 86(2) :283–303, 2000.

[46] P. Laug and H. Borouchaki. The BL2D Mesh Generator : Beginner's Guide, User's and Programmer's Manual. *Technical report RT-0194, Institut National de Recherche en Informatique et Automatique (INRIA), Rocquencourt, Le Chesnay, France*, 1996.

[47] J.-L. Lions. *Optimal control of systems governed by partial differential equations*, volume Band 170 of *Die Grundlehren der mathematischen Wissenschaften.* Springer-Verlag, New York-Berlin, 1971. Translated from the French by S. K. Mitter.

[48] W. Liu and N. Yan. Quasi-norm local error estimators for p-Laplacian. *SIAM J. Numer. Anal.*, 39(1) :100–127, 2001.

[49] W. Liu and N. Yan. Some a posteriori error estimators for p-Laplacian based on residual estimation or gradient recovery. *J. Sci. Comput.*, 16(4) :435–477, 2001.

[50] W. B. Liu and J. W. Barrett. Quasi-norm error bounds for the finite element approximation of some degenerate quasilinear elliptic equations and variational inequalities. *RAIRO Modél. Math. Anal. Numér.*, 28(6) :725–744, 1994.

[51] A. Loseille and F. Alauzet. Continuous mesh framework part I : well-posed continuous interpolation error. *SIAM J. Numer. Anal.*, 49(1) :38–60, 2011.

[52] A. Lozinski, M. Picasso, and V. Prachittham. An anisotropic error estimator for the Crank-Nicolson method : application to a parabolic problem. *SIAM J. Sci. Comput.*, 31(4) :2757–2783, 2009.

[53] S. Micheletti and S. Perotto. Reliability and efficiency of an anisotropic Zienkiewicz-Zhu error estimator. *Comput. Methods Appl. Mech. Engrg.*, 195(9-12) :799–835, 2006.

[54] S. Micheletti, S. Perotto, and M. Picasso. Stabilized finite elements on anisotropic meshes : a priori error estimates for the advection-diffusion and the Stokes problems. *SIAM J. Numer. Anal.*, 41(3) :1131–1162, 2003.

[55] J.-M. Mirebeau. Optimally adapted meshes for finite elements of arbitrary order and $W^{1,p}$ norms. *Numer. Math.*, 120(2) :271–305, 2012.

[56] P. Passelli and M. Picasso. Anisotropic adaptive finite elements for a p-Laplacian problem. *Submitted to : Computational Methods in Applied Mathematics.*

[57] P. Passelli and M. Picasso. Adaptive finite elements with large aspect ratio for aluminium electrolysis. *in : admos2023*, 2023.

[58] M. Picasso. Adaptive finite elements for a linear parabolic problem. *Comput. Methods Appl. Mech. Engrg.*, 167(3-4) :223–237, 1998.

[59] M. Picasso. An anisotropic error indicator based on Zienkiewicz-Zhu error estimator : application to elliptic and parabolic problems. *SIAM J. Sci. Comput.*, 24(4) :1328–1355, 2003.

[60] M. Picasso. Numerical study of the effectivity index for an anisotropic error indicator based on Zienkiewicz-Zhu error estimator. *Comm. Numer. Methods Engrg.*, 19(1) :13–23, 2003.

[61] M. Picasso. An adaptive algorithm for the Stokes problem using continuous, piecewise linear stabilized finite elements and meshes with high aspect ratio. *Appl. Numer. Math.*, 54(3-4) :470–490, 2005.

[62] M. Picasso. Adaptive finite elements with large aspect ratio based on an anisotropic error estimator involving first order derivatives. *Comput. Methods Appl. Mech. Engrg.*, 196(1-3) :14–23, 2006.

[63] M. Picasso. Numerical study of an anisotropic error estimator in the $L^2(H^1)$ norm for the finite element discretization of the wave equation. *SIAM J. Sci. Comput.*, 32(4) :2213–2234, 2010.

[64] S. B. Pope. *Turbulent flows.* Cambridge University Press, Cambridge, 2000.

[65] J.-F. Remacle, X. Li, M. S. Shephard, and J. E. Flaherty. Anisotropic adaptive simulation of transient flows using discontinuous Galerkin methods. *Internat. J. Numer. Methods Engrg.*, 62(7) :899–923, 2005.

[66] S. Renaudier. Modélisation de l'écoulement dans les cuves d'électrolyse. Technical report, Rapport Interne, LRF, 2015.

[67] J. Rochat. Approximation numérique des écoulements turbulents dans des cuves d'électrolyse de l'aluminium. Technical report, EPFL, 2016.

[68] Y. Safa. Simulation numérique des phénomènes thermiques et magnétohydrodynamiques dans une cellule de hall-héroult. Technical report, EPFL, 2005.

[69] E. T. P. Soutter. A mixture model to take into account diluted gas in liquid flow : applications to aluminium electrolysis. Technical report, EPFL, 2022.

[70] G. Steiner. Simulation numérique de phénomènes mhd. Technical report, EPFL, 2009.

[71] R. Verfürth. A posteriori error estimation and adaptive mesh-refinement techniques. In *Proceedings of the Fifth International Congress on Computational and Applied Mathematics (Leuven, 1992)*, volume 50, pages 67–83, 1994.

[72] R. Verfürth. *A posteriori error estimation techniques for finite element methods*. Numerical Mathematics and Scientific Computation. Oxford University Press, Oxford, 2013.

[73] R. Verfürth. *A review of A Posteriori Error Estimation and Adaptive Mesh-Refinement Techniques*. Wiley-Teubner, 1996.

[74] J. Xu and Z. Zhang. Analysis of recovery type a posteriori error estimators for mildly structured grids. *Math. Comp.*, 73(247) :1139–1152, 2004.

[75] O. C. Zienkiewicz and J. Z. Zhu. A simple error estimator and adaptive procedure for practical engineering analysis. *Internat. J. Numer. Methods Engrg.*, 24(2) :337–357, 1987.

[76] O. C. Zienkiewicz and J. Z. Zhu. The superconvergent patch recovery and a posteriori error estimates. I. The recovery technique. *Internat. J. Numer. Methods Engrg.*, 33(7) :1331–1364, 1992.

PARIDE PASSELLI

Education

PhD in Applied Mathematics: EPF Lausanne, 2019 – 2024
Thesis title: Adaptive Finite Elements With Large Aspect Ratio. Application to Aluminium Electrolysis.

MSc in Mathematics: EPF Lausanne, 2018 – 2019
Thesis title: An Advection Diffusion Optimal Control Problem Related to Aluminium Production.
Master project title: Numerical Methods for Deterministic Seismic Source Inversion.

BSc in Mathematics: EPFL Lausanne, 2014 – 2018

Skills

Programming: Python, C++, Matlab, FEniCS, Octave, FreeFem++.
Other tools: git, svn, Jupyter, UNIX/Linux, bash, Paraview, Ensight, Latex.

Languages

English, Fluent.
French, Fluent.
German, Conversational.
Italian, Native.

Publications

Passelli P., Picasso M., *Anisotropic Adaptive Finite Elements for p-Laplacian Problem.* Computational Methods in Applied Mathematics (2023). Under consideration after revision.

Dubuis, S., Passelli, P., Picasso, M., *Anisotropic Adaptive Finite Elements for an Elliptic Problem with Strongly varying Diffusion Coefficient.* Computational Methods in Applied Mathematics, vol. 22, no. 3, 2022, pp. 529-543. doi.org/10.1515/cmam-2022-0036

Passelli, P., Picasso, M., *Adaptive Finite Elements with Large Aspect Ratio for Aluminium Electrolysis,* in Presentations to 11th international Conference on Adaptive Modelling and Simulation (ADMOS) (2023). DOI: 10.23967/admos.2023.060

Passelli, P., Picasso, M., *Adaptive Finite Elements with Large Aspect Ratio for Aluminium Electrolysis.* in Presentations and videos to 10th international Conference on Adaptive Modelling and Simulation (ADMOS) (2021). DOI: 10.23967/admos.2021.014

Oral Presentations

ECCOMAS Congress, 11-15 January 2021 (Virtual).

ADMOS, 21-23 June 2021 (Virtual).

ECCOMAS Congress, 5-9 June 2022 Oslo.

CANUM 45eme Congrès National d'Analyse Numérique, 13-17 June 2022 Evian-les-Bains.

Reliable Methods of Mathematical Modeling, 21-23 June 2022 Lausanne (Local Co-organizer).

15th World Congress on Computational Mechanics & 8th Asian Pacific Congress on Computational Mechanics, 31 July- 5 August 2022 (Virtual).

Swiss Numerics Day, 12 September 2022 Zurich.

22nd Computational Fluids Conference, 25-28 April 2023 Cannes.

CMS summer meeting, 2-5 June 2023 Ottawa.

ADMOS 2023, 19-21 June 2023 Gothenburg.

Personal Information

Swiss. Born 29. Mai 1995.